

WELDING OF DISSIMILAR METALS (ALUMINIUM 8000 SERIES WITH ALUMINIUM 6000 SERIES) USING COLD METAL TRANSFER (CMT) WELDING TECHNIQUE

A Thesis Submitted

**In Partial Fulfilments of the Requirements
for the Degree of**

DOCTOR OF PHILOSOPHY

by

INDRA JEET SINGH

[Roll No. 2K18/PHDME/510]

Under the Supervision of

Prof. Qasim Murtaza

(Professor)

Mechanical Engineering Department

Dr. Paras Kumar

(Associate Professor)

Mechanical Engineering Department



Department of Mechanical Engineering

DELHI TECHNOLOGICAL UNIVERSITY, DELHI

(Formally Delhi College of Engineering)

Shahbad Daultpur, Main Bawana Road, Delhi-110042

July, 2025



DELHI TECHNOLOGICAL UNIVERSITY, DELHI
(Formerly Delhi College of Engineering)
Shahbad Daultpur, Main Bawana Road, Delhi-110042

ACKNOWLEDGMENT

I express my deepest sense of gratitude to my supervisors, **Prof. Qasim Murtaza** and **Dr. Paras Kumar (Associate Professor)**, for their invaluable guidance, unwavering support, and constant encouragement throughout the course of my doctoral research. Their expertise and mentorship have been instrumental in shaping this thesis.

I am sincerely thankful to **Prof. Atul Agarwal**, DRC Chairman, for his continuous guidance and insightful suggestions. I also extend my heartfelt thanks to **Tekchand Sir** and **Veeran Sir** for their support and assistance during various phases of this work.

I am deeply grateful to my family for their constant love and support. My father, **Shri Somendra Singh Yadav**, and my mother, **Smt. Gargi Devi**, have been my pillars of strength, whose blessings and sacrifices have made every achievement possible. I sincerely thank my brother **Kamal Jeet**, my sister **Kirti**, and my wife **Dipti** for their patience, encouragement, and understanding throughout this demanding journey. My little ones, **Anant Jeet** and **Bhargavi**, though too young to understand this milestone, have been a source of immense joy and inspiration, bringing light and warmth to even the toughest days. I also affectionately acknowledge my nephew **Aarya** and **Raghav Krishna**, who have always added happiness to our home. This thesis is lovingly **dedicated to my late grandmothers Smt. Kanthshree Devi (Ammu) and Smt. Aruna Devi (Maiya)**. Their blessings continue to guide me at every step.

Above all, I bow with devotion to my **Guru Maharaj Shree Bajrang Bali**, whose divine blessings made this journey possible.

ॐ हनुमते नमः

मनोजवं मारुततुलं जितेन्द्रि बुद्धिमत् वरिष्ठ ।
वातात्म वानरयूथमु श्रीरामद्वयं शरणं प्रपद्ये ॥

Indra Jeet Singh



DELHI TECHNOLOGICAL UNIVERSITY, DELHI
(Formally Delhi College of Engineering)
Shahbad Daultpur, Main Bawana Road, Delhi-110042

DECLARATION

I Indra Jeet Singh hereby certify that the work which is being presented in the thesis entitled **Welding of Dissimilar Metals (Aluminum 8000 series with Aluminum 6000 series) Using Cold Metal Transfer (CMT) Welding Technique** in partial fulfillment of the requirements for the award of the Degree of Doctor of Philosophy, submitted in the Department of Mechanical Engineering, Delhi Technological University is an authentic record of my own work carried out during the period from August 2018 to July 2025 under the supervision of Prof. Qasim Murtaza, and Dr. Paras Kumar. The matter presented in the thesis has not been submitted by me for the award of any other degree of this or any other Institute.

Candidate Signature

This is to certify that the student has incorporated all the corrections suggested by the examiners in the thesis and the statement made by the candidate is correct to the best of our knowledge.

Signature of Supervisors

Signature of External



DELHI TECHNOLOGICAL UNIVERSITY, DELHI
(Formally Delhi College of Engineering)
Shahbad Daulatpur, Main Bawana Road, Delhi-110042

CERTIFICATE BY THE SUPERVISOR

This is to certify that the Ph.D. thesis entitled "**Welding of Dissimilar Metals (Aluminum 8000 series with Aluminum 6000 series) Using Cold Metal Transfer (CMT) Welding Technique**" being submitted by **Mr. INDRA JEET SINGH** for the award of the degree of Doctor of Philosophy in Mechanical Engineering, to Delhi Technological University, Delhi, India, is a Bonafide record of original research work carried out by him under my guidance and supervision. The work presented in this thesis has not been submitted to any other university or institution for the award of any degree or diploma.

Prof. Qasim Murtaza

Professor,

Department of Mechanical Engineering

Delhi Technological University, Delhi

Dr Atul Kumar Agarwal

DRC Chairman

Department of Mechanical Engineering

Delhi Technological University, Delhi

Dr. Paras Kumar

Associate Professor

Department of Mechanical Engineering

Delhi Technological University

Abstract

The present study investigates the successful fabrication of dissimilar aluminum alloys AA6061 and AA8011 using the Cold Metal Transfer (CMT) welding technique. CMT welding, characterized by its low heat input and stable arc behavior, has emerged as an effective process for joining aluminum alloys with distinct thermal and mechanical properties. This research aims to optimize the key input parameters—welding current, welding speed (WS), and gas flow rate (GFR)—and to evaluate their influence on critical output responses such as ultimate tensile strength (UTS), percentage strain, hardness in the weld fusion zone (WFZ), and residual stress.

A comprehensive statistical analysis was performed using Analysis of Variance (ANOVA) to quantify the significance of each input parameter. The results confirmed that all three input variables significantly affected the output responses, as indicated by P-values below the 0.05 threshold. The F-values for UTS (21.96), percentage strain (15.32), hardness (18.13), and residual stress (16.81) further validated the statistical significance of the developed models and the strong influence of input parameters on weld performance. Microstructural characterization revealed that the weld fusion zone predominantly consisted of Mg₂Si precipitates and globular primary α -Al phases, with α -particles aligning along the grain boundaries. The heat-affected zone (HAZ), subjected to a more intense thermal cycle, exhibited a decreased population of α -Al particles and a lower level of precipitate formation, distinguishing its structure from that of the base metal. These microstructural transformations played a critical role in determining the mechanical behavior of the joint. The mechanical testing results highlighted a maximum UTS of 108.74 MPa for sample 11 and a minimum of 72.69 MPa for sample 5. The enhanced mechanical properties, particularly in the WFZ, were attributed to the refined grain structure and the formation of fine secondary phases. The hardness in the weld zone corresponded well with these microstructural features. Residual stress analysis indicated that the maximum compressive stress of -65 MPa occurred at a welding current of 80 A, WS of 10 mm/s, and GFR of 14 l/min. Conversely, the lowest compressive stress of -9 MPa was observed at a current of 60 A, WS of 10 mm/s, and GFR of 18 l/min. These findings underline the crucial role of process parameters in controlling residual stress levels, which in turn affect joint integrity.

Through numerical optimization, the ideal set of process parameters was determined to be a welding current of 77.86 A, a welding speed of 9.26 mm/s, and a gas flow rate of 15.26 l/min. At these conditions, the predicted optimized output responses were an ultimate tensile strength of 89.19 MPa, percentage strain of 11.36%, hardness of 78.88 HV, and residual stress of -36.47 MPa.

Keywords: Cold metal transfer, Microstructure, Tensile strength, Microhardness, Intermetallic Compounds, Residual stress

List of Publications

Journal Publication

1. Indra Jeet Singh, Qasim Murtaza, Paras kumar, A comprehensive review on effect of cold metal transfer welding parameters on dissimilar and similar metal welding, Journal of Engineering Research, 2023, <https://doi.org/10.1016/j.jer.2023.12.009>. (Elsevier)
2. Indra Jeet Singh, Qasim Murtaza, Paras kumar, Effect of welding speed on metallurgical characterization of CMT welding of dissimilar aluminium alloys of AA6061 and AA8011, Silicon, 2024, <https://doi.org/10.1007/s12633-024-02961-6>. (Springer)
3. Indra Jeet Singh, Qasim Murtaza, Paras kumar, Effect of CMT Welding Process Parameters on the Microstructural and Mechanical Properties of Dissimilar Aluminum Alloys of AA8011 and AA6061, Transactions of the Indian Institute of Metals, 2024, <https://doi.org/10.1007/s12666-024-03471-0>. (Springer)
4. Indra Jeet Singh, Qasim Murtaza, Paras kumar, Optimization of input and output process parameters and microstructural analysis of CMT dissimilar aluminum welded joint of AA8011 and AA6061. Journal of Materials Engineering and Performance, 2025, <https://doi.org/10.1007/s11665-025-11632-5>. (Springer)
5. Indra Jeet Singh, Qasim Murtaza, Paras kumar, Optimization of process parameters and microstructural analysis of CMT welded joints of dissimilar aluminum alloys. JOM, 2025, <https://doi.org/10.1007/s11837-025-07871-5>. (Springer).

Conference Publications

1. Indra Jeet Singh, Qasim Murtaza, Paras kumar, An overview of cold metal transfer welding of similar materials, International Journal on Interactive Design and Manufacturing (IJIDeM), 2024, <https://doi.org/10.1007/s12008-023-01719-5>. (Springer)
2. Indra Jeet Singh, Qasim Murtaza, Paras kumar, An Overview of Dissimilar Metals Welding by Cold Metal Transfer Technique, Journal of Polymer & Composites, 2024, DOI (Journal): 10.37591/JoPC (STM Journals)

Table of Contents

ACKNOWLEDGMENT.....	i
DECLARATION	ii
CERTIFICATE BY THE SUPERVISOR.....	iii
Abstract	iv
List of Publications.....	v
Table of Contents	1
List of Tables.....	4
List of Figures	5
List of Abbreviation	8
List of Symbols	9
CHAPTER- 1	10
1 Introduction.....	10
1.1 Shielded Metal Arc Welding (SMAW).....	12
1.2 Gas Metal Arc Welding (GMAW) technique	13
1.3 GTAW process	14
1.4 Cold Metal Transfer (CMT) welding process parameter	15
1.4.1 Wire Feed Speed (WFS)	17
1.4.2 Welding Current.....	17
1.4.3 Arc Voltage	17
1.4.4 Travel Speed.....	18
1.4.5 Shielding Gas Composition and Flow Rate	18
1.4.6 Torch Angle and Position.....	18
1.5 CMT droplet transfer cycle	18
1.6 Various types of filler materials	22
1.6.1 ER4043 Filler Wire	23
1.6.2 ER4045 Filler Wire	23
1.6.3 ER5356 Filler Wire	23
1.6.4 ER5556 Filler Wire	24
1.6.5 ER5183 Filler Wire	24
1.7 Effect of different shielding gases in CMT weldments.....	25
1.7.1 Argon	25
1.7.2 Helium.....	26
1.7.3 Carbon Dioxide (CO ₂).....	26
1.7.4 Combination of different shielding gases	26
1.8 Aluminum alloy.....	29
1.9 Types of Al-alloys	30
1.9.1 1XXX series	30
1.9.2 2XXX series	30
1.9.3 3XXX series	31
1.9.4 4XXX series	31
1.9.5 5XXX series	31
1.9.6 6XXX series	31
1.9.7 7XXX series	32
1.9.8 8XXX series	32

1.10	History of parent material.....	33
1.10.1	AA6061	33
1.10.2	AA8011	33
1.11	Problem Formulation.....	35
1.12	Motivation	36
1.13	Novelty	37
CHAPTER-2	38
2	Literature Review	38
2.1	CMT welding of dissimilar alloys.....	39
2.1.1	CMT welding of Al/Mg alloys.....	39
2.1.2	CMT welding of Al and Ti alloys	43
2.1.3	CMT welding of aluminum and steel.....	45
2.1.4	CMT welding of steel and Ti alloys.....	52
2.2	Welding of similar alloys	54
2.2.1	CMT welding of Mg- alloys	55
2.2.2	CMT welding of Ti alloys.....	59
2.2.3	CMT welding of Cu alloys.....	61
2.3	Heat Input analysis	63
2.4	Numerical analysis of CMT weldments	64
2.4.1	Heat Transfer Governing Equation in CMT Welding.....	64
2.4.2	Strain Components in Thermo-Mechanical Modeling.....	65
2.4.3	Thermal and Elastic Strain Formulations.....	66
2.5	Research Gaps from the Literature.....	74
2.6	Objectives	75
CHAPTER-3	76
3	Research Methodology	76
3.1	Chemical elements of the base metal	77
3.2	Experimental procedure	77
3.3	V groove preparation.....	77
3.4	Fabrication of CMT welded joint.....	78
3.4.1	CMT machine.....	79
3.4.2	Welding Torch	80
3.4.3	Speed Control Device	80
3.4.4	Rail Track.....	81
3.4.5	Gas Cylinder (Shielding Gas Supply)	82
3.4.6	Arc Ignition and Droplet Transfer.....	82
3.4.7	Arc Stability During Welding	83
3.5	Design of Experiments	83
3.5.1	Specimens' preparation.....	85
3.5.2	Tensile test	87
3.5.3	Micro-hardness.....	88
3.5.4	Residual stress measurement.....	89
3.5.5	Metallurgical Characteristics Evaluation	90
3.5.6	Experimental damping setup.....	93
CHAPTER-4	96
4	Results and discussion	96
4.1	Introduction	96

4.2	Adequacy of the developed model	96
4.3	Developing a regression model	100
4.4	Input and output response's correlation of the welded joints.....	102
4.5	Predicted vs actual scattered diagram.....	110
4.6	Mechanical properties	114
4.7	Microstructure analysis	116
4.8	XRD analysis.....	122
4.9	Tensile strength	126
4.10	Hardness evaluation	128
4.11	TEM analysis of welded joint.....	135
4.12	Fractography analysis.....	136
4.13	Damping behavior of CMT welded joints of AA 8011 and AA6061	137
CHAPTER-5		141
5	Conclusions.....	141
5.1	Future works and scope	143
References		145
6	List of Publications and their proof	154

List of Tables

Table 1: Typical Processing Parameters in CMT Welding.....	19
Table 2: Common Filler Rods for CMT Welding of Aluminum Alloys	25
Table 3: Overview of Base Metals and Filler Wires Used in CMT Welding for Aluminum–Steel Dissimilar Joints [56].....	51
Table 4: Percentage (weight) of chemical elements in the filler and base metals	77
Table 5: CMT welding parameters and their ranges	83
Table 6: Design of experiments in expanded form	84
Table 7: ANOVA table of UTS of CMT weldment of AA8011 and AA6061	97
Table 8: ANOVA table of % strain for CMT weldments of AA8011 and AA6061 ..	98
Table 9: ANOVA table of hardness for CMT weldments	99
Table 10: ANOVA table of residual stress for CMT weldments	99
Table 11: Fit Statistics data for UTS, % strain, and hardness values for CMT weldments	100
Table 12: Mechanical characteristics of the weldments of AA8011 and AA6061 with different process parameters	115
Table 13: CMT welding parameters	126
Table 14: Mechanical Properties of the CMT welded joint of AA8011 and AA6061	127

List of Figures

Figure 1: Working process of SMAW [28].....	12
Figure 2: Gas metal arc welding [29].....	13
Figure 3: Working of GTAW [30].....	14
Figure 4: CMT machine at DTU, Delhi	16
Figure 5: Sequential arc evolution during a stable CMT droplet detachment cycle under Group 4 parameters — (a) Arc behavior in Electrode Positive (EP) polarity, (b) Arc dynamics in Electrode Negative (EN) polarity [31].....	19
Figure 6: Comparison of Droplet Volume Growth Trends in Rapid and Slow Growth Stages under Different CMT Welding Parameter Groups [31]	20
Figure 7: High-speed photographic sequence of droplet transfer behavior in T-CMT-DED at different deposition currents: (a) 100 A, (b) 125 A, (c) 150 A, and (d) 175 A [32].....	21
Figure 8: Variation of current and frequency to the diameters of molten droplet [32]	22
Figure 9: Variation of different shielding gases on the weld bead and their penetration [37]	27
Figure 10: OM images of CMT weldments with different shielding gasses, (a) 50% He +50%Ar, (b) 50% He, 45% Ar+5%O ₂ , (c) 45% He+ 45% Ar+10% N ₂ , (d) 100% He [38]	28
Figure 11: Variation of hardness dissemination from the weld center, (a) upper surface, (b) lower surface, A: 50% He +50%Ar, B: 50% He, 45% Ar+5% O ₂ , C: 45% He+ 45% Ar+10% N ₂ , D: 100% He [38]	28
Figure 12: Flowchart of CMT Welding Process and Its Applications in Metal Joining	38
Figure 13: OM images CMT weldments of AA1060 and AZ31, (a) weld Interface, (b-c) microstructure at different welded region (A, B, and C) [39]	40
Figure 14: Hardness Distribution Across AZ31B/AA6061 Dissimilar Weld Joint [40]	42
Figure 15: Cross-sectional View of Al/Ti Multi-layered Structure Fabricated by WAAM on Ti Substrate [43].....	44
Figure 16: Hybrid Joining Process of AISI 321 Stainless Steel and AA2219 using Friction Surfacing and CMT Welding [47].....	46
Figure 17: Influence of Aluminum Coating Thickness on Interfacial Microstructure of Al/SS Hybrid Lap Joints Formed by Friction Surfacing and CMT Welding [47]	47
Figure 18: Schematic Diagram of CMT Welding Setup for Dissimilar Aluminum-Steel Lap Joint Configuration [49].....	48
Figure 19: Current and Voltage Characteristics Illustrating the Metal Transfer Mechanism in the CMT Process [53].....	50
Figure 20: Influence of EP: EN Polarity Ratio on Thermal Distribution, Intermetallic Layer Thickness, Ti Si Distribution, and Tensile Strength in Ti-6Al-4V/304L CMT Weldments [57]	53
Figure 21: EBSD and IPF analysis of Ni-based and Fe-based coatings deposited by the CMT process—(a) IPF map of Ni-based coating, (b) IPF map of Fe-based	

coating, (c) misorientation angle distribution of Ni-based coating, (d) misorientation angle distribution [61]	54
Figure 22: CMT weld bead at different process parameters [64]	56
Figure 23: SEM Micrographs of the WFZ in AZ31 Welded by CMT at Different WS: (a) 8 mm/s, (b) 10 mm/s, (c) 12 mm/s, and (d) 14 mm/s [67]	57
Figure 24: Fractured images of CMT weldments of AZ31, (a) longitudinal direction, (b) transverse direction [68]	58
Figure 25: Microstructure of single-track deposition, (a, b) weld appearance, (c) non UPT condition, (d) UPT condition [71]	59
Figure 26: SEM images of fractured surface of CMT weldments of Ti6Al4V, (a) ZX orientation, (b) XY orientation [72]	60
Figure 27: Variation of micro-hardness along the deposition height of Cu-Al alloy deposited using the CMT process at different holding durations (0 h, 6 h, 12 h, and 24 h) after Deep Cryogenic Treatment (DCT) [73]	61
Figure 28: Tensile properties (UTS, YS, and elongation) of Cu-Al-Si alloy deposited using CMT process at different Deep Cryogenic Treatment (DCT) holding durations [73]	62
Figure 29: Thermal strain–temperature relationship of steel during heating and cooling cycles, illustrating hysteresis behavior and phase transformation effects [85]	67
Figure 30: Variation in Thermal Physical and Mechanical Properties of Steel Used in CMT Weldments [85]	67
Figure 31: Velocity contour along the longitudinal direction during CMT welding at various time intervals [86]	68
Figure 32: Flow chart of existing research work	76
Figure 33: 60° V groove plates before CMT welding	78
Figure 34: (a) CMT welding machine, (b, c) CMT welding process.....	79
Figure 35: CMT welding torch	80
Figure 36: Speed control device.....	81
Figure 37: Rail track arrangement of CMT welding.....	82
Figure 38: CMT welded joints of AA8011 and AA6061	85
Figure 39: (a) Removal of weld bead by shaper machine, (b) finishing of the welded plate	86
Figure 40: Schematic diagram of Microstructure, hardness and tensile test specimen preparation.....	86
Figure 41: UTM machine at DTU, Delhi.....	87
Figure 42: Vickers micro hardness testing process.....	88
Figure 43: Apparatus for analyzing the residual stresses.....	89
Figure 44: (a) polishing with emery paper, (b) polishing with emery cloth with Al ₂ O ₃ powder, (c) specimen after polishing, (d) making etching solution.....	91
Figure 45: (a) Optical microscopic (Shobhit University, Meerut) and SEM machine (IIT Delhi)	92
Figure 46: Experimental Modal Analysis Setup for Evaluating Damping Characteristics of Welded Joints.....	94
Figure 47: 3D contour and their responses of tensile strength of the CMT weldments	104
Figure 48: 3D contour of % strain of the CMT weldments	105

Figure 49: 3D contour of hardness of the CMT weldments	106
Figure 50: Profile of residual stress, Debye ring, and distortion profile of the weldments, (a) Sample 7, (b) Sample 8, (c) Sample 11	107
Figure 51: 3D contour of residual stress of the weldments.....	108
Figure 52: Predicted vs actual diagram of the weldments, (a) Tensile strength, (b) % strain, (c) Hardness, (d) Residual stress	111
Figure 53: Perturbation curve of CMT weldments (a) Tensile strength, (b) % strain, (c) Hardness, (d) Residual stress	112
Figure 54: Optimize value of input and output responses of CMT weldments	113
Figure 55: Mechanical properties of the CMT weldments of AA8011 and AA6061, (a) 60 A, (b) 70 A, (c) 80 A.....	116
Figure 56: Optical images of parent material, (a) AA6061, (b) AA8011	117
Figure 57: (a) Macrostructure of the welded joint, (b) OM image of weldments at the fusion for sample 8, (c) HAZ image, (d) WFZ for sample 11	118
Figure 58: SEM images CMT weldments of AA8011 and AA6061, (a) Sample No 7, (b) Sample No 11, EDS images of the weldments, (c) Sample No. 7, (d) Sample No. 11.....	120
Figure 59: XRD peaks of the weldments	122
Figure 60: Stress-strain diagram of CMT welded joint	127
Figure 61: Variation of microstructure of the welded joint from the weld centre ...	129
Figure 62: Different zone of CMT weldments of AA8011 and AA6061 with filler ER4043.....	131
Figure 63: Optical microstructure of the CMT welded joint of AA8011 and AA6061 at the WFZ, (a) WS-5mm/s, current 50 A, (b) WS-10mm/s, current 60 A, (c) WS-15 mm/s, current 70 A, (d) WS- 20 mm/s, current 80 A.....	132
Figure 64: High magnification SEM images of CMT welded joint at the WFZ, (a) CMT-P1, (b) CMT-P2, (c) CMT-P3, (d) CMT-P4	134
Figure 65: High magnification TEM images of CMT welded joint of AA8011 and AA6061, (a) FZ, (b) HAZ	136
Figure 66: SEM images of fractured surface, (a) specimen number 5, (b) Specimen number 11	137
Figure 67: Time-Domain Acceleration Response of CMT Welded Joints (a) CMT-P1, (b) CMT-P2, (c) CMT-P3, and (d) CMT-P4 for AA6061-AA8011 Dissimilar Welds.....	138
Figure 68: Damping behaviour of the CMT welded joints, (a) 10 mm/sec and 60 A, (b) 15 mm/sec and 70 A, (c) 20 mm/sec and 80 A,	139

List of Abbreviation

GTAW	Gas Tungsten Arc Welding
GMAW	Gas Metal Arc Welding
CMT	Cold Metal Transfer
THI	Thermal heat input
TWBs	Tailor-welded blanks
DSAW	Double-sided arc welding
PWHT	post-weld heat treatments
IMCs	Intermetallic compounds
WFS	Wire Feed Speed
SMAW	Shielded Metal Arc Welding
HAZ	heat-affected zone
SEM	Scanning Electron Microscopy
EDS	Energy-Dispersive X-ray
XDR	X-ray Diffraction
GFR	Gas flow rate
WS	Welding Speed
DOE	Design of Experiments
ANOVA	Analysis of Variance
FRF	frequency response function)
WFZ	Weld Fusion Zone
PMZ	Partially Melted Zone
WAAM	Wire arc additive manufacturing

List of Symbols

E	Young's modulus, Poisson's ratio, Kronecker delta.
V	voltage
I	Welding current
S	Welding speed process efficiency material density (kg/m ³)
c	Specific heat capacity (J/kg·K),
k	Thermal conductivity (W/m·K),
T	Temperature (K)
q	Volumetric internal heat generation rate (W/m ³)
t	time (s).
Q	Net heat flux from the surface (W/m ²), Heat transfer coefficient (W/m ² ·K).
S_e	Solute content in the AMC
C_p	Element's concentration
C_i	Solute's concentration
\bar{S}	Mean solute content in the AMC
f	Volume fraction
b	28.4×10^{-11}
M	3.1 (Taylor constant)
γ	0.2 (Interface energy of particle)
r_i	Radius of particle
β	0.37 (Dissolution constant)
G	27.0×10^{-11} N/m ³
D	Coefficient of diffusion
E_0	16.22 kJ/mol (Nucleation's energy barrier)
\bar{r}	Mean particle radius
V_m	39.5×10^{-6} m ³ /mol
r	Radius of particles
r_c	Critical radius
N_i	Particle's density number
C_{Fe}	Scaling factor of Fe
C_{Si}	Scaling factor of Si
C_{Mg}	Scaling factor of Mg
k_{Si}	Concentration of Si
k_{Fe}	Concentration of Fe
k_{Mg}	Concentration of Mg
F_i	Particle radius' function

CHAPTER- 1

Introduction

Welding is a process used to join two materials—either similar or dissimilar—by creating a strong bond at their contact surfaces. This bonding can occur with or without melting the base materials. When pressure is used without melting to form the joint, the process is referred to as pressure welding or solid-state welding. On the other hand, if the base materials are melted and fused together, the process is called fusion or autogenous welding. In many cases, fusion welding involves the addition of a filler material, typically in the form of a rod or wire, which melts and fills the joint area to strengthen the bond. Common examples of fusion welding include arc welding, gas welding, Gas Tungsten Arc Welding (GTAW) welding, and Gas Metal Arc Welding (GMAW) welding. These techniques vary based on the heat source, filler usage, and shielding methods. Among the numerous welding processes available, certain arc welding methods are especially predominant due to their efficiency and adaptability. Arc welding processes, in particular, are widely adopted across various sectors and are fundamental to modern fabrication and manufacturing practices.

The Cold Metal Transfer (CMT) technique is an advanced technique of the conventional GMAW welding process. Despite its designation as cold, the process still uses heat to fuse metals. However, it dramatically lowers the thermal heat input (THI), thereby reducing the risk of distortion, particularly during short-circuit metal transfer, where current does not fall to zero [1]. What makes CMT unique is its use of advanced digital control to synchronize wire feeding and retracting with the short-circuiting cycle. This enables the molten droplet to detach cleanly from the wire tip, enhancing weld quality and minimizing spatter and heat input when compared to conventional MIG processes [2].

In recent years, Al-alloys have progressively replaced steel in the various industries including shipbuilding, aerospace, automotive manufacturing, and infrastructure. The primary driving force behind this transition is aluminum's lightweight, which contributes to improved fuel efficiency and lower energy consumption in transportation sectors. This switch also aligns with global sustainability initiatives. Moreover, aluminum alloys exhibit excellent corrosion resistance and high strength, which are critical for long-term structural applications. One such alloy, AA8011, primarily contains Si, Fe, and Mn as its alloying constituents [3]. The presence of trace elements like Mn and Mg enhances the metallurgical properties of the alloy. Thin aluminum sheets are rapidly gaining popularity, particularly in automotive design. These sheets offer a balance of lightweight, mechanical durability, and recyclability, making them attractive for environmentally conscious manufacturing. The automotive industry is leveraging these properties to improve engine performance and fuel efficiency through weight reduction [4,5]. Among the numerous aluminum grades available, 6082-T6 and 6061-T6 stand out due to their exceptional strength, which is largely attributed to the presence of Mg and Si [6–9]. These alloys are widely adopted in sectors ranging from transportation to

construction and defense. Despite its benefits, welding thin aluminum sheets remains challenging, especially when using traditional arc welding techniques. The thermal conductivity of aluminum is significantly higher than that of steel, which can lead to over-penetration, poor weld bead control, and excessive spatter during conventional MIG welding. These limitations can lead to increased post-processing efforts. The CMT process effectively overcomes these difficulties by allowing for better heat regulation, improved control, and minimal spatter, making it ideal for thin-section aluminum welding [10,11]. In CMT welding, argon is often favored over helium as the shielding gas. Argon offers superior thermal conductivity, a lower ionization potential, and optimal density, which collectively result in stable arcs, uniform bead profiles, and minimal weld contamination [11]. These properties enhance weld quality while reducing the formation of defects. The optimized use of argon also supports the development of tailor-welded blanks (TWBs), which are fabricated by joining different aluminum sheets. TWBs offer significant advantages in automotive design, allowing engineers to customize the thickness and mechanical characteristics of individual sections of a component, ultimately reducing vehicle weight [12–16]. Aluminum alloy-based TWBs are gaining popularity in high-performance vehicles. Components such as bonnets, door panels, and structural reinforcements benefit from this technology. Various joining methods, including double-sided arc welding (DSAW) and friction stir welding (FSW), have been evaluated for their ability to effectively join these aluminum sheets. Among these methods, CMT remains a favorable option due to its minimum input heat and minimal distortion characteristics [16]. For instance, a successful implementations of different welding techniques for aluminum TWBs, reinforcing the versatility and effectiveness of these approaches in advanced vehicle design was presented [17]. Numerous research work has studied on the technical aspects of CMT welding, such as weld parameter optimization, residual stress, and mechanical characterization [17-23]. The mechanical and metallurgical properties in various aluminum alloys was studied and, offering vital information for extending the service life of welded structures [19]. In addition, highlighted the benefits of post-weld heat treatments (PWHT) was highlighted [24, 25]. These treatments were found to enhance tensile strength and fatigue resistance while minimizing residual stresses and microstructural anomalies. In terms of filler materials, the 4000 series aluminum alloys, particularly ER4043, are commonly used in CMT applications. These alloys are preferred due to their high Si content, which contributes to improved flowability and lower susceptibility to hot cracking. Their fluidity ensures better wetting of the base material, leading to fewer weld defects. 4000-series filler wires produced welds with superior strength and lower porosity than other aluminum alloy families [26]. ER4043, being a Si-rich filler, is especially known for its excellent fluid behavior and reduced tendency for defect formation, making it an optimal choice for welding applications requiring high integrity [27]. Efforts to join aluminum to steel using hybrid methods have also shown promising results. One such technique is the laser/dual-pulse MIG (DP-MIG) hybrid welding process. This method addresses the challenges posed by the vastly different thermal properties of aluminum and steel. Researchers have successfully applied this approach to aluminum-steel hybrid assemblies, achieving superior metallurgical properties when compared to traditional MIG joints. Studies indicate that plasma control within the hybrid system resulting the growth of Intermetallic compounds

(IMCs), which are typically brittle and compromise joint integrity. With optimized process parameters, joint strengths as high as 271.8 MPa have been achieved, with the improved adhesion area and reduced IMC brittleness being key contributors to enhanced tensile performance

1.1 Shielded Metal Arc Welding (SMAW)

SMAW is one of the utmost economical and generally used arc welding techniques. In this method, an electric arc is generated between the electrode and the base metal, producing the necessary heat to melt the metals. The protective shielding is produced by the breakdown of the electrode coating, which prevents the molten weld pool from reacting with O_2 and N_2 . This helps maintain the quality of the weld. The process does not require any external pressure, and the electrode itself serves as the filler material. SMAW is highly versatile and is widely applied to weld ferrous metals in various positions across a range of industrial applications.

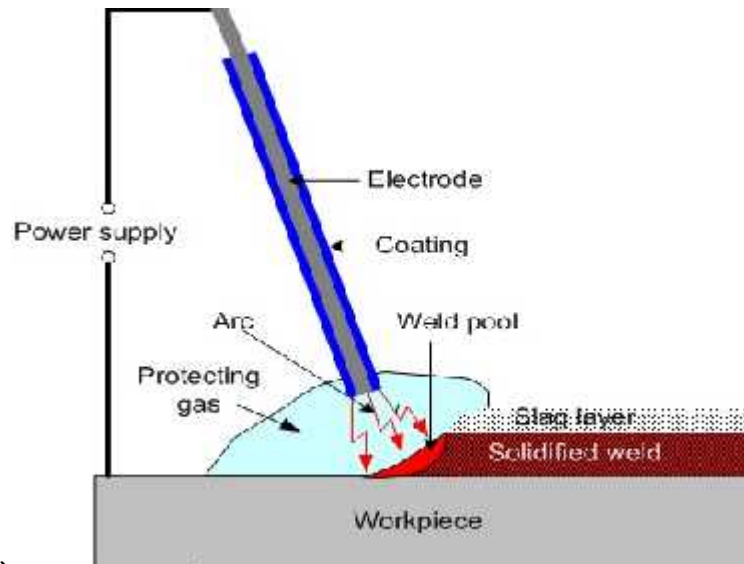


Figure 1: Working process of SMAW [28]

Figure 1 illustrates the SMAW process which generated electric arc between a workpiece and a coated consumable electrode and the workpiece using an external power supply. The electrode, which is both a filler metal and a conductor, is covered with a flux coating that plays a crucial role during welding. Upon arc initiation, the concentrated thermal energy rapidly liquefies the electrode tip and the uppermost layer of the substrate, forming a localized molten weld pool. As the process advances, the consumable electrode undergoes continuous fusion, transferring molten filler metal into the joint region. Simultaneously, the thermal decomposition of the electrode's flux coating generates protective gaseous byproducts, which establish a transient shielding envelope. This gaseous barrier is critical in isolating the molten weld metal from reactive atmospheric constituents—primarily oxygen and nitrogen—that would otherwise induce metallurgical imperfections such as gas porosity, embrittlement, or inclusions within the solidified weld. Additionally, the

melted flux forms a slag layer that covers the solidifying weld metal, providing further protection during cooling. This slag must be chipped away after the weld has fully solidified. The end result is a solidified weld joint that bonds the two workpieces together. This process is widely used due to its simplicity, portability, and effectiveness in welding ferrous metals, especially in construction, maintenance, and pipeline industries.

1.2 Gas Metal Arc Welding (GMAW) technique

Figure 2 represents a GMAW process, a high-efficiency arc welding technique utilized extensively in structural and industrial fabrication. In this process, a continuously driven consumable wire electrode functions simultaneously as the current conductor and filler material. The wire is automatically fed through the torch assembly, which also delivers a shielding gas envelope—commonly inert gases like argon or gas mixtures such as argon-carbon dioxide—into the weld zone. This shielding gas displaces ambient air, forming a protective environment that prevents oxidation and absorption of nitrogen and hydrogen into the molten metal, which would otherwise lead to metallurgical defects such as porosity, undercutting, or hydrogen-induced cracking.

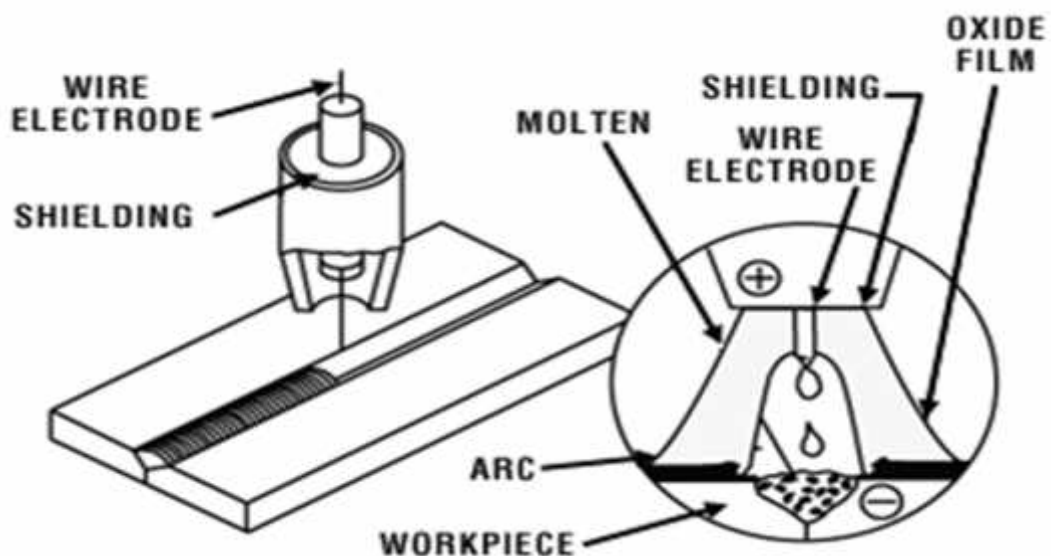


Figure 2: Gas metal arc welding [29]

The figure distinctly illustrates the establishment of a high-intensity thermal arc plasma between the electrode terminus and the workpiece substrate. The concentrated arc energy induces localized fusion of both the electrode and the base metal surface, resulting in the formation of a transient molten weld pool. As the thermal input ceases and the system undergoes rapid solidification, the molten metal resolidifies to form a metallurgically bonded fusion zone, this pool solidifies to form a homogeneous metallurgical bond. The presence of an oxide film in the illustration emphasizes the need for effective shielding to ensure weld integrity.

As welding progresses, the molten metal solidifies to create a strong, continuous weld. The inset in the figure highlights the role of shielding gas in enveloping the arc zone, preventing oxidation and ensuring a clean, stable arc. It also shows the oxide film that may be present on the surface of the workpiece, which is typically removed or penetrated by the arc during welding. GMAW is known for its high deposition rate, ease of automation, and minimal post-weld cleanup due to the absence of slag, making it a preferred method for welding non-ferrous metals like aluminum as well as steels in automotive, manufacturing, and construction applications.

1.3 GTAW process

Figure 3 depicts the operational mechanism of GTAW. This is a high-precision arc welding technique to generate an arc that creates localized melting of the base metal. In the process illustrated, a tungsten electrode is mounted in the GTAW torch, which also channels inert shielding gas—typically Ar or He—around the arc region. The shielding gas prevents atmospheric gases like H_2 , O_2 , and N_2 from contaminating the molten weld pool, which would otherwise cause weld discontinuities such as porosity, oxidation, and embrittlement.

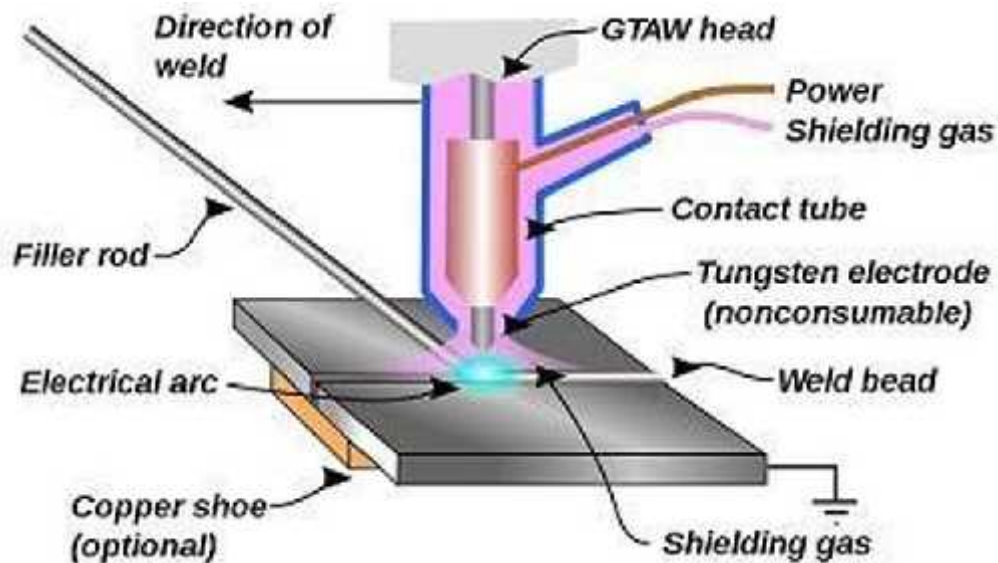


Figure 3: Working of GTAW [30]

An electric arc is struck between the tungsten electrode and the workpiece, and the intense heat generated melts the base material to form a molten weld pool. A separate filler rod is manually used, when filler material is required. However, the process can be autogenous as well, meaning no filler is used if the base metals are sufficient to form a joint. A constant current power source—either DC or AC—is used depending on the application. DC is suitable for carbon and stainless steels, while AC is preferred for reactive metals like aluminum and Mg due to its oxide-cleaning action on the electrode's positive half-cycle.

The figure also shows the formation of a stable arc column between the base plate and electrode, with the filler rod being angled into the leading edge of the molten pool. The weld bead forms as the arc progresses along the joint, with the solidified

metal forming a dense, defect-free fusion zone. For additional thermal management and to support the molten metal in thin sections, a copper shoe can be optionally placed beneath the workpiece to act as a heat sink and reduce burn-through.

GTAW provides excellent arc stability and allows precise control over weld bead geometry and penetration. The use of a non-consumable electrode ensures minimal contamination and high metallurgical quality. This process is usually for high-specification applications that demand defect-free, aesthetically clean welds. However, it requires a high level of operator skill due to manual filler metal addition and the need to maintain consistent arc length and torch travel speed, which limits its suitability for high-volume fabrication unless quality is the primary concern.

Despite the slower weld rate, GTAW is widely used in sectors such as aerospace, nuclear, food-grade piping, and automotive manufacturing, where metallurgical integrity and precision outweigh speed. The process excels in welding thin-gauge materials, critical assemblies, and dissimilar metal joints. The high-temperature-resistant tungsten electrode, inert gas shielding, and manual filler control make. Figure 3 effectively encapsulates these technical aspects, highlighting the coordination between arc initiation, shielding environment, filler rod feed, and weld pool solidification.

1.4 Cold Metal Transfer (CMT) welding process parameter

Figure 4 depicts a CMT welding setup, an advanced and innovative welding technique developed by Fronius, designed specifically to address the limitations of conventional arc welding processes, especially when working with dissimilar and thin materials like aluminum and steel. This process is a highly refined version of Gas Metal Arc Welding (GMAW), controlled wire movement and extremely low heat input to ensure precision, quality, and minimal spatter during welding. The machine in the image is a Fronius CMT welder, equipped with a sophisticated wire feeding mechanism. The red-colored torch, marked with "CMT," is fixed on a clamping system to provide stability and uniformity during operation. During each short circuit, the wire momentarily retracts, breaking the arc and allowing the molten droplet to detach without forceful ejection. This precise control significantly reduces the thermal heat input (THI), which helps prevent distortion, over-penetration, and undesirable metallurgical changes in the base material. CMT is especially useful in joining thin aluminum sheets, which are difficult to weld using conventional methods due to formation of aluminum's high oxide layer and thermal conductivity. This is mostly relevant in industries such as automotive, aerospace, shipbuilding, and packaging, where aluminum alloys like AA8011 and AA6061 are commonly used. In these industries, weight reduction is a crucial factor. However, its low melting point and tendency to form brittle IMCs when welded with other materials make it a challenging metal to work with—challenges that CMT is uniquely designed to overcome. In the image, a high-pressure gas cylinder supplies inert shielding gas to the welding zone to protect the molten pool from atmosphere. The welding is performed on a precision fixture table with multiple clamping options, allowing rigid positioning of the metal plates and ensuring consistent weld quality. The CMT torch is associated to the power source through a flexible cable, and the welding

parameters are likely monitored and controlled through a digital interface on the main welding unit.

A distinct metallurgical advantage of CMT welding lies in its precision-controlled arc dynamics, enabling the fabrication of Tailor Welded Blanks (TWBs). These engineered blanks—comprising dissimilar gauges or alloys—are integral to advanced vehicular structural assemblies, including hoods, door panels, and load-bearing chassis frameworks. The process ensures minimal heat input, reducing distortion and facilitating high-integrity fusion in applications demanding optimized strength-to-weight ratios and superior crash energy management. By enabling the joining of dissimilar thickness or material combinations with minimal thermal distortion and spatter, CMT contributes to higher mechanical integrity and improved fatigue performance of the final component.



Figure 4: CMT machine at DTU, Delhi

The image shows an operational CMT welding setup, utilizing a Fronius advanced arc welding system. In CMT welding, a robotic torch precisely coordinates the movement of the filler wire with synchronized arc pulsation. During the welding cycle, the wire is fed forward and then retracted in rapid pulses, minimizing short-

circuit duration. This action reduces the heat input drastically compared to conventional GMAW processes, enabling high-quality welds with negligible spatter. The shielding gas—supplied via the connected gas cylinder—creates an inert atmosphere around the arc zone, preventing oxidation and contamination. The fixture and clamping setup shown ensures consistent alignment and thermal control during welding. The CMT process excels in joining dissimilar materials and thin sheets with minimal distortion due to its controlled droplet transfer and low thermal load. The system's digital control interface and real-time arc management allow precise tuning of welding parameters.

1.4.1 Wire Feed Speed (WFS)

WFS is a fundamental parameter in CMT welding that directly affects the rate at which filler material is fed into the weld pool. In CMT, the wire movement is mechanically controlled and synchronized with the welding current. An increase in WFS generally results in a higher deposition rate, which can improve productivity. However, excessively high WFS may lead to increased spatter or poor fusion. In contrast to traditional MIG, CMT uses a push-pull wire system that allows precise control of wire retraction during short-circuit transfer. This minimizes metal droplet size and heat input, making WFS critical in achieving clean, spatter-free welds—especially when welding thin aluminum sheets or dissimilar materials.

1.4.2 Welding Current

The welding current in CMT is significantly lower than that in conventional MIG or GMAW processes. This low and controlled current reduces the thermal input, thereby minimizing distortion and residual stress. The current alternates between peak and background values in sync with the wire motion. This synchronized current control helps in clean metal transfer and stable arc formation. In CMT, current pulses are often used to enhance arc stability and control droplet detachment. Fine-tuning the welding current ensures better penetration control, reduced burn-through, and improved weld bead appearance, especially when dealing with thin or heat-sensitive materials like aluminum alloys.

1.4.3 Arc Voltage

Arc voltage in CMT affects arc length and consequently influences arc stability and heat distribution. A stable and optimal voltage ensures that the arc does not extinguish during the low-current phases of the cycle. Unlike conventional welding, where higher voltage often leads to excessive spatter, CMT maintains arc stability through synchronized voltage and current control. Higher arc voltage increases the arc length, leading in a broader HAZ, while lower voltage can concentrate heat, improving penetration. However, too low a voltage may result in an unstable arc. Thus, careful adjustment of voltage is essential to balance heat input and penetration.

1.4.4 Travel Speed

In CMT welding, travel speed significantly influences bead geometry, penetration depth, and the extent of the HAZ. A higher travel speed may lead to incomplete fusion or undercut defects, while too slow a speed increases heat input, negating the benefits of CMT's low-heat feature. Optimal travel speed is vital to maintaining uniform bead profile and avoiding burn-through in thin sheets. When set correctly, it allows the controlled deposition of metal while retaining excellent weld quality, particularly in automated or robotic CMT systems.

1.4.5 Shielding Gas Composition and Flow Rate

In CMT welding, pure Ar, CO₂ or a mixture of Ar and CO₂ or helium is generally employed as a shielding gas, depending on the base material. The choice of gas affects arc characteristics, penetration, and metal transfer behavior. Argon provides a stable arc and is ideal for aluminum, while helium increases arc temperature and improves penetration in thicker materials. The flow rate must be optimized—too low may allow oxygen intrusion, and too high can disturb the arc or cause turbulence. Thus, maintaining appropriate gas composition and flow rate ensures weld cleanliness and stability.

1.4.6 Torch Angle and Position

Torch angle, including work angle and travel angle, influences weld bead shape, fusion, and spatter generation. In CMT, the precise control of wire movement allows greater flexibility in torch positioning without compromising weld quality. However, incorrect torch angle can still lead to poor fusion, lack of penetration, or excessive spatter. For butt welds and fillet welds, maintaining a torch angle between 10° to 20° from vertical is often optimal. Proper torch alignment ensures uniform arc distribution across the joint and maximizes the effectiveness of controlled droplet transfer, a hallmark of the CMT process.

1.5 CMT droplet transfer cycle

Figure 5 illustrates the time-resolved images of a steady CMT droplet transfer cycle, divided into two polarity phases: (a) Electrode Positive (EP) and (b) Electrode Negative (EN). The images in the EP phase (Fig. 5a) show a bright and dynamic arc evolution from 0.0 to 7 ms, with the arc intensity increasing rapidly from 1.0 ms onward. The arc reaches peak brightness between 2.0 ms and 3.5 ms, indicating elevated arc temperatures. The latter part of the EP phase (4.0–7.0 ms) reveals a bluish hue, associated with cooling and the gradual development of the molten droplet. In contrast, the EN phase (Figure 5b) displays a visibly dimmer arc throughout the cycle (0.0–6.5 ms), characterized by a softer pink glow and limited droplet evolution, implying reduced energy input and arc temperature. Unlike earlier droplet transfer images, these were captured without background laser illumination, and the number of optical filters was reduced to enhance arc visibility. This

adjustment in imaging conditions allowed for more accurate observation of the arc characteristics [31].

Table 1: Typical Processing Parameters in CMT Welding

Parameter	Typical Range	Effect on Welding
Welding Current	30 – 100 A	Heat input, penetration, droplet size
Arc Voltage	10 – 20 V	Arc stability, bead shape
Wire Feed Speed	3 – 15 m/min	Metal transfer rate, arc behavior
Travel Speed	100 – 600 mm/min	Bead width, penetration
Shielding Gas	Ar / Ar-He/ Ar-H	Arc stability, spatter, oxidation
Shielding Gas Flow Rate	10 – 25 L/min	Weld protection, spatter control
Electrode Stick-Out	8 – 15 mm	Arc length, heat distribution
Torch Angle	10° – 15° forward	Fusion control, bead uniformity
Interpass Temperature	<150°C (Al alloys)	Mechanical property preservation
Pulse Parameters (if used)	Application-specific	Refined control over arc.

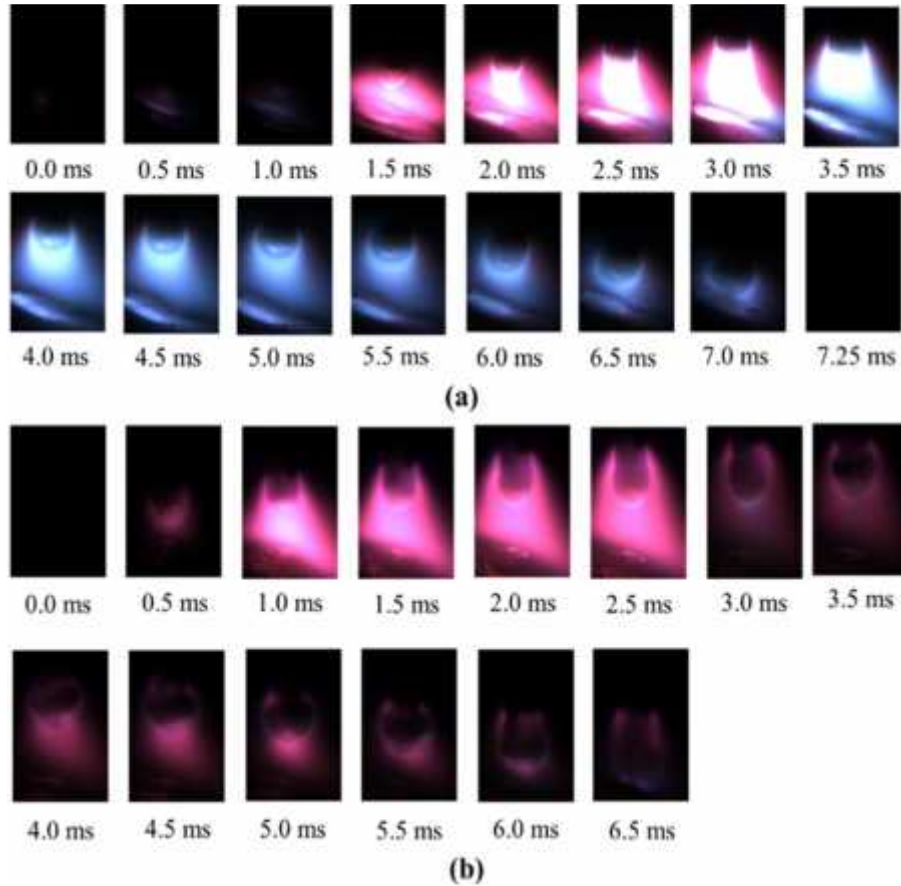


Figure 5: Sequential arc evolution during a stable CMT droplet detachment cycle under Group 4 parameters — (a) Arc behavior in Electrode Positive (EP) polarity, (b) Arc dynamics in Electrode Negative (EN) polarity [31]

Observations of the arc behavior revealed that its brightness was noticeably higher when operating under EP polarity compared to EN. This indicates that the arc temperature is substantially higher during the EP phase. When the welding polarity

changes from EN to EP, the system demands extra energy to increase the arc's temperature, which initially limits droplet formation at the beginning of the EP stage. This pattern aligns with findings by Huisman, who investigated droplet temperatures in variable polarity GMAW) of aluminum alloys. His results showed that as the proportion of EN polarity increased, the droplet temperature decreased. This trend indirectly supports the conclusion that EP polarity generates a hotter arc than EN polarity. Understanding this behavior is important for controlling heat input, metal transfer, and weld quality, especially when working with materials like aluminum that are sensitive to temperature variations during welding.

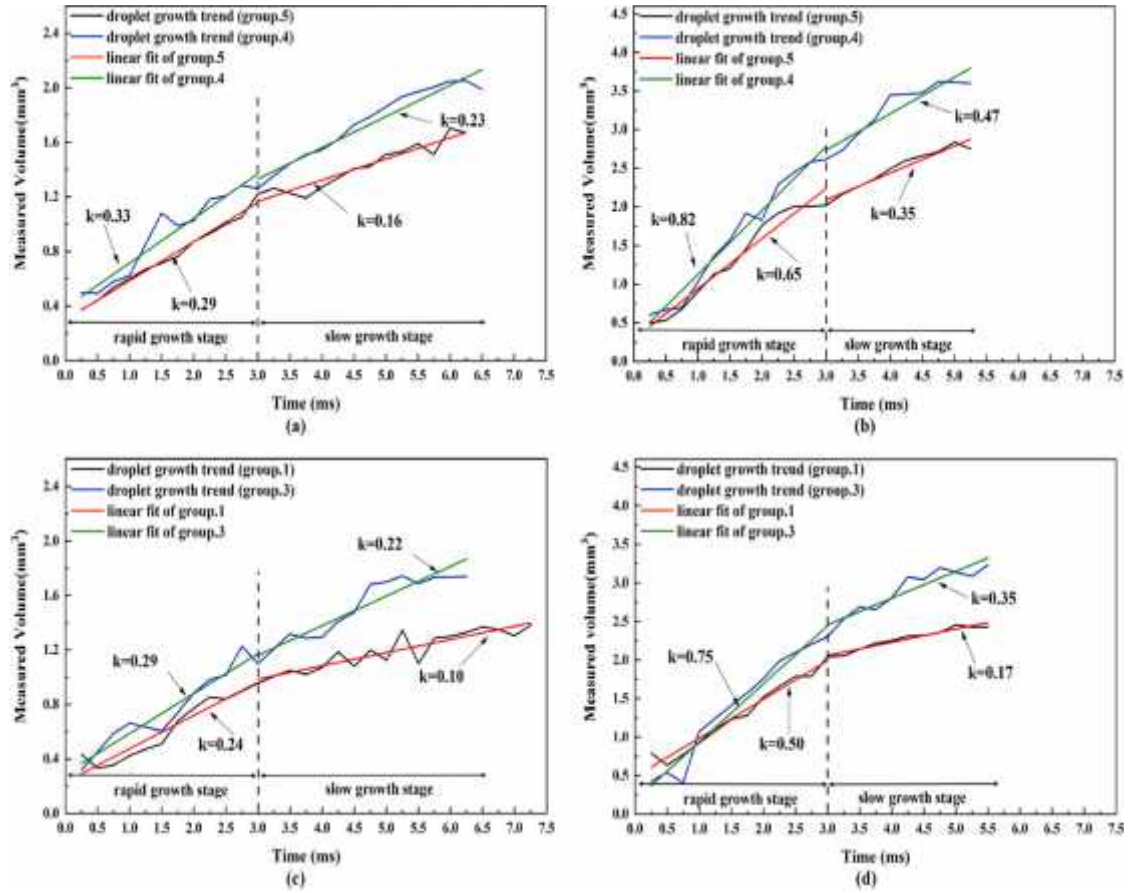


Figure 6: Droplet Volume Growth Trends in Rapid and Slow Growth Stages under Different CMT Welding Parameter Groups [31]

Figure 6 illustrates the droplet volume growth trends over time for various experimental groups during the CMT process. Each subfigure represents a comparison between two groups: (a) group 4 vs. group 5, (b) group 4 vs. group 5 (with higher volume range), (c) group 1 vs. group 3, and (d) group 1 vs. group 3 (with higher volume range). The droplet growth process is divided into two distinct phases—rapid growth stage and slow growth stage, separated by a vertical dashed line at approximately 3.0 ms [31]. The growth rates, denoted as k , are derived from the slopes of linear fits during each stage. In subfigures (a) and (b), group 5 exhibits consistently higher growth rates in both stages (e.g., $k = 0.33$ and 0.23 in (a), and $k = 0.82$ and 0.47 in (b)), compared to group 4 ($k = 0.29$ and 0.16 in (a), and $k = 0.65$ and

0.35 in (b)). This indicates that group 5 allows more rapid droplet volume accumulation due to higher arc energy or thermal input.

Similarly, in subfigures (c) and (d), group 1 demonstrates a steeper droplet volume increase ($k = 0.29$ and 0.22 in (c), and $k = 0.75$ and 0.35 in (d)) than group 3, which shows slower growth trends ($k = 0.24$ and 0.10 in (c), and $k = 0.50$ and 0.17 in (d)). These comparisons suggest that droplet formation and detachment dynamics are highly sensitive to process parameters, with groups having higher energy input or optimized arc conditions promoting faster and more consistent droplet growth.

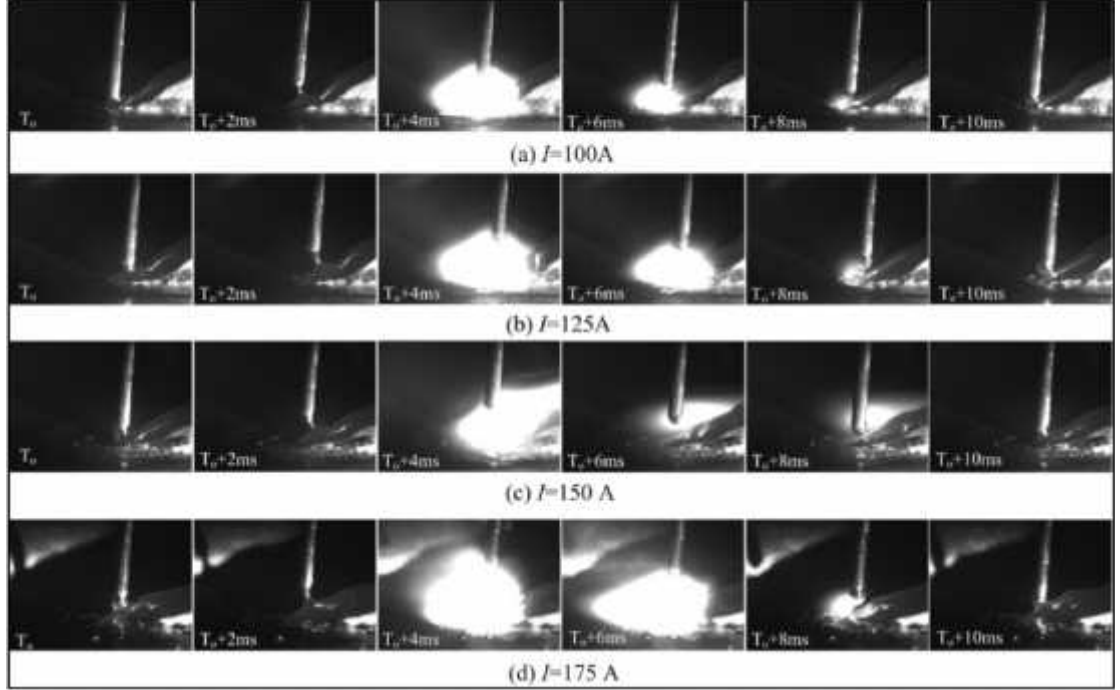


Figure 7: High-speed photographic sequence of droplet transfer behavior in T-CMT-DED at different deposition currents: (a) 100 A, (b) 125 A, (c) 150 A, and (d) 175 A [32]

Figure 7 illustrates the high-speed photographic analysis of droplet transfer behavior in the T-CMT-DED process at varying currents deposition ranges from 100 to 175 A [32], while maintaining other process parameters constant. The sequential arc frames distinctly reveal that the metal transfer mechanism adheres to a consistent short-circuiting regime across all current intensities. Arc re-ignition is initiated near $T_0 + 4$ ms, triggering the nucleation of a molten droplet at the terminus of the filler wire. The droplet undergoes progressive volumetric growth driven by arc energy and surface tension dynamics. By approximately $T_0 + 8$ ms, the droplet establishes electrical contact with the weld pool, facilitated by the constrained short-circuit current magnitude, which limits excessive electromagnetic pinch force and minimizes spatter ejection. At this moment, the wire feeder responds to the electrical signal and initiates the backward movement of the filler rod. A new droplet transfer cycle begins from this detachment. Throughout the short-circuit phase, the deposition current remains low, minimizing thermal input and thereby promoting a smoother, more controlled droplet transfer. This characteristic transfer mode contributes to

stable arc behavior, reduced spatter, and improved deposition quality, which are essential for precision applications in additive manufacturing processes [33].

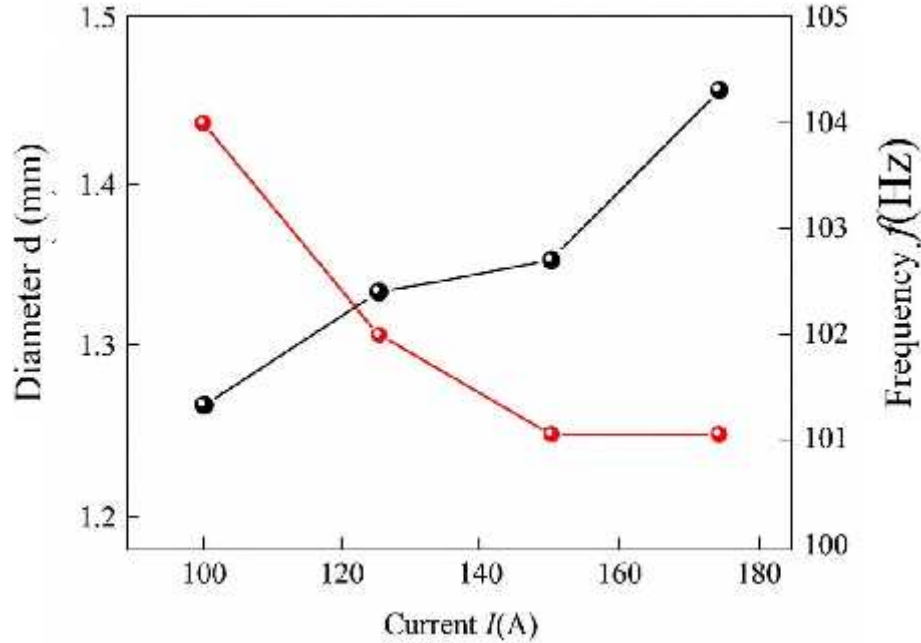


Figure 8: Variation of current and frequency to the diameters of molten droplet [32]

Figure 8 reveals the influence of varying current deposition on both the frequency and diameter of molten droplets in the T-CMT-DED process [32]. The data clearly show that as the current increases, the droplet diameter also increases, whereas the droplet transfer frequency decreases. This trend is primarily driven by the increased thermal input associated with higher current levels, which accelerates the melting of the filler wire. As a result, larger droplets are formed due to the more rapid accumulation of molten metal. Moreover, the elevated wire surface temperature reduces the molten metal's surface tension, allowing a greater volume to build up before detachment occurs. Although this leads to an increase in droplet size, it also delays the formation and release of each droplet, causing a decline in the number of droplet transfers per unit time. The gravitational pull on the larger droplets further lengthens the formation and detachment cycle, contributing to the observed reduction in transfer frequency. Overall, these interactions highlight how deposition current critically influences droplet dynamics, affecting both the size and timing of material transfer in T-CMT-DED processes.

1.6 Various types of filler materials

The performance and quality of CMT welds is basically depends on the selection of an appropriate filler wire. The filler rod must be metallurgically compatible with the base material to ensure good mechanical properties, resistance to cracking, and corrosion resistance. The selection also affects weld fluidity, arc behavior, and final joint characteristics. The filler rod in the CMT welding is critical to achieving high-quality welds with desirable mechanical properties. Filler rods not only contribute to

the metallurgical composition of the weld but also influence the fluidity, penetration, crack resistance, and final strength of the welded joint. The filler metal must be chosen to suit both the base material and the specific demands of the application. Below is an explanation of commonly used filler rods in CMT welding, with a focus on their characteristics, applications, and limitations. Below are the most widely used filler rods in CMT welding of aluminum alloys:

1.6.1 ER4043 Filler Wire

ER4043 is an Al-Si alloy filler wire containing between 4 to 5.8% Si is widely used filler material in the 6xxx series (like AA6061 and AA6082) and some 3xxx and 7xxx series alloys. The occurrence of Si reduces the melting point of the filler wire, resulting in improved fluidity during welding. This enhances wetting behavior, helping produce smoother weld beads and minimizing weld defects like lack of fusion or porosity. In CMT welding, ER4043 performs exceptionally well due to its compatibility with low-heat input processes. It helps maintain good arc stability and minimizes spatter generation, key advantages in the CMT technique. However, despite its good fluidity and weld appearance, ER4043 tends to form brittle IMCs when used on Mg-rich alloys like those from the 5xxx series. This leads to reduced ductility and an increased risk of hot cracking. Consequently, it should not be used with Al-Mg alloys (e.g., AA5083, AA5456) where the Mg content exceeds 2.5%, as it may lead to the formation of Mg₂Si, compromising the joint integrity.

Applications: Automotive panels, structural components in the 6xxx series, and decorative aluminum parts where aesthetic weld quality is important.

1.6.2 ER4045 Filler Wire

ER4045 is a Si-rich aluminum filler rod containing approximately 12% Si, offering significantly improved fluidity and wetting characteristics compared to more commonly used filler rods like ER4043. This enhanced fluidity allows for exceptionally smooth, flat weld beads and reduces the risk of hot cracking during the welding process. ER4045 is particularly advantageous when welding thin aluminum sheets or castings, as it lowers the melting point of the filler metal, facilitating better control of the weld pool during low-heat input processes like CMT. Although it provides good aesthetics and low crack sensitivity, its mechanical strength is relatively lower than Mg-based fillers, making it more suitable for non-structural or semi-structural applications where appearance and weldability are prioritized over tensile strength.

1.6.3 ER5356 Filler Wire

ER5356 is an Al-Mg based filler wire containing up to 5%–6% Mg, making it ideal for welding 6061 and 7075. Compared to ER4043, ER5356 offers better tensile strength and improved ductility, making it suitable for load-bearing applications. In CMT welding, ER5356 delivers excellent arc characteristics and a clean, strong weld with minimal porosity. The wire's excellent feeding behavior and compatibility with

both manual and robotic CMT processes further enhance its popularity in automated welding lines.

However, the main limitation of ER5356 lies in its poor performance at elevated temperatures. Above 65°C, it is prone to stress corrosion cracking due to the precipitation of aluminum-Mg IMCs along grain boundaries. This limits its use in high-temperature applications or components exposed to cyclic thermal loads.

Applications: Marine vessels, pressure vessels, storage tanks, truck trailers, and welded structures requiring high strength and corrosion resistance.

1.6.4 ER5556 Filler Wire

ER5556 is a high-strength aluminum filler rod primarily alloyed with Mg (around 5%) and additional elements such as Mn, Cr, and Ti, which together enhance both its mechanical properties and corrosion resistance. This filler wire is ideal for welding 5xxx series aluminum alloys used in marine, offshore, and defense applications due to its superior resistance to saltwater corrosion and stress corrosion cracking. ER5556 delivers stronger welds than ER5356 and is capable of withstanding more demanding service conditions. However, like other Mg-based filler rods, it is not recommended for applications that will operate continuously above 65°C, as long-term exposure to high temperatures can lead to microstructural degradation.

1.6.5 ER5183 Filler Wire

ER5183 is a specialized aluminum filler rod engineered for high-performance structural applications. It contains a higher level of Mg (~4.3–5%) than ER5356 and is carefully alloyed to provide superior tensile strength and excellent fracture toughness. ER5183 is especially suitable for critical components in various industries, where weld integrity and mechanical performance cannot be compromised. It is designed to match the high-strength characteristics of 5xxx series base metals, like AA5083 or AA5456, providing weld joints that retain their strength even under demanding service conditions. Though it offers less fluidity than Si-based filler rods, its combination of high strength, corrosion resistance, and reliable performance makes it one of the top choices for heavy-duty and mission-critical aluminum welding using the CMT process. Table 2 demonstrates the different filler rod materials used in CMT welding of Al-alloys. ER4043, a Si-rich wire (4.5–6%), is ideal for 6xxx and some 3xxx/7xxx alloys, offering high fluidity and moderate strength and corrosion resistance—best for non-structural applications. ER5356, a Mg-based wire, is widely used for 5xxx and 6xxx alloys, providing high strength and excellent corrosion resistance, though limited to 65°C service temperature. ER4045, with ~12% Si, is preferred for thin 6xxx or cast aluminum, offering very high fluidity and smooth bead appearance, though with moderate strength. ER5556, alloyed with Mg, Mn, and Cr, suits high-strength 5xxx applications, offering superior strength and corrosion resistance. ER5183, rich in Mg, is ideal for structural 5xxx alloys, delivering very high strength and good corrosion resistance, especially in marine or aerospace applications. Each rod serves specific alloy types and conditions to ensure optimal weld performance.

Table 2: Common Filler Rods for CMT Welding of Aluminum Alloys

Filler Rod	Major Alloying Element	Best for Alloy Series	Strength	Fluidity	Corrosion Resistance	Service Temp Limit
ER4043	Si (4.5–6%)	6xxx, some 3xxx/7xxx	Medium	High	Moderate	Moderate
ER5356	Mg (5-6%)	5xxx, 6xxx	High	Moderate	Excellent	65°C
ER4045	Silicon (~12%)	Thin 6xxx, Cast Al	Medium	Very High	Moderate	Low to Moderate
ER5556	Mg + Mn + Cr	5xxx	Very High	Moderate	Excellent	65°C
ER5183	High Mg	5xxx (Structural Use)	Very High	Moderate	Good	65°C

1.7 Effect of different shielding gases in CMT weldments

Shielding gases play a vital role in arc welding processes by safeguarding the molten weld pool from harmful atmospheric gases such as H_2 , N_2 , and O_2 . These atmospheric elements can react with the molten metal, leading to weld defects such as porosity, oxidation, and reduced mechanical strength. To prevent these issues, inert or semi-inert gases are employed, as they are chemically stable and do not react with the weld pool. These gases typically possess high ionization energy, low thermal conductivity, and low electron affinity, which contribute to maintaining a stable arc, ensuring smooth droplet transfer, and producing cleaner, higher-quality welds [34]. Moreover, their higher density compared to air enables them to effectively blanket the weld zone, preventing atmospheric intrusion. A correctly maintained shielding gas flow results in a uniform, spatter-free weld bead. Conversely, inadequate gas coverage often causes porosity and surface imperfections [35]. Among the most commonly used shielding gases are Ar, He, and CO_2 , either used alone or in various combinations. The selection of a suitable gas depends on the base material, desired penetration profile, and specific welding process being applied. Proper gas selection and regulation are essential to achieve optimal weld integrity and appearance.

1.7.1 Argon

Argon is widely used in welding non-ferrous metals like Al, and Mg alloys [36]. Being heavier than air, it requires a lower flow rate to maintain effective shielding. Argon has low electrical resistance and low ionization energy, which facilitates stable arc initiation and supports short-circuiting transfer in CMT welding. Its low thermal conductivity results in a concentrated and deep penetration profile, often described as "finger-like," which is particularly useful for high-precision applications. These characteristics make Argon the preferred choice for many researchers and industrial users alike. Additionally, its inertness prevents chemical

reactions with the molten metal, ensuring a cleaner weld with minimal oxidation and spatter [37].

1.7.2 Helium

Helium is the second most commonly used shielding gas after Argon, especially in the joining of light metal alloys. It has a lower density than air, requiring a higher gas flow rate (GFR) to provide sufficient coverage over the weld pool. Helium produces a hotter arc due to its high ionization potential, which results in a wider and more fluid weld bead [36]. This can be beneficial when broader fusion is required. However, Helium is significantly more expensive than Argon, limiting its use in large-scale production. Furthermore, Helium can lead to less stable arcs and higher spatter rates, particularly when welding steel, making it less favorable for such applications. Despite these drawbacks, Helium remains a valuable shielding gas for specific applications that demand deeper penetration and enhanced heat input [37].

1.7.3 Carbon Dioxide (CO₂)

CO₂ is a widely used and economical shielding gas, particularly in welding ferrous metals like carbon steel. It promotes deeper penetration due to its oxidizing nature, which helps achieve strong fusion between base metals [36]. However, excessive CO₂ can cause increased spatter and may lead to porosity if not properly balanced with other gases. CO₂ also releases hydrogen during welding, which can negatively affect weld quality by causing hydrogen-induced porosity. While pure CO₂ can result in unstable arcs, blending it with inert gases like Argon improves arc characteristics and reduces spatter. Its affordability and availability make it a practical choice for many industrial applications, but precautions must be taken to avoid excessive oxidation and the formation of toxic by-products like carbon monoxide, especially in moist conditions.

1.7.4 Combination of different shielding gases

The use of mixed shielding gases in welding, particularly argon blended with He, CO₂, and O₂, significantly influences arc characteristics, weld quality, and material compatibility. When argon is combined with helium, the resulting mixture stabilizes the arc while increasing arc temperature. Helium raises the heat input, promoting deeper penetration and a more concentrated weld bead, which is especially beneficial for welding thicker sections and high thermal conductivity materials like aluminum and copper alloys [36]. This blend allows better arc control and consistent fusion in demanding welding conditions. In contrast, introducing CO₂ into argon modifies metal transfer behavior. Depending on the ratio, argon-CO₂ mixtures support globular or spray transfer modes, enhancing deposition rates and improving the overall appearance of the weld bead. This combination is widely used in GMAW due to its cost-effectiveness and ability to balance spatter control with penetration depth [33]. Additionally, small additions of oxygen to argon further improve arc stability and penetration. Oxygen increases arc energy and helps reduce surface tension in the molten pool, resulting in smoother, more refined welds. This is particularly useful

when welding carbon or low-alloy steels, as it enhances fusion and wetting characteristics while maintaining acceptable mechanical properties [37]. The careful selection and proportioning of shielding gas mixtures are therefore critical in achieving optimal weld quality, depending on base material, joint configuration, and desired mechanical performance.

The influence of various shielding gas compositions on the metallurgical characteristics of super austenitic stainless steel during hybrid welding was systematically evaluated. As illustrated in Figure 9(a–d), a clear distinction in grain morphology was observed between the lower and upper regions of the weldment—corresponding to the GMAW and laser zones, respectively

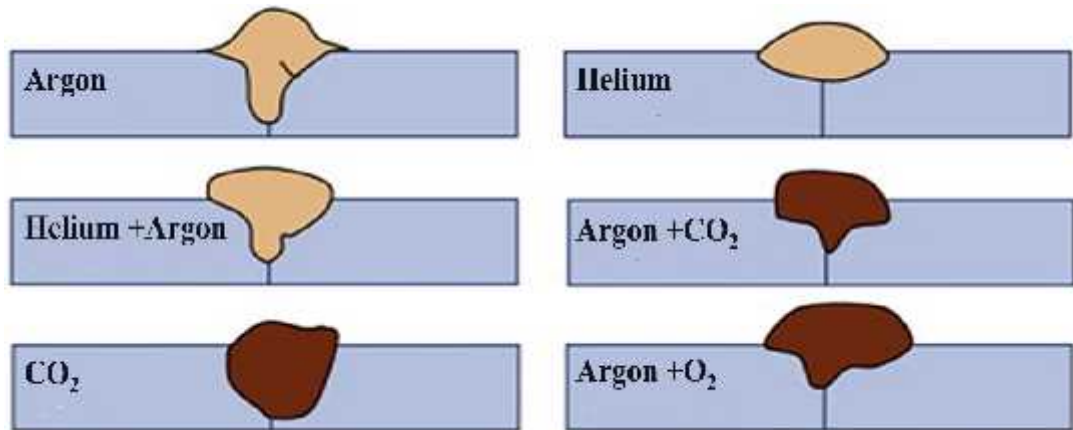


Figure 9: Variation of different shielding gases on the weld bead and their penetration [37]

The variation in grain size and structure is primarily attributed to differences in thermal gradients, cooling rates, and solidification mechanisms governed by the shielding gas composition. The upper GMAW zone predominantly exhibited coarse equiaxed grains interspersed with a higher proportion of long columnar grains, particularly in gas compositions (a) and (b) [38]. In contrast, the lower laser zone, influenced by higher cooling rates, showed finer equiaxed grains and a reduced percentage of columnar structures, as seen in Figure 10. The elemental partitioning during solidification played a critical role; elements like carbon, nitrogen, and nickel tended to enrich the primary dendritic cores, while ferrite-promoting elements such as Si, molybdenum, and chromium segregated in the interdendritic regions. Impurities further contributed to the formation of secondary interdendritic phases.

An automated area detection module was employed to quantify the area fractions of dendritic and interdendritic phases, offering precise phase distribution data across different gas mixtures. These findings deepen the understanding of how shielding gas composition influences the microstructure of the weldments [38]. Figure 11 presents the hardness distribution profiles across the weldment at two specific depths: (a) 1 mm below the top surface, representing the GMAW (Gas Metal Arc Welding) zone, and (b) 1 mm further below, corresponding to the laser weld region. Four shielding gas combinations were evaluated: 50% Argon + 50% Helium, 5% Oxygen + 45% Argon + 50% Helium, 10% Nitrogen + 45% Argon + 45% Helium, and 100%

Helium [38]. The profiles clearly demonstrate a consistent trend: the laser zone (Figure 11b) exhibits significantly higher hardness compared to the GMAW zone

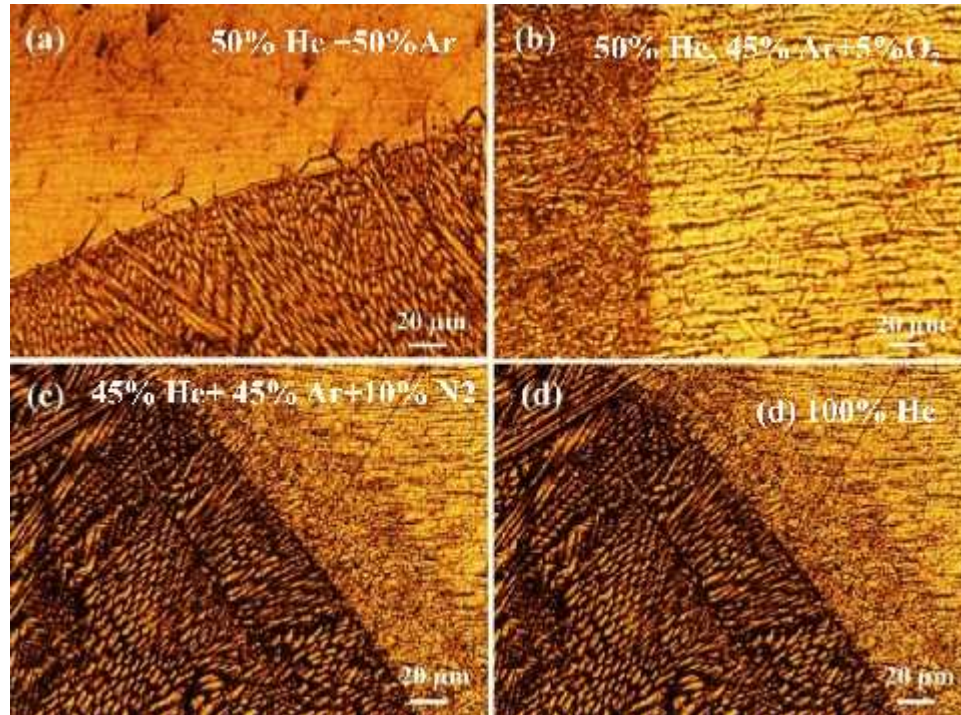


Figure 10: OM images of CMT weldments with different shielding gases [38]

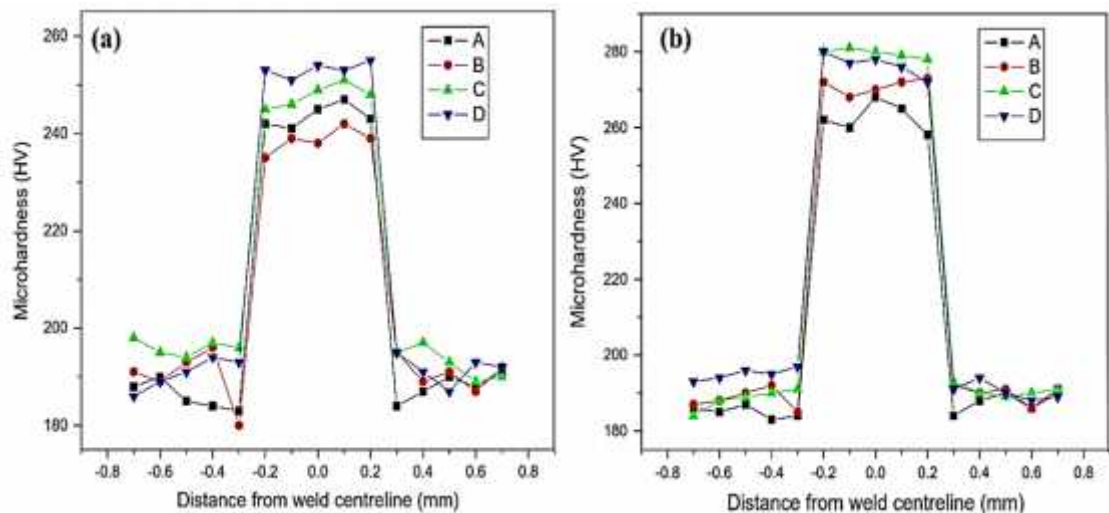


Figure 11: Variation of hardness dissemination from the weld center, (a) upper surface, (b) lower surface [38]

(Figure 11a) for all shielding gas types. This disparity is primarily attributed to the distinct solidification rate and thermal cycles in the two zones. The laser zone experiences a much higher cooling rate due to the concentrated heat source, which promotes undercooling, enhances nucleation rates, and refines the microstructure. These rapid solidification conditions result in the formation of precipitation of

strengthening phases, both of which contribute to increased hardness. In the GMAW region (Figure 11a), among the four shielding gases, 100% Helium (D) produces the highest hardness values. This is due to helium's higher ionization energy, which leads to a tighter, hotter arc, facilitating more localized heating and finer grain size during solidification. Helium also encourages the formation of secondary interdendritic phases, known for their role in improving hardness. Compared to gas mixtures A, B, and C, helium-based shielding not only improves arc concentration but also modifies the weld pool dynamics, resulting in enhanced microstructural features in the GMAW layer. In contrast, in the laser zone (Figure 11b), the highest hardness is observed with the shielding gas mixture containing 10% Nitrogen (C). The introduction of nitrogen has a dual effect. First, it suppresses the plasma plume, allowing more laser energy to be delivered directly to the weld pool. Second, nitrogen acts as a strong austenite stabilizer and solid solution strengthener, especially in stainless steels. This leads to greater heat absorption, a rapid cooling rate, and refined grain structure, all of which significantly enhance hardness. Compared to other gases, the He-Ar-N₂ mixture results in a more homogeneous and fine-grained microstructure due to deeper laser-material interaction and nitrogen's role in reducing porosity and segregation. Furthermore, the hardness distribution across the weld exhibits a "peak plateau" in the central weld region and steep drops near the fusion boundaries. This is a typical hardness trend in fusion welding due to differences in thermal gradient.

1.8 Aluminum alloy

Al alloys are primarily composed of aluminum as the BM, combined with various alloying elements to enhance their properties. Common alloying elements include Si, Mg, Cu, Sn, Zn, Mn, and Fe. Among these, Si-based Al-alloys (Al-Si), which typically contain 3.5% to 12% Si, are widely used due to their excellent casting characteristics. These alloys are especially valuable in the metal-skinned aircraft. Mg-based Al-alloys are also widely utilized, known for being even lighter than standard Al-alloys. Al-alloys possess a naturally appealing appearance, often shiny or lustrous, and are valued for their recyclability, making them both environmentally and economically beneficial. They are also known for being easy to fabricate and join.

The chemical composition, grain size, and microstructure suggestively affect the metallurgical, chemical, and mechanical properties of Al-alloys. The total alloying elements typically do not exceed 10%, while impurities are kept below 0.15%.

Al-alloys offer several advantages over steel:

- Their density is about one-third that of steel.
- They exhibit high tensile strength, toughness, and ductility, contributing to an excellent strength-to-weight ratio.
- They provide strong resistance to corrosion, even in challenging environments, and are suitable for cryogenic applications.
- Al-alloys have high thermal and electrical conductivity and excellent reflectivity.
- They are non-toxic and non-magnetic, making them ideal for food and beverage packaging.

These unique properties make Al-alloys highly versatile for a broad range of industrial applications.

1.9 Types of Al-alloys

Aluminum alloys represent a critical class of lightweight, high-strength engineering materials extensively utilized across in various engineering field. These alloys offer remarkable performance under mechanically demanding conditions. Classified into wrought and cast categories, and further subdivided into heat-treatable and non-heat-treatable grades, aluminum alloys exhibit distinct mechanical behaviors influenced by alloying elements i.e. Cu, Mg, Zn, Si, Mn, and Fe. These elements enhance properties such as UTS, hardness, wear resistance, and machinability. Through precise thermo-mechanical processing techniques—including solution treatment, artificial aging, cold working, and recrystallization—aluminum alloys can be engineered to achieve tailored microstructural characteristics and mechanical performance. Their capability to maintain mechanical integrity under cyclic loading, combined with excellent formability and weldability, positions them as indispensable materials in the design of high-performance, weight-sensitive components. The aluminum alloy can be divided into several groups based on the alloying elements, which are listed below.

1.9.1 1XXX series

Wrought Al alloys in the 1XXX series, such as 1100 and 1135, contain small amounts of natural impurities that originate from the smelting process. These impurities include elements like Si, iron, and copper, with copper having defined minimum and maximum limits. The 1XXX series is known for its excellent corrosion resistance, as well as outstanding thermal and electrical conductivity. These properties make them ideal for electrical and chemical applications. Although these alloys have relatively low strength, it can be significantly improved through strain hardening, making them suitable for applications requiring lightweight and conductive materials.

1.9.2 2XXX series

The 2XXX series Al-alloys primarily use copper (Cu) as the main alloying element, with Mg serving as a secondary addition. These alloys require heat treatment to achieve optimal mechanical and physical properties. Once heat treated, the strength of 2XXX series alloys can match or even surpass that of low carbon steel. However, their corrosion resistance is lower compared to other Al-alloys, and they may also be susceptible to intergranular corrosion. Despite this limitation, they possess an excellent strength-to-weight ratio. Due to their high strength and lightweight characteristics, these alloys are widely used in automotive and aerospace industries, including applications such as structural components, truck frames, aircraft wheels, and suspension systems.

1.9.3 3XXX series

The 3XXX series Al-alloys primarily use Mn as the main alloying element. These alloys offer approximately 20% higher strength compared to the 1XXX series. Although they are non-heat-treatable, they exhibit excellent corrosion resistance. Mn content is typically limited to about 1.5%, and it forms stable precipitates such as Al₃(Mn, Fe) or Al₆(Mn, Fe)₂Si within the Al matrix. These precipitates enhance the overall strength and corrosion resistance of the alloy. Due to their durability and resistance to chemical attack, 3XXX series alloys are commonly used in cookware, architectural structures, and chemical processing equipment.

1.9.4 4XXX series

The 4XXX series Al-alloys primarily contain Si as the main alloying element, which can be added up to 12% to reduce the melting temperature without making the material brittle. The Al-Si alloys are commonly utilized as welding filler materials, particularly for joining dissimilar or similar Al alloys. Most alloys in this series are non-heat-treatable. One of the most widely used filler wires is ER4043, known for its good performance in welding applications. Due to the presence of Si, these alloys are also preferred for architectural components and are used in the manufacturing of forged engine pistons and other automotive parts.

1.9.5 5XXX series

In the 5XXX series Al-alloys, Mg is the primary alloying element. When combined with Mn, it results in moderate to high-strength alloys that can be strain-hardened. Mg is a more effective hardening agent than Mn; for instance, 0.8% Mg provides a similar strengthening effect as 1.25% Mn. These alloys are known for their excellent corrosion resistance, particularly in marine environments, and they also exhibit outstanding weldability. A commonly used Mg-based filler wire is ER5356, which is ideal for welding various Al-alloys using MIG or GTAW welding methods due to its strength and corrosion resistance.

1.9.6 6XXX series

In this series, Al, Si, and Mg are the primary alloying elements, typically present in concentrations of less than 1% each. Minor elements such as Cu, Cr, Mn, and Zn are also added in small amounts. The main strengthening phase in these alloys is magnesium silicide (Mg₂Si). However, 6XXX series alloys are prone to weld metal cracking. This issue can be minimized by using filler materials with higher Si content, such as ER4043, or with slightly higher Mg content like ER5356, though the latter carries a greater risk of hot cracking.

Strength reduction in these alloys is less significant in the naturally aged condition compared to artificially aged states. During welding, the strength in the heat-affected and weld zone of artificially aged alloys typically drops to the level of the naturally aged condition. These results from the development of a narrow solution-treated region adjacent to the weld and an over-aged area farther away, both exhibiting

reduced strength compared to the original T6 temper condition. These zones contribute to a decline in mechanical properties around the welded joint. However, using low-heat input welding methods helps retain more strength, often close to that of the T4 temper, rather than reducing it to annealed levels.

Due to good corrosion resistance and their balanced mechanical properties, 6XXX series alloys are extensively used in architectural applications and automotive components, particularly in extrusions where moderate strength and good weldability are essential.

1.9.7 7XXX series

The 7XXX series Al alloys are classified into two categories depending on their weldability characteristics. The first category consists of high-strength alloys with copper content exceeding 1%, commonly utilized in the aerospace industry. Due to their high tendency to crack during welding, these alloys are generally not joined using welding methods and are instead assembled through mechanical fastening techniques. The second category includes medium-strength alloys that have been specifically engineered to offer improved weldability. These variants are more suitable for welding applications, making them preferable for structures where fusion joining methods are required without compromising performance.

Zinc and aluminum form a eutectic system with a solid solubility of about 83% Zn in aluminum and 1.14% Al in Zn. When Mg is added, more complex ternary eutectics and IMCs form, including MgZn, which contributes to precipitation strengthening. Copper further enhances strength through the formation of CuAl and copper-zinc intermetallic phases, which help improve mechanical performance. A unique challenge in welding 7XXX series alloys is the rapid oxidation of zinc during the process. This oxidation disrupts the weld pool's surface tension and can lead to fusion defects. To counter this, welding procedures require a current approximately 10–15% higher than that used for 5XXX series alloys. Additionally, employing a shorter arc length—bringing the metal transfer close to the globular range—can improve weld quality. These adjustments help manage oxidation and promote better fusion, enabling the use of welding in selected 7XXX alloy applications where strength and performance are critical.

1.9.8 8XXX series

The 8XXX series Al-alloys include compositions that do not fall into other conventional series, such as 8020 (Al-Sn) and 8001 (Al-Ni-Fe). One of the most notable groups within this series is the aluminum-lithium (Al-Li) alloys. These alloys offer considerable advantages, including weight reduction. For every 1% of lithium added, there is approximately a 3% decrease in material density, making Al-Li alloys ideal for aerospace applications where weight savings are crucial. Their ability to replace heavier 2XXX series alloys while remaining weldable enhances their value in advanced structural applications. Another emerging group within the 8XXX series is aluminum-scandium alloys. Scandium, a rare earth element, is still being explored but shows great promise in improving mechanical properties. It contributes significantly to age hardening and grain refinement, which are especially beneficial

in weld zones. Alloys combining scandium with elements like zirconium, Mg, zinc, or lithium have shown excellent results, achieving tensile strengths over 600 MPa in laboratory tests. Although these scandium-containing alloys are still in the development phase and await formal designation, they represent the next generation of high-performance aluminum materials. These innovations within the 8XXX series are paving the way for advanced, lightweight, and strong Al-alloys suitable for demanding engineering and aerospace applications.

1.10 History of parent material

1.10.1 AA6061

The inherent physical and mechanical properties of pure Al are constant and relatively limited. However, by alloying aluminum with two or more metallic elements, it is possible to create Al-alloys with significantly improved characteristics. These enhancements result in alloys that are more flexible, durable, and often nearly as strong as steel. One of the most widely used Al alloys is AA6061, developed in 1935. It is a heat-treatable alloy primarily composed of Mg and Si, with additional elements such as Cr, Mn, Fe, Cu, Zn, and Ti included in smaller quantities to refine its properties. AA6061 stands out among Al-alloys for its good balance of strength, corrosion resistance, and weldability. Unlike many other Al alloys that pose challenges during welding due to poor thermal conductivity and complex chemical composition, AA6061 is more manageable due to its heat-treatable nature.

The versatility of AA6061 has made it a preferred material in various sectors. It is commonly used in the fabrication of automotive parts, bicycle frames, valves, yacht structures, couplings, camera lenses, and electrical fittings. Its combination of light weight, good machinability, ensures its continued relevance in modern manufacturing and engineering applications. As industries continue to seek lightweight, strong, and corrosion-resistant materials, AA6061 remains a reliable and efficient choice.

1.10.2 AA8011

AA8011 is a widely used Al-alloy primarily known for its versatility in non-heat-treatable applications. Its history is deeply tied to the evolution of aluminum manufacturing and processing technologies, particularly during the mid-20th century, when the demand for lightweight, corrosion-resistant, and formable materials grew across multiple industries. Originally developed as part of the 8xxx series, AA8011 was designed to improve upon the limitations of earlier commercial-grade aluminum, specifically in terms of strength, corrosion resistance, and workability. Unlike other alloy families such as the 5xxx or 6xxx series, which are based on Mg and Mg-Si systems respectively, the 8xxx series (including AA8011) comprises a more complex combination of elements like Fe, Si, and Mn, which contribute to the alloy's unique properties.

The introduction of AA8011 is largely attributed to the expanding requirements of the packaging industry, especially in the production of aluminum foil. Prior to AA8011, pure aluminum or lower-alloyed grades were commonly used, but they

lacked sufficient strength and formability. AA8011 offered an ideal balance—it maintained excellent ductility while improving mechanical strength and resistance to oxidation, which was critical for food and pharmaceutical packaging. The alloy's iron and Si content provided better strength at thinner gauges, allowing manufacturers to produce ultra-thin foils without compromising integrity. This development marked a significant technological leap in rolled product manufacturing.

By the 1970s and 1980s, AA8011 had become the industry standard for household aluminum foil, air conditioner fins, bottle caps, and container packaging. The alloy's ability to be rolled into thin sheets while retaining good mechanical properties made it irreplaceable in applications where flexibility and surface quality were essential. Over time, the alloy found additional applications in automotive heat exchangers, electrical cable sheathing, and architectural products, particularly in areas where weight reduction and corrosion resistance were crucial. Although not suitable for structural loads, AA8011's formability and surface finish made it a preferred choice for aesthetic and protective uses. AA8011 is typically processed through cold rolling and is often supplied in tempers like O (annealed), H14 (partially hard), and H18 (full hard), depending on the application. The alloy is not strengthened by heat treatment, but by cold working processes that modify its grain structure. In more recent developments, manufacturers have improved the alloy by controlling trace elements and refining processing techniques to enhance its surface cleanliness, thermal conductivity, and recyclability. As industries continue to shift toward more sustainable and energy-efficient materials, AA8011 remains highly relevant due to its excellent recyclability and lower environmental footprint.

1.11 Problem Formulation

Despite the increasing industrial demand for lightweight and high-strength joints, especially in the automotive and aerospace sectors, the CMT welding process remains significantly underexplored for joining dissimilar aluminum alloys, particularly between the AA 8000 and AA 6000 series. A comprehensive review of existing literature reveals a substantial research gap in optimizing the CMT process parameters for such dissimilar combinations, which are inherently challenging due to differences in thermal properties, chemical composition, and weldability.

Moreover, critical mechanical properties of CMT weldments—such as hardness distribution, UTS, and residual stress behavior—have not been adequately addressed for these specific alloy systems. Equally, the physical microstructural characterization of such weldments, which plays a pivotal role in determining joint integrity and long-term performance, has received minimal attention. Limited studies employing advanced tools like SEM, EDX, and XRD indicate a need for deeper insight into phase formations, intermetallic compound distribution, and elemental diffusion across the weld zone.

Therefore, the proposed research aims to systematically investigate the CMT welding of dissimilar aluminum alloys (AA 8000 series and AA 6000 series) with the following objectives:

- Using SEM, EDX, and XRD to study the microstructural and phase evolution at the weld interface.
- Through tensile testing, hardness profiling, and impact testing to evaluate the joint strength and performance.
- Optimization of CMT Process Parameters to enhance joint quality and mechanical reliability, ensuring the most favorable combination of heat input, current, and welding speed.

1.12 Motivation

In the modern era of engineering and manufacturing, the push towards lighter, stronger, and more efficient materials has driven extensive use of light metal alloys. Among these, the AA 8000 series alloys are extensively utilized in electrical engineering and due to their superior conductivity and corrosion resistance, while the AA 6000 series alloys are preferred for structural applications owing to their excellent strength, weldability, and machinability. A reliable joining method for these dissimilar alloys can open new opportunities for multi-functional components that combine the best properties of both series. However, joining AA 8000 to AA 6000 presents considerable challenges. These include different melting points, which lead to defects such as poor wettability, excessive heat input, microcracking, and brittle IMC formation. Traditional fusion welding techniques like TIG or MIG often introduce excessive heat, resulting in large HAZ, distortion, and inadequate joint strength. This scenario demands a welding process that can ensure minimal heat input, precise control over arc behavior, and high-quality joint formation. Cold Metal Transfer (CMT) welding stands out in this regard due to its controlled, low-energy arc characteristics and spatter-free operation, achieved by the synchronized retraction of the filler wire during each short-circuit cycle. These features significantly reduce thermal stresses and enable the formation of defect-free joints even between metals with vastly different properties.

Despite the clear advantages of CMT welding, limited research works were found on dissimilar aluminum alloys, particularly the AA 8000 and AA 6000 series. There is a notable deficiency of systematic studies examining the mechanical performance (e.g., UTS, micro-hardness, residual stress) and microstructural evolution (grain morphology, phase formation, and elemental diffusion) of such joints.

The motivation behind this research is to bridge this critical knowledge gap by exploring the potential of CMT welding for AA 8000–AA 6000 dissimilar joints. The goal is to achieve high-quality weldments with optimal mechanical properties and minimal defects through systematic experimental analysis, microstructural characterization (using SEM, EDX, and XRD), and parametric optimization. This work will contribute to enhancing the applicability of CMT in advanced structural applications and offer a deeper scientific understanding of dissimilar aluminum alloy welding.

1.13 Novelty

The proposed research introduces a novel approach to welding dissimilar aluminum alloys—specifically AA 8000 and AA 6000 series—using the CMT process, which has not been extensively explored in current literature. While CMT has proven advantages in reducing heat input and improving weld quality, its application to dissimilar aluminum alloy systems remains underdeveloped, particularly for combinations involving the AA 8000 series, which is primarily used in electrical and utility applications. This study addresses a critical research gap by being among the first to systematically investigate the weldability, mechanical performance, and microstructural evolution of these alloys when joined using CMT.

A key novelty lies in the integration of advanced characterization techniques—such as SEM, EDX, and XRD—to comprehensively evaluate the interfacial behavior, phase transformations, and elemental diffusion in the weld zone. The study also aims to optimize CMT process parameters to enhance joint efficiency, minimize the formation of brittle IMCs, and enhanced mechanical properties.

Additionally, the work proposes a comparative analysis of shielding gases (Ar, He, CO₂, and their combinations) and their influence on heat input and weld quality—an area with limited prior exploration for aluminum dissimilar alloys. By addressing these unexplored aspects, the research not only advances fundamental understanding but also contributes practical insights for industries seeking reliable, low-heat welding solutions for dissimilar aluminum alloys. Hence, this study is both technically innovative and industrially relevant, offering a new pathway for high-performance, lightweight multi-material components.

CHAPTER-2

Literature Review

Unlike conventional welding processes, CMT utilizes a precisely synchronized wire feeding mechanism that allows for short-circuiting without excessive spatter, minimizing heat-affected zones and distortion. This is especially beneficial for Al-alloys, which are known for their high thermal conductivity and sensitivity to thermal cycles, often leading to issues such as hot cracking, porosity, and reduced mechanical strength in traditional welding techniques. Researchers have focused on optimizing process parameters to achieve defect-free welds with refined grain structures and improved tensile properties.

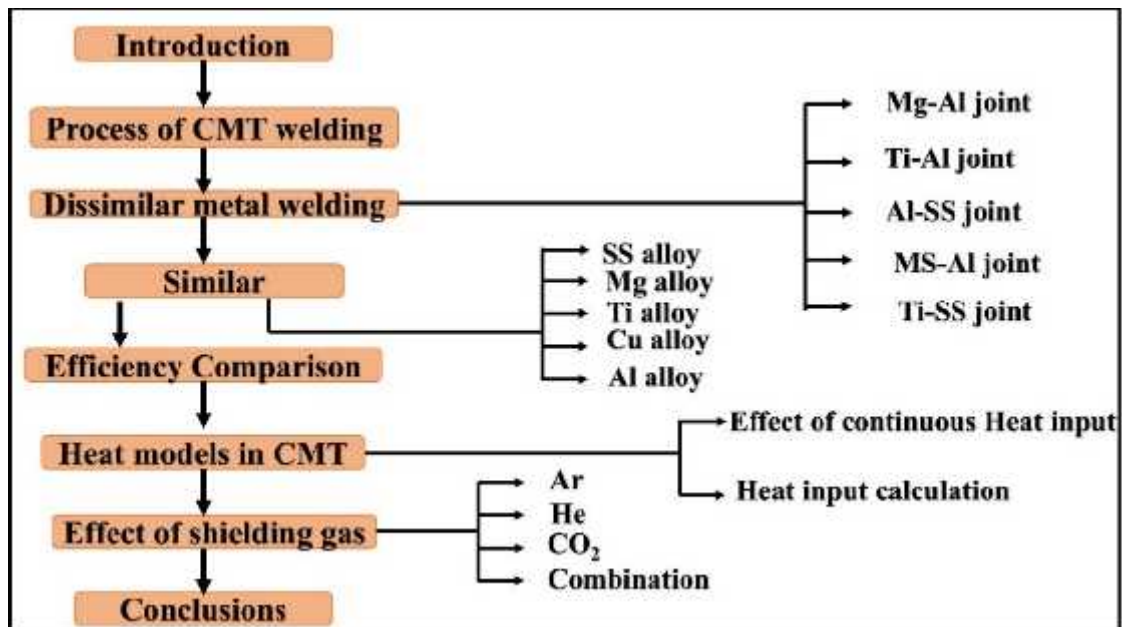


Figure 12: Flowchart of CMT Welding Process and Its Applications in Metal Joining

Furthermore, CMT's adaptability to various Al-alloy series (e.g., 5xxx, 6xxx, and 7xxx) and its applicability in dissimilar metal welding—such as aluminum to steel—have broadened its industrial relevance, particularly in automotive, aerospace, and marine sectors. The current literature also delves into the metallurgical characteristics of CMT welds, including IMC formation, heat input management, and Post Weld Heat Treatment (PWHT) aimed at enhancing corrosion resistance and fatigue life. As research continues to expand, CMT stands out as a promising solution for joining Al-alloys efficiently while maintaining structural integrity and minimizing thermal damage, paving the way for its widespread adoption in advanced manufacturing applications. Figure 12 presents a structured flowchart outlining the key components of a Research work on CMT welding, particularly focusing on its applications in both similar and dissimilar metal joining. It begins with an Introduction, followed by

a detailed description of the CMT welding process. The next major branch addresses dissimilar metal welding, which is further divided into specific joint combinations like Mg-Al, Ti-Al, Al-SS, MS-Al, and Ti-SS, showcasing the versatility of CMT in bonding metals with contrasting properties. Parallel to this, the chart also explores similar metal welding, including common alloys such as stainless steel (SS), Mg, Ti, Cu and Al. It then transitions to an efficiency comparison, possibly discussing how CMT performs relative to other welding techniques across different material combinations. The discussion progresses into the thermal modeling aspects of CMT welding, emphasizing two fundamental components: the influence of continuous heat input and the accurate calculation of heat input. These elements are crucial for interpreting thermal profiles and their metallurgical consequences during welding. Additionally, significant attention is given to the role of shielding gases, including argon (Ar), He, CO₂, and their various mixtures. These gases critically affect arc stability, weld pool behavior, penetration characteristics, and overall weld quality. The analysis also touches on how different shielding gas compositions interact with Al-alloys during the welding process. The section concludes with a summary of findings, offering interpretations and practical recommendations based on the various thermal and chemical interactions studied. Overall, this overview delivers a structured and comprehensive understanding of the key parameters influencing CMT welding, especially concerning material compatibility, heat control, and atmospheric effects.

2.1 CMT welding of dissimilar alloys

CMT is an advanced MIG welding process that have precisely control heat input with minimal spatter, making it particularly appropriate for joining dissimilar alloys. Unlike conventional welding processes, CMT operates with a controlled short-circuiting transfer mode, where the filler wire is retracted during droplet transfer, significantly reducing heat input. This is especially advantageous in dissimilar alloy welding—where differences in thermal conductivity, melting point, and thermal expansion often result in defects like intermetallic compound (IMC) formation, cracking, and poor joint strength. CMT helps mitigate these issues by enabling low-heat input welding, which reduces the formation of brittle IMCs and promotes better metallurgical bonding. Additionally, the flexibility to control welding parameters allows for fine-tuning the weld characteristics for specific alloy combinations. However, despite its potential, more research is needed to optimize CMT for a wider range of dissimilar alloys, particularly in understanding microstructural evolution and improving mechanical performance.

2.1.1 CMT welding of Al/Mg alloys

The dissimilar welding of Mg-alloy AZ31 and AA1060 using the CMT process was investigated [39]. Their study found no observable welding defects, which they attributed to the process's low heat input and rapid thermal cycle. These conditions are critical because they prevent the excessive generation of brittle IMCs, which are typically detrimental to joint efficiency in Mg–Al welds. The mixture of low thermal input and high cooling rates inhibits the diffusion and interaction between Mg and

aluminum atoms, thereby limiting IMC formation. An additional factor contributing to the suppression of brittle phases was the incorporation of Si into the weld.

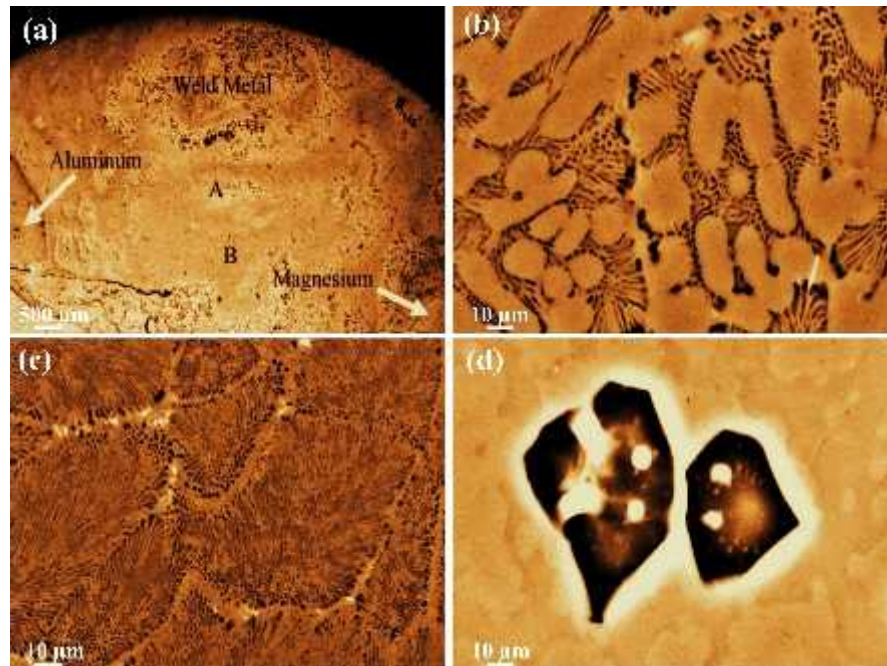


Figure 13: OM images CMT weldments of AA1060 and AZ31, (a) weld Interface, (b-c) microstructure at different welded region (A, B, and C) [39]

The presence of Si plays a dual role: it modifies the solidification pathway and influences the distribution and morphology of IMCs, making them less continuous and less detrimental to mechanical integrity. As a result, the welded joint displayed improved tensile performance relative to conventional fusion methods. Despite these advantages, a complex microstructure was perceived in the weld fusion zone (WFZ) near the Mg substrate. This region contained a multilayer configuration consisting of a solid solution matrix, eutectic structures, and IMCs such as Mg-Al and Mg_2Al_3 . Although such structures might seem beneficial from a metallurgical standpoint, the brittle nature of these IMCs negatively affected the mechanical strength of the joint. Tensile testing revealed premature failure in this region, highlighting the need for further optimization. Fractographic analysis provided further insights into the failure mechanism. Three distinct fracture modes, all indicative of brittle behavior, were identified. These modes emphasize the intricate relationship between welding parameters. The study thus reinforces the notion that even subtle changes in thermal conditions or alloy chemistry can lead to significant changes in performance. Microstructural observations using optical microscopy revealed a significant contrast between the substrate and the weld metal. The weld region was marked by pronounced elemental segregation, likely a consequence of the controlled heat input inherent to the CMT process. CMT facilitates a highly regulated heating and cooling cycle, minimizing the duration at elevated temperatures. This rapid thermal cycling restricts the time available for elemental diffusion, thus reducing the formation of Mg-Al IMCs. Three visually distinct zones were identified in the weld metal revealed in Figure 13b-d. These zones were characterized by

different morphologies; each linked to specific thermal conditions during solidification. Zone A contained predominantly white columnar dendrites, indicative of directional solidification and thermal gradients near the fusion boundary. Zone B showed equiaxed grains, suggesting a more uniform thermal field and a shift toward nucleation-dominated solidification. Zone C featured polygonal particles distributed within a dendritic matrix. Interestingly, Zone C also exhibited occasional shrinkage porosity, likely due to the wide solidification temperature range of the constituent alloys and the resulting thermal contraction. This multi-zonal structure provides a comprehensive understanding of how the CMT process influences weld morphology. The variation in grain structure and defect formation across the weld cross-section demonstrates the sensitivity of weld quality to thermal gradients and solidification behavior. The distinct microstructural features observed across the different zones serve as evidence of the complex interplay between thermal input, alloy interactions, and solidification dynamics.

A study on dissimilar welding between AZ31B and AA6061 using the CMT process was conducted [40]. During welding, the inclusion of Si played a crucial role in influencing the metallurgical interactions. Specifically, Si demonstrated a strong tendency to react with Mg, leading to increased melting activity near the Mg side of the joint and promoting the formation of Mg-Si intermetallic phases. This chemical affinity led to microstructural transformations that significantly influenced the weld characteristics. One notable observation was a sharp increase in hardness within the WFZ adjacent to the Mg substrate. This rise in hardness was attributed to a eutectic solidification reaction that occurred during cooling, resulting in the formation of a solid solution of α -Mg along with the intermetallic β -phase (Mg₂Si). XRD analysis verified the occurrence of these phases. While these IMCs contributed to local strengthening, they also introduced brittleness into the joint. As a result, tensile testing revealed that fractures predominantly occurred in the weld region, exhibiting a brittle failure mechanism. The localized hardening due to intermetallic formation, although increasing hardness, negatively impacted the joint's ductility and tensile strength. In a related investigation, The lap joining of A6061-T6 aluminum and AZ31B using the CMT process under four distinct heat input conditions was explored. AlSi5 wire was selected as the filler metal due to its compatibility and ability to mitigate excessive IMC formation. Their work focused on understanding how varying heat input influenced the mechanical integrity, residual stresses, and corrosion performance of the weldments. The researchers observed that increasing heat input had a beneficial impact on weld quality. Higher heat input levels allowed for more uniform temperature distribution across the weld bead, which resulted in more consistent cooling rates throughout the weld cross-section. This uniform cooling helped to minimize residual stresses and refine the grain structure in both the upper and lower layers of the joint. The finer microstructure translated into improved mechanical strength. Additionally, better thermal management due to higher heat input enhanced corrosion resistance, as fewer microstructural discontinuities and stress concentrations were present in the weld zone.

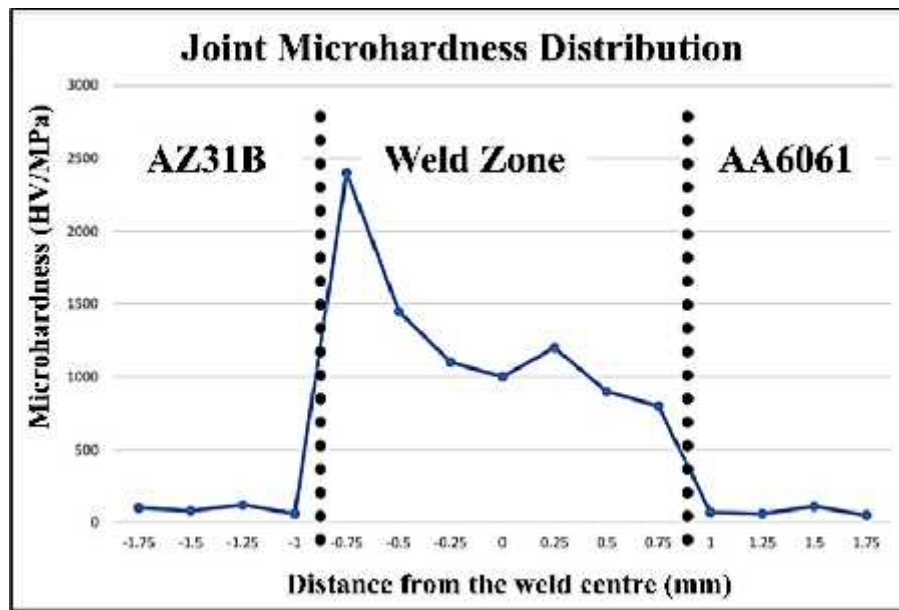


Figure 14: Hardness Distribution Across AZ31B/AA6061 Dissimilar Weld Joint [40]

Figure 14 illustrates the hardness distribution profile across the dissimilar weld joint between AZ31B and AA6061 Al-alloy, fabricated using the CMT welding process. The horizontal axis represents the distance from the weld center (in mm), while the vertical axis indicates the hardness values measured in HV/MPa. From the graph, it is evident that the AZ31B base metal region (to the left of -1.0 mm) maintains a relatively low and consistent hardness level. However, a sharp increase in hardness is observed as the measurement approaches the weld zone, reaching a peak at approximately -0.75 mm. This sudden rise in hardness is attributed to the formation of hard IMCs and solid solution strengthening that occurs during the rapid solidification of the weld pool. The peak value signifies the location with the highest degree of metallurgical transformation due to welding thermal cycles. Following this peak, the hardness gradually decreases across the weld zone, indicating a transition from the highly alloyed region near the Mg side to a more homogenized structure closer to the Al side. Minor fluctuations in microhardness within the WFZ may be due to heterogeneous microstructures or varying distributions of precipitates and IMCs. As the profile reaches the AA6061 base metal (beyond 1.0 mm), the hardness stabilizes at a lower level again, similar to the AZ31B side. This behavior confirms that the base metals retain their original mechanical properties, while the weld zone shows significant variation due to metallurgical transformations. Dynamic corrosion testing was agreed out to evaluate the pitting corrosion resistance of the weldments. The occurrence of IMCs was found to enhance corrosion resistance, primarily attributed to the influence of higher input heat during welding. A dissimilar metals AZ31B and 6061 Al-alloy were successfully welded using the CMT technique with variable polarity [42]. The process employed different Electrode Positive/Electrode Negative (EP/EN) ratios, and ER4043 filler wire was utilized to facilitate the joining. The study revealed that as the EP/EN ratio decreased, there was a notable reduction in the filler metal penetration into the base materials. Additionally, the thickness of the IMCs formed near the AZ31B substrate and the WFZ also diminished with the reduction in the EP/EN ratio. This reduction in IMC thickness was reflected in the

hardness profiles, where hardness peaks were observed due to the presence of these hard and brittle IMCs. Interestingly, lowering the EP/EN ratio led to a significant enhancement in the UTS of the joints—by more than 100% in some cases. However, the fracture mechanism remained brittle, predominantly due to the existence of IMCs in the weld zone. These IMCs, especially those rich in Mg, were found in substantial amounts near the Mg base plate, contributing to increased hardness within the WFZ. Despite the enhancement in mechanical strength, the brittleness induced by the intermetallic phases caused the joints to fail under tensile stress, with strength levels that did not match those of either base metal. This highlights the trade-off between strength improvement and brittleness in dissimilar metal welding involving Mg and Al-alloys.

2.1.2 CMT welding of Al and Ti alloys

The application of CMT welding in WAAM for joining dissimilar metals was explored, specifically AlSi5 and Ti-6Al-4V alloys. Their experimental setup utilized Direct Current (DC) CMT welding, and the resulting deposition behaviors of the two alloys revealed key differences. The Al-alloy demonstrated a smooth, shiny, and defect-free deposition surface, indicating uniform heat distribution and stable melt flow. In contrast, the titanium alloy layers appeared irregular and featured surface grooves, which were primarily attributed to the lower thermal conductivity of titanium. This property caused inconsistent surface temperatures, leading to uneven solidification during deposition. The authors provided a detailed explanation of the solidification processes and interfacial phenomena observed in both alloys. Si atoms from the Al-alloy diffused into the titanium matrix, leading to the development of a brittle IMC identified as Ti_3AlSi on the titanium side of the joint. Simultaneously, titanium atoms diffused into the Al-alloy, forming another IMC, $\text{Ti}(\text{Al} - x\text{Si}_x)$, in the aluminum matrix. These IMCs significantly influenced the joint's mechanical behavior. Due to the thermal expansion mismatch between the two metals, residual stresses developed during cooling, which, combined with the presence of brittle IMCs, caused crack propagation at the interface and ultimately led to fracture. An axial magnetic field during CMT welding of aluminum-titanium dissimilar joints was introduced. They investigated the effect of magnetic fields on arc stability and metal transfer. Alternating current (AC) was used to better control the magnetic effects. The application of the Lorentz force, induced by the magnetic field, modified the arc trajectory by rotating it away from the weld pool center. This widened the molten zone and promoted better mixing of materials at the interface. The improved arc behavior under the magnetic field enhanced droplet transfer, refined the weld profile, and led to the formation of thinner and more uniform intermetallic layers. These changes resulted in increased shear tensile strength and a noticeable shift in the fracture path away from the interface, indicating improved mechanical bonding. A dissimilar lap welding of 1 mm thick Ti-6Al-4V and A6061-T6 using ER4043 filler wire was studied [45]. Two setups were evaluated by alternating the top and bottom positions of the titanium and aluminum plates. The thermal properties of the materials influenced the weld quality. When the aluminum plate was placed on top, the joint suffered from severe spattering and deformation due to aluminum's lower melting point and higher thermal conductivity. In contrast,

positioning the titanium plate on top resulted in cleaner weld beads, minimal distortion, and less spatter. This setup facilitated better wetting of the titanium by the aluminum-Si filler, leading to improved metallurgical bonding. The joint's cross-sectional analysis revealed a combination of welding and brazing mechanisms, with thin intermetallic layers forming at the Ti-Al interface, enhancing the structural integrity.

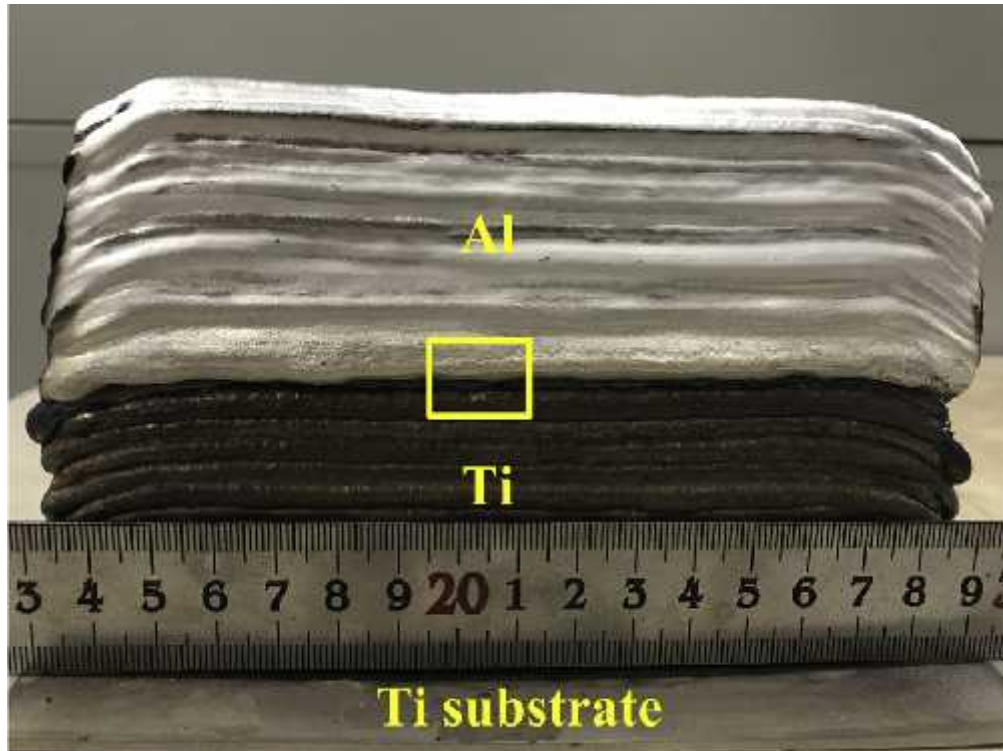


Figure 15: Cross-sectional View of Al/Ti Multi-layered Structure Fabricated by WAAM on Ti Substrate [43]

Figure 15 illustrates a segment of a multi-layered build formed using WAAM with dissimilar metals, specifically aluminum (Al) and titanium (Ti) [43]. The image clearly showcases the deposition of alternating layers, where the upper portion is composed of Al layers and the lower section consists of Ti layers. These layers were deposited sequentially during the CMT process, with the entire structure resting on a titanium substrate, as labeled at the bottom of the image. The interface between the two metals is marked within the yellow rectangle, indicating the critical region where metallurgical bonding occurs between aluminum and titanium. This interfacial zone is of particular importance due to the formation of IMCs such as Ti-Al-Si and $\text{Ti}(\text{Al} - x\text{Si}_x)$, which are known to be brittle and can significantly influence the mechanical performance of the joint. The uniform layering observed in both metal sections suggests consistent process parameters and effective heat control during deposition. Moreover, the distinct color contrast between the Al and Ti regions visually emphasizes their compositional differences. The relatively smooth and bright appearance of the aluminum layers indicates stable melt flow and solidification, while the darker, slightly rougher titanium layers reflect the material's different thermal and physical properties. The Ti substrate serves as a base to support

the structure and absorb the heat generated during the deposition process. This image is significant as it not only demonstrates successful deposition of dissimilar metals using WAAM but also visually supports the microstructural and mechanical analyses discussed in the related research. It highlights the challenges and achievements in fabricating multi-material components where thermal compatibility, bonding, and microstructural control are critical to performance. The cooling rate played a crucial role in influencing the thickness of the intermetallic layer, which became more pronounced compared to the outermost weld layers. The HAZ in the aluminum region experienced failure due to the joint's tensile strength being lower than that of the base aluminum material. Hardness measurements indicated that the dissociation of Mg Si contributed to a softening effect within the Al-alloy. AlSi5 filler wire in the CMT welding of commercially pure titanium with aluminum was employed [46]. To assess the metallurgical transformations, variations were introduced in the positioning of the plates and the wire feed speed. The results revealed a combination of fusion welding and brazing at the joint interface. The thickness of the intermetallic layer was found to be significantly affected by plate configuration. Specifically, placing the aluminum plate on top resulted in a thinner intermetallic layer and, consequently, improved mechanical strength compared to the arrangement with the titanium plate on top.

2.1.3 CMT welding of aluminum and steel

A hybrid manufacturing approach combining CMT welding with friction surfacing to fabricate lap joints between AA2219 and AISI321 was investigated. In this method, aluminum coatings were applied to stainless steel substrates using friction stir processing, as illustrated in Figure 16. The aluminum used for the coating originated from rods with a diameter of 20 mm. To achieve the required coating characteristics, process parameters such as rotational speed, horizontal feed rate, axial pressure, and dwell time were systematically varied. This enabled the formation of aluminum coatings with 1.2 mm thickness on the stainless-steel surface.

Subsequently, CMT welding was employed to fabricate lap joints where the aluminum-coated stainless-steel sheet was joined with another aluminum sheet. Among various samples, the joint with a 0.6 mm aluminum coating exhibited the highest shear tensile strength, reaching up to 260 N/mm² (as seen in Figure 16). This enhancement was attributed to the optimal melting and retention of the aluminum coating during the CMT process, which enhanced metallurgical bonding. In contrast, joints with a thicker 1.2 mm aluminum coating experienced reduced strength, likely due to misalignment or loading eccentricity during testing.

Metallographic analysis revealed the presence of a distinct interface between the weld metal and the aluminum coating in the joints with 0.6 mm and 1.2 mm coatings. These joints showed a well-developed dendritic microstructure and favorable bonding. However, the 0.3 mm coating joint showed complete melting of the aluminum layer during welding, which led to the absence of a stable metallurgical interface. The residual aluminum layer in the 0.6 mm joint measured between 50–100 μm , while in the 1.2 mm joint, it ranged from 200–400 μm . The thickness of the remaining unmelted aluminum significantly affected the fusion behavior of the weldment.

Additionally, the interface between the aluminum layer and stainless steel was deliberately engineered with a zigzag surface morphology prior to friction surfacing, which improved mechanical interlocking and enhanced joint strength. While a thinner unmelted aluminum layer (50–100 μm) helped optimize joint strength, excessive residual coating (200–400 μm) in thicker layers introduced stress concentration and reduced performance. These findings emphasize the importance of controlling coating thickness and bonding quality for achieving high-strength dissimilar metal joints using hybrid CMT techniques.

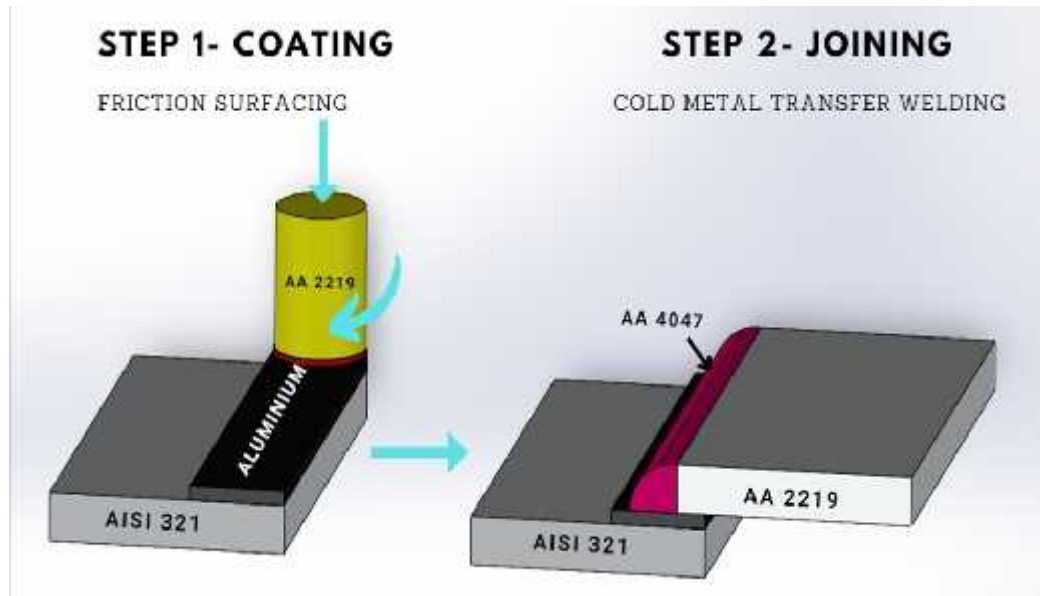


Figure 16: Hybrid Joining Process of AISI 321 Stainless Steel and AA2219 using Friction Surfacing and CMT Welding [47]

Figure 17 illustrates a two-step hybrid joining process used to bond dissimilar metals—specifically AISI 321 austenitic stainless steel and AA2219. In Step 1, friction surfacing is employed to coat the stainless-steel surface with aluminum. During this step, a rotating aluminum rod (AA2219) is brought into contact with the stainless-steel substrate under pressure, generating frictional heat that plasticizes the aluminum. The softened aluminum is then deposited onto the stainless surface as a solid-phase coating, forming a metallurgically bonded aluminum layer without melting either material. This pre-coated surface facilitates improved wettability and bonding for the subsequent step [47]. In Step 2, the actual joining is carried out using the CMT welding process. Here, the pre-coated aluminum layer (AA2219) is welded to another aluminum workpiece using a compatible filler wire (AA4047). The CMT technique, known for its low heat input and precise control over droplet transfer, helps minimize the formation of brittle IMCs at the dissimilar metal interface. This step ensures a strong, ductile joint between the SS and Al base via the aluminum interlayer, overcoming the typical metallurgical incompatibility issues associated with direct Al–Fe bonding.

Overall, the figure represents an innovative and effective approach to joining aluminum to stainless steel by first creating a compatible aluminum coating and then performing controlled fusion welding. This hybrid method enhances joint strength,

reduces residual stress, and mitigates the formation of brittle phases, making it suitable for structural and aerospace applications where dissimilar metal joining is required.

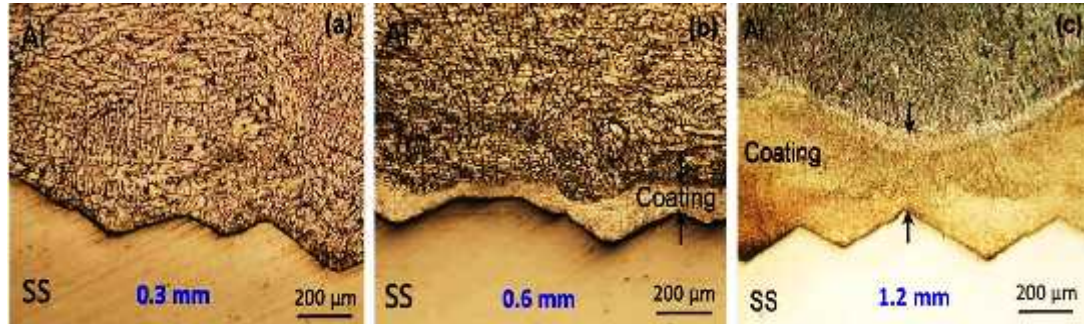


Figure 17: Influence of Aluminum Coating Thickness on Interfacial Microstructure of Al/SS Hybrid Lap Joints Formed by Friction Surfacing and CMT Welding [47]

Figure 17 displays the cross-sectional microstructures of SS and Al lap joints formed using a hybrid technique combining friction surfacing and CMT welding, showing the influence of varying aluminum coating thicknesses on joint quality. The three sub-figures—(a), (b), and (c)—correspond to Al coating thicknesses of 0.3 to 1.2 mm, respectively.

In Figure 17(a), with a 0.3 mm coating, the aluminum layer is entirely melted during the CMT welding process. As a result, no distinct interface remains between the Al coating and the SS. This leads to insufficient metallurgical bonding, as the entire Al layer is absorbed into the weld pool, reducing joint integrity. The absence of a residual coating can limit bonding strength and durability. Figure 17(b) shows the joint with a 0.6 mm coating, where a thin layer of unmelted aluminum (approximately 50–100 μm) remains at the interface. This residual coating promotes strong metallurgical bonding characterized by a fine dendritic structure, leading to better mechanical performance. The retained Al layer serves as a buffer that enhances wetting and fusion, reducing the formation of brittle intermetallics and increasing shear tensile strength—reported to be the highest among the three configurations.

In Figure 17(c), with a 1.2 mm coating, a thicker residual Al layer (about 200–400 μm) is visible. Although the metallurgical bonding is still present, the excessive coating introduces weld pool eccentricity and inconsistent fusion characteristics, which can negatively affect joint strength. The thick unmelted layer may also trap oxides or create voids, reducing mechanical stability. In summary, Figure 17 demonstrates that an optimal coating thickness—specifically 0.6 mm—yields the best combination of interfacial bonding and mechanical performance in Al/SS lap joints. Too thin or too thick coatings either eliminate beneficial interfaces or create instability during welding, making coating thickness a critical parameter in hybrid welding of dissimilar metals. The use of CMT welding combined with an external axial magnetic field (EMF) to join dissimilar metals—specifically, 5A06 and 304 stainless steel was analyzed. The introduction of the EMF had a significant impact on the welding process. By rotating the arc during welding, the EMF enhanced the thermal distribution within the molten pool, thereby expanding the area exposed to

heat and preheating the base materials more effectively. This improved thermal management led to better weld quality and more stable arc characteristics. The presence of the EMF also influenced the overall weld morphology. One of the notable improvements was the reduction in the thickness of the brittle IMCs, particularly the iron-aluminum (Fe/Al) IMC layer that typically forms at the interface of these dissimilar metals. A thinner IMC layer is generally associated with better mechanical performance due to reduced brittleness. Moreover, the EMF helped to suppress the undesirable dilution of iron into the aluminum matrix, which further enhanced the integrity of the joint. Mechanically, the use of the EMF resulted in a significant boost in tensile strength. All joints produced under the influence of the magnetic field exhibited higher strength values compared to those welded without EMF assistance. Notably, the strongest joint fabricated with EMF showed an improvement in tensile strength by approximately 45% over the best-performing joint produced without the magnetic field. This demonstrates the clear benefits of integrating an external axial magnetic field in CMT welding, especially for challenging dissimilar metal combinations.

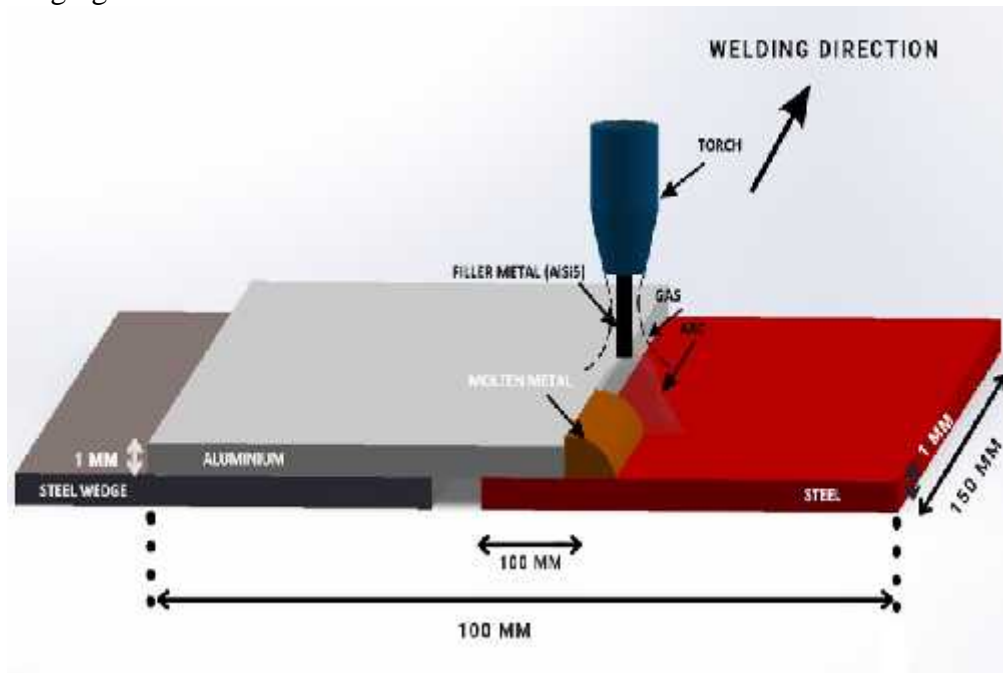


Figure 18: Schematic Diagram of CMT Welding Setup for Dissimilar Aluminum-Steel Lap Joint Configuration [49]

An experimental study was conducted to produce dissimilar joints between aluminum and steel using CMT welding. The materials selected for this investigation were zinc-coated low-carbon steel (DC01) and 6016-T4. The filler material used was a 1.2 mm diameter ER4043 aluminum-Si welding wire. To maintain an inert welding atmosphere and ensure high-quality welds, at GFR of 12 liters per minute. A lap joint configuration was adopted for the welding trials, where the Al sheet was positioned on top of the steel with a 10 mm overhang. The mechanism of the CMT process, shown in Figure 18, is based on a precisely controlled waveform that coordinates the wire feeding and current supply to minimize heat input. During the high-energy pulse phase, an electrical arc melts the tip of the filler wire. This is followed by a short

“wait” phase, where the molten droplet makes contact with the aluminum surface under a significantly reduced current. Once the droplet forms and the arc collapses momentarily due to short-circuiting, the filler wire retracts quickly. This retraction allows the molten metal droplet to detach and transfer smoothly into the weld pool. The arc is then re-established, and the cycle repeats. This alternating cycle of feeding, short-circuiting, and retracting ensures precise metal deposition with reduced thermal impact on the base materials. As a result, the CMT process proves effective in joining aluminum to steel, where controlling heat input is crucial to limiting the formation of brittle IMCs and achieving improved weld quality. Figure 18 illustrates a schematic representation of the CMT welding setup used to join dissimilar materials—aluminum and steel—in a lap joint configuration. In this configuration, a 1 mm thick steel wedge is placed beneath a 100 mm long aluminum plate, which is then joined to a 150 mm long steel plate of similar thickness (1 mm). The plates are aligned such that the aluminum overlaps the steel on one end. The welding process is carried out using a CMT torch, which deposits filler metal (AlSi5) between the aluminum and steel sheets. The torch is angled to direct the arc at the interface between the aluminum and steel. A controlled gas flow, typically argon, shields the weld zone from atmospheric contamination. The arc generated between the torch and base materials melts the filler wire and parts of the base metals to form a molten pool, enabling metallurgical bonding between the dissimilar materials. The welding direction is indicated by an arrow, moving from left to right, along the interface. The use of a steel wedge underneath ensures proper positioning and leveling during welding. This layout helps achieve stable arc ignition and uniform filler deposition, minimizing the heat input to avoid excessive IMCs formation—a common issue in dissimilar aluminum-steel welding. A comparative investigation on the corrosion resistance of dissimilar joints formed between mild steel and AA5052 was conducted [50], utilizing both Gas Metal Arc Welding (GMAW)-brazing and CMT techniques. The primary objective of their study was to analyze how variations in welding parameters, particularly WS and wire feed rate, influence corrosion behavior. The corrosion performance of the joints was evaluated according to the ASTM G67-04 standard. Lap joints were fabricated using an aluminum-Si filler containing 5% Si. Post-corrosion characterization involved Scanning Electron Microscopy (SEM) for microstructure evaluation, nano-indentation testing for hardness profiling, and XRD to identify phase compositions. The findings highlighted significant intergranular corrosion regardless of the welding method. The study concluded that the thickness of the IMC layer is directly influenced by the heat input; higher thermal energy results in thicker, potentially more brittle intermetallic regions. The welding of AA5052 to DP780 advanced high-strength steel using an advanced CMT plus Pulse (CMT+P) process was analyzed [51]. They observed that the geometry of the weld bead and the wetting angle were significantly affected by the additional heat transferred from the thicker aluminum plate, which hindered proper wetting. Metallurgical examination revealed the presence of IMCs at the aluminum-steel interface, primarily involving Fe-Al-Si phases due to limited solubility between iron and aluminum.

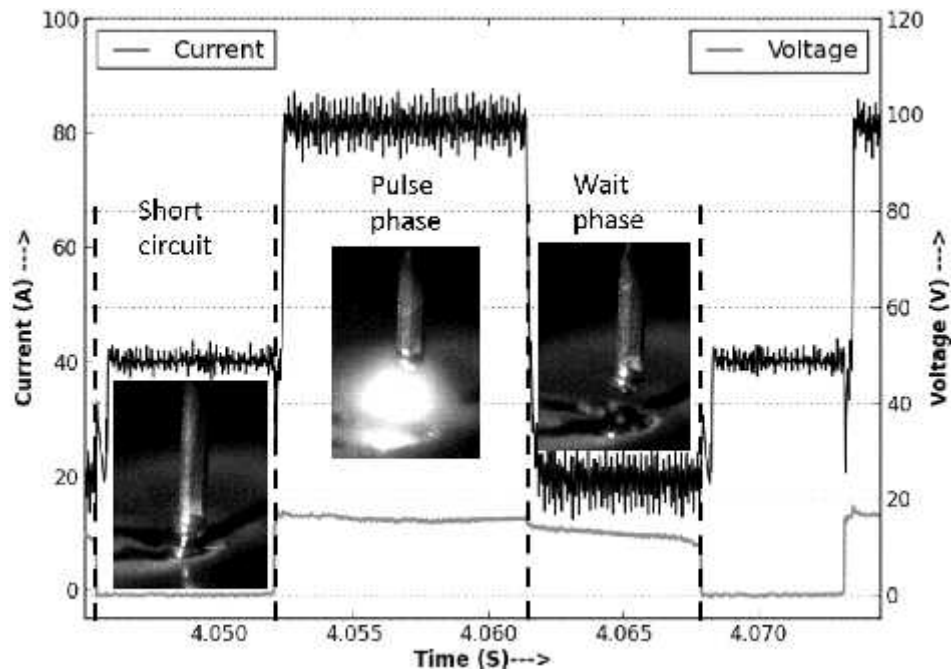


Figure 19: Current and Voltage Characteristics Illustrating the Metal Transfer Mechanism in the CMT Process [53]

These IMCs grew thicker with higher wire feed rates as more base metal was available for reaction. The brittle nature of these compounds contributed to crack initiation and propagation, resulting in reduced mechanical performance [53]. Their results emphasized that the composition of the filler wire had a more pronounced influence on the resulting joint microstructure than the welding parameters themselves. Fillers with higher Si content were found to effectively suppress the formation of thick intermetallic layers. However, the impact of varying Mg content in the filler wires on IMC development remained inconclusive. Figure 19 illustrates the metal transfer mechanism during the CMT welding process, highlighting the variations in current and voltage over time across three distinct phases: short circuit, pulse. The filler wire makes contact with the weld pool, causing a drop in voltage and a modest current level in the short circuit. This initiates the transfer of molten metal without generating excessive heat or spatter. The process then transitions into the pulse phase, where the wire is retracted, and a high-intensity current pulse is applied to reignite the arc. This pulse melts the wire tip and forms a droplet ready for deposition. Subsequently, the wait phase begins, characterized by a reduction in current and voltage as the arc stabilizes and prepares for the next cycle. The inset images corresponding to each phase visually depict the wire behavior and arc activity. The synchronized control of wire motion and arc energy in CMT ensures a stable, low-heat welding process, making it especially suitable for joining dissimilar materials like aluminum and steel with minimal spatter and intermetallic formation. The experiments on welding zinc-coated carbon steel to Al-alloys using the CMT technique was conducted [52].

Table 3: Filler wires and Base Metals used in the CMT process for Aluminum–Steel Dissimilar Joints [56]

S.No	Base Materials	Filler Wire Details
1	6061-T4 paired with zinc-coated low-carbon steel	ER4043 filler wire, 1.2 mm diameter
2	H32 5052 joined to galvanized mild steel	Al-5%Si wire, 1.2 mm in diameter
3	Dual-phase steel (DP780) coupled with AA502	AlSi5 wire of 1.2 mm diameter
4	EN AW 6014 T4 combined with galvanized dual-phase steel (HCT 450X + ZE 75/75)	A mix of commercial (EN AW 5183, 5087, 6082, Al-3Si-1Mn) and experimental wires (Al-4Mg-0.6Sc, Al-0.3Mg-0.5Sc-0.4Zr, Al-0.3Mg-0.4Sc-0.3Zr)
5	6061-T6 and thick zinc-coated mild steel	ER4043 filler with 1.2 mm wire diameter
6	AC 170 PX joined to galvanized ST 06 Z steel	Both ER4043 and ER4047 wires, each 1.2 mm in diameter
7	Various Al-alloys (AA6061, AA7075, AA5183) with galvanized mild steel	Filler wires used: Al4043, Al4047, and Al5356, all of 1.2 mm diameter

ER4043 filler wire, with a diameter of 1.2 mm, was employed during the process. According to their findings, the vaporization of zinc from the coated steel introduced several complications—such as wavy weld edges, formation of pores, and inadequate fusion at both the sidewall and root. The presence of Si in the filler helped in partially dissolving the formed IMCs within the metal matrix, resulting in a thinner IMC layer. To manage zinc vaporization, a deliberate gap between the plates was maintained, allowing vapor to escape from the molten weld pool. This approach enhanced joint fusion and improved the bonding geometry by lowering the bonding angle, leading to an increase in the UTS of the weld [54]. Two different filler wires, ER4043 and ER4047, were assessed. The ER4043-based joints demonstrated better wettability, longer bonding length, and higher joint strength compared to those made with ER4047 under identical parameters. Electron Probe Micro-Analyzer (EPMA) is used to analyzed the phase composition. The lower wettability of the ER4047 filler contributed to failure initiation in tensile shear strength testing. Fractographic analysis revealed that ER4043 joints displayed a combination of brittle and ductile fracture modes, while ER4047 joints exhibited ductile behavior with visible dimples. The lap welding of Al-alloy to galvanized mild steel, both 1 mm in thickness was investigated [55] Taguchi design of experiments was used, incorporating seven variables at three levels each to determine the optimal welding parameters. A quadratic regression model was developed to correlate welding parameters with joint strength. Microstructural analysis revealed only Fe-Al intermetallics, with no trace of zinc due to its evaporation under the intense arc heat. Notably, the mechanical performance of the steel–aluminum dissimilar weld was comparable to that of an aluminum-to-aluminum weld. However, hardness measurements confirmed that HAZ softening in the aluminum side contributed to a minor reduction in joint strength relative to the aluminum base metal. Table 3 presents a summary of various

studies that employed CMT welding to join dissimilar combinations of Al-alloys and steels. It lists the base metals used—ranging from different grades of Al-alloys (e.g., 6061-T4, 5052, 6014 T4) to galvanized and dual-phase steels (e.g., DP780, HCT 450X). The table also highlights the filler wires applied in these studies, most commonly ER4043 and Al-Si-based alloys, with some studies exploring custom or commercial variants such as Al-4Mg-0.6Sc. This comparative overview helps identify the effect of different base metal-filler combinations on weld quality and performance in CMT welding.

2.1.4 CMT welding of steel and Ti alloys

The influence of variable polarity CMT arc brazing using ER CuSi filler wire to reduce the brittleness of Ti-Fe IMCs [57]. By adjusting the EP/EN ratios, they assessed how polarity changes impacted the heat distribution, weld penetration, tensile strength, and resulting microstructures. Lower EP/EN ratios led to greater energy input into the filler wire, which effectively reduced the duration of high-temperature exposure. The EP/EN ratio varied from 8:1 to 1:8, and a reduction in the Ti Si intermetallic layer thickness and the Ti-Cu transition zone was observed—from 118 μm to 81 μm . Despite these changes, tensile strength only slightly decreased from 216.89 MPa to 211.29 MPa. With increasing EP/EN ratios, the Ti Si layer and transition zone thickened, which negatively affected joint strength. The optimal tensile performance was observed at an EP/EN ratio of 8:8, indicating a favorable balance between intermetallic thickness and transition zone formation [58]. The team varied the filler wire feed speed in three stages and used ERCuSi-A as the filler material. It was found that increasing the wire feed rate significantly improved the joint strength, although all samples demonstrated brittle fracture behavior. Figure 20 illustrates the effect of varying EP: EN polarity ratios on the thermal distribution, intermetallic layer thickness, Ti Si phase distribution, and tensile strength of Ti-6Al-4V/304L dissimilar joints welded using the CMT process [57]. The thermal distribution images reveal that a higher EP ratio (8:1) concentrates more heat on the Ti-6Al-4V side, while a more balanced ratio (8:8) results in a more even thermal spread across the joint. Corresponding microstructural analysis shows that the thickness and uniformity of the intermetallic layer, consisting of a Ti-Cu base and Ti Si phase, improve significantly at the 8:8 polarity ratio. This balanced setting leads to a thinner and more refined intermetallic layer compared to the 8:1 and 1:8 ratios. The Ti Si distribution is quantitatively assessed, with the 8:8 ratio showing the lowest standard deviation and coefficient of variation, indicating a more homogeneous and stable phase formation. As a result, tensile strength is maximized at this ratio, reaching 267.69 MPa, while extreme polarity ratios yield lower strength due to uneven phase distribution and thicker, brittle intermetallic layers. Overall, the 8:8 EP:EN ratio provides the most favorable combination of thermal control, microstructural refinement, and mechanical performance. A wire feed rate of 5.5 m/min, corresponding to higher heat input, resulted in the strongest joint. The microstructural changes were closely linked to both the wire speed and torch position. Notably, higher heat input led to a considerably thicker Cu-Ti interfacial region—three times thicker than that observed at lower input levels. Additionally, the Cu-Fe interface showed a clear dependence on wire feed rate. As heat input

increased, more extensive melting of the stainless steel occurred, enhancing weld pool mixing and reducing IMC formation. The butt joint welding between titanium alloy AMS4911 and 316L stainless steel using the CMT process was successfully fabricated [59], with both materials having a thickness of 2 mm. Their findings indicated that at lower wire feed rates, poor wettability of the stainless steel by the weld metal resulted in undercut defects at the SS-weld interface.

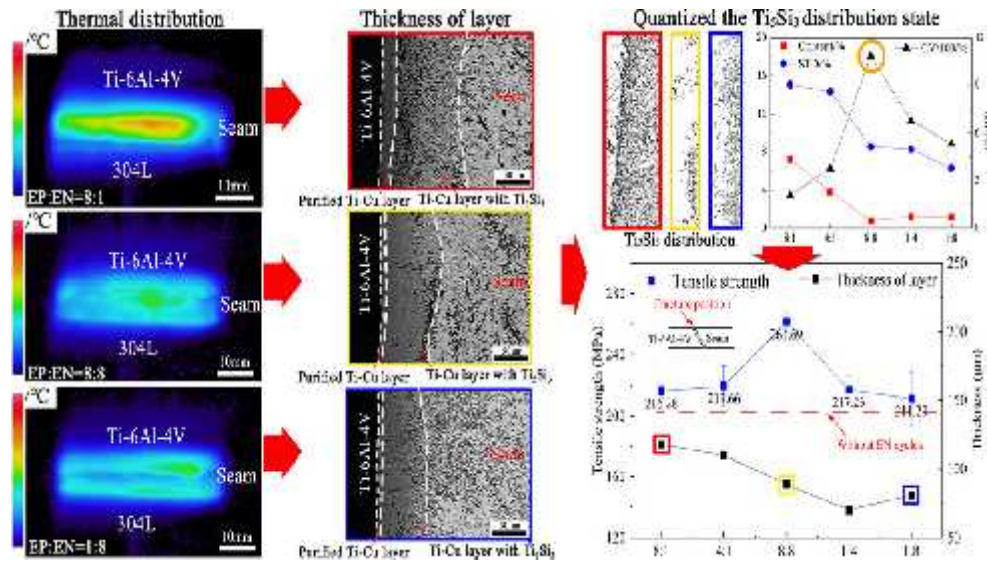


Figure 20: Influence of EP: EN Polarity Ratio on Thermal Distribution, Intermetallic Layer Thickness, Ti Si Distribution, and Tensile Strength in Ti-6Al-4V/304L CMT Weldments [57]

This lack of proper fusion directly contributed to a decrease in the tensile strength of the joint. Improved wettability was shown to be crucial for enhancing mechanical performance in such dissimilar metal welds. The influence of varying EP:EN polarity ratios on thermal distribution, intermetallic layer thickness, and the mechanical performance of Ti-6Al-4V/304L stainless steel joints brazed using CMT with ERCuSi filler wire [57]. The thermal images show that an EP:EN ratio of 8:1 results in a higher heat concentration within the seam, leading to prolonged high-temperature exposure, whereas a balanced ratio of 8:8 generates a more uniform thermal distribution, and a 1:8 ratio shows reduced heat input to the seam. This variation in heat input significantly affects the thickness of the IMCs at the interface, particularly the Ti Si compound. Cross-sectional images reveal that as the EP:EN ratio shifts from 8:1 to 1:8, the thickness of the Ti Si layer decreases, with the thinnest and most uniform layer observed at the 8:8 ratio. Quantitative analysis further confirms this trend, showing that the 8:8 ratio yields the most consistent Ti Si distribution, characterized by the lowest standard deviation and coefficient of variation. This optimal distribution correlates with the highest measured tensile strength of 267.69 MPa. In contrast, imbalanced ratios such as 8:1 and 1:8 produce thicker and more irregular intermetallic layers, reducing the joint strength due to brittleness. Therefore, the optimizing the EP:EN ratio—specifically maintaining it at 8:8—can significantly enhance the mechanical integrity of dissimilar Ti/SS joints by improving thermal control and minimizing the formation of brittle IMCs.

Metallurgical analysis confirmed that the formation of IMCs was unavoidable during welding. However, the IMCs produced with a copper weld bead exhibited improved ductility compared to those formed between titanium and iron. A lap welding technique was applied to join titanium (TA2) with galvanized Q235 steel [60]. These dissimilar joints were also compared against similar material lap joints. Observations indicated that titanium's low thermal conductivity adversely affected the weld quality across all configurations. The joint with steel positioned on top and titanium at the bottom exhibited higher hardness at the titanium interface due to the presence of Cu-Fe-Ti IMCs, compared to both the base and weld metals. The tensile strength of this configuration reached approximately 93% of the strength of the steel-to-steel joint. Fracture analysis revealed that failure in the top Ti–bottom steel joint occurred at the titanium–weld interface, whereas in the top steel–bottom titanium and steel–steel joints, failure initiated in the steel base metal. Table 4 provides a summary of CMT-welded dissimilar joints between titanium alloys and stainless steel.

2.2 Welding of similar alloys

Ni-based and Fe-based filler coatings onto SS304 using the CMT process was applied to enhance resistance against wear and cavitation erosion [61]. The results showed that the coated surfaces had significantly lower cumulative volume and weight loss—nearly ten times less than the uncoated substrate.

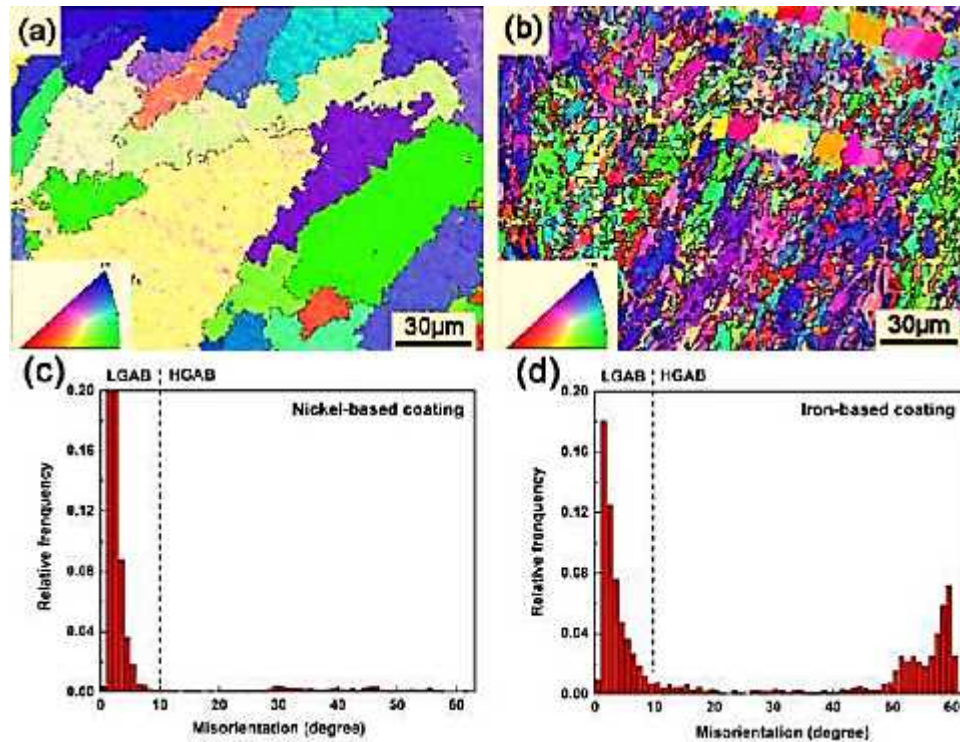


Figure 21: EBSD and IPF analysis of Ni-based and Fe-based coatings deposited by the CMT process—(a) IPF map of Ni-based coating, (b) IPF map of Fe-based coating, (c) misorientation angle distribution of Ni-based coating, (d) misorientation angle distribution [61]

The superior wear resistance of the iron-based coating was attributed to the presence of fine carbides and enhanced material toughness. In contrast, the corrosion and cavitation resistance of the nickel-based coating was improved due to its dominant alloy phases. Cross-sectional microstructural analysis of both coatings revealed differences in grain structure and solidified droplet interfaces, as seen in Figure 21 (a, b), indicating non-uniform heat distribution during deposition. This uneven cooling led to localized grain growth near the interface, affecting the heat dissipation behavior and increasing the grain size and G/R (growth-to-rate) ratio. Figure 21 (c, d) illustrates the crystallographic misorientation behavior, highlighting the dominance of Low-Angle Grain Boundaries (LAGBs), which are common in clad coatings. The iron-based coating (Figure 21d) had a higher fraction of HAGBs, possibly resulting from recrystallization phenomena. Since HAGBs are known to obstruct dislocation movement and improve toughness, this suggests that the iron-based coating is particularly well-suited for wear-intensive applications. Furthermore, the iron-based coating exhibited a finer grain structure, averaging 1.26 μm , compared to 1.88 μm in the nickel-based counterpart. Figure 21 presents a comparative microstructural analysis of iron-based and nickel-based coatings deposited on 304 austenitic stainless steel via the CMT process. Images (a) and (b) show the Inverse Pole Figure (IPF) maps obtained from EBSD for Ni-based and Fe-based coatings, respectively. The Ni-based coating (Figure 21a) reveals relatively coarse, equiaxed grains, indicating slower solidification or reduced thermal gradients. In contrast, the Fe-based coating (Figure 21b) displays a refined, highly oriented grain structure with elongated grains, suggesting rapid solidification and directional heat flow during deposition. Figure 21 (c) and (d) illustrate the misorientation angle distributions corresponding to the Ni- and Fe-based coatings. The Ni-based coating (Figure 21c) is dominated by Low-Angle Grain Boundaries (LAGBs) with very few High-Angle Grain Boundaries (HAGBs), reflecting a more uniform microstructure with limited recrystallization. On the other hand, the Fe-based coating (Figure 21d) exhibits a notable presence of HAGBs along with LAGBs, which is typically associated with dynamic recrystallization and increased material toughness. The higher fraction of HAGBs in the Fe-based coating implies greater resistance to dislocation movement, thereby enhancing the coating's wear resistance. This comprehensive EBSD and IPF analysis underscores the microstructural advantages of Fe-based coatings for applications requiring superior mechanical durability.

2.2.1 CMT welding of Mg- alloys

Mg's lightweight properties make it advantageous for structural applications, but its welding behavior presents notable challenges. During welding, Mg tends to form large molten droplets, which can lead to spatter if they detach and fall outside the weld pool. This issue is exacerbated by the narrow difference between Mg's melting and boiling points, which increases the likelihood of droplet overheating and vaporization or even explosive behavior under unstable conditions [62, 63]. The Mg-alloys are highly reactive, making them susceptible to oxidation and evaporation during the welding process. Other common issues include grain coarsening, thermal stresses, and hot cracking, all of which can severely compromise weld integrity. Therefore, to maintain a stable arc and produce high-quality welds, meticulous

control of heat input is essential. The CMT welding process offers potential benefits due to its low heat input and controlled droplet transfer. However, although CMT has been applied to Mg-alloy welding, current understanding of arc stability in this specific context remains limited, highlighting the need for further in-depth investigation [64]. In CMT welding, the contact angle between the weld bead and the substrate is a crucial parameter, especially for repair and cladding applications. This angle influences the ability to deposit successive layers effectively. Figure 22 illustrates how cladding appearance changes with different welding parameters. Although CMT's low heat input offers advantages such as minimal distortion, it can also result in narrow beads with small contact angles, which may hinder weld bead overlap and layer build-up. An increase in wire feed speed (WFS) leads to greater heat input and material deposition per unit length, causing the molten pool to spread more and resulting in an increased contact angle [65].

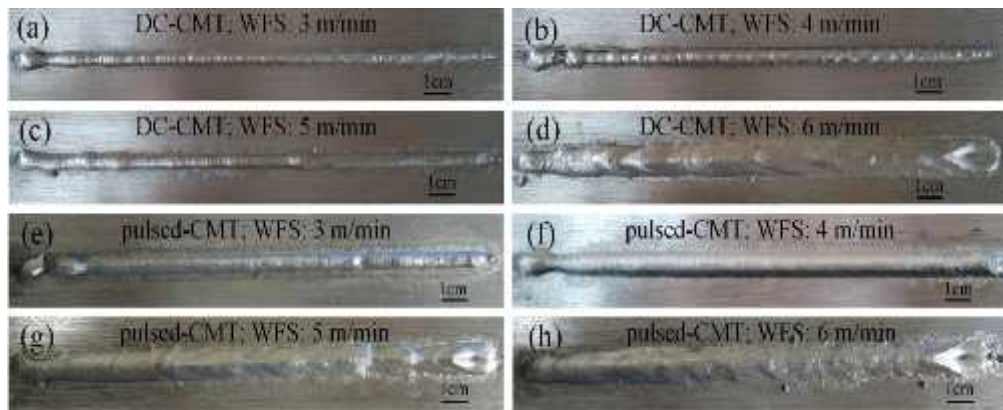


Figure 22: CMT weld bead at different process parameters [64]

For direct current CMT (DC-CMT), the contact angles remained below 90° at WFS values ranging from 3 to 5 m/min. Angles approaching 90° can destabilize the arc during subsequent passes, causing it to jump between the reinforcement and base metal, potentially leading to a lack of fusion between layers [66]. Pulsed-CMT (P-CMT) showed similar behavior at 3 m/min, but when the WFS was raised to 4 m/min, the contact angle improved significantly, reaching 117° , which is favorable for stable, overlapping clads. Research by Ola and Doern [66] emphasized that contact angles above 115° facilitate smoother deposition in multipass cladding. However, further increases in WFS beyond 4 m/min led to arc instability and unsatisfactory weld bead profiles. Thus, maintaining a balance between contact angle and arc behavior is essential. Ultimately, pulsed-CMT at a WFS of 4 m/min was found optimal for cladding light metals, ensuring a stable arc and effective successive pass deposition. This makes it a promising approach for achieving high-quality weld overlays in applications requiring minimal heat input and precise control of bead geometry [65, 66]. Figure 23 presents the SEM images of the WFZ in AZ31 welded using CMT at varying WS [67].

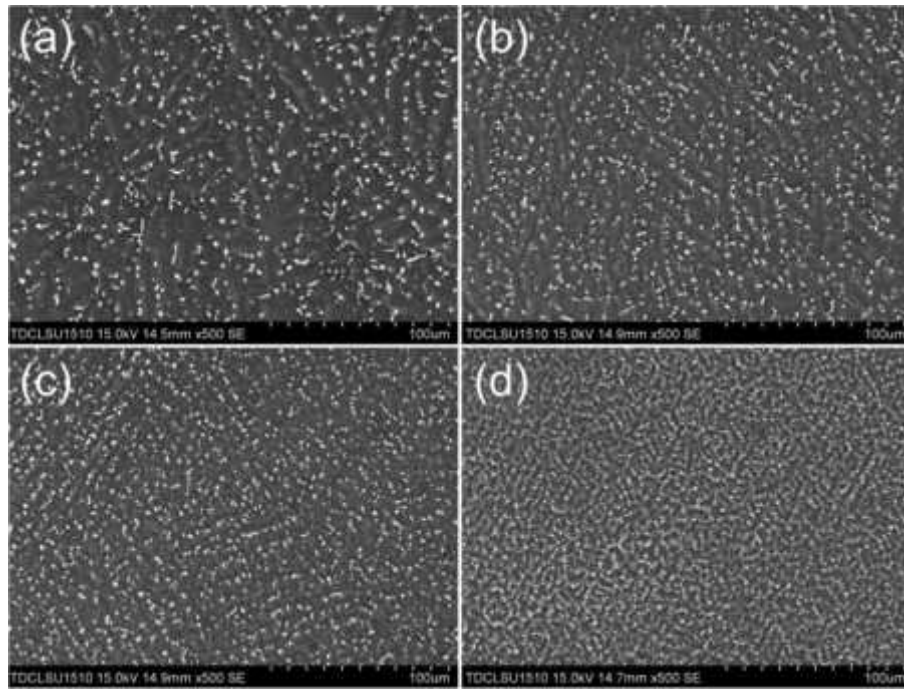


Figure 23: SEM Micrographs of the WFZ in AZ31 Welded by CMT at Different WS: (a) 8 mm/s, (b) 10 mm/s, (c) 12 mm/s, and (d) 14 mm/s [67]

The SEM micrographs illustrate the evolution of the microstructure as the welding speed increases. At a lower speed of 8 mm/s (Figure 23a), the microstructure is coarser, with relatively larger and more elongated solidification structures. This indicates a slower cooling rate, allowing more time for grain growth and coarsening in the WFZ. As the welding speed increases to 10 mm/s and 12 mm/s (Figures 23b), the grain size becomes finer and more uniformly distributed. This refinement is attributed to a higher cooling rate associated with faster WS, which limits grain growth and promotes more homogeneous nucleation. The density of fine grains also increases, which can positively influence the mechanical properties, such as strength and toughness. At the highest welding speed of 14 mm/s (Figure 23d), the microstructure exhibits the finest and most densely packed grains, indicating rapid solidification. Such a structure results from a significant increase in the cooling rate, which not only restricts grain growth but may also help in reducing welding defects like porosity and hot cracking.

Overall, the SEM images demonstrate that increasing the welding speed during CMT welding of AZ31 leads to progressive refinement of the WFZ microstructure, enhancing the weld quality. This trend is essential for optimizing process parameters in CMT welding of Mg-alloys to achieve desirable mechanical and metallurgical characteristics. The microstructural evolution of AZ31 welded by the CMT process at various WS is shown in Figure 23.

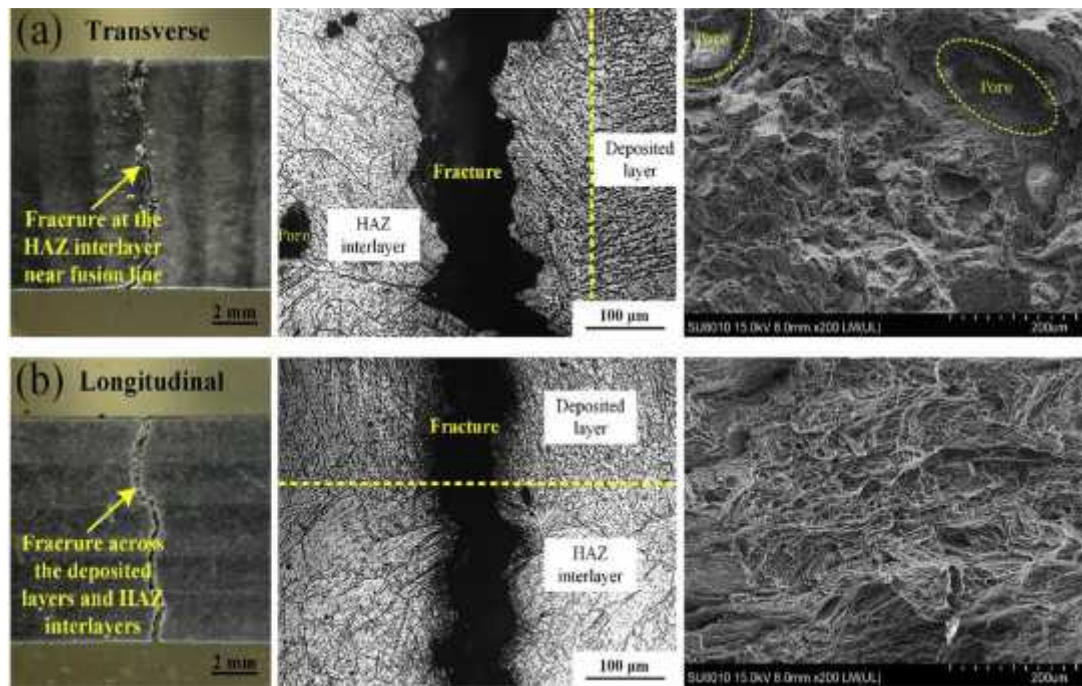


Figure 24: Fractured images of CMT weldments of AZ31, (a) longitudinal direction, (b) transverse direction [68]

As the welding speed increases, a notable refinement occurs in both the β -phase and the overall grain structure within the fusion zone (FZ). This refinement is largely attributed to the reduced heat input associated with higher WS, which in turn leads to lower peak temperatures and accelerated cooling rates. These thermal conditions promote finer grain formation. At a WS of around 14 mm/s, however, the FZ displays the presence of multiple pores, which can detrimentally affect the mechanical integrity of the weld [68]. These pores form when gas becomes trapped during solidification and cannot escape quickly enough due to the rapid cooling. The relatively low density of Mg-alloys makes them more prone to such porosity issues compared to heavier metals like stainless steel. At lower speeds (below 14 mm/s), the absence of pores in the FZ suggests that gases have sufficient time and pathways to escape before solidification completes. Additionally, the smaller grain size in the FZ compared to the base metal (BM) results from the inherently low heat input of the CMT process, combined with the high thermal conductivity and low heat capacity of Mg-alloys, all of which suppress grain growth.

Figure 24 illustrates the fracture morphologies of AZ31 specimens produced through the CMT-WAAM process. Both transverse and longitudinal tensile specimens exhibited ductile fracture characteristics; however, notable differences in their fracture patterns were observed due to the anisotropic mechanical response and layered deposition structure.

In the transverse specimens, failure consistently occurred near the fusion line, specifically in the HAZ interlayers. This region exhibited a higher concentration of pores, which acted as initiation sites for cracking. On the other hand, longitudinal specimens failed along the HAZ interlayers, traversing the deposited layers and the build direction. The fracture surfaces in this orientation were marked by smaller dimples, indicating limited ductility. The occurrence of pores and coarse grain

structures within the HAZ interlayers played a significant role in reducing mechanical strength, especially the ultimate tensile strength (UTS) along the deposition direction. This behavior is consistent with findings in related studies, where interlayer porosity in Al-6Mg alloy components produced by CMT-WAAM has been linked to directional variations in tensile strength. Similarly, porosity introduced in laser-MIG welded AZ31 joints has been shown to reduce elongation and effective cross-sectional area [69, 70]. To enhance the tensile performance of CMT-WAAM AZ31 components, it is essential to address the microstructural weaknesses in the HAZ. Strategies such as minimizing porosity formation and preventing grain coarsening in the HAZ interlayers can significantly improve strength and reduce anisotropy. Reducing the softening effect in these critical zones will lead to more uniform mechanical behavior and greater structural reliability in thin-walled components manufactured via the CMT-WAAM process.

2.2.2 CMT welding of Ti alloys

A novel enhancement technique involving ultrasonic peening treatment (UPT) in three orthogonal directions was introduced to mitigate the microstructural anisotropy in Ti-6Al-4V alloy components fabricated by CMT-Wire Arc Additive Manufacturing (CMT-WAAM) [71]. The primary objective of this approach is to refine the morphology of columnar prior- grains and secondary β -phase grains, which commonly develop during CMT-based deposition and significantly influence the mechanical properties of the final structure. The UPT process applies high-frequency mechanical impacts to the alloy surface, resulting in beneficial plastic deformation, stress redistribution, and grain refinement in the surface and near-surface zones. Ti-6Al-4V is a titanium-based alloy extensively used in aerospace, biomedical, and structural applications due to its excellent strength-to-weight ratio and corrosion resistance.

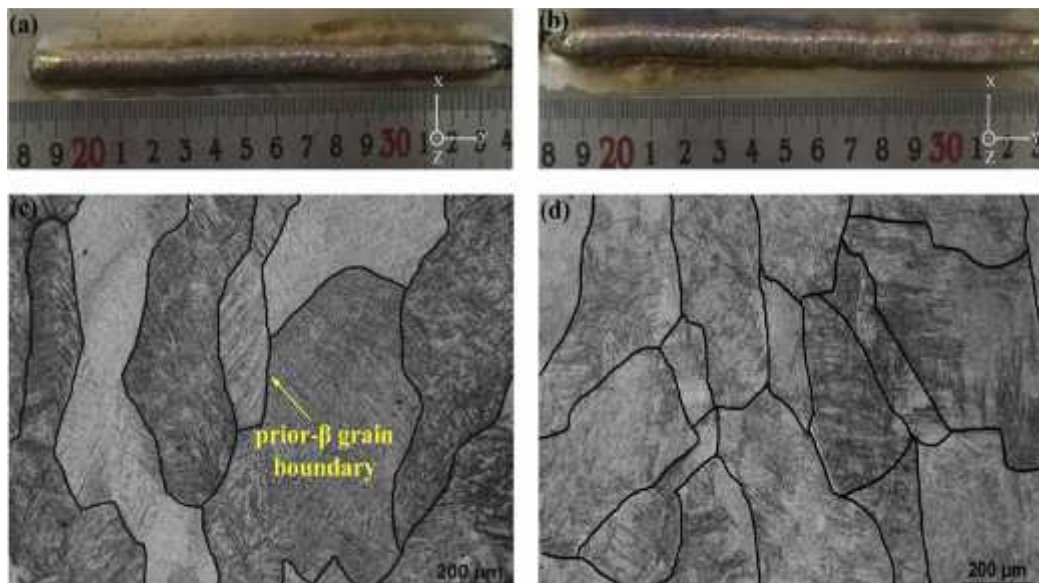


Figure 25: Microstructure of single-track deposition, (a, b) weld appearance, (c) non UPT condition, (d) UPT condition [71]

However, one of the most pressing challenges in additive manufacturing (AM) of this alloy—especially through arc-based processes like CMT—is the development of anisotropic mechanical behavior, which is predominantly attributed to the growth of coarse, columnar grains aligned along the deposition direction. UPT in three orthogonal directions successfully disrupted the typical grain growth pattern, yielding a more equiaxed and homogeneous microstructure throughout the thin-wall structure [72].

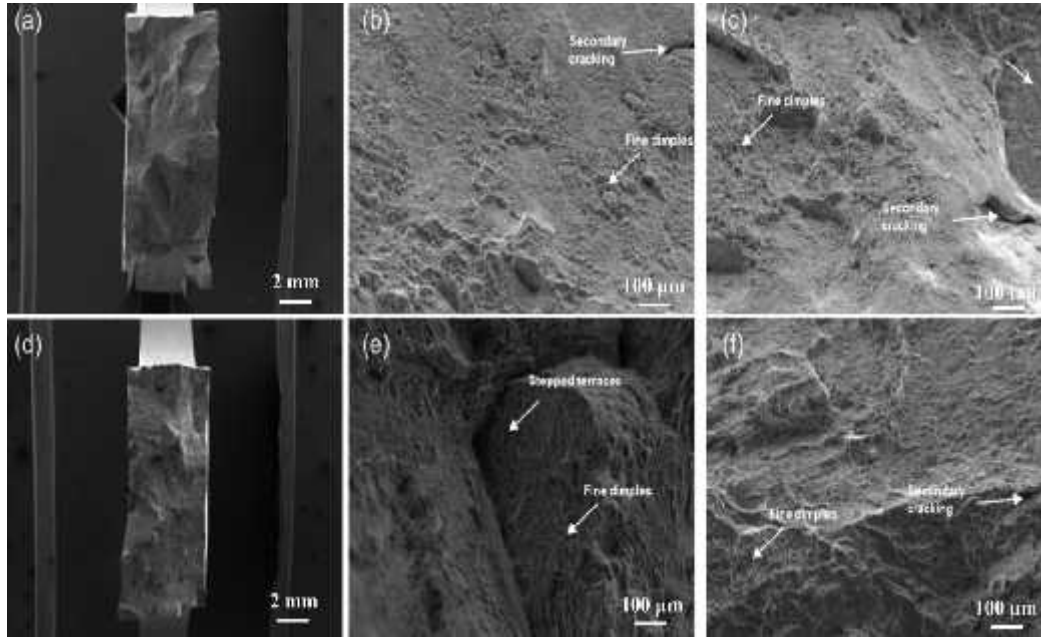


Figure 26: SEM images of fractured surface of CMT weldments of Ti6Al4V, (a) ZX orientation, (b) XY orientation [72]

Figure 25 illustrates the microstructural and mechanical improvements achieved by directional UPT. Post-treatment analysis confirmed that the refined grains and more uniformly distributed β -phase grains improved the tensile response of the material, particularly in the transverse direction. This multidirectional peening approach not only reduced internal residual stresses but also enhanced the isotropy of the mechanical behavior, making the fabricated Ti-6Al-4V components more reliable and structurally sound for critical load-bearing applications. Further insight into the mechanical integrity of CMT-WAAM Ti-6Al-4V components was obtained by examining their fracture surfaces via Scanning Electron Microscopy (SEM), as shown in Figure 26 [71]. Fractographic studies were conducted on samples extracted from both XZ (build height direction) and XY (layer deposition direction) planes to evaluate the failure mechanisms under tensile loading. The observations revealed a predominance of ductile failure features, characterized by fine dimples and shear lips on the fracture surface. These ductile signatures confirm a degree of plastic deformation prior to fracture, suggesting that the material retains some energy absorption capability. However, the analysis also uncovered terraced, planar regions with small step features, especially in the coarser grain areas. These features are typically associated with intergranular cracking occurring along grain boundaries, particularly at the interface between the parent grains and the β -phase boundaries.

This cracking behavior signifies a microstructural vulnerability—the grain boundary γ -phase acts as a preferred fracture path, contributing to premature crack initiation and propagation. As a result, the presence of large, columnar grains and thick layers at grain boundaries limits the ductility and toughness of the printed structure. To enhance the mechanical resilience of Ti-6Al-4V parts produced via CMT-WAAM, grain refinement strategies are imperative. The formation of coarse grain boundary γ -phases by optimizing CMT parameters such as heat input, travel speed, interpass temperature, and cooling rates was controlled and minimized [71]. The integration of UPT further assists in disrupting grain coarsening tendencies by introducing localized plastic deformation and dynamic recrystallization effects. In conclusion, the application of multi-directional ultrasonic peening [71], offers a viable post-processing method to significantly improve the isotropy, ductility, and structural performance of CMT-WAAM Ti-6Al-4V components. When combined with tailored welding parameters, this approach presents a pathway toward the reliable use of arc-based AM for high-performance titanium alloy structures in demanding industrial sectors.

2.2.3 CMT welding of Cu alloys

The effects of Deep Cryogenic Treatment (DCT) on Cu-Al-Si alloy components fabricated using the CMT process was explored [73]. Their investigation focused on evaluating how varying DCT holding durations (0, 6, 12, and 24 hours) influenced mechanical properties such as hardness, tensile strength, and grain structure evolution. Results showed that DCT significantly enhanced the alloy's hardness, tensile strength, and hardness, with improvements reaching approximately 10% in some cases.

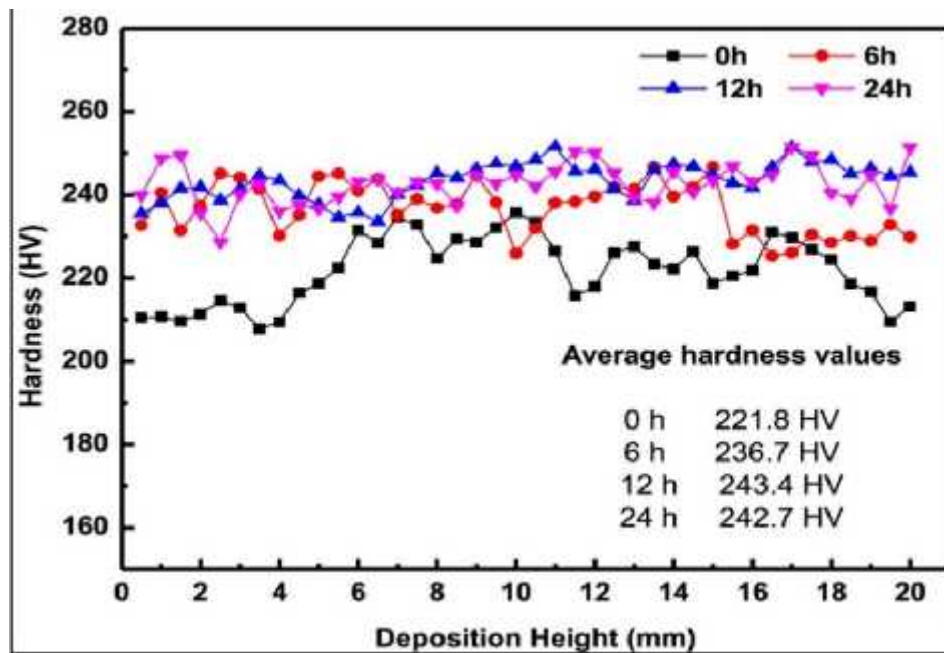


Figure 27: Variation of micro-hardness along the deposition height of Cu-Al alloy deposited using the CMT process at different holding durations (0 h, 6 h, 12 h, and 24 h) after Deep Cryogenic Treatment (DCT) [73]

The microstructural evolution during DCT involved the formation of sub-grains, twin boundaries, fine grain refinement, and texture randomization, which collectively contributed to the mechanical strengthening of the alloy. Figure 27 [73] depicts the variation in hardness along the central vertical axis of the wall samples after different cryogenic holding times. In contrast to the as-deposited condition (average ~220 HV), samples treated for 6 and 12 hours exhibited increases in hardness by 6.72% and 9.73%, respectively. Although a 24-hour DCT still yielded an improvement—approximately 9.42% higher than the untreated sample—it did not surpass the performance observed at the 12-hour mark. Figure 27 illustrates the micro-hardness distribution along the deposition height (in mm) of Cu-Al alloy deposited using CMT technique at different holding times after Deep Cryogenic Treatment (DCT), namely 0 h, 6 h, 12 h, and 24 h. The hardness values (in HV) are plotted on the Y-axis, while the deposition height is shown on the X-axis. At 0 h (black squares), the hardness values are comparatively lower and fluctuate significantly across the deposition height, with an average hardness of 221.8 HV.

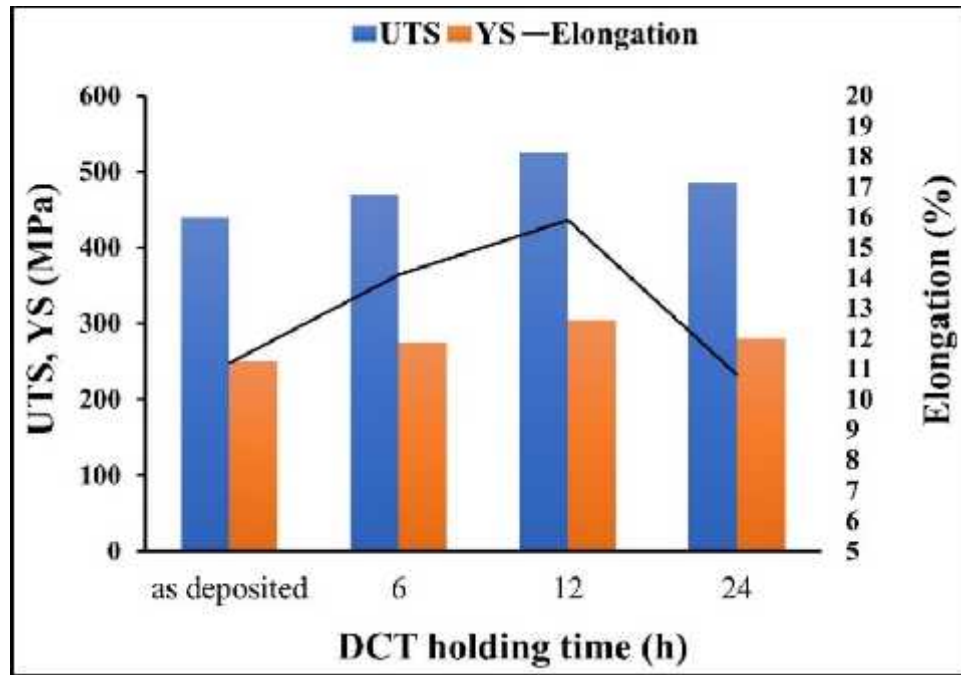


Figure 28: Tensile properties (UTS, YS, and elongation) of Cu-Al-Si alloy deposited using CMT process at different Deep Cryogenic Treatment (DCT) holding durations [73]

. A noticeable improvement is observed at 6 h (red circles), with a more stable profile and a higher average hardness of 236.7 HV. The trend continues with 12 h (blue triangles) and 24 h (magenta inverted triangles) holding durations, showing further enhancement in hardness to 243.4 HV and 242.7 HV, respectively. These two durations display the most consistent and elevated hardness values across the entire height, indicating effective grain refinement and internal stress relief due to prolonged cryogenic exposure. Overall, the figure suggests that increasing the holding time after DCT significantly improves the hardness of CMT-deposited Cu-Al alloy, with 12 h and 24 h treatments yielding the best mechanical performance in

terms of hardness uniformity and magnitude. This enhancement can be attributed to the transformation of retained phases and the development of a more refined and stress-relieved microstructure due to prolonged cryogenic treatment. Figure 28 presents the tensile properties of the Cu-Al-Si alloy deposited by the CMT technique at various Deep Cryogenic Treatment (DCT) holding times: as-deposited, 6 h, 12 h, and 24 h. The chart displays the UTS and Yield Strength (YS) on the left Y-axis (in MPa), while the right Y-axis represents elongation (in %), plotted against the DCT holding time on the X-axis. In the as-deposited condition, the UTS and YS are relatively low, and elongation is also minimal. Upon 6 h of DCT, both UTS and YS show noticeable improvement, accompanied by an increase in elongation, indicating enhanced ductility. The mechanical performance reaches its peak at 12 h, where the UTS, YS, and elongation attain their highest values among all conditions. This suggests an optimal balance between strength and ductility due to favorable microstructural transformations and stress relief during this holding time. However, a slight decline in all three properties is observed at 24 h, though the values still remain higher than the as-deposited state. These findings indicate that DCT significantly enhances the tensile performance of Cu-Al-Si alloys, with the 12 h holding duration yielding the best combination of strength and ductility [73]. Furthermore, the 24-hour treatment displayed a more consistent hardness distribution but slightly lower peak values compared to the 12-hour duration. Interestingly, the as-deposited samples exhibited more pronounced hardness fluctuations along the deposition height, indicating thermal instability and heterogeneous grain growth during the CMT process. In contrast, DCT-treated specimens showed more uniform hardness profiles, likely due to stress relaxation and refined microstructures induced by cryogenic exposure. Figure 28 [73] compares the tensile properties of the as-deposited and DCT-treated Cu-Al-Si alloy samples. Notably, at a 12-hour DCT duration, both Yield Strength (YS) and UTS increased, with YS improving by 2.03% and UTS by a significant 19.9% over untreated samples. These findings underscore the beneficial role of DCT in enhancing the structural performance of CMT-fabricated Cu-Al-Si alloys through microstructural optimization and residual stress reduction.

2.3 Heat Input analysis

An advanced heat source model tailored for CMT welding that incorporates the cyclical characteristics of arc ignition and metal deposition was developed [74]. Their model utilizes a dual ellipsoidal heat source framework, enabling both the heat input and geometric parameters to evolve over time. This dynamic representation effectively mirrors the repetitive nature of arc cycles in CMT, facilitating more accurate simulation of weld pool behavior and prediction of the mechanical properties of the resulting welds. A three-dimensional, transient simulation model to examine various physical phenomena in the CMT process was introduced [75]. This model accounts for heat conduction, electromagnetic effects, and fluid dynamics, offering comprehensive analysis across all critical domains, including the arc, filler wire, substrate, and molten weld pool. A 3D multilayer model was presented to assess how different cooling strategies and deposition sequences impact weld integrity in multi-pass CMT applications [76].

Despite its precision, the CMT process still poses challenges such as residual stress development, porosity, and material distortion—especially in carbon steel welding scenarios [77-79]. The continuous application of heat can expand both the fusion and heat-affected zones (HAZ), raising susceptibility to stress corrosion and potential brittle fracture. As the weld pool cools, it can contract unevenly, generating compressive residual stresses around the weld center and tensile residual stresses in the surrounding zones. These stress gradients may cause plastic deformation, leading to warping or distortion of the welded plate. Moreover, higher heat inputs generally result in more significant deformation compared to processes operating under controlled, lower thermal inputs [80]. Numerous studies confirm that heat input plays a vital role in determining the final shape and mechanical properties of the weld, as it governs the solidification rate and thermal gradients across the weld zone [81]. Controlling the heat input is, therefore, a key factor in optimizing weld quality and minimizing structural defects. To achieve high-quality welds, accurate prediction and regulation of heat input transferred to the base material are essential [82]. In arc welding, the heat input per unit length (H , in W/mm) can be calculated using the following equation:

$$H = \eta \frac{V \times I \times 60}{S \times 1000} \quad (2.1)$$

Here, V is the arc voltage (volts), I represents the welding current (amperes), and S is the Welding speed (in mm/s). The term η stands for process efficiency, representing the fraction of electrical energy effectively transferred to the workpiece [83]. According to [84], not all energy produced in the welding arc contributes to melting the metal; some is lost to radiation, convection, or conduction to surrounding components. Thus, efficiency is critical in analytical and computational heat transfer modeling. Understanding and accurately determining η helps refine thermal simulations, enabling more reliable control over weld quality and performance.

2.4 Numerical analysis of CMT weldments

2.4.1 Heat Transfer Governing Equation in CMT Welding

The primary mechanism governing heat transfer during CMT welding is described by the transient heat conduction equation. This equation accounts for temperature variation with time and spatial coordinates while incorporating internal heat generation. It is given by:

$$\rho c \frac{\partial T}{\partial t} - \nabla \cdot (k \nabla T) - q = 0 \quad (2.2)$$

Where

ρ is the material density (kg/m³), c is the specific heat capacity (J/kg·K), k is the thermal conductivity (W/m·K), T is the temperature (K), q is the volumetric internal heat generation rate (W/m³), and t is time (s).

This differential equation models the dynamic behavior of temperature in response to welding heat input. The thermal properties (ρ , c , and k) vary significantly with temperature, especially during welding, where extreme thermal gradients are present. To solve this equation numerically, it is typically implemented in a finite element (FE) framework. The heat loss from the plate surfaces due to convection and radiation is captured by an equivalent boundary condition. An effective heat transfer coefficient (h) is introduced to simplify the treatment of these surface losses:

$$Q_s = h(T - T_a) \quad (2.3)$$

Here,

Q_s is the net heat flux from the surface (W/m²), T is the surface temperature, T_a is the ambient temperature (commonly 293 K), and h is the combined convective-radiative heat transfer coefficient (W/m²·K).

This equation is essential for accurately modeling how heat dissipates from the welded component. The use of transient finite element analysis enables detailed simulation of heat flow and cooling patterns. Such thermal analysis provides the foundation for predicting microstructure evolution, residual stresses, and potential defects in the weldment due to thermal cycling.

2.4.2 Strain Components in Thermo-Mechanical Modeling

During welding, the total strain experienced by a material point is influenced by multiple mechanisms. These include elastic deformation, plastic yielding, thermal expansion, and strain due to phase transformation. The comprehensive strain relationship is expressed as:

$$d\varepsilon_{ij}^{total} = d\varepsilon_{ij}^{elastic} + d\varepsilon_{ij}^{plastic} + d\varepsilon_{ij}^{thermal} + d\varepsilon_{ij}^{phase} \quad (2.4)$$

Where:

i and j are directional indices (1, 2, 3), $d\varepsilon_{ij}^{elastic}$ is the incremental elastic strain, $d\varepsilon_{ij}^{plastic}$ is the incremental plastic strain, $d\varepsilon_{ij}^{thermal}$ is the thermal strain, and $d\varepsilon_{ij}^{phase}$ is the strain due to phase transformation.

This equation forms the backbone of thermo-mechanical simulations in welding. It captures the combined effects of temperature-induced changes and mechanical behavior during the heating and cooling cycles. Specifically, in CMT welding, the repeated thermal cycling imposes complex stress and strain paths, which must be resolved to understand distortions and mechanical integrity.

A robust simulation model employs the Updated Lagrangian approach using Green-Lagrange strain formulation to capture finite deformation effects. The general expression of Green strain is:

$$d\varepsilon_{ij}^{total} = \frac{1}{2} \left(\frac{\partial u_i}{\partial x_j} + \frac{\partial u_j}{\partial x_i} + \frac{\partial u_k}{\partial x_i} \frac{\partial u_k}{\partial x_j} \right) \quad (2.5)$$

Where:

X_i is the material point's original coordinate,

u_i is the displacement component, k represents the summation index over dimensions.

This strain formulation effectively handles geometric nonlinearities, particularly important for thin plates or complex weld geometries. It allows accurate predictions of stress concentrations and residual stresses that influence weld performance.

2.4.3 Thermal and Elastic Strain Formulations

Thermal strain arises from temperature-induced expansion or contraction of materials. It is quantified using the thermal expansion coefficient and the local temperature change as:

$$D\varepsilon_{ij}^{thermal} = (\alpha(T).dT.\delta_{ij}) \quad (2.6)$$

Where:

$\alpha(T)$ is the thermal expansion coefficient, dT is the temperature increment, δ_{ij} is the Kronecker delta (1 for $i = j$, 0 otherwise).

This relationship assumes isotropic expansion and provides a simplified way to incorporate thermal strain into finite element models. Phase transformation-induced volume changes are treated similarly in welding simulations due to their thermal nature. Elastic strain increments, meanwhile, relate to stress components via Hooke's Law for isotropic materials. This is captured as:

$$D\varepsilon_{ij}^{elastic} = \frac{1+\nu}{E} d\sigma_{ij} - \frac{\nu}{E} d\sigma_{kk} \delta_{ij} \quad (2.7)$$

Where:

ν is Poisson's ratio, E is Young's modulus, $d\sigma_{ij}$ and $d\sigma_{kk}$ are the stress increments, δ_{ij} is the Kronecker delta.

This expression forms the elastic constitutive relationship, crucial for determining reversible deformation in response to applied stress. The combined application of thermal and elastic strain models allows prediction of temperature-driven stress development and helps evaluate the impact of material stiffness and temperature dependency on structural behavior. Such relationships are vital for designing weld schedules that minimize residual stresses and distortions, improving joint quality and service life. Figure 29 illustrates the thermal strain behavior of steel across a wide temperature range, highlighting the differences between heating and cooling cycles. As the temperature increases from room temperature, thermal strain increases almost linearly up to around 250°C, indicating typical thermal expansion behavior. However, between 250°C and 400°C, there is a noticeable deviation in the curve, especially during heating, where the strain increases more steeply. This deviation is likely due to phase transformations or recovery processes within the microstructure. Upon further heating, the strain continues to increase gradually, with distinct inflection points observed at around 720°C and 800°C, suggesting significant microstructural events such as austenite formation.

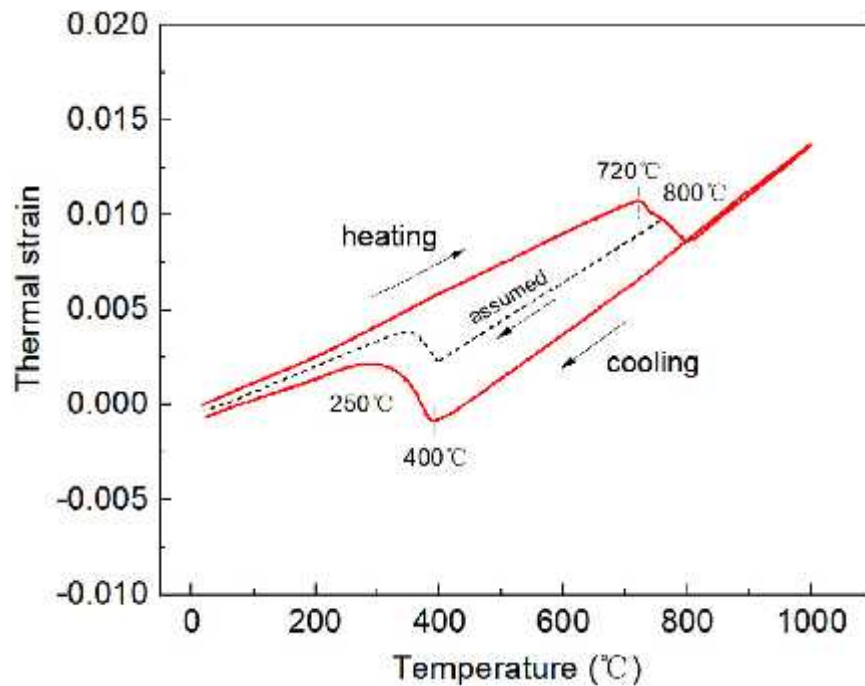


Figure 29: Thermal strain–temperature relationship of steel during heating and cooling cycles, illustrating hysteresis behavior and phase transformation effects [85]

During cooling, the thermal strain follows a different path than heating, demonstrating a hysteresis loop, which is a common characteristic of materials undergoing phase transformations. The strain decreases more gradually compared to its rise during heating and does not follow the same curve back. This difference is attributed to phase transformation lag, transformation-induced plasticity, or residual effects retained from the heating cycle. The area enclosed by the loop between heating and cooling paths represents the energy associated with these irreversible changes. The dotted line labeled as "assumed" indicates a simplification often used in modeling, where thermal expansion is treated as linear and reversible, ignoring phase transformation effects.

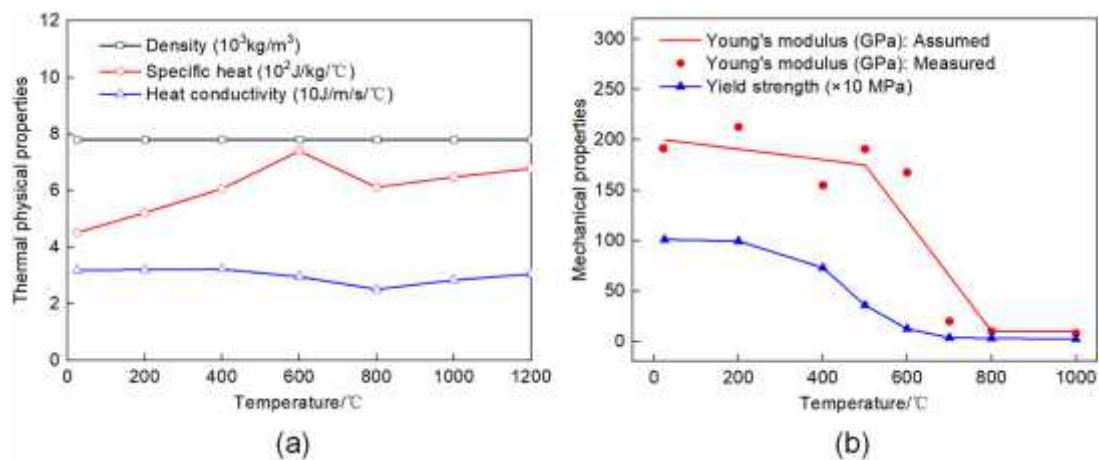


Figure 30: Variation in Thermal Physical and Mechanical Properties of Steel Used in CMT Weldments [85]

Figure 30 illustrates the variation in thermal physical and mechanical properties of steel used in CMT weldments as a function of temperature [85]. In Figure 30(a), the thermal properties—density, specific heat, and thermal conductivity—are shown across a temperature 1100°C. The density of the steel remains relatively stable around $7.8 \times 10^3 \text{ kg/m}^3$, with minor fluctuations throughout the temperature range. Specific heat increases steadily with rising temperature, peaking near 700°C, indicating a higher capacity of the material to absorb heat as the temperature rises. In contrast, thermal conductivity shows a decreasing trend with temperature increase, especially beyond 600°C, which suggests reduced efficiency of heat transfer within the material at elevated temperatures. These thermal properties are crucial in thermal analysis and heat flow modeling for welding simulations. Young's modulus and yield strength. Young's modulus, both assumed (solid line) and measured (dots), shows a significant decline as temperature increases, particularly above 600°C, where it drops sharply to near-zero levels by 900°C.

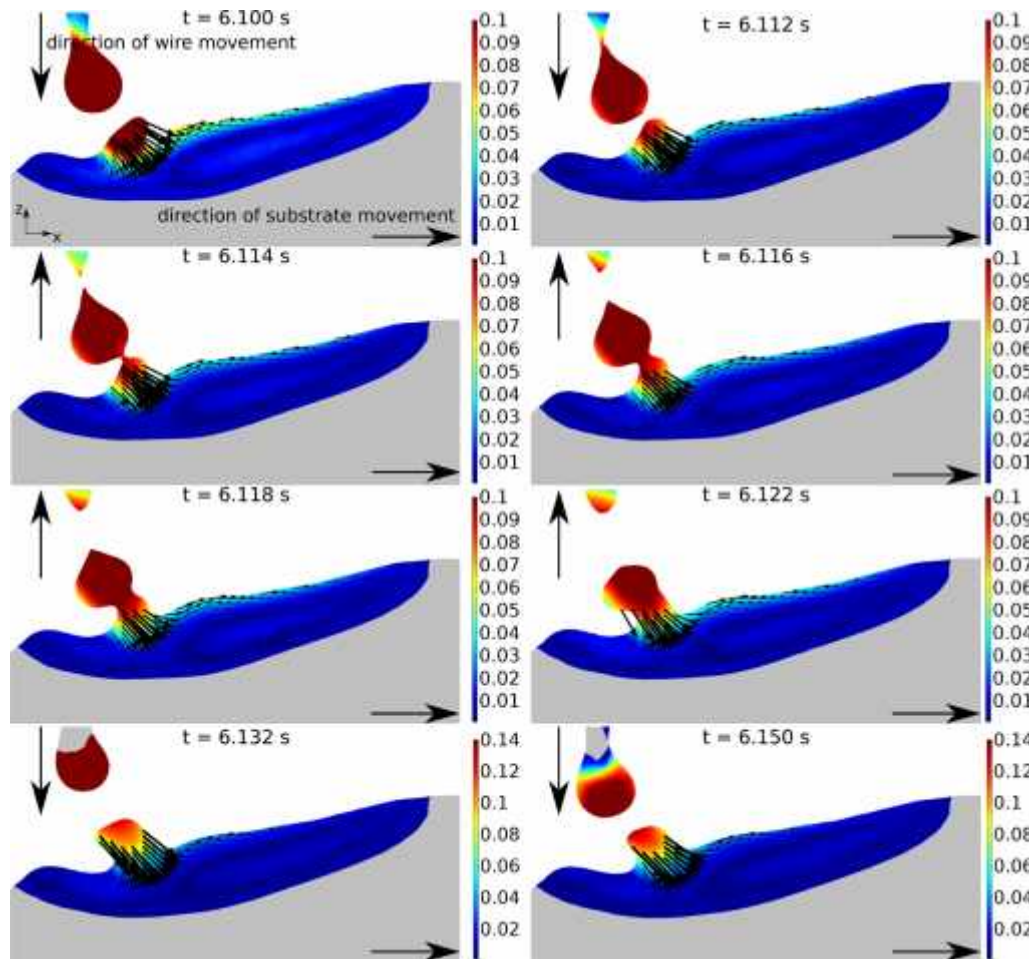


Figure 31: Velocity contour along the longitudinal direction during CMT welding at various time intervals [86]

This dramatic decrease indicates severe weakening of the material's stiffness at high temperatures. Similarly, the yield strength (blue triangles) declines continuously

from room temperature to about 800°C, underscoring the steel's reduced ability to withstand stress without undergoing plastic deformation at elevated temperatures. These mechanical property degradations are critical for understanding weld distortion, residual stress formation, and structural integrity of welded joints at high service temperatures. Together, these plots provide valuable input data for finite element simulations of welding processes, enabling accurate modeling of thermal and mechanical behavior during and after CMT welding. Figure 31 presents a sequence of velocity contour snapshots that vividly illustrate the dynamic interaction between the droplet and the molten pool in the CMT welding process. The images correspond to various time intervals ranging from 6.100 seconds to 6.150 seconds, capturing the transient response of the molten pool during metal droplet detachment and impact. The direction of wire movement (downward) and substrate movement (rightward) is clearly indicated, offering a contextual framework for understanding the fluid motion observed in the simulations. This model is meticulously constructed to replicate the complex physical behavior occurring during welding. It provides a comprehensive view of how liquid metal flows and redistributes in response to external inputs, such as droplet detachment, gravitational forces, and substrate motion. By analyzing the flow trajectories, the model reveals critical aspects of heat transfer, momentum exchange, and metal deposition. Notably, the visualization uncovers a consistent flow pattern triggered during each droplet's impact on the molten surface, revealing the droplet's penetration and subsequent disturbance of the fluid surface. The model highlights a clear variation in velocity magnitudes across the molten pool. The maximum velocity is consistently observed at the droplet impact point, peaking at approximately 0.07 m/s. This indicates a strong localized energy transfer due to the kinetic momentum of the descending droplet. In stark contrast, the forward region of the melt pool exhibits relatively lower velocities, with typical values around 0.01 m/s. This differential suggests that energy dissipation decreases as the distance from the droplet impact site increases, affecting the overall fluid motion and pool shape. Velocity vectors mapped in the figure further detail the direction and magnitude of molten metal flow. These vectors help visualize how the molten metal is pushed and pulled within the pool due to wire motion and the subsequent droplet interactions. The upward and downward directional changes of the wire affect the trajectory of the molten stream, emphasizing the impact of wire feed timing and droplet detachment frequency on the welding process. An essential insight derived from the numerical simulation is the vital role of the droplet's momentum in weld bead formation. The pressure and velocity fields generated by the impacting droplet create a localized depression in the pool, followed by fluid redistribution, promoting deeper fusion into the substrate. This dynamic significantly enhances the weld's penetration profile and mechanical properties. Furthermore, the simulation's accuracy in replicating these thermal-fluid phenomena makes it an effective tool for predicting weld morphology. The interplay of high-velocity zones and low-velocity fronts demonstrates how fluid inertia and surface tension act in unison to govern pool stability. The oscillatory behavior seen in successive frames reinforces that metal transfer is not merely a mass addition event but an energetic exchange that continuously reshapes the molten boundary. In summary, the insights gained from this velocity contour analysis elevate our understanding of the CMT welding mechanism. Beyond simply observing molten behavior, the model

elucidates the physics of droplet impact, wire-substrate interaction, and molten metal redistribution. These findings provide a framework for refining weld parameters to enhance joint strength, bead geometry, and metallurgical soundness. Ultimately, this fluid dynamic approach, grounded in numerical modeling and supported by empirical observations, represents a vital step in optimizing advanced arc welding technologies for industrial applications [86].

The CMT process represents a cutting-edge innovation derived from the conventional GMAW welding method. Although the term “cold” might suggest an absence of heat, it actually pertains to the notably low thermal input delivered during the fusion welding process. Unlike traditional arc welding methods, CMT operates at a significantly reduced thermal heat input (THI), which helps prevent excessive material distortion, especially during the critical short-circuit phase, even when non-zero current is applied [87]. One of the fundamental breakthroughs of the CMT process lies in its highly controlled wire feeding mechanism. Through the implementation of a digitally regulated power system, the process precisely manages the retraction and advancement of the filler wire. This control enables accurate detachment of the molten metal droplet from the wire tip during short-circuiting, thereby optimizing metal transfer efficiency and stability.

Distinct from standard GMAW welding, CMT substantially minimizes the effects of electromagnetic forces, which are typically responsible for arc instability and spatter formation. This reduction in spatter and heat input not only enhances weld quality but also contributes to the suitability of CMT for welding thin sheets and heat-sensitive materials [88]. This technological advancement is particularly relevant given the increasing adoption of aluminum as a viable alternative to steel in numerous industrial domains. Aluminum’s role as a substitute for steel is becoming more prominent in sectors like automotive manufacturing, aerospace engineering, shipbuilding, boiler fabrication, and infrastructure development. The principal factor driving this substitution is aluminum’s considerably lower density compared to steel, which translates into significant weight reduction. This decrease in weight directly correlates with lower transportation costs, reduced fuel consumption, and a marked improvement in energy efficiency—factors that align closely with today’s environmental sustainability goals. Moreover, aluminum and its associated alloys possess commendable mechanical and chemical attributes, such as high strength-to-weight ratios and excellent resistance to corrosion. These properties make aluminum ideal for components exposed to harsh environments or demanding mechanical loads. One such alloy, AA 8011, contains key elements like Si, Fe, and Mn, which improve both strength and corrosion resistance [89]. Specifically, the presence of Mg (0.05%) and Mn (0.20%) in AA 8011 enhances its ability to withstand oxidation and corrosive environments. Heat treatment processes further augment the mechanical properties of this alloy by increasing its hardness and strength, while simultaneously reducing the chances of crack initiation and propagation. Globally, there has been a noticeable surge in the usage of thin aluminum sheets, particularly within the automotive industry. These sheets are favored due to their lightweight nature, durability, recyclability, and formability. Automobile manufacturers are increasingly incorporating aluminum panels in vehicle body structures to meet performance and environmental standards. This shift not only results in lighter vehicles but also

improves engine performance and fuel economy, making aluminum a cornerstone of modern vehicle design [90, 91].

Light metal alloys are extensively recognized for their superior mechanical characteristics, including high tensile strength and improved fatigue resistance. These properties are largely attributed to the presence of alloying elements like Mg and Si, which strengthen the material while preserving its corrosion resistance. As a result, these alloys are extensively used in various high-stress applications across industries ranging from transportation to construction [92-95]. Despite the numerous advantages offered by aluminum, welding thin aluminum sheets remains a significant challenge due to the metal's unique thermal properties. These limitations make it difficult to produce clean, high-quality welds without advanced process controls.

This is where the CMT process proves exceptionally beneficial. By offering precise control over wire feeding and arc characteristics, CMT mitigates common welding problems associated with aluminum. The process allows for accurate heat input management, enabling the effective welding of thin sheets without excessive melting or distortion [96, 97]. Another critical advantage of CMT is its compatibility with shielding gases. Among these, argon is generally preferred over helium due to its superior thermal conductivity, optimal density, and favorable ionization characteristics. These properties contribute to better weld pool stability, consistent penetration profiles, and minimized spatter levels during welding operations [98].

The advantages of CMT are not limited to thin sheet welding alone. The technique also supports the production of tailor-welded blanks (TWBs), which are composite metal sheets created by joining dissimilar or similar materials. TWBs enable customized strength and thickness distribution across vehicle parts, supporting weight reduction and cost-efficiency in automotive design [99-102]. These blanks are especially useful in manufacturing critical vehicle components such as bonnets, inner doors, and structural reinforcements. Their application facilitates targeted material usage without compromising safety or performance.

To exploit the full potential of aluminum TWBs, researchers and manufacturers have explored a variety of welding methodologies. These include double-sided arc welding (DSAW), FSW, and advanced laser-based techniques. Each of these approaches offers unique benefits depending on the material composition and intended application. For example, FSW is renowned for its solid-state joining capabilities, which eliminate common fusion-related defects.

Recent research has illustrated the effectiveness of these welding processes in fabricating aluminum TWBs [103]. Their findings highlight the adaptability of these methods across different Al-alloys and demonstrate substantial improvements in mechanical properties and formability. These advancements reinforce the growing role of aluminum and CMT welding in shaping the future of automotive and structural manufacturing.

Recent advancements in the study of CMT welding have delved deeper into its process characteristics, particularly focusing on welding parameters, mechanical behavior, and residual stress development in weldments [104-110]. These studies have contributed to a better understanding of how various input parameters influence the quality and durability of welds produced using the CMT process. Such insights are particularly crucial when working with Al-alloys, which, while offering numerous benefits, pose distinct challenges during welding due to their thermal

sensitivity and tendency to form brittle IMCs. An in-depth examination of specific Al-alloys, investigating their mechanical properties alongside their susceptibility to stress corrosion cracking [105]. Their findings offer valuable guidance for tailoring welding processes in applications where environmental resistance and mechanical integrity are paramount. Moreover, investigations by Elrefaey and Ross [110] and Ahmad and Bakar [111] emphasized the critical role of PWHT in enhancing the performance of weldments. Their research showed that carefully selected heat treatments and mechanical post-processing techniques can significantly improve the strength, toughness, and overall durability of aluminum welds, making them more appropriate for structural applications. In experimental settings, the choice of filler material plays a vital role in influencing the quality and mechanical performance of the welded joint. For the current study, a filler wire from the 4000 series—specifically ER4043—was chosen. Alloys in the 4000 series are widely utilized in welding and brazing operations due to their excellent fluidity and low susceptibility to hot cracking. Their ability to flow smoothly during welding ensures consistent filler distribution and a defect-free weld bead. The 4000 series demonstrated superior performance in terms of both strength and porosity compared to other aluminum filler categories [112]. Within this series, ER4043 stands out due to its Si-rich composition, which not only improves fluidity but also minimizes common welding defects, leading to more reliable joints [113]. Recent studies have extended beyond similar aluminum joints to explore hybrid material assemblies. One such promising direction involves aluminum-steel joints created using laser-assisted double-pulse MIG (DP-MIG) hybrid welding-brazing techniques. These assemblies address the inherent challenges of joining dissimilar materials, such as differences in thermal expansion coefficients and the propensity for thick, brittle IMC layers at the interface. By incorporating laser preheating and hybrid brazing-welding, this technique enhances metallurgical bonding and improves the wettability of the joint interface compared to traditional GMAW approaches. An in-depth analysis of the laser/DP-MIG process revealed that plasma characteristics during welding play a pivotal role in mitigating excessive IMC growth. By suppressing undesirable phase transformations, the resulting joints exhibit improved mechanical performance. In one reported instance, a remarkable joint strength of 271.8 N/mm was achieved, emphasizing the significance of maintaining an optimal balance between adhesion area and IMC brittleness [114]. In another study, laser-assisted DP-MIG hybrid welding-brazing was effectively applied to join 5052 with Al-Si-coated boron steel. The process achieved optimal performance at a input heat of 162 J/mm, resulting in a highest UTS of 170 MPa. Detailed metallographic analysis demonstrated the occurrence of distinct intermetallic layers and microstructural zones that contributed to the joint's strength and clarified potential failure mechanisms [115]. These insights further validate the relevance of CMT and hybrid welding techniques in tackling the complexities of dissimilar material joints. A noteworthy innovation lies in the application of CMT welding to dissimilar Al-alloys, such as AA8011 and AA6061. The joining of dissimilar alloys presents multiple challenges, including the risk of forming brittle phases and differential thermal expansion effects. However, CMT offers a controlled thermal profile with a lower and more stable heat input compared to conventional welding techniques. This allows the reduction of thermal distortion, minimizes IMC formation, and ensures the retention of favorable

mechanical properties across the joint. In industrial contexts, the ability to effectively join dissimilar Al-alloys using CMT holds considerable promise. It addresses key manufacturing concerns such as material compatibility, joint reliability, and structural integrity—factors crucial in automotive, aerospace, and marine sectors. Furthermore, leveraging CMT for such applications provides additional operational benefits. It facilitates efficient use of base materials, reduces post-weld processing requirements, and lowers defect rates, contributing to more sustainable and cost-effective manufacturing practices [116]. By enhancing joint performance while conserving resources, the use of CMT in dissimilar aluminum applications represents a major stride toward environmentally conscious industrial processes. Ultimately, the implementation of CMT welding for dissimilar aluminum joints marks a significant shift in the welding landscape. It aligns with contemporary industrial needs, offering a reliable solution to weld lightweight, high-performance materials without compromising strength or longevity. The reduction in energy consumption and enhanced joint integrity makes CMT a valuable asset in achieving both economic and environmental objectives [117].

2.5 Research Gaps from the Literature

1. It has been observed, upon a thorough analysis of research work, that CMT welding process of joining composite materials such as Aluminum (AA) 8000 with Aluminum (AA) 6000 has not been explored, greatly.
2. CMT process for joining such metals is yet to be optimized with respect to different mechanical properties (micro-hardness, tensile behaviour and residual stresses) of composite materials.
3. Physical microstructure characterization of the weld by CMT has not been studied thoroughly, very few work is done on this characterization.
4. While WS and microstructural changes have been studied, there is insufficient research on the exact nature and kinetics of phase transformations (e.g., formation of IMCs) in the CMT welding of dissimilar Al-alloys.
5. Most current studies focus on the weld metal zone. The evolution of the HAZ—particularly in the weaker—under varying WS and process parameters is not thoroughly investigated.
6. There is a lack of real-time thermal cycle measurements (temperature gradients, cooling rates) during CMT welding, which are crucial to understanding microstructure-property relationships.
7. Multi-objective optimization that considers trade-offs among strength, hardness, distortion, and energy consumption is limited.
8. Studies generally focus on tensile strength or hardness but often overlook fatigue behavior, fracture toughness, or creep resistance of the weldments under long-term service conditions.

2.6 Objectives

The objective of the proposed research work is to join dissimilar metals (AA 8000 series and AA 6000 series) using CMT to achieving the following study:

1. Structural behavior of dissimilar metals (AA 8000 series and AA 6000 series) will be carried out using XRD for phase detection and SEM along with EDX for microstructural and elemental analysis.
2. Mechanical behavior of dissimilar metals weldment (AA 8000 series and AA 6000 series) will be studied using Hardness test, Impact test, Tensile test.
3. Optimize the process parameters of CMT in the weldment of AA 8000 series and AA 6000 series.
4. Damping behavior of CMT welded joints of AA8000 and AA6000 series

CHAPTER-3

Research Methodology

Figure 32 illustrates a systematic flow chart of the research methodology adopted for optimizing process parameters in welding experiments, particularly applicable to CMT welding of dissimilar Al-alloys like AA8011 and AA6061. The process begins with the selection of base materials, followed by determining the range of relevant process parameters such as current, voltage, WS, and wire feed rate.

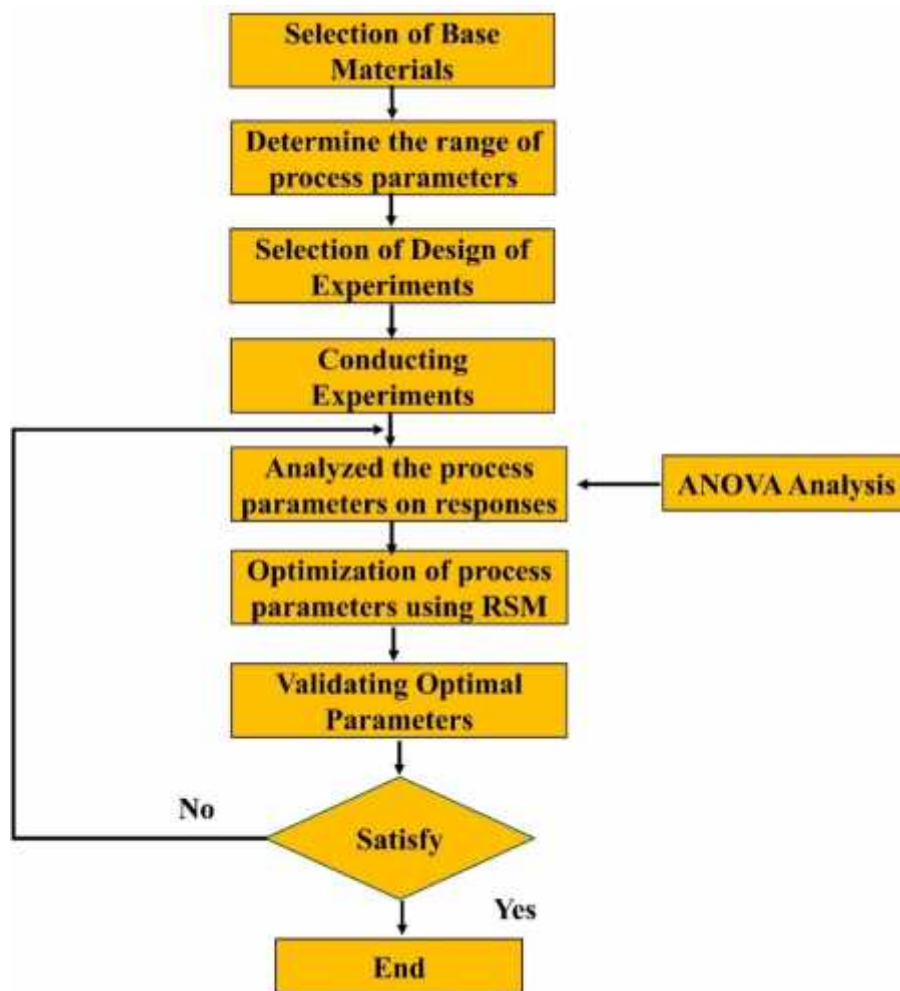


Figure 32: Flow chart of existing research work

Next, an appropriate Design of Experiments (DOE) is selected, ensuring that all combinations of process variables are covered efficiently. Experiments are then conducted as per the DOE matrix, and the resulting data (mechanical properties, bead geometry, etc.) are collected. These results are then analyzed to evaluate the influence of process parameters, often using ANOVA (Analysis of Variance) to identify statistically significant factors. After analysis, Response Surface

Methodology (RSM) is used to optimize the process parameters to achieve the desired outputs. The optimal parameters are then validated experimentally. If the results meet expectations, the process concludes. If not, the cycle is repeated. This iterative feedback loop ensures high accuracy and reliability of the optimization process in welding research.

3.1 Chemical elements of the base metal

Table 4 demonstrated the chemical elements of the filler metal ER4043 and the base metals, each selected based on their specific alloying elements and intended applications. ER4043, used as a filler metal, contains a high Si content of 5.87%, which enhances weld fluidity and reduces the risk of solidification cracking during the welding process. It contains only trace amounts of other elements like Fe, Cu, Mn, and Mg, ensuring compatibility with a wide range of Al-alloys. ER4043 is commonly used in the welding of automotive, aerospace, and structural components where smooth welds and good crack resistance are essential. AA6061, a heat-treatable, has notable amounts of Mg (0.96%) and Si (0.59%), which combine to form the Mg₂Si phase, providing excellent strength through precipitation hardening. Small additions of copper and chromium enhance its corrosion resistance and mechanical performance suitable in transportation, marine, and structural engineering. In contrast, AA8011 is a non-heat-treatable alloy with higher iron (1.00%) and Si (0.90%) content, which improve formability and casting properties but may lead to brittle intermetallic formation during welding. This alloy is widely used in non-structural applications like household foil, packaging, and bottle caps where high strength is not a primary requirement. The distinct compositions and corresponding applications of these alloys highlight the importance of using a filler like ER4043 to ensure metallurgical compatibility and weld quality when joining dissimilar materials such as AA8011 and AA6061.

Table 4: Percentage (weight) of chemical elements in the filler and base metals

Material	Si	Fe	Mn	Cu	Mg	Ti	Zn	Cr	Al
ER4043	5.87	0.80	0.05	0.30	0.05	0.02	0.10	0.05	Rest
AA6061	0.59	0.26	0.09	0.32	0.96	0.03	0.08	0.12	Rest
AA 8011	0.90	1.00	0.20	0.10	0.05	0.08	0.10	0.05	Rest

3.2 Experimental procedure

3.3 V groove preparation

Figure 33 illustrates the prepared base metal plates of AA8011 and AA6061 Al-alloys of thickness 6.2 mm arranged for CMT welding. The plates are aligned in a butt joint configuration with a 60° V-groove at the interface to facilitate effective weld penetration and fusion between the two dissimilar materials. The dimensions of each plate are clearly marked as 150 mm in length and 100 mm in height, ensuring sufficient surface area for welding and subsequent testing. The V-groove design helps to localize the arc and filler metal, ensuring consistent filler deposition and proper bonding along the joint line.

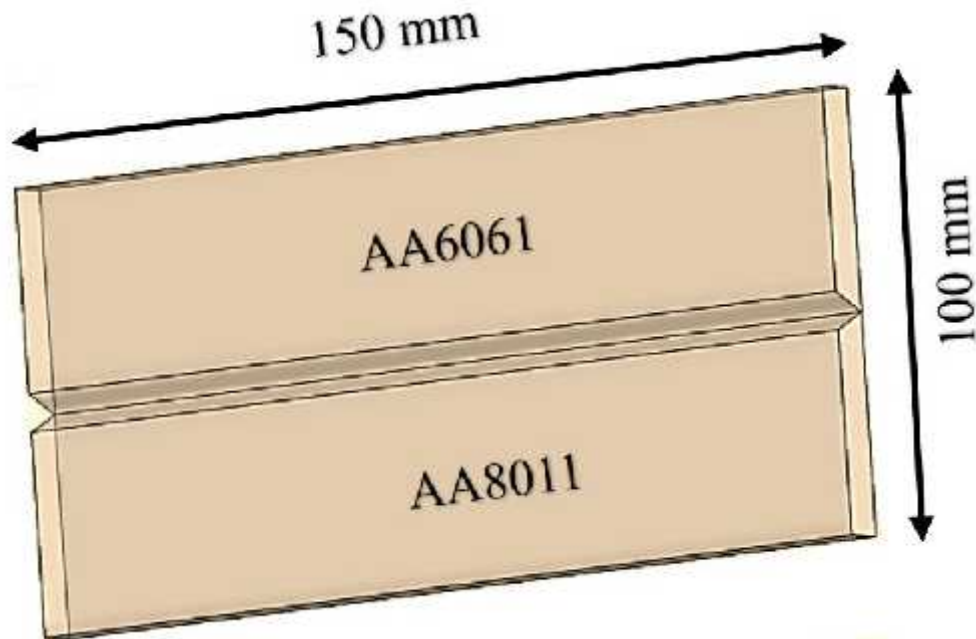


Figure 33: 60° V groove plates before CMT welding

The top plate, made of AA6061, while the bottom plate, AA8011, is a non-heat-treatable alloy commonly used for non-structural applications. The configuration shown in the figure is crucial for achieving a uniform weld bead, minimizing defects, and allowing for thorough evaluation of the joint's mechanical and metallurgical properties after the CMT welding process. This setup forms the basis for studying the influence of process parameters on dissimilar aluminum welding.

3.4 Fabrication of CMT welded joint

CMT welding is an advanced GMAW-based process well-suited for joining dissimilar Al-alloys such as AA6061 and AA8011. The process is characterized by its low heat input, controlled arc behavior, and mechanical retraction of the filler wire, enabling precise metal transfer with minimal spatter. When welding AA6061 to AA8011, challenges arise due to differences in their thermal conductivity, melting points, and metallurgical behavior. CMT overcomes these by employing rapid short-circuiting cycles and reduced arc energy, which prevent excessive mixing and minimize the formation of brittle IMCs at the weld interface. Typically, ER4043 filler wire is used due to its high Si content, promoting fluidity and reducing cracking. The process ensures a stable arc, smooth bead profile, and refined microstructure, resulting in a welded joint with improved mechanical properties. CMT welding of these alloys is ideal for applications requiring lightweight structures with good corrosion resistance, such as in automotive, aerospace, and packaging industries, where joining dissimilar aluminum components is essential. The following step have followed during the CMT welding.

3.4.1 CMT machine

The Fronius TPS 400i is an advanced, intelligent welding power source specifically designed to support the CMT process. It delivers high-frequency control over current, voltage, and wire movement, which is essential for the CMT cycle's precise operation. This system works with a digital control interface that synchronizes the wire retraction and current reduction during short-circuit transfer. The TPS 400i is capable of performing low-spatter, low-heat welding, which is crucial when joining dissimilar metals like AA8011 and AA6061. It also features built-in data logging, waveform control, and real-time monitoring, allowing users to optimize welding parameters such as arc length, wire speed, and pulse timing. The system is modular and programmable, enabling its integration with automated setups, making it suitable for both research and industrial applications. Its advanced control unit ensures repeatable, high-quality welds even under varying environmental or material conditions.

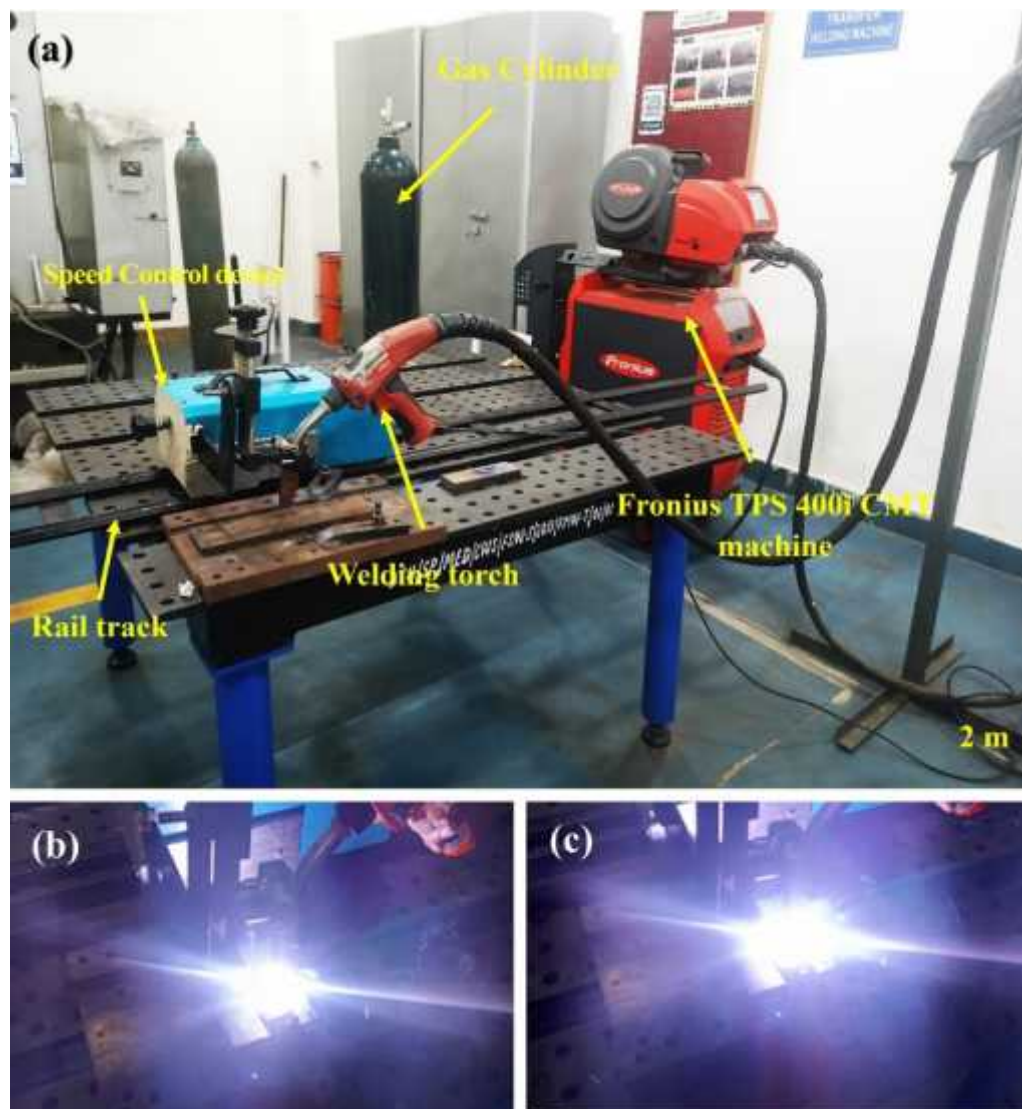


Figure 34: (a) CMT welding machine, (b, c) CMT welding process

3.4.2 Welding Torch

The welding torch in the CMT setup plays a central role by serving as the interface between the welding power source and the workpiece shown in Figure 35. In CMT, the torch not only delivers the arc but also supports mechanical wire retraction and advancement, synchronized with arc pulses. This unique feature enables controlled, short-circuit droplet transfer, minimizing heat input and spatter. The torch houses the contact tip, shielding gas nozzle, and liner, ensuring continuous wire feed and arc stability. It is often water- or air-cooled, depending on current levels, and is designed to handle the repetitive motion of the wire without causing fatigue or feed instability. The torch's positioning and angle are critical, especially in automated systems, to maintain optimal arc length and avoid weld defects. In the Fronius CMT system, the torch's motion and wire feed are electronically coordinated to ensure precise, clean droplet transfer, essential for welding sensitive materials such as Al-alloys.



Figure 35: CMT welding torch

3.4.3 Speed Control Device

Figure 36 reveals the speed control device, which regulates the linear travel speed of the welding torch along the weld path. In automated CMT systems, precise speed control is vital because even slight fluctuations can affect heat input, bead geometry, and penetration depth. This device is often integrated with a programmable logic controller (PLC) or digital interface that allows operators to set desired speeds based on material type and thickness. In CMT welding of dissimilar alloys, consistent torch movement ensures uniform fusion between metals like AA8011 and AA6061, which have different melting points and thermal conductivities. The speed control device can be fine-tuned for different segments of the weld, allowing ramp-up, steady travel, and ramp-down stages. By preventing overlap or underfill, the speed controller

ensures quality and repeatability, especially important in research or precision fabrication. This device also helps to synchronize WS with wire feed speed, which is crucial in maintaining a stable arc during the CMT cycle.



Figure 36: Speed control device

3.4.4 Rail Track

Figure 37 presents the rail track system utilized during the CMT welding process, which plays a critical role in ensuring mechanical stability and linear guidance for the movement of the welding torch along the weld seam. This precision-guided infrastructure is essential for maintaining consistent welding speed, orientation, and arc positioning, particularly in automated or semi-automated welding setups. The rail track is designed to minimize the variability associated with manual operations, thereby reducing human-induced errors such as torch misalignment, inconsistent travel speed, or uneven heat input—factors that can negatively affect weld quality, especially in dissimilar metal welding. In CMT welding, precise control of arc movement and droplet transfer is vital due to the process's inherently low and controlled heat input. The rail track ensures repeatability by keeping the torch at a uniform height and angle relative to the workpiece surface, thereby promoting stable arc behavior and efficient metal deposition. Typically fabricated from high-strength materials like structural-grade steel or aerospace-grade aluminum, the rail system provides a smooth gliding surface for the torch carriage and is often equipped with an integrated speed control unit to maintain a constant travel rate. This is crucial for achieving uniform heat distribution and consistent penetration depth.

The system is particularly advantageous for welding large or elongated workpieces, such as the 150 mm × 100 mm aluminum alloy plates referenced earlier, where maintaining a perfectly straight weld path over long distances is challenging. The controlled and repeatable motion enabled by the rail setup enhances bead uniformity,

reduces spatter, and improves metallurgical bonding at the interface of dissimilar alloys like AA 8000 and AA 6000. Ultimately, the rail track ensures that each weld pass adheres to optimized parameters, leading to superior joint strength, improved structural integrity, and reduced post-weld defects.

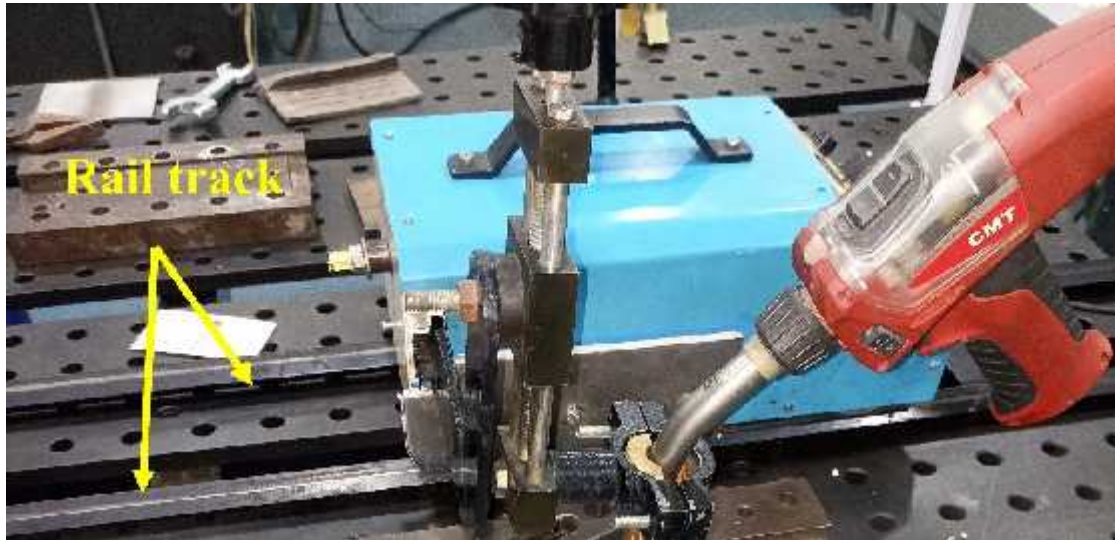


Figure 37: Rail track arrangement of CMT welding

3.4.5 Gas Cylinder (Shielding Gas Supply)

The gas cylinder in the CMT setup supplies the shielding gas, typically 99.9% argon, which is essential for protecting the molten weld pool. Throughout welding, the aluminum surface is highly reactive with oxygen and nitrogen, leading to defects like porosity, oxidation, and inclusions if not properly shielded. The choice of shielding gas also affects the arc characteristics, heat input, and bead wetting behavior. In the CMT process, the shielding gas is delivered through the torch nozzle at a controlled flow rate, often between 15–20 l/min. The gas cylinder is equipped with a pressure regulator and flow meter to maintain consistent delivery. In welding dissimilar Al-alloys like AA8011 and AA6061, maintaining a contamination-free environment is crucial for ensuring proper fusion and avoiding the formation of brittle intermetallic

3.4.6 Arc Ignition and Droplet Transfer

Arc ignition in the CMT process begins with a controlled low-energy pilot arc, which gently initiates the molten pool without generating excess spatter. Once the arc is established, the CMT welding cycle involves a series of high-frequency short-circuits, where the filler wire momentarily touches the molten pool, melts, and is retracted by the system. This action results in clean, controlled droplet detachment and transfer to the joint. Unlike traditional GMAW, where molten metal is transferred continuously with higher heat input, CMT uses mechanical wire motion synchronized with pulsed current, producing much less heat. This is especially beneficial when welding materials like AA8011, which are prone to burn-through, and AA6061, which can form hard intermetallic under excessive heat. The low-spatter, low-energy arc characteristics of CMT make it ideal for thin-gauge or

dissimilar aluminum welding, ensuring minimal distortion and better mechanical properties in the joint area.

3.4.7 Arc Stability During Welding

Maintaining arc stability throughout the welding process is crucial to achieving consistent weld quality. In CMT, arc stability is enhanced by the synchronized movement of the filler wire and the precise modulation of current and voltage. The system continuously monitors arc length and wire position, adjusting parameters in real-time to prevent arc instability, wandering, or extinguishing. A stable arc results in uniform heat distribution, controlled bead profile, and minimal defect formation. This is particularly important when welding dissimilar Al-alloys, where differences in thermal expansion and conductivity can disrupt arc behavior. Arc stability also impacts droplet size and detachment frequency, directly affecting the microstructure and mechanical performance of the welded joint. Visual indicators of arc stability, such as consistent brightness and uniform bead appearance, confirm that the system is operating optimally. Overall, arc stability in the CMT process ensures repeatability, reliability, and high-quality welds, which are essential in both research and industrial manufacturing settings.

3.5 Design of Experiments

Table 5 presents the key CMT welding parameters and their respective notation, operating ranges, and coded levels used for experimental design and optimization. The table includes three major input variables: welding current (A), WS (B), and GFR (C), all of which significantly influence the quality and performance of the welded joint. The current (A) ranges from 60 to 80 amps, with coded levels of -1 (60 A), 0 (70 A), and +1 (80 A). This parameter directly affects the heat input and melting rate of the filler wire, thereby influencing weld penetration and bead formation. The WS (B) is varied between 2 mm/s and 10 mm/s, with levels set at 2, 6, and 10 mm/s. This parameter determines the interaction time between the arc and base material, affecting bead width and potential HAZ size. Lastly, the shielding GFR (C) is adjusted within a range of 14 to 18 liters per minute, with coded levels of 14 (-1), 16 (0), and 18 (+1). This controls arc stability and protects the weld pool from atmospheric contamination. These levels serve as inputs in statistical design techniques like RSM to optimize the process and improve mechanical and metallurgical outcomes in the welding of dissimilar Al-alloys like AA8011 and AA6061.

Table 5: CMT welding parameters and their ranges

Parameters	Notation	Range	Levels		
			-1	0	1
Current (Amp)	A	60-80	60	70	80
Welding speed (mm/s)	B	2-10	2	6	10
Gas flow rate (l/min)	C	14-18	14	16	18

In addition to defining the operational windows for CMT welding, the parameter ranges listed in Table 5 serve as the foundation for developing statistically valid experimental models. These coded levels (-1, 0, +1) are essential for conducting Design of Experiments (DOE) such as Box-Behnken or Central Composite Design under RSM. By systematically varying each parameter within its range, researchers can assess both individual and interaction effects on weld quality, including mechanical strength, bead geometry, and microstructural evolution. Moreover, using these precise ranges helps in maintaining process consistency, reducing variability, and enhancing the reproducibility of welding trials across different setups.

Table 6: Design of experiments in expanded form

Sample number	A: Current (A)	B: Welding Speed (mm/s)	C: GFR (l/min)
1	70	6	18
2	80	2	18
3	70	6	16
4	60	10	14
5	60	6	16
6	70	6	16
7	60	2	14
8	60	10	18
9	70	6	16
10	70	10	16
11	80	10	14
12	70	6	16
13	70	6	16
14	70	6	14
15	80	10	18
16	60	2	18
17	70	2	16
18	80	6	16
19	80	2	14
20	70	6	16

Table 6 displays the expanded Design of Experiments (DOE) matrix developed for the CMT welding process involving dissimilar Al-alloys. This table includes 20 experimental runs where three key input parameters—Current (A), WS (mm/s), and (GFR, l/min)—are varied according to a structured plan. Each sample number corresponds to a unique combination of these variables.

The DOE matrix ensures a balanced distribution of parameter levels across the experimental space. The current ranges between 60 A and 80 A, WS varies from 2 mm/s to 10 mm/s, and GFR ranges from 14 to 18 l/min. Some experiments repeat the central point (e.g., Sample 3, 6, 9, 12, 13, and 20) with values 70 A, 6 mm/s, and 16 l/min, which is essential for estimating experimental error and ensuring model accuracy. This expanded DOE layout supports statistical modeling and optimization

using RSM. It helps evaluate the main effects and interactions between parameters, contributing to better understanding and improvement of weld quality and process reliability.

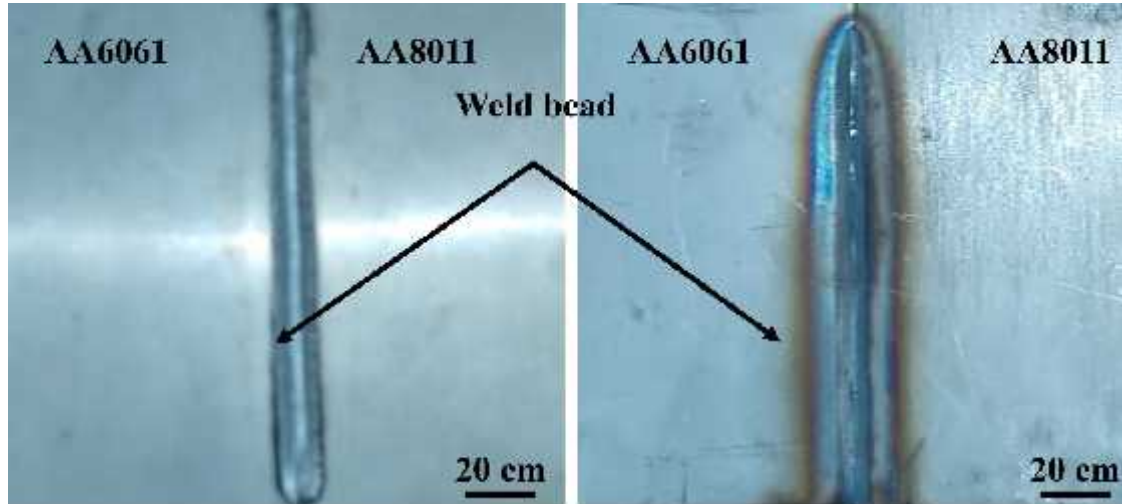


Figure 38: CMT welded joints of AA8011 and AA6061

Figure 38 shows the macro view of CMT weldments between dissimilar Al-alloys AA8011 and AA6061. The images clearly depict the weld bead formation along the joint line, where the two plates are fused together using the CMT process. On both sides of the weld bead, the respective base metals—AA8011 and AA6061—are marked, highlighting the transition zone. The left image demonstrates a clean and uniform bead with minimal surface oxidation and discoloration, indicating low heat input and stable arc control typical of the CMT process. The right image, though showing slightly more heat tinting, still reflects good fusion and penetration, with no visible surface defects such as cracks or excessive spatter. The 20 cm scale at the bottom of both images emphasizes the length and consistency of the weld bead across the entire joint. Overall, Figure 38 confirms that the CMT process is highly effective in producing high-quality welds between dissimilar Al-alloys by maintaining controlled heat input, minimizing IMC formation, and ensuring a sound metallurgical bond with excellent surface finish.

3.5.1 Specimens' preparation

Figure 39 illustrates the post-welding finishing operations applied to the CMT welded joint between AA8011 and AA6061 Al-alloys. In Figure 39(a), the weld bead is being removed using a shaper machine, a precise mechanical cutting tool that levels the weld bead by trimming the excess material from the joint surface. This process ensures a flat and uniform surface, which is critical for subsequent testing and evaluation of mechanical and metallurgical properties. Figure 39(b) shows the finished welded plate after the bead removal. The surface appears smooth and refined, indicating proper finishing, which is essential for accurate characterization of the welded specimen. This step also prepares the sample for further procedures such as tensile testing, microstructural analysis, or residual stress evaluation. Overall, these finishing operations play a crucial role in standardizing the weld surface,

eliminating inconsistencies, and ensuring that the final joint is ready for reliable performance assessment and comparison.



Figure 39: (a) Removal of weld bead by shaper machine, (b) finishing of the welded plate

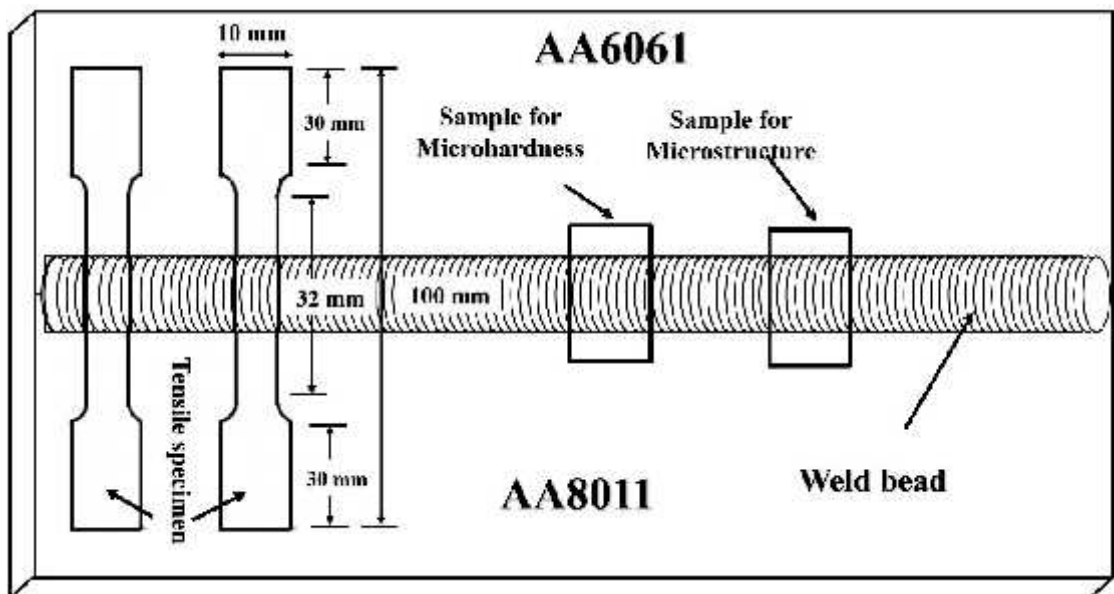


Figure 40: Schematic diagram of Microstructure, hardness and tensile test specimen preparation

Figure 40 presents a schematic diagram illustrating the preparation of specimens for microstructure analysis, UTS, residual stress and microhardness testing from a dissimilar welded joint between AA8011 and AA6061 Al-alloys. The figure shows that the welding was achieved along the longitudinal axis of the base plate, creating a continuous weld bead at the interface of the two materials. To evaluate the mechanical and metallurgical characteristics of the welded joint, samples were extracted from specific regions. On the left side, tensile specimens were cut perpendicular to the weld line, each having a gauge length of 32 mm and an overall height of 100 mm, with a narrow section of 10 mm width and 30 mm height for

accurate stress distribution during testing. Two rectangular sections were also marked for hardness and microstructural analysis. The hardness sample was taken near the interface to assess hardness variations across the weld zone and heat-affected zones (HAZ), while the microstructure sample was cut from the central region of the weld to examine grain morphology, phase transformation, and interface bonding between AA8011 and AA6061.

3.5.2 Tensile test

Figure 41 depicts the tensile testing setup used to evaluate the tensile properties of the dissimilar welded joint between AA8011 and AA6061 Al-alloys. The image shows a UTM equipped with hydraulic grips firmly holding the tensile specimen, which has been prepared in accordance with standard dimensions to ensure consistent and reliable results. The specimen is aligned vertically between the top and bottom fixtures to facilitate uniaxial loading during the test. The connected digital control panel and computer interface allow precise control and real-time monitoring of test parameters such as load, elongation, and stress-strain behavior. The UTM software visible on the monitor records data continuously, generating tensile curves that help in determining the UTS, yield strength, and elongation percentage of the welded joint.

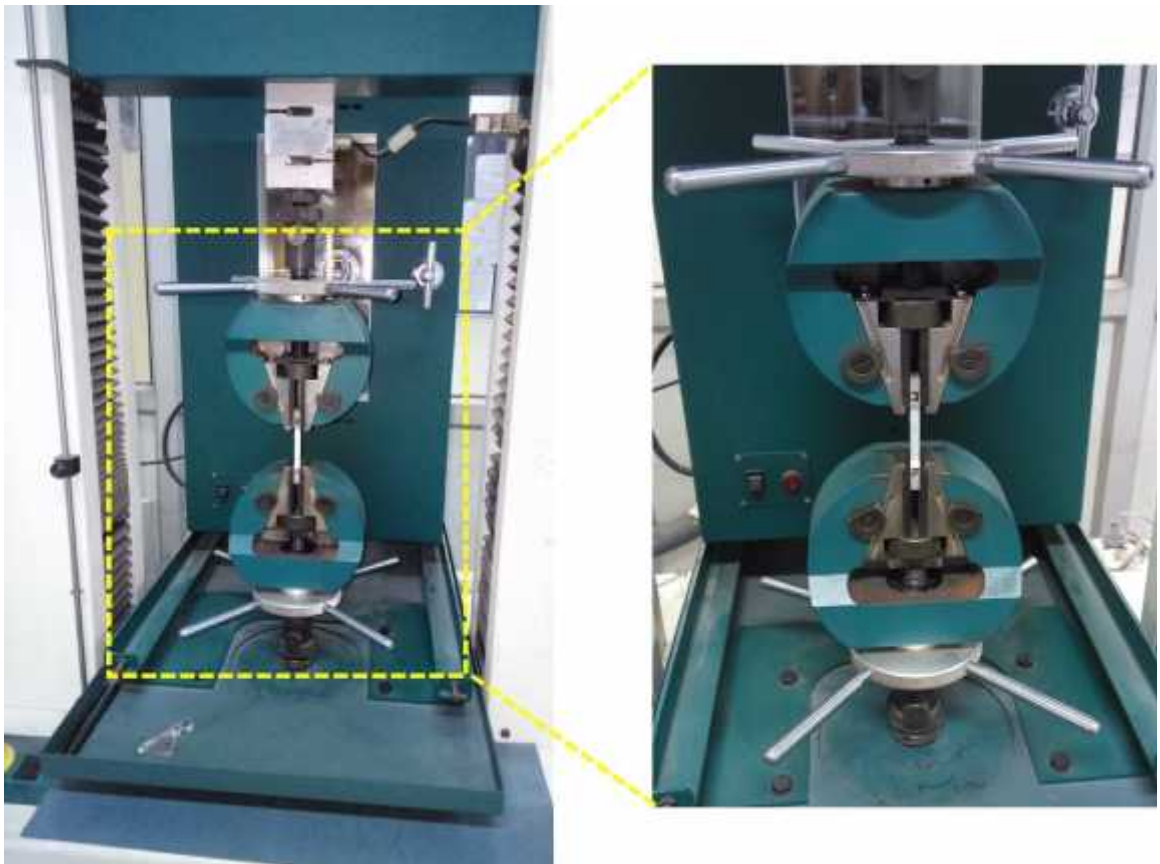


Figure 41: UTM machine at DTU, Delhi

This experimental setup is critical for assessing the mechanical integrity and performance of the weld zone and adjacent base materials (AA8011 and AA6061), ensuring that the dissimilar weld meets structural and application-specific requirements. The tensile specimens were prepared as per ASTM E8 standards. The specimens were extracted from the weldments using a milling cutter and then precisely machined using a shaper machine. For each welding condition, three specimens were prepared and tested at ambient temperature. The average of the three test results was considered for evaluation. Prior to testing, each specimen was carefully inspected to ensure the absence of any visible defects such as cracks, notches, or other imperfections that could potentially compromise the integrity of the test outcomes.

3.5.3 Micro-hardness

Figure 42 illustrates the hardness testing setup used to evaluate the hardness profile across the dissimilar welded joint between AA8011 and AA6061 alloys. The equipment shown is a Vickers hardness tester (TRUEMET), which operates by applying a controlled load through a diamond indenter onto the polished surface of the sample. The indentation left on the surface is then measured using a built-in microscope to calculate the hardness value in Vickers Hardness Number (VHN).



Figure 42: Vickers micro hardness testing process

The specimen is mounted securely on the adjustable stage, which allows precise positioning of the weld cross-section for traversing the hardness test across different zones—namely the base metal (BM), HAZ, and weld zone (WZ). This analysis helps in identifying the variation in hardness due to thermal cycling and metallurgical transformations. By mapping the hardness along the weld cross-section, critical insights can be gained into the mechanical integrity and localized property changes in the dissimilar joint, which are essential for predicting service performance and failure behavior

3.5.4 Residual stress measurement

Figure 43 illustrates the apparatus setup used for analyzing residual stresses in weldments using an XRD technique. The left part of the image shows the XRD equipment, specifically the Rigaku μ -X360n, which is a portable X-ray stress analyzer. This non-destructive testing method uses X-rays to measure the spacing between atomic planes in crystalline materials, which varies under residual stress conditions. The equipment is housed within a safety-shielded environment clearly marked with a “CAUTION: X-ray” sign to ensure operator safety from radiation exposure. The specimen is positioned beneath the X-ray head for precise alignment, and the beam is directed at specific zones of interest, such as the weld centerline or HAZ. The right portion of the figure shows the results output displayed on a computer screen, where software captures the diffraction patterns and calculates residual stress values in different directions.



Figure 43: Apparatus for analyzing the residual stresses

This setup is essential for understanding the stress distribution in welded components, which directly affects their fatigue life, crack propagation behavior, and structural reliability. Residual stress measurements in the weldments of AA8011 and AA6061 alloys were conducted using a portable XRD system. The $\cos\psi$ method was employed to analyze stress variations in the transverse direction of the welded samples. The X-ray beam was set at an incident angle of 35° with five oscillations per scan, and each measurement took approximately 4–5 minutes. A beam spot size of 2.5 mm was used with a 1.2 mm pinhole collimator, capturing surface diffraction images at a resolution of $50\ \mu\text{m}$. This method enabled residual stress evaluation using a single incident X-ray beam and a two-dimensional detector. The equipment

provided accurate and stable measurements, with clearly visible 3D Debye rings and distortion patterns in the welded samples. The stability of the peak center throughout the process confirmed consistent residual stress data across all samples examined under these conditions.

3.5.5 Metallurgical Characteristics Evaluation

Figure 44 presents a step-by-step visual representation of the specimen preparation process for metallographic analysis, particularly focusing on the weldments. In Figure 44(a), the specimen is shown being polished using emery paper, a crucial initial step to remove surface irregularities and scratches from the sample surface. This is followed by Figure 44(b), where finer polishing is performed using an emery cloth combined with Al_2O_3 (aluminum oxide) powder. This abrasive material ensures a smoother and mirror-like finish essential for accurate microstructural observation.

Figure 44(c) displays the polished specimens embedded in resin mounts, ready for microscopic or hardness analysis. The polished surface is clean, flat, and free from deformation marks, indicating the specimen is well-prepared for subsequent etching or imaging processes. In Figure 44(d), the laboratory setup for etchant preparation is shown. Various chemical bottles, glassware, and containers used for mixing acids or reagents are visible. The etching process reveals the grain structure and phase boundaries in the welded joint by selectively corroding different metallurgical phases. This comprehensive preparation process ensures that the microstructural features of the welded samples are clearly visible and reliable for analysis under optical or electron microscopes. The following steps were opted for making microstructure samples.

- To begin the microstructural and compositional evaluation of the CMT weldments, small specimens measuring $5\text{ mm} \times 5\text{ mm} \times 3\text{ mm}$ were carefully sectioned from the welded plates. These dimensions were selected to provide an adequate area for microstructural, hardness, and compositional analysis while being small enough to handle and process efficiently. The selected samples represented different zones of the welded region, including the WFZ, HAZ, and base metals (BMs). Precision cutting was essential to avoid introducing deformation or thermal effects that could alter the microstructure. Proper labelling and orientation of the samples were ensured to maintain positional reference throughout subsequent testing stages. This step forms the foundation of all further metallurgical examination, allowing accurate characterization of the weld quality and associated properties.
- Once the samples were sectioned, their surfaces were prepared by manual polishing using emery abrasive papers. This process started with coarser grits (typically 400 grit) and progressively advanced to finer grits (up to 3000 grit). Each polishing step was performed in a unidirectional manner, and the direction was changed by 90° with each grit. This careful approach produced a flat and scratch-free surface, which is critical for achieving accurate microstructural images under microscopy. Surface preparation is not only essential for revealing true microstructural features but also for ensuring consistent etching and minimizing artifacts that could mislead the interpretation. Proper cleaning

between each polishing stage using distilled water or ethanol further enhanced the surface quality.



Figure 44: (a) polishing with emery paper, (b) polishing with emery cloth with Al_2O_3 powder, (c) specimen after polishing, (d) making etching solution

- After completing manual polishing with emery paper, the specimens were subjected to final polishing using alumina (Al_2O_3) powder on a rotating disc polishing machine, as shown in Figures 44a, b. This polishing process helped achieve a mirror-like finish, crucial for high-resolution microscopy. The alumina particles, being extremely fine, remove very minimal surface material while refining the surface to a flawless condition. The polishing machine's consistent rotational motion ensures even pressure and finish across the entire sample. This stage is important for eliminating residual scratches and deformation layers introduced during earlier mechanical grinding. The mirror finish achieved here ensures accurate visualization of grain boundaries, inclusions, and other microscopic features when the sample is examined under optical or electron microscopes. Without this step, reliable imaging and interpretation would be severely compromised.
- To expose the grain boundaries and phase morphology in the aluminum weld samples, the finely polished specimens were chemically etched according to ASTM E407 standards. The etching solution used was Keller's reagent, consisting of 8 ml of nitric acid (HNO_3), 4 ml of hydrofluoric acid (HF), and 6 ml of hydrochloric acid (HCl). This reagent selectively attacks grain boundaries and second-phase particles, allowing them to become visible under a microscope. The etching was conducted under controlled conditions to avoid over-etching, which could distort the microstructure. Typically, the solution was applied for a few seconds, and the sample was immediately rinsed under running water to halt the etching reaction. Etching is a critical step as it highlights the metallurgical transformations in different zones, including grain refinement due to CMT process parameters.

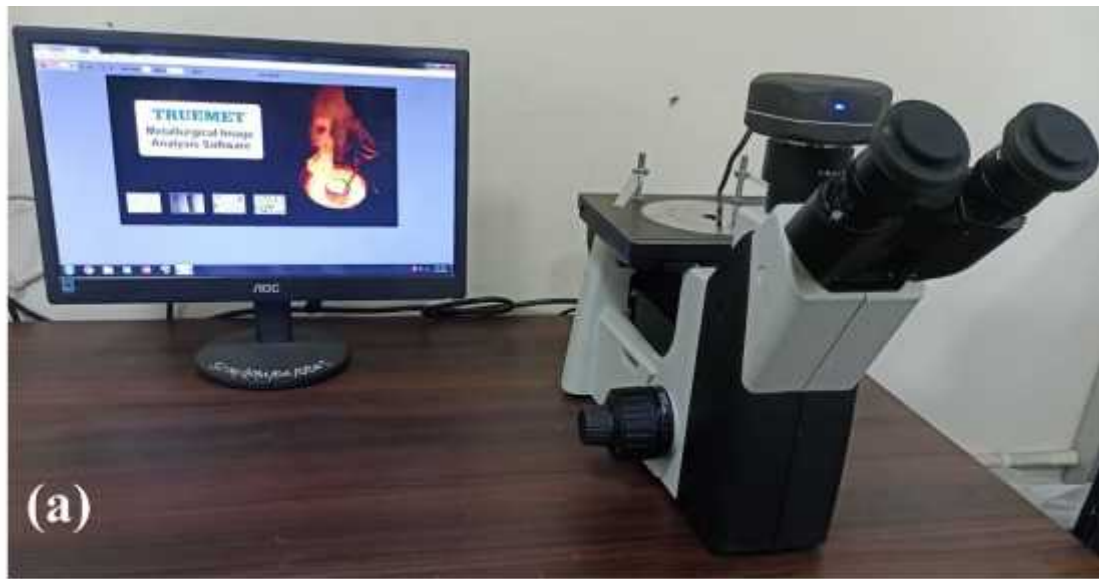


Figure 45: (a) Optical microscopic (Shobhit University, Meerut) and SEM machine (IIT Delhi)

- Figure 45 illustrates the advanced imaging instruments used for microstructural characterization of weldments. In Figure 45(a), an optical microscope installed at Shobhit University, Meerut, is shown alongside a computer loaded with metallurgical image analysis software (TRUOMET). This setup enables precise observation of the etched microstructure. It is particularly useful for conducting

grain size analysis, phase identification, and documenting the metallurgical transformations induced by welding.

- Figure 45(b) depicts the SEM model ZEISS EVO 18 Special Edition, located at IIT Delhi. SEM provides high-resolution imaging at magnifications far beyond what is achievable with optical microscopy. It allows for detailed observation of the weld morphology, fracture surfaces, inclusion particles, and fine microstructural features. The integrated computer interface and joystick controls enable accurate navigation and data collection. Together, these instruments are crucial for comprehensive microstructural and failure analysis of welded samples.
- To investigate the fracture behavior of the weldments after tensile testing, the fractured specimens were again treated with Keller's reagent. This selective etching helped distinguish the fracture morphology, highlighting the boundaries between ductile and brittle regions. The prepared fracture surfaces were then examined under SEM at high magnifications, allowing the visualization of dimples, cleavage steps, and void coalescence patterns. This analysis revealed the failure mechanisms involved, such as ductile tearing in the WFZ or brittle cracking near the HAZ. Understanding the fracture path is essential for evaluating the joint integrity and reliability under mechanical stress. The insights gained from this analysis contributed to identifying weak zones in the weld and improving the welding parameters to achieve better performance in future joints.
- To complement the microstructural and mechanical evaluations, EDS or EDX was carried out to determine the elemental composition of the base materials (AA8011 and AA6061) and the welded zones. This technique was integrated with the SEM system and involved focusing the electron beam on specific regions of interest. The emitted X-rays provided elemental fingerprints that confirmed the presence and distribution of key alloying elements such as Al, Mg, Si, Cu, Fe, and others. EDS analysis was crucial in detecting elemental diffusion across the weld interface, segregation of elements, or any contamination that could affect joint performance. The acquired spectra and maps validated the chemical integrity of the weld and ensured that the CMT welding had not introduced any detrimental compositional variations.

3.5.6 Experimental damping setup

Figure 46 depicts a modal analysis test rig designed to evaluate the dynamic response and damping characteristics of welded joints between aluminum alloys AA6061 and AA8011. The objective of this setup is to determine how these welded joints behave under vibrational excitation, primarily to assess their damping capacity and dynamic stiffness.

3.5.6.1 Sample for Testing

The sample under investigation is a welded joint fabricated from dissimilar aluminum alloys—AA6061 and AA8011. These samples are rigidly mounted to a fixture using a heavy clamp or vice to simulate fixed boundary conditions. This is crucial to eliminate any external degrees of freedom and ensure that only the

vibrational behavior of the sample itself is recorded. The test sample includes the HAZ and WFZ, which are of particular interest because these regions typically exhibit altered damping characteristics due to microstructural changes from welding.

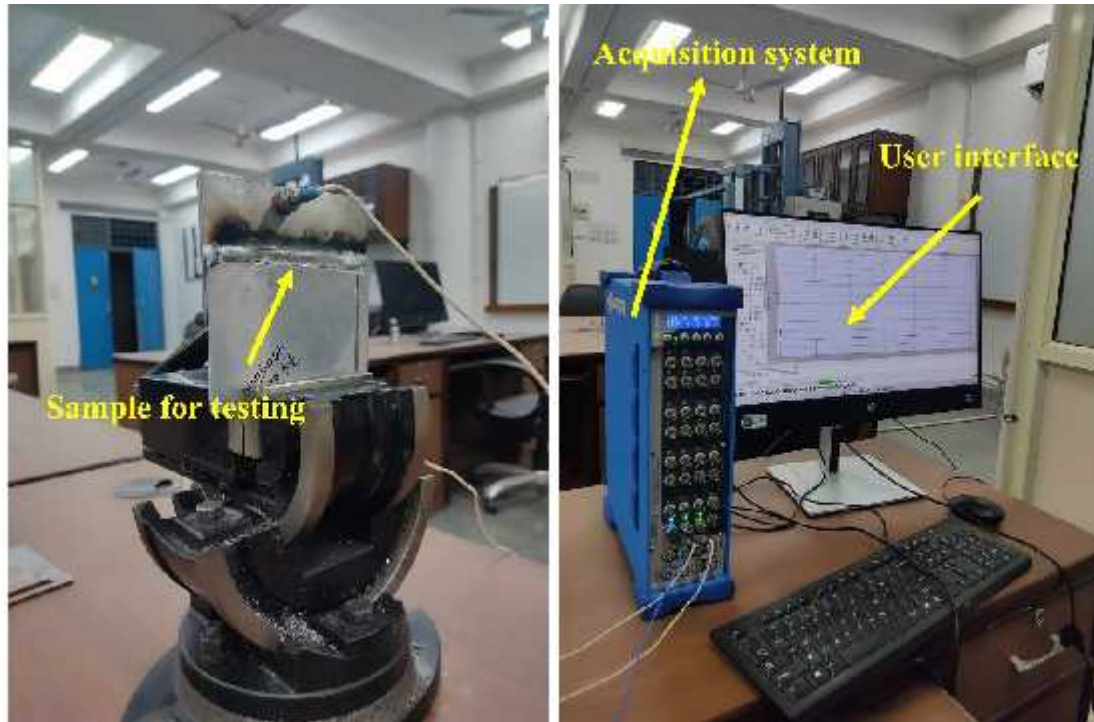


Figure 46: Experimental Modal Analysis Setup for Evaluating Damping Characteristics of Welded Joints

3.5.6.2 Impact Hammer

The excitation of the specimen is performed using an instrumented impact hammer, which has a built-in piezoelectric force sensor in its head. When the hammer is struck against the test sample, it delivers a known mechanical impulse, initiating transient vibrations over a broad frequency range. This input force is precisely measured and recorded. The selection of the hammer tip material (soft or hard) depends on the desired frequency range. For metallic specimens like AA6061 and AA8011, a steel or hard plastic tip is commonly used to excite higher modes of vibration. The purpose of using an impact hammer is to apply a non-destructive, controlled input force for modal testing.

3.5.6.3 ICP Accelerometer

An ICP (Integrated Circuit Piezoelectric) accelerometer is mounted directly onto the welded joint or a representative location on the sample. Its role is to sense and quantify the dynamic response of the structure (acceleration over time) following the hammer strike. The ICP technology includes built-in signal conditioning, allowing the sensor to produce a clean voltage output that is proportional to the experienced acceleration. The placement of the accelerometer is critical; it should be aligned with the expected direction of vibration and located away from nodal points to capture the

most accurate dynamic behavior of the joint. The data collected from the accelerometer helps in calculating the frequency response function (FRF) of the welded structure.

3.5.6.4 Acquisition System

The acquisition system (often a multichannel data acquisition hardware like LMS or NI PXI) serves as the central unit for signal processing and digitization. It collects synchronized input from both the impact hammer (input force) and the accelerometer (output response). The system has high sampling rates and resolution to accurately capture transient vibrational signals. It computes Frequency Response Functions (FRFs) in real-time, which relate the input force to the output acceleration. These FRFs are used to extract modal parameters such as natural frequencies, damping coefficients, and mode shapes. For welded joints, variations in damping behavior can be analyzed based on the weld quality and material mismatch.

3.5.6.5 User Interface (Laptop)

The user interface typically consists of a laptop running dedicated modal analysis or structural dynamics software such as LMS Test. Lab, NI Sound and Vibration Assistant, or MATLAB-based tools. The software provides real-time visualization of acquired signals, force response curves, coherence, and frequency spectra. The user can configure test parameters (e.g., sampling frequency, number of averages), initiate data acquisition, and perform post-processing such as curve fitting, peak picking, and damping ratio extraction. The interface also helps in comparing modal data across multiple test specimens (e.g., AA6061-only joint vs. AA6061-AA8011 dissimilar weld).

3.5.6.6 Objective of the Setup

The primary objective of this experimental setup is to assess the damping capacity, dynamic stiffness, and modal behavior of welded joints involving dissimilar aluminum alloys. Damping is a critical property for structures exposed to cyclic or vibrational loading, as it governs the ability of a structure to dissipate vibrational energy. The results help engineers understand the influence of welding on mechanical integrity, fatigue life, and vibrational performance, especially in lightweight structures such as automotive or aerospace components.

CHAPTER-4

Results and discussion

4.1 Introduction

CMT welding has emerged as a highly controlled arc welding technique that offers significant advantages for joining dissimilar Al-alloys, AA8011 and AA6061. These advantages include lower heat input, minimal spatter, and refined microstructure, which are crucial for high-performance structural applications. However, understanding the complex relationships between welding process parameters and resulting mechanical properties is essential to optimize joint strength and quality. Given this necessity, the current research aims to develop a statistically sound regression model that predicts key mechanical outputs—including UTS, strain percentage, hardness, and residual stress—based on critical process inputs such as welding current, WS, and GFR. The motivation behind this work is rooted in the lack of predictive modeling tools that can account for the nonlinear and interaction effects of these variables. Employing techniques such as ANOVA, regression analysis, and Lack-of-Fit (LOF) tests, the study systematically establishes the statistical significance and adequacy of the developed models. These models not only help in identifying dominant process parameters but also enable the formulation of response surface plots to guide parameter optimization. By integrating both experimental data and statistical tools, this research provides a robust framework for enhancing the predictability, reliability, and performance of dissimilar Al-alloy weldments fabricated via the CMT process.

4.2 Adequacy of the developed model

The validation and reliability of a mathematical model developed for CMT weldments are crucial in assessing its capability to predict mechanical and microstructural characteristics under varying welding conditions. This model serves as a predictive tool, correlating different input process parameters with corresponding output responses such as UTS, strain percentage, hardness, residual stress, and grain refinement. By examining how the output changes with respect to the input variables, the model provides insights into the underlying metallurgical transformations and mechanical behavior of dissimilar weldments. To evaluate the robustness and adequacy of the developed model, ANOVA was employed. ANOVA serves as a statistical method to analyze the significance of each process parameter and their interactions in influencing the response variables. The ANOVA tables for UTS, strain, hardness, and residual stress are presented in Tables 7 to Table 10, respectively. These tables help determine whether the observed variations in the output data are statistically significant or due to random chance. A model is considered statistically significant when it produces a high F-value and a low P-value—specifically, a P-value less than 0.05—which indicates that the influence of the input variables on the output response is not due to randomness but is, in fact,

meaningful [118]. The obtained F-values for the different responses—21.96 for UTS, 15.32 for % strain, 18.13 for hardness at the WFZ, and 16.81 for residual stress—demonstrate a strong statistical influence of the selected input parameters on these respective output responses revealed in Table 7 to 10. These values confirm the model's statistical significance, establishing that the variation in mechanical and microstructural properties can be effectively attributed to changes in process parameters. In addition to ANOVA results, regression coefficients such as R^2 (coefficient of determination) and adjusted R^2 are essential for further validating the model's adequacy. A value closer to 1.0 implies that the model has a high predictive accuracy. However, R^2 alone may be misleading if the number of predictors is large, which is why adjusted R^2 is also evaluated. Adjusted R^2 accounts for the number of input variables in the model and adjusts the R^2 value accordingly to provide a more accurate representation of the model's performance. When the R^2 and adjusted R^2 values are in close agreement, the model is considered to have high reliability and is not overfitted. This close alignment indicates that the model not only fits the experimental data well but also has the potential to accurately predict outcomes in new or unseen data sets. In this study, the high R^2 and adjusted R^2 values reinforce the model's suitability for predicting mechanical behavior and guiding the optimization of CMT process parameters.

Table 7: ANOVA table of UTS of CMT weldment of AA8011 and AA6061

Source	Sum of Squares	df	Mean Square	F-value	p-value	
Model	2502.17	9	278.02	21.96	< 0.0001	significant
A-Current	1002.80	1	1002.80	79.20	< 0.0001	
B-Welding Speed	371.49	1	371.49	29.34	0.0003	
C-GFR	168.02	1	168.02	13.27	0.0045	
AB	79.00	1	79.00	6.24	0.0316	
AC	64.18	1	64.18	5.07	0.0481	
BC	211.77	1	211.77	16.72	0.0022	
A ²	75.18	1	75.18	5.94	0.0350	
B ²	209.41	1	209.41	16.54	0.0023	
C ²	323.95	1	323.95	25.58	0.0005	
Residual	126.62	10	12.66			
Lack of Fit (LOF)	61.92	5	12.38	0.9569	0.5187	not significant
Pure Error (PE)	64.71	5	12.94			
Cor Total	2628.80	19				

The impact of input process parameters on the output responses in CMT welding was thoroughly evaluated using statistical tools, revealing a strong correlation between the independent variables and resulting mechanical properties. This relationship was confirmed by analyzing the P-values, which are fundamental indicators of statistical significance. A P-value less than 0.05 indicates that the corresponding parameter has a statistically significant influence on the response variable at a 95% confidence interval (CI) [119]. In this study, all models generated P-values below the 0.05 threshold, confirming that the variations in tensile strength, % strain, hardness, and residual stress were meaningfully affected by the changes in the selected input

parameters. In addition to P-values, the models' adequacy and predictive performance were further validated using the coefficient of determination (R^2). The R^2 values represent the proportion of the variability in the response data that can be explained by the independent variables. High R^2 values are desirable as they indicate a strong fit between the predicted and experimental results. The obtained R^2 values were 95.18% for UTS, 93.24% for % strain, 94.22% for hardness, and 93.80% for residual stress, as shown in Table 11. These values demonstrate that more than 93% of the variance in each response could be accurately accounted for by the models. Such high percentages validate the model's capability in capturing the influence of process parameters on output responses with high precision. Furthermore, the closeness of the adjusted R^2 and predicted R^2 values across all models highlights the reliability and robustness of the regression models. While the regular R^2 indicates how well the model fits the sample data, the adjusted R^2 corrects for the number of predictors and is particularly useful in multiple regression models. When the adjusted R^2 aligns closely with the predicted R^2 , it suggests that the model is neither overfitted nor underfitted and can generalize well to new data.

Table 8: ANOVA table of % strain for CMT weldments of AA8011 and AA6061

Source	Sum of Squares	df	Mean Square	F-value	p-value	
Model	11.49	9	1.28	15.32	< 0.0001	significant
A-Current	1.70	1	1.70	20.37	0.0011	
B-Welding Speed	0.3881	1	0.3881	4.66	0.0493	
C-GFR	0.8940	1	0.8940	10.73	0.0084	
AB	0.8256	1	0.8256	9.91	0.0104	
AC	1.52	1	1.52	18.27	0.0016	
BC	0.9316	1	0.9316	11.18	0.0074	
A ²	0.4788	1	0.4788	5.75	0.0375	
B ²	1.88	1	1.88	22.61	0.0008	
C ²	0.8864	1	0.8864	10.64	0.0086	
Residual	0.8333	10	0.0833			
LOF	0.4451	5	0.0890	1.15	0.4421	not significant
PE	0.3881	5	0.0776			
Cor Total	12.33	19				

The F-value, derived from the ANOVA, is another essential metric used to evaluate model adequacy. This value reflects the ratio of the model variance to the residual error variance. A higher F-value suggests that the variance explained by the model is significantly greater than the variance due to random error. In this study, the high F-values reported for UTS, % strain, hardness, and residual stress confirm that the regression models explain a substantial portion of the variability in the output responses. Additionally, the models were subjected to the LOF test, which assesses whether the model appropriately fits the experimental data. A non-significant LOF, indicated by a P-value greater than 0.1, confirms that there is no significant deviation between the model and the actual data points. In this case, all models exhibited non-significant LOF values, further establishing that the models provide an adequate fit and reinforce their validity.

Table 9: ANOVA table of hardness for CMT weldments

Source	Sum of Squares	df	Mean Square	F-value	p-value	
Model	603.73	9	67.08	18.13	< 0.0001	significant
A-Current	134.47	1	134.47	36.34	0.0001	
B-Welding Speed	78.34	1	78.34	21.17	0.0010	
C-GFR	44.44	1	44.44	12.01	0.0061	
AB	43.95	1	43.95	11.88	0.0063	
AC	18.03	1	18.03	4.87	0.0518	
BC	24.96	1	24.96	6.74	0.0266	
A ²	19.93	1	19.93	5.38	0.0427	
B ²	33.27	1	33.27	8.99	0.0134	
C ²	104.46	1	104.46	28.23	0.0003	
Residual	37.00	10	3.70			
LOF	7.68	5	1.54	0.2618	0.9162	not significant
PE	29.33	5	5.87			
Cor Total	640.73	19				

Table 10: ANOVA table of residual stress for CMT weldments

Source	Sum of Squares	df	Mean Square	F-value	p-value	
Model	3338.32	9	370.92	16.81	< 0.0001	significant
A-Current	1232.10	1	1232.10	55.84	< 0.0001	
B-Welding Speed	220.90	1	220.90	10.01	0.0101	
C-GFR	211.60	1	211.60	9.59	0.0113	
AB	153.12	1	153.12	6.94	0.0250	
AC	153.12	1	153.12	6.94	0.0250	
BC	465.13	1	465.13	21.08	0.0010	
A ²	184.09	1	184.09	8.34	0.0161	
B ²	265.09	1	265.09	12.01	0.0061	
C ²	375.28	1	375.28	17.01	0.0021	
Residual	220.63	10	22.06			
LOF	177.80	5	35.56	4.15	0.0722	not significant
Pure Error	42.83	5	8.57			
Cor Total	3558.95	19				

The ANOVA results, summarized in Table 7 to Table 10, clearly illustrate the significant influence of welding process parameters on the mechanical performance of CMT weldments between AA8011 and AA6061 Al-alloys. The evaluation was conducted for four key mechanical responses: UTS, % strain, hardness, and residual stress. The findings confirm that these responses are highly sensitive to variations in input parameters such as welding current, WS, and GFR, along with their interactions and quadratic effects. For UTS, the model was statistically significant, with a high F-value of 21.96 and a P-value less than 0.0001, confirming the strong relationship between the process variables and UTS. Among the input parameters,

welding current had the most pronounced effect, with an F-value of 79.20, making it the dominant factor in influencing UTS. WS and GFR also showed meaningful contributions, though to a lesser extent.

Additionally, both interaction terms (such as current \times speed) and quadratic terms were statistically significant, suggesting the existence of nonlinear relationships and complex interdependencies among the variables. The model's strength was validated through a high coefficient of determination ($R^2 = 0.9518$), an adjusted R^2 of 0.9085, and an adequate precision value of 17.80, indicating excellent signal-to-noise ratio and strong model reliability. A similar trend was observed for % strain (Table 8), where welding current again played the most influential role, with an F-value of 20.37. All the interaction and quadratic terms for strain were statistically significant, further confirming the complexity of the response surface. The model exhibited a robust R^2 value of 0.9324 and an adequate precision score of 14.65, reinforcing its strong predictive capabilities for elongation behavior in CMT joints.

In the case of hardness at the WFZ (Table 9), the welding current continued to dominate, showing an F-value of 36.34, significantly higher than the other parameters. The overall model quality was again validated with an R^2 of 0.9422, indicating that over 94% of the variation in hardness was captured by the model. These results underscore the sensitivity of hardness to changes in current and reinforce the importance of precise current control in achieving optimal weld hardness. However, while the residual stress model (Table 10) was statistically significant ($F = 16.81$, $P < 0.0001$), and welding current remained the most impactful factor ($F = 55.84$), the model's predictive accuracy was limited. The predicted R^2 value was found to be negative (-0.0718), which indicates poor alignment between predicted and experimental data for this response. This discrepancy suggests that the model may be overfitted or lacks sufficient data complexity to accurately forecast residual stress outcomes, and hence, it may not be suitable for reliable prediction without further refinement or additional experimental input.

Table 11: Fit Statistics data for UTS, % strain, and hardness values for CMT weldments

Properties	Std. Dev.	Mean	C.V. %	R^2	Adjusted R^2	Predicted R^2	Adeq Precision
UTS	3.56	85.19	4.18	0.9518	0.9085	0.7364	17.8052
% Strain	0.2887	10.42	2.77	0.9324	0.8716	0.5492	14.6494
Hardness	1.92	74.11	2.60	0.9422	0.8903	0.7443	17.113
Residual stress	4.70	-103.45	4.54	0.9380	0.8822	-0.0718	16.6797

4.3 Developing a regression model

A regression model was formulated to accurately predict key mechanical responses of CMT-welded dissimilar joints, specifically hardness, % strain, UTS, and residual stress. These models were developed based on the experimental variation of critical input parameters, including welding current, WS, and GFR. The strength and significance of these input variables in affecting each output response were systematically evaluated using the ANOVA. The relationship between the input and

output variables was mathematically represented through quadratic polynomial equations, allowing the response surface to be clearly interpreted and enabling the modeling of non-linear behavior. These regression models are listed in Equations 1–4, each correlating to a specific response variable. This mathematical framework enabled a comprehensive understanding of how individual parameters and their interactions influence weld performance metrics.

To determine the statistical adequacy and significance of the models, Fisher’s F-test was applied at a 95% confidence interval (CI). A model was considered statistically significant when the associated P-value was found to be less than 0.05, indicating that the model reliably explained the variation in the response data attributable to the input parameters [120]. All developed models met this criterion, suggesting that the selected process parameters significantly affected each mechanical property.

An additional validation of the model’s reliability was conducted through the LOF test, which assesses how well the model fits the experimental data. In this study, the LOF was found to be non-significant, implying that the difference between the predicted and actual experimental values was not statistically meaningful. This confirms that the model provides a good fit for the data and can be confidently used for predictive analysis. The developed regression equations, grounded in the RSM, provide a powerful tool for both optimization and prediction. By understanding the effects of welding current, speed, and GFR on the mechanical behavior of weldments, this model enables the identification of optimal processing windows. It facilitates the design of experiments aimed at achieving desired material characteristics under varied process conditions, ultimately supporting efficient, cost-effective, and high-performance welding of dissimilar Al-alloys.

$$\text{UTS} = 797.18 - 4.524 \times A + 9.812 \times B - 75.11 \times C + 0.0785 \times A \times B - 0.142 \times A \times C - 0.6431 \times B \times C + 0.052 \times A^2 - 0.545 \times B^2 - 2.713 \times C^2 \quad (4.1)$$

$$\% \text{ Strain} = -24.59 - 0.242 \times A - 0.575 \times B + 5.66 \times C + 0.008 \times A \times B - 0.022 \times A \times C + 0.043 \times B \times C + 0.0041 \times A^2 - 0.051 \times B^2 - 0.142 \times C^2 \quad (4.2)$$

$$\text{Hardness} = -235.65 - 2.55A - 5.73 \times B + 52.18 \times C + 0.058 \times A \times B - 0.075 \times A \times C + 0.22 \times B \times C + 0.0269 \times A^2 - 0.217 \times B^2 - 1.54 \times C^2 \quad (4.3)$$

$$\text{Residual stress} = -825.47 + 7.5A - 13.78B + 74.72 \times C - 0.109 \times A \times B + 0.218 \times A \times C + 0.953 \times B \times C - 0.082 \times A^2 + 0.613 \times B^2 - 2.92 \times C^2 \quad (4.4)$$

The developed regression equations (4.1–4.4) provide a clear and statistically validated representation of how the input process parameters—welding current, WS, and GFR—influence the mechanical responses of CMT-welded AA8011 and AA6061 joints. These models integrate both linear and nonlinear terms, allowing for the evaluation of direct effects as well as the influence of interaction and squared terms, offering a comprehensive understanding of process-response relationships. In the case of UTS, the regression model indicates that welding current and GFR negatively influence the strength of the joint, while WS contributes positively to enhancing UTS. Notably, the coefficient for gas flow in this model is $-75.11C$, highlighting its significant impact on reducing UTS at higher flow rates. This

suggests that excessive shielding gas may alter heat transfer dynamics or disturb arc stability, thereby weakening the joint. Conversely, optimized WS promotes better fusion and load-bearing capability. For % strain, a measure of ductility, the model reveals a strong positive influence from GFR, represented by a coefficient of +5.66C, suggesting that proper gas flow enhances joint elongation characteristics. Meanwhile, welding current and speed exert a slight negative influence, indicating that increased energy input or travel rate may reduce the material's capacity to deform plastically. In terms of hardness, the model demonstrates that GFR again plays a dominant positive role, with a coefficient of +52.18C, signifying improved hardness in the weld region. However, both welding current and speed negatively impact hardness, potentially due to higher heat input causing coarser grain structures or softening in the WFZ. The model for residual stress shows a different trend. Here, both current (+7.5A) and GFR (+74.72C) contribute to increased internal stresses, likely due to higher thermal gradients and more intense localized heating. In contrast, WS helps to reduce residual stress (−13.78B), possibly by lowering heat input per unit length and promoting faster cooling rates. The inclusion of interaction terms and nonlinear components, such as BC in residual stress (+0.953) and C² in UTS (−2.713), emphasizes the complex interdependence between process parameters. These nonlinearities confirm that the influence of each factor is not constant but varies with its magnitude and in combination with other variables. Overall, the regression models demonstrate that GFR is a consistently influential parameter across all mechanical responses. However, achieving a balanced optimization of strength, ductility, hardness, and residual stress requires precise tuning of all three input parameters. This highlights the value of these models in guiding process optimization to produce high-quality weldments.

4.4 Input and output response's correlation of the welded joints

Figure 47 provides a detailed visualization of the effects of varying input parameters on the output responses in the CMT welding process for dissimilar Al-alloys AA8011 and AA6061. These 3D response surface and contour plots, derived from the developed regression models, present a graphical interpretation of how combinations of welding current, WS, and GFR influence the UTS of the weldments. In the plots, the x-axis and y-axis denote the selected independent process parameters (such as current and WS, or WS and GFR), while the z-axis reflects the output response, i.e., UTS. The contour lines displayed on the surfaces connect points that yield equal tensile strength values, thereby enabling the identification of parameter combinations that produce optimal weld properties. These visual aids are essential for understanding the interaction between two input variables while keeping the third constant, a common constraint in contour-based visualization techniques.

From the response surface plots in Figure 47, a clear trend is observed when analyzing the impact of welding current and WS on UTS. As the current increases from 60 A to 80 A, the UTS shows a consistent upward trend. This behavior is attributed to the fact that a higher welding current leads to more uniform heat distribution, an enhanced cooling rate, and refined grain structure within the WFZ. The increased thermal input also promotes the formation of finer IMCs, which are beneficial for mechanical strength. These metallurgical factors collectively improve

the load-bearing capacity of the joint, thereby increasing its tensile strength [121]. Conversely, when considering the effect of WS, the UTS initially increases and then decreases beyond a specific threshold. At moderate WS, the interaction between arc energy and travel rate is balanced, leading to optimal fusion and a stable thermal cycle. However, excessively high travel speeds may not allow sufficient time for complete fusion, causing defects such as incomplete penetration or porosity, which weaken the weld. Similarly, very slow travel speeds may introduce excess heat, resulting in grain coarsening and the evaporation of strengthening elements, ultimately degrading mechanical performance.

The impact of GFR presents a more complex relationship with UTS. As the GFR increases from 12 to 16 l/min, the tensile strength initially decreases, then increases. This non-linear behavior results from the interplay between heat input uniformity, shielding effectiveness, and arc behavior. At lower GFR values, the shielding may be insufficient, allowing atmospheric gases to enter the weld pool, leading to porosity and microstructural inconsistencies. However, as GFR reaches an optimal level around 16 l/min, the shielding improves, minimizing oxidation and porosity, while contributing to grain refinement and enhanced mechanical integrity of the joint. The initial reduction in tensile strength with increasing GFR can also be linked to excessive arc turbulence. Higher gas flow velocities disturb the stability of the molten weld pool, potentially resulting in lack of fusion and porosity formation. At optimal GFR values, these effects are minimized, and the weld pool remains stable enough to allow for a consistent thermal gradient, promoting fine grain structures and low defect rates. Furthermore, the development of beneficial compressive residual stresses at moderate GFR values contributes positively to the weld's tensile properties.

Nevertheless, further increasing the GFR beyond 16–18 l/min shows a detrimental effect on UTS. The amplified turbulence and gas dispersion negatively affect the shielding coverage, increasing the likelihood of entrapped gases, oxidation, and spatter formation, which introduce defects and microvoids into the weld. Such imperfections act as stress concentrators during mechanical loading, thereby reducing tensile strength. Additionally, excessive GFR leads to higher operational costs, as more shielding gas is consumed, impacting the economic efficiency of the welding process [122]. An important observation from the response surface analysis is that welding current consistently demonstrates a positive influence on tensile strength within the tested range. This can be attributed to its direct role in controlling the thermal cycle, which affects grain morphology, fusion depth, and solidification behavior. Increased current enhances arc energy, promoting better fusion between the base materials and reducing the risk of defects such as cold laps and voids. However, it must be carefully controlled, as excessive current beyond the studied range might lead to excessive melting, warping, or distortion. In terms of interaction effects, the regression model equations include interaction and quadratic terms, such as the BC term in the residual stress model and C^2 in the UTS model, which highlight how process parameters do not act independently. Their influence changes based on the levels of other variables. For instance, the effect of GFR on tensile strength is significantly modified when considered in conjunction with welding current or speed.

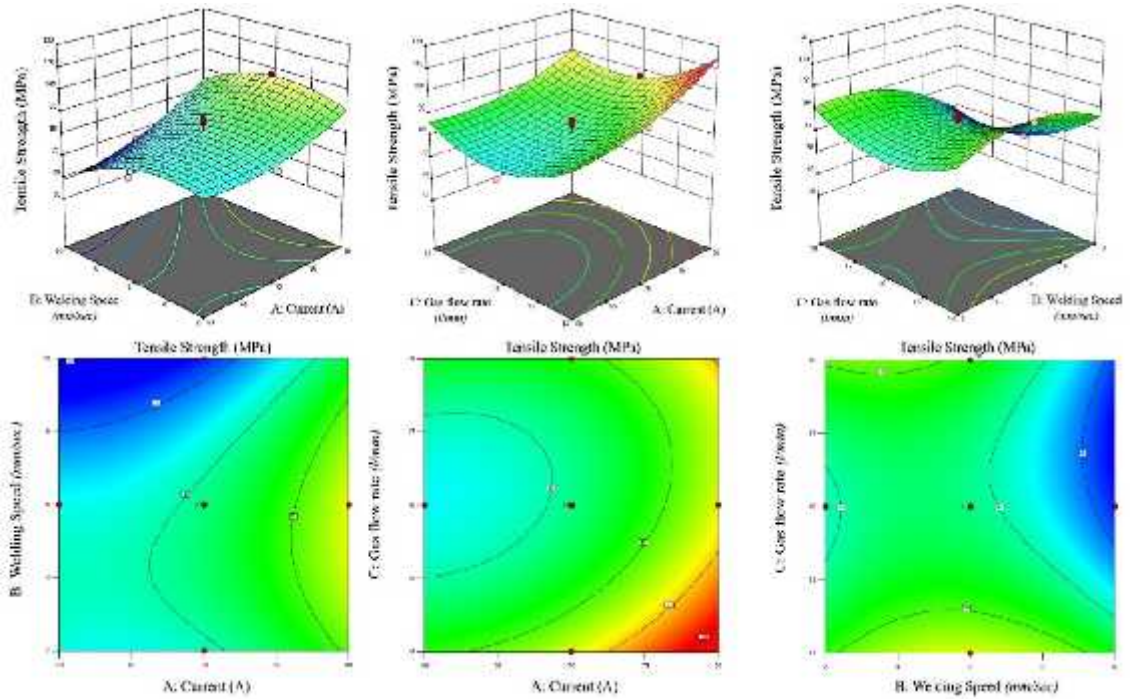


Figure 47: 3D contour and their responses of tensile strength of the CMT weldments

This highlights the need for multi-variable optimization rather than relying on single-factor tuning. The detailed analysis of Figure 47 thus provides critical insights into how to strategically adjust the welding current, speed, and GFR to maximize tensile strength while minimizing defects and residual stress. It underscores the importance of using RSM to capture the complex interactions and non-linear behaviors of the process. Through such visual and statistical analysis, optimal welding windows can be defined for CMT processes involving AA8011 and AA6061, ensuring high joint integrity, structural reliability, and cost-efficiency in real-world manufacturing scenarios. Figure 48 presents the three-dimensional (3D) response surface along with the associated contour plots that illustrate the variation in % strain of the CMT-weldments of AA8011 and AA6061 under different processing parameters. This output response, which reflects the ductility of the welded joint, is influenced by the combined and individual effects of WS, welding current, and GFR. The plots in Figure 48 are generated using the regression models derived through RSM, offering a visual interpretation of how changes in two input parameters simultaneously impact joint ductility while holding the third constant. The influence of WS on % strain follows a nonlinear trend. As WS increases from 2 mm/s to 10 mm/s, the % strain initially improves and subsequently declines. This behavior implies that at moderate speeds, better material fusion and bonding are achieved, which enhances the joint's ductility. The improved ductility at these intermediate speeds is likely due to a balanced heat input and travel rate, which promotes optimal wetting of the substrate and reduces the risk of defects such as cold laps or incomplete fusion. However, at excessively high WS, the arc exposure time decreases, limiting the heat input and fusion between the base materials. This reduction in energy can impair metallurgical bonding and grain refinement, leading to weaker joints with reduced strain capacity. With respect to welding current, the % strain demonstrates a consistent upward trend

as the current increases from 60 A to 80 A, as illustrated in Figure 48. This steady enhancement in ductility can be attributed to better weld pool mixing and homogenization due to increased arc energy. Higher current promotes the formation of a more stable and refined grain structure by intensifying the thermal gradient and cooling rate, both of which play a pivotal role in developing fine, equiaxed grains that are beneficial for plastic deformation. The refined grain structure ensures uniform stress distribution across the welded joint during loading, thereby increasing the joint's ability to withstand strain without premature failure. This enhancement in ductility directly correlates with the joint's improved metallurgical quality and interfacial bonding. The role of shielding GFR in determining ductility is particularly critical and exhibits a dual-phase response. As GFR increases from 14 l/min to 16 l/min, there is a notable rise in % strain, indicating that this GFR range provides effective shielding, which protects the weld pool from atmospheric contamination. Proper shielding reduces oxidation and porosity formation, both of which can compromise ductility. The improvement in % strain within this optimal GFR range is also due to enhanced arc stability and controlled heat input, which support uniform solidification and improved joint integrity.

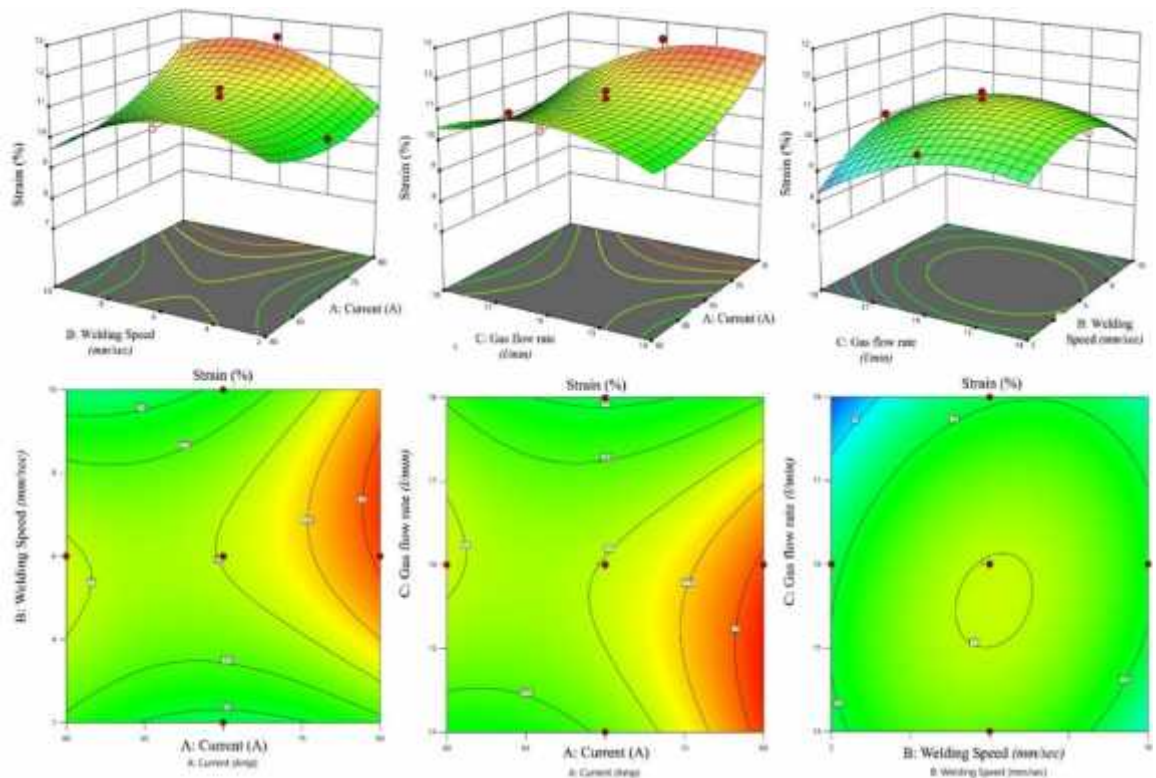


Figure 48: 3D contour of % strain of the CMT weldments

However, a further increase in GFR from 16 l/min to 18 l/min results in a decline in % strain. This reduction is most likely caused by increased turbulence and gas dispersion associated with excessive shielding gas flow. When GFR becomes too high, it can disturb the molten pool's surface and reduce the protective barrier's effectiveness, allowing potential contamination by ambient gases. These conditions may introduce porosity, inclusions, or incomplete fusion, all of which adversely

affect ductility. Furthermore, the aggressive flow may alter the shape of the weld bead, increasing stress concentration points that act as crack initiation sites under tensile loading.

Therefore, Figure 48 effectively demonstrates that achieving high ductility in CMT weldments requires a careful balance of process parameters. The ideal GFR range lies between 14 and 16 l/min, beyond which the benefits begin to decline. Similarly, moderate WS and higher currents are favorable for enhancing ductility, as they promote optimal heat distribution and grain refinement. It is crucial to note that while current consistently improves % strain, WS and GFR exhibit threshold-dependent behavior, where exceeding certain levels leads to degradation in performance. Figure 49 presents the 3D response surface and contour plots illustrating the variation in hardness of the CMT-weldments of AA8011 and AA6061 as a function of WS, welding current, and GFR. The trends displayed in these plots are generated from the regression models and provide valuable insights into how changes in process parameters influence the microstructural characteristics of the weld zone, particularly the WFZ.

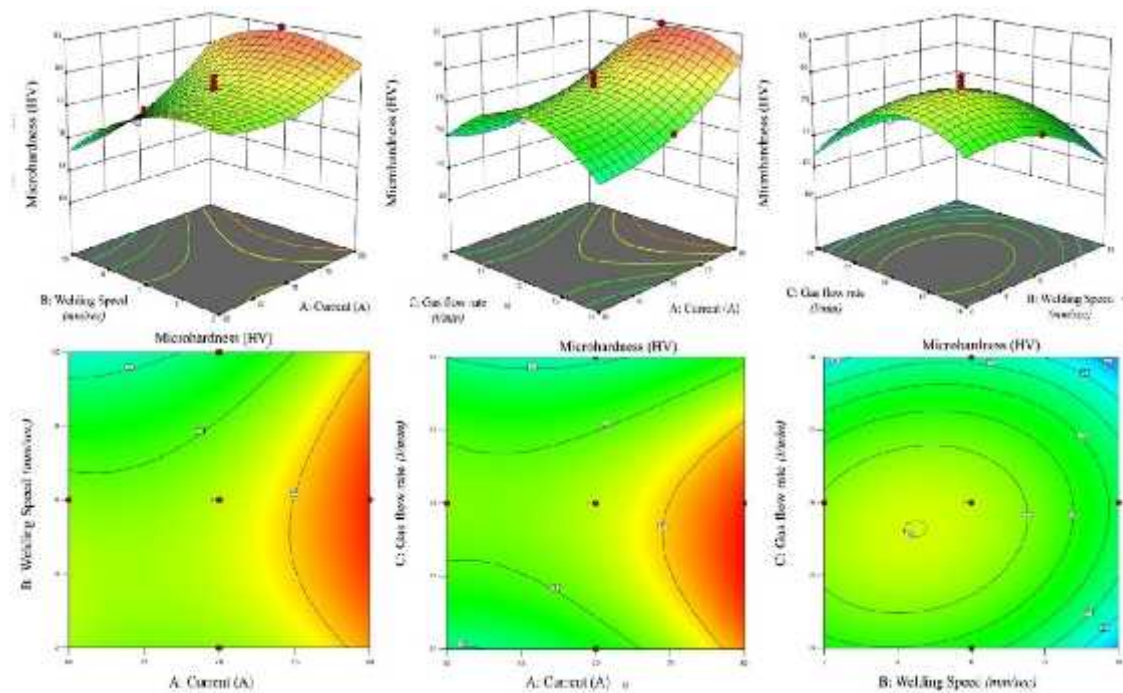


Figure 49: 3D contour of hardness of the CMT weldments

As shown in Figure 49, the hardness of the joint initially increases with increasing welding speed, reaching an optimal point, after which it begins to decline. This behavior is linked to variations in microstructural development during welding. A moderate increase in WS allows for more uniform heat input, facilitating better control over grain refinement and promoting the formation of IMCs. However, at excessively high WS, the energy input becomes insufficient for complete fusion and uniform grain development, leading to a coarser microstructure and reduced hardness. The relationship between grain size and hardness is well explained by the Hall–Petch equation, which states that hardness is inversely proportional to grain

size. Finer grains enhance resistance to dislocation movement, thus increasing hardness. Consequently, microstructural features such as grain size, temperature distribution, strain rate, and the presence of IMCs significantly affect the hardness profile within the WFZ. The effect of welding current on hardness is also evident in the surface plots.

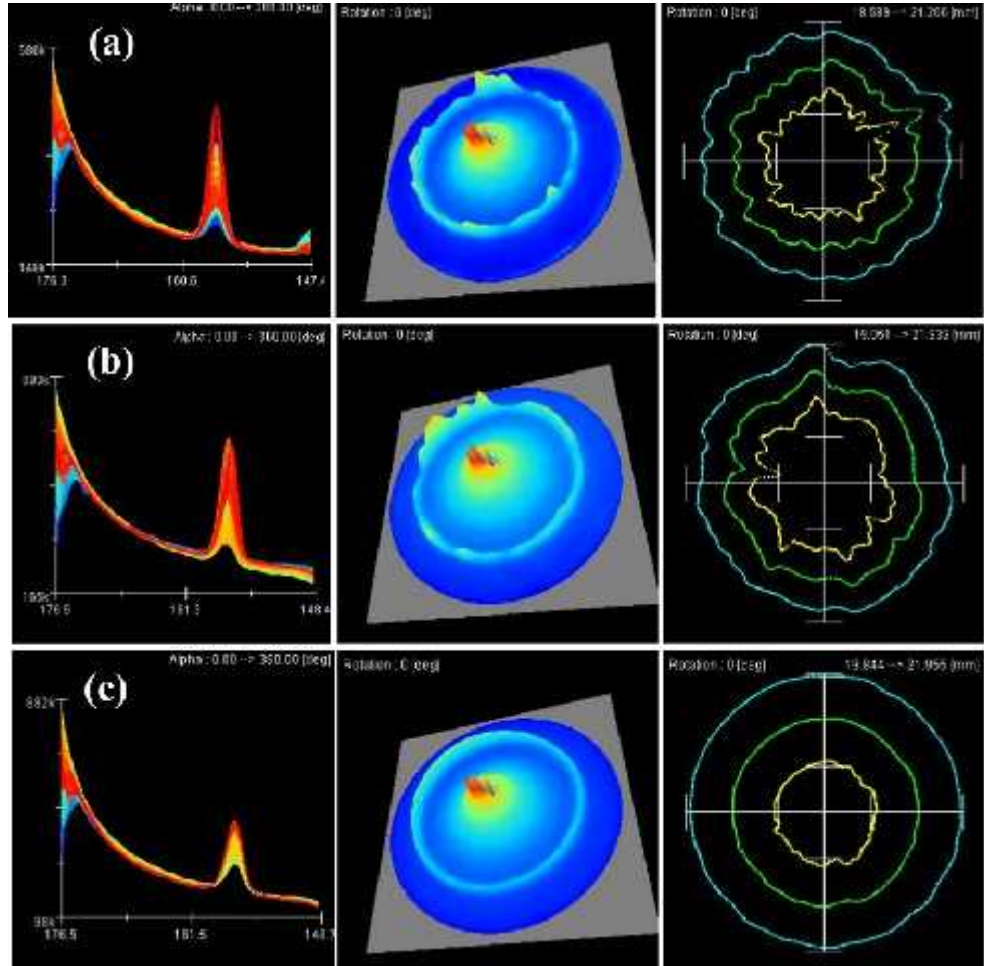


Figure 50: Profile of residual stress, Debye ring, and distortion profile of the weldments, (a) Sample 7, (b) Sample 8, (c) Sample 11

As the current increases from 60 A to 80 A, the hardness of the joint exhibits a rising trend due to increased heat input, which results in better material mixing, enhanced bonding, and refined grains. In this optimal range, the thermal gradients are balanced, and the heat is more uniformly distributed, promoting microstructure homogenization and porosity reduction, which positively influence the hardness of the welded region. However, at very high current levels, the heat input may become excessive, causing grain coarsening, dissolution of strengthening IMCs, and potentially degrading the hardness. This emphasizes the importance of maintaining the welding current within a controlled optimal range, as both underheating and overheating negatively affect microstructural integrity and hardness performance [123]. The influence of welding current and shielding GFR on the hardness of the WFZ is further highlighted in Figure 49, showcasing the significance of precise

control over thermal and shielding conditions during the CMT welding process. At higher welding currents, although initial increases contribute positively by improving heat transfer and refining grain structures, excessively large currents introduce adverse effects. Specifically, high current levels generate intense arc turbulence and instability in the weld pool, which can lead to increased porosity formation and weakened metallurgical bonding. These defects deteriorate the hardness properties of the weld, reducing the mechanical integrity of the joint. Moreover, elevated current levels result in excessive heat input, which may cause localized over-tempering or rapid cooling of the weld metal. These thermal fluctuations negatively influence the formation of fine microstructures, promoting grain coarsening and reducing hardness.

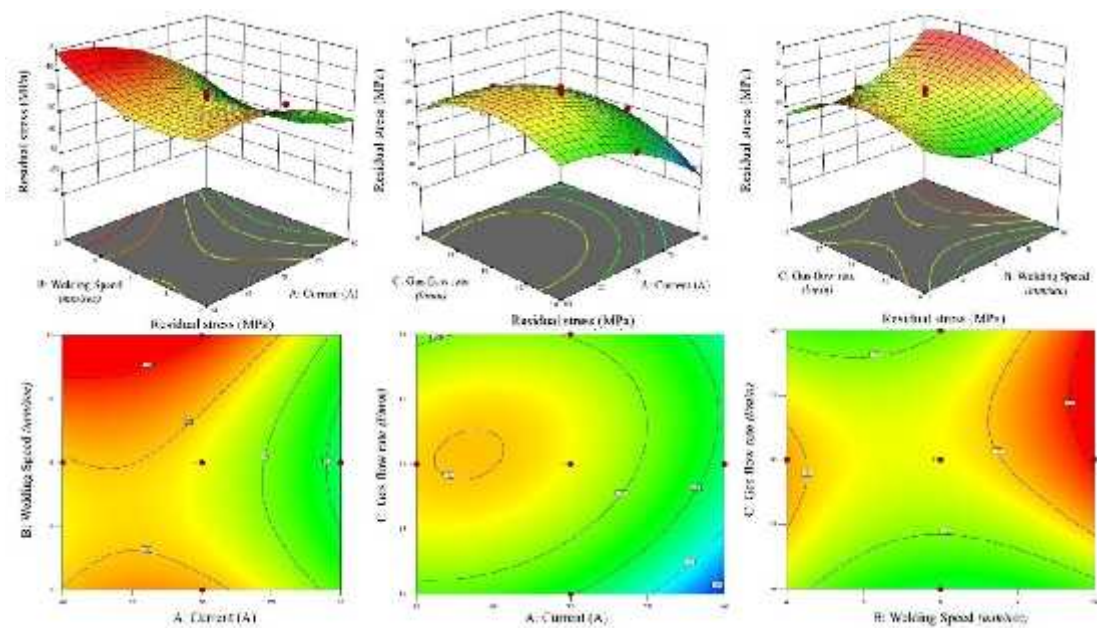


Figure 51: 3D contour of residual stress of the weldments

Thus, while moderate current enhances the mechanical properties, a threshold exists beyond which the benefits diminish due to the destabilization of the thermal profile and increased defect formation [124, 125]. The shielding GFR also plays a crucial role in determining the hardness of the welded joint by influencing the thermal behavior and protective efficiency of the shielding gas during welding. As illustrated in Figure 49, when the GFR is increased from 14 l/min to 16 l/min, the hardness of the WFZ improves significantly. This improvement is attributed to the creation of a stable and effective shielding atmosphere, which minimizes the risk of oxidation and atmospheric contamination, thereby preserving the chemical purity of the weld pool. The consistent gas coverage promotes arc stability, enhances thermal regulation, and contributes to uniform cooling rates, all of which refine the grain structure and increase the hardness of the weld. However, further increasing the GFR beyond 16 l/min, particularly up to 18 l/min, leads to a decline in WFZ hardness. This deterioration is likely due to excessive gas turbulence, which disrupts the shielding environment and can unintentionally allow ambient gases, such as oxygen or nitrogen, to enter the weld pool. The resulting contamination, coupled with arc

instability, introduces irregularities in heat input and solidification patterns. This leads to inconsistent fusion and non-uniform grain morphology, ultimately reducing the hardness and quality of the joint. Figure 50 presents a detailed depiction of the residual stress distribution, Debye ring pattern, and distortion profiles for various CMT-weldments of AA8011 and AA6061 specimens. This analysis was conducted to assess the residual stresses induced by different welding conditions. Residual stress refers to the internal stresses retained in a material even after the welding process is completed and no external forces or temperature gradients are present. These stresses originate primarily from non-uniform heating and cooling during the welding cycle, which causes differential expansion and contraction across the weldment. The development and magnitude of residual stresses are influenced by several key factors, including heat input, WS, cooling rates, and the material properties of both the filler and base metals. In weldments, residual stresses are typically categorized into tensile and compressive types. Tensile residual stresses are generally considered detrimental because they can lead to crack formation, reduce fatigue life, and compromise the joint's mechanical integrity. On the other hand, compressive residual stresses are generally beneficial as they tend to inhibit crack propagation and improve the structural performance of the weld. In this study, compressive residual stresses were predominantly observed, especially along the weld bead, where they were found to be greater than in both the WFZ and the base metal. This enhancement in compressive stress at the weld bead is attributed to rapid cooling rates, which induce significant surface contraction, thereby generating compressive forces across the joint. Figure 51 illustrates the 3D contour plots for residual stress variation under different process parameters. It is evident from the response surface that WS plays a pivotal role in determining the level of residual stress. As WS increased from 2 mm/s to 10 mm/s, residual stress levels rose accordingly. This can be explained by the fact that at higher WS, the heat input per unit length is reduced, and the weld pool experiences shorter exposure to high temperatures. Consequently, the surface region of the weld cools more rapidly than its inner layers, inducing greater thermal contraction at the surface. The imbalance in cooling rates leads to the formation of compressive residual stresses as the outer material attempts to contract against a hotter, still-expanding interior. The influence of welding current on residual stress follows a dual-phase trend. Initially, when the current increases from 60 A to 70 A, the heat input becomes more substantial, resulting in elevated temperatures in the weld pool. This causes steeper thermal gradients and faster cooling, which amplify the generation of compressive stresses due to greater shrinkage effects during solidification. However, when the current is further increased from 70 A to 80 A, the weld remains at elevated temperatures for longer durations. This extended high-temperature exposure reduces the cooling rate and minimizes thermal gradients, leading to slower solidification and reduced contraction, which in turn diminishes the magnitude of compressive residual stresses. The variation in GFR also contributes to the observed stress behavior, although its impact is less dominant compared to WS and current. A lower GFR, such as 14 l/min, tends to produce higher compressive residual stress due to more stable arc characteristics and controlled heat transfer, which enhances cooling uniformity. In contrast, a higher GFR (e.g., 18 l/min) may induce gas turbulence around the weld zone, potentially disrupting arc stability and causing uneven cooling.

This disturbance can diminish the formation of beneficial compressive stresses, leading to lower residual stress values. The maximum compressive residual stress of -65 MPa was recorded at a welding current of 80 A, a WS of 10 mm/s, and a GFR of 14 l/min, indicating that this combination provides the optimal balance of heat input and cooling rate to achieve the most favorable residual stress condition. Conversely, the minimum compressive residual stress of -9 MPa was observed at a lower current of 60 A, WS of 10 mm/s, and GFR of 18 l/min, a set of conditions likely associated with reduced thermal gradients and inefficient stress generation mechanisms.

4.5 Predicted vs actual scattered diagram

Figures 52a–d present the actual versus predicted plots for the output responses of the CMT-weldments, including UTS, % strain, hardness, and residual stress. These diagrams serve as a critical validation tool for the RSM models developed during the experimental phase. The primary objective of these plots is to compare the experimental (actual) results with the predicted outcomes derived from the mathematical regression models, which were constructed using the input process parameters.

In each graph, the x-axis represents the experimentally observed values of the respective mechanical property, while the y-axis shows the values predicted by the developed model. Ideally, if the model accurately predicts the responses, the data points should align closely along a 45° reference line, representing perfect correlation between predicted and actual outcomes. As observed in Figure 52, the data points for all four output responses are generally clustered around this 45° diagonal line, demonstrating a strong correlation and suggesting that the regression models are highly effective in capturing the relationship between the input process parameters and output responses. This alignment affirms that the models are statistically robust and experimentally validated, indicating that they can reliably predict performance characteristics such as UTS, strain, hardness, and residual stress under varying welding conditions. Any deviations from this reference line highlight areas where discrepancies exist between model predictions and actual experimental data. These deviations, although relatively minimal in this study, can offer useful insights into model limitations, unaccounted process variables, or experimental anomalies. Such analysis is vital for refining the regression equations, enhancing model precision, and identifying parameters that may require more accurate measurement or broader experimental range in future studies. In addition to the actual vs. predicted plots, Figures 53a–d present perturbation plots for each of the four output responses. These plots provide a graphical representation of the sensitivity of each response to changes in one specific input parameter, while the other two parameters are held constant at their center or average levels. Perturbation plots are particularly useful for visualizing the relative influence of each parameter in isolation, making them valuable tools in understanding how slight deviations in a specific input affect the mechanical and structural properties of the weld. For example, in Figure 53a, the perturbation curve for UTS may show that increasing the current significantly influences tensile strength, while changes in GFR have a lesser effect. Similarly, Figure 53b might indicate that % strain is highly sensitive to current but relatively less influenced by welding speed.

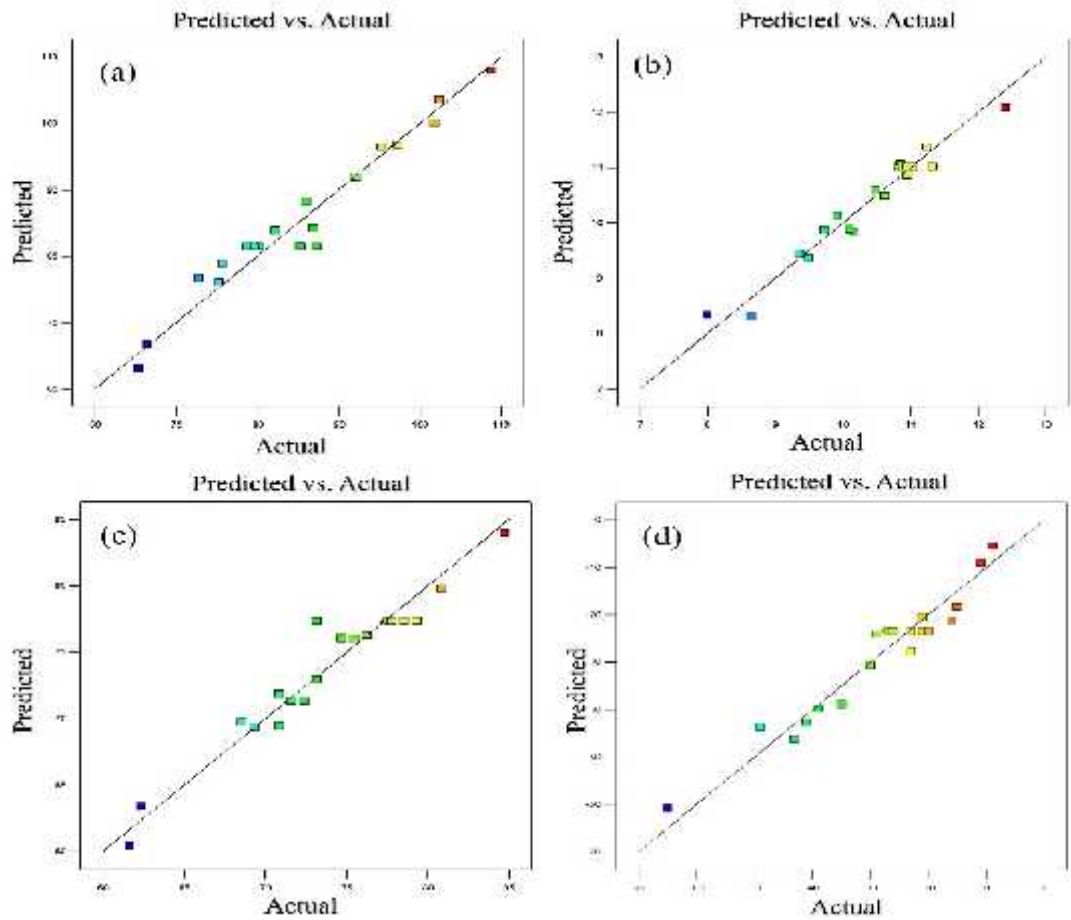


Figure 52: Predicted vs actual diagram of the weldments, (a) Tensile strength, (b) % strain, (c) Hardness, (d) Residual stress

The slope of each curve reflects the degree of sensitivity: a steep slope indicates a strong influence of that parameter on the response, whereas a flatter curve suggests a weaker effect. These perturbation plots further validate the findings from the ANOVA and regression models, confirming which parameters are most critical for optimizing specific weld properties. For instance, in this study, welding current consistently emerged as the most influential parameter across all output responses, significantly affecting the mechanical performance of the joints. Figure 53 illustrates the perturbation curves for the weldments, which provide a clear depiction of how variations in individual input parameters influence the mechanical properties of the welds. These curves are plotted by maintaining all other parameters at their central values, allowing the effect of a single variable to be independently observed on the output responses such as UTS, % strain, hardness, and residual stress. The perturbation curve serves as a critical analytical tool for evaluating the sensitivity of the output response to changes in each individual process parameter. The slope of the curve plays a key role in this interpretation: a steep slope indicates that even a small variation in the parameter results in a significant change in the output response, signifying high sensitivity. Conversely, a flatter curve suggests that the parameter

exerts a minimal influence on the response, implying lower sensitivity under the examined conditions.

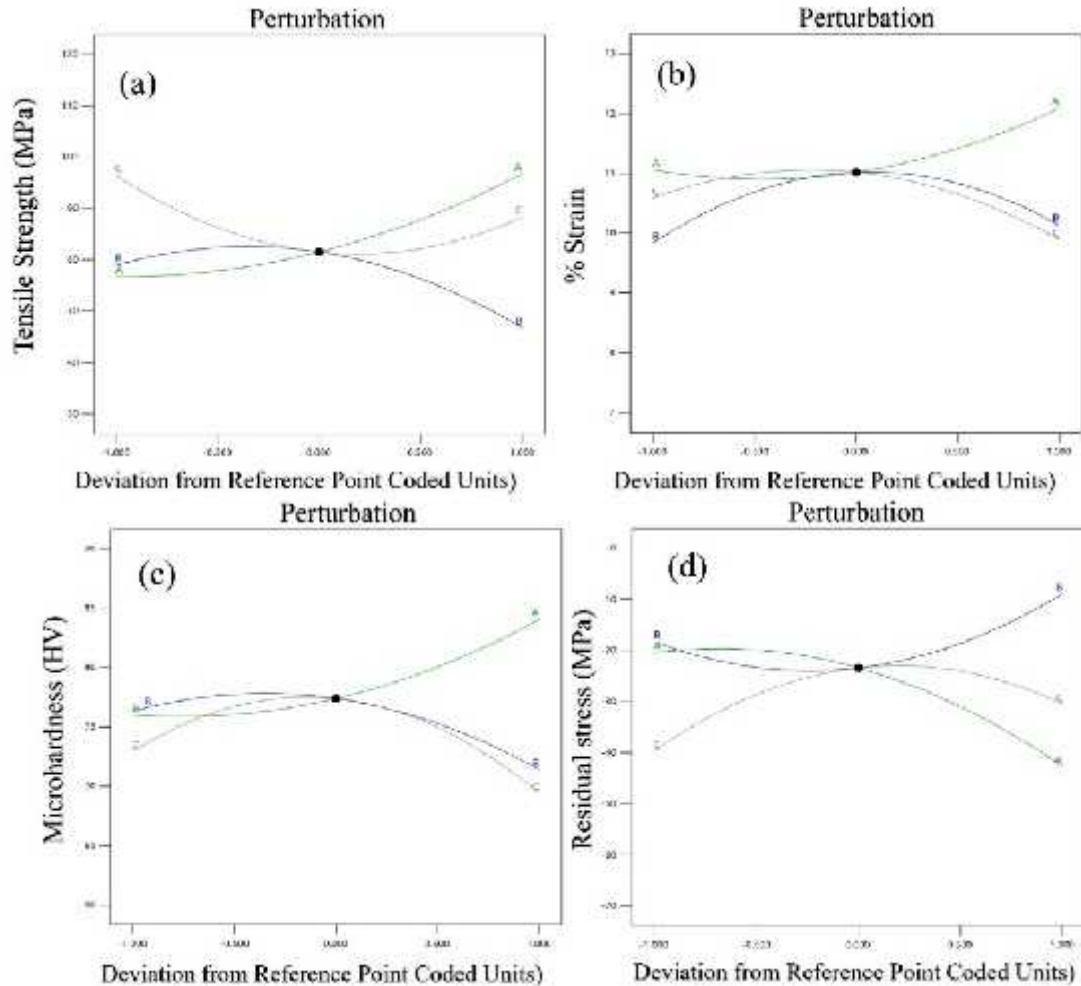


Figure 53: Perturbation curve of CMT weldments (a) Tensile strength, (b) % strain, (c) Hardness, (d) Residual stress

For instance, as WS increases, the perturbation curve for UTS may display either a rising or declining trend, depending on the specific heat input and cooling rates achieved during the welding operation. Increased WS typically reduces the heat input per unit length, which can lead to finer grain structures and potentially increase strength. However, beyond an optimal point, further increases in WS may result in insufficient fusion and weaker joints, leading to a drop in tensile strength. The exact trend is reflected in the curvature and direction of the perturbation plot.

Likewise, the welding current is shown to have a profound effect on all mechanical responses. As current increases, the associated heat input into the weld zone also rises. This elevated thermal input influences the solidification rate, grain structure, and distribution of IMCs, all of which affect hardness and tensile strength. A steep slope in the curve related to current—particularly in the UTS and hardness graphs—highlights its critical role in weld optimization. A pronounced deviation from the baseline curve indicates that current must be carefully controlled to maintain

desirable mechanical performance. The GFR is another essential factor, particularly influencing hardness and % strain. The perturbation curve for GFR demonstrates how shielding effectiveness varies with gas flow. Within an optimal range (typically around 14–16 l/min), proper gas shielding enhances arc stability and reduces porosity, improving weld ductility and surface quality.

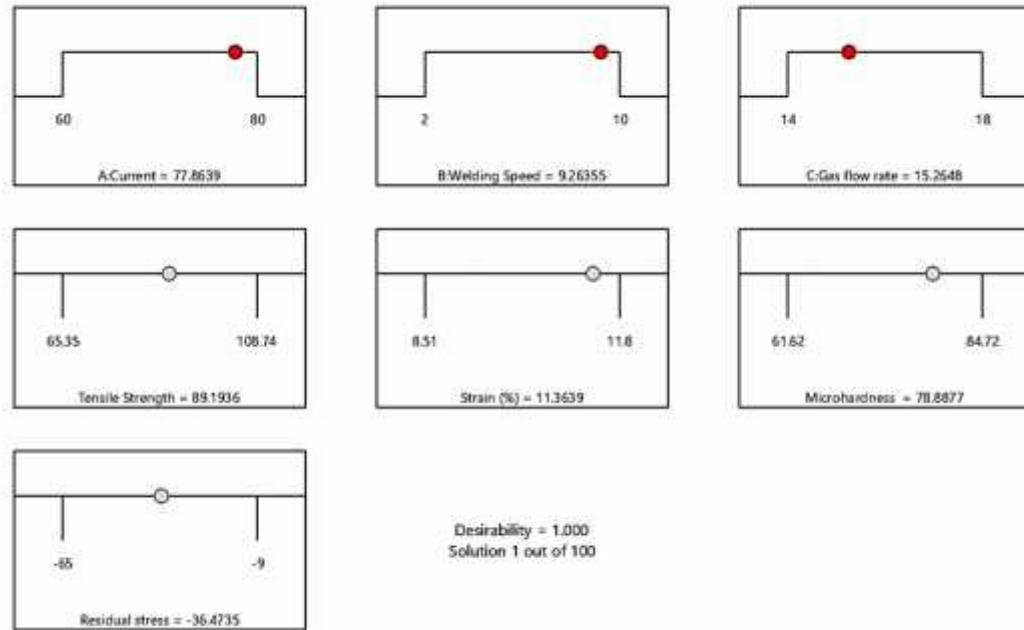


Figure 54: Optimize value of input and output responses of CMT weldments

However, excessive GFR may induce arc turbulence or gas dispersion, leading to oxidation, defects, and reduced mechanical properties. The sharpness of the perturbation curve in this region indicates that GFR is highly sensitive and must be tuned precisely to avoid weld degradation. Figure 54 presents the desirability test results through a ramp chart, offering a comprehensive visualization of the relationship between the input parameters and the optimized output responses. This graphical tool plays a crucial role in the multi-objective optimization process by simultaneously balancing all desired outcomes and identifying the optimal combination of process variables to achieve the best mechanical performance in the weldments. The ramp chart clearly highlights how adjustments in the welding current, WS, and GFR influence the predicted mechanical properties of the CMT-weldments. Based on the desirability analysis, the optimal input parameters were determined to be a welding current of 77.86 A, welding speed of 9.26 mm/s, and GFR of 15.26 l/min. These parameters collectively contribute to achieving the most desirable outcomes across all measured responses. Correspondingly, the optimized output responses under these conditions were predicted as follows: UTS of 89.19 MPa, % strain of 11.36%, hardness of 78.88 HV, and residual stress of -36.47 MPa. These results suggest that the selected combination of input variables effectively enhances weld quality by improving strength, ductility, and hardness while minimizing residual stress.

The desirability function approach not only streamlines parameter selection but also provides a reliable guide for achieving balanced mechanical properties in dissimilar Al-alloy weldments, thereby supporting improved structural performance and manufacturing efficiency.

4.6 Mechanical properties

The influence of varying input parameters on the output responses of CMT-welded AA8011–AA6061 joints is comprehensively detailed in Table 12, which highlights the performance metrics for multiple specimens. To assess mechanical behavior, test samples were extracted transversely from the weld zone. Among all tested joints, Specimen 11 exhibited the highest UTS of 108.74 MPa, highlighting the influence of optimized process parameters on weld quality. This superior performance is attributed to a refined microstructure and uniform grain distribution achieved at ideal processing conditions. In contrast, Specimen 8, welded under less optimal settings, displayed irregular grain formation and coarsening, resulting in reduced mechanical efficiency and lower joint performance.

The microstructural features directly correlate with UTS variations. Specifically, under optimal parameters—80 A current, 10 mm/s WS, and 14 l/min GFR—Specimen 11 demonstrated an excellent strain capacity of 11.23% and a significant hardness value of 74.69 HV, despite the presence of high compressive residual stress (-65 MPa). This emphasizes the importance of controlled heat input in refining grains and enhancing strength. Additionally, Specimen 6 recorded the maximum strain value of 11.80% when welded at 80 A current, 6 mm/s WS, and 16 l/min GFR, revealing that slightly reduced travel speed promotes greater ductility. The hardness for this configuration peaked at 84.72 HV, indicating that the increased shielding and appropriate heat input enhanced hardness. The corresponding residual stress for this condition was measured at -41 MPa, suggesting effective thermal control without excessive internal stress buildup. Hardness analysis across the weld zone demonstrates noticeable variations, particularly in the WFZ, Partially Melted Zone (PMZ), and HAZ, reflecting differences in grain morphology and thermal exposure. Notably, Specimen 18 displayed the highest WFZ hardness (84.72 HV), while Specimen 4 recorded a significantly lower average of 61.62 HV, emphasizing the impact of current, WS, and GFR on microstructural hardening. The hardness variation, detailed in Table 12, supports the influence of thermal cycles on material characteristics. Lower hardness in the HAZ is consistent with grain coarsening due to prolonged thermal exposure. The PMZ region exhibited variations due to phase dissolution and grain transformation influenced by current fluctuations [126].

The microstructural inhomogeneity across welded regions—especially PMZ and HAZ—is attributed to inadequate material flow and rapid cooling or overheating, leading to distinct hardness gradients [127]. Grain size refinement in response to controlled heat input is consistent with the Hall–Petch relationship, wherein smaller grains enhance hardness.

Table 12: Mechanical characteristics of the weldments of AA8011 and AA6061 with different process parameters

Sample number	A: Current (A)	B: Welding Speed (mm/s)	C: GFR (l/min)	UTS (MPa)	Joint efficiency (%)	Strain (%)	Hardness	Residual stress
							(HV)	(MPa)
1	70	6	18	85.98	68.93	10.1	69.32	-30
2	80	2	18	101.77	81.59	8.51	68.53	-49
3	70	6	16	85.12	68.25	11.04	77.52	-23
4	60	10	14	75.19	60.28	9.18	61.62	-16
5	60	6	16	72.69	58.28	10.75	75.46	-21
6	70	6	16	78.65	63.06	11.12	80	-26
7	60	2	14	86.81	69.6	9.72	74.21	-29
8	60	10	18	75.35	60.41	9.85	62.37	-9
9	70	6	16	80.24	64.33	10.52	73.15	-21
10	70	10	16	76.38	61.24	9.91	71.61	-11
11	80	10	14	108.74	87.19	11.23	74.69	-65
12	70	6	16	87.23	69.94	10.81	77.77	-26
13	70	6	16	85.24	68.34	11.32	79.31	-20
14	70	6	14	95.25	76.37	10.48	73.15	-39
15	80	10	18	82.14	65.86	10.62	72.38	-23
16	60	2	18	92.12	73.86	9.49	70.84	-35
17	70	2	16	75.69	60.69	10.15	76.23	-15
18	80	6	16	97.29	78.01	11.8	84.72	-41
19	80	2	14	102.36	82.07	10.95	80.85	-43
20	70	6	16	79.63	63.84	10.85	78.54	-27

In lower current weldments, coarse IMCs, such as Al Fe and Mg Si, reduce hardness and compromise the joint's overall mechanical integrity. These observations confirm that optimal welding current and shielding parameters are critical for suppressing IMC formation and promoting favorable grain morphology [128]. Figure 55 provides visual representation of the influence of WS and GFR on UTS, hardness, and % strain at different welding currents. The best performance was observed at WS = 6 mm/s and GFR = 16 l/min, producing a UTS of 108.74 MPa, hardness of 84.72 HV, and strain of 11.8%, reflecting well-balanced strength and ductility. On the other hand, the lowest UTS (101.77 MPa) and strain (8.51%) were recorded at WS = 2 mm/s and GFR = 18 l/min, indicating that excessively low speed or high gas flow can compromise fusion quality and material bonding. Joint efficiency is a crucial performance metric, and this study demonstrates that maximum efficiency of 87.19% was attained under 80 A current, 10 mm/s WS, and 14 l/min GFR. Another configuration—Run 19—also yielded high efficiency (82.07%) at 80 A current, 2 mm/s WS, and 14 l/min GFR, indicating that increased current enhances heat input for better fusion, even when speed is low. These results underscore that the energy supplied through current is the dominant parameter influencing weld quality. The lowest joint efficiency of 58.28% was observed at 60 A current, 6 mm/s WS, and 16 l/min GFR, which corresponds to suboptimal heat input and shielding, causing

incomplete fusion and poor joint quality. Specimens fabricated at 70 A and 6 mm/s WS, with GFR ranging between 14 and 18 l/min, generally exhibited joint efficiencies between 63–70%, indicating moderate mechanical performance. These variations in efficiency further confirm that precise control of all three parameters—current, WS, and GFR—is essential for enhancing weld integrity and minimizing performance discrepancies.

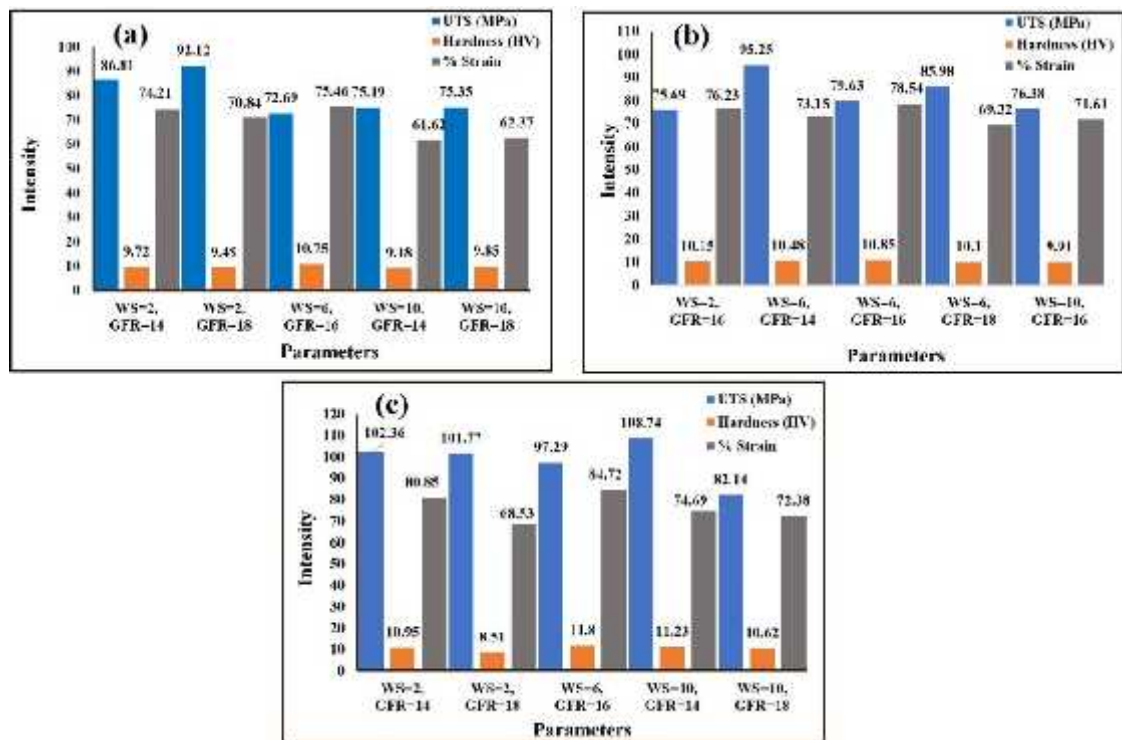


Figure 55: Mechanical properties of the CMT weldments of AA8011 and AA6061, (a) 60 A, (b) 70 A, (c) 80 A

4.7 Microstructure analysis

Figure 56a, b depicts the optical microstructures (OM) of the base materials, AA8011 and AA6061, respectively, showcasing notable differences in grain morphology. The microstructure of AA8011 in Figure 56a displays elongated and columnar grains oriented in a specific direction. This directional grain alignment is likely the result of its manufacturing process and can significantly influence its anisotropic mechanical behavior. Such grain orientation tends to enhance strength in the direction of elongation while potentially reducing it in the transverse direction. Conversely, Figure 56b illustrates the microstructure of AA6061, which features a predominantly equiaxed and uniform grain structure. These grains are nearly spherical and uniformly distributed, resulting in more isotropic mechanical properties. The presence of equidimensional grains contributes to balanced strength, ductility, and toughness across multiple directions, making AA6061 highly favorable for structural applications.

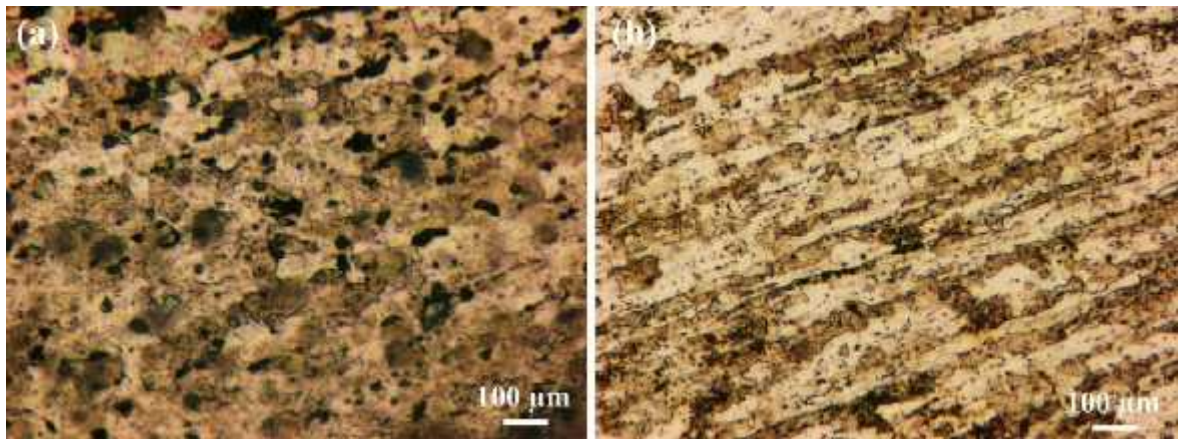


Figure 56: Optical images of parent material, (a) AA6061, (b) AA8011

The observed variation in grain morphology between these two alloys can be attributed to differences in their chemical composition, thermal conductivity, and the heat treatment processes they undergo during solidification. When these dissimilar materials are joined using the ER4043 filler through the CMT welding process, the resulting weld region exhibits a heterogeneous grain structure. This heterogeneity arises due to mismatches in solidification behavior and thermal gradients between the filler and the base metals, leading to distinct grain size and phase distribution across the welded joint. Such structural differences can influence the joint's mechanical performance, requiring careful process control to achieve optimal properties. Figure 57a depicts the optical microstructure of various welding zones observed in the CMT-welded AA8011–AA6061 joint. The image reveals clearly differentiated regions—namely the Partially Melted Zone (PMZ), WFZ, and HAZ—each exhibiting distinct grain morphologies influenced by local thermal cycles. Immediately adjacent to the WFZ lies the PMZ, which exhibits a characteristic columnar grain pattern aligned with the direction of heat flow. On the AA6061 side of the PMZ, columnar grains show signs of partial melting at grain boundaries, a consequence of the alloy's higher thermal conductivity and slower cooling rate. These semicrystalline structures result from uneven solidification during cooling and reflect AA6061's susceptibility to boundary remelting. In contrast, on the AA8011 side of the PMZ, the grains appear semi-molten and non-spontaneously nucleated, which disrupts regular grain growth and produces an alternating, patchy appearance. This distinctive structure arises from AA8011's higher melting temperature and differing elemental composition, which together yield heterogeneous grain development across the PMZ. Moving outward from the PMZ, the HAZ encompasses the region that heated below the melting point, yet experienced thermal cycles sufficient to alter its microstructure. The grains in this area are notably coarse, a result of thermal exposure causing recrystallization and growth during cooling. The observed grain coarsening confirms the importance of thermal cycle control in welding, as larger grains are typically associated with reduced strength and toughness. As noted in Figure 57a, the coarse-grain HAZ underscores the need to manage heat input in the CMT process to mitigate potential strength degradation [129]. Figure 57b delivers a detailed view of sample 8's WFZ, providing insight into grain formation and defect distribution under suboptimal welding conditions. The

WFZ exhibits uneven and dual-grained microstructures, combining coarse columnar grains with finer equiaxed grains—an indication of unstable thermal gradients and inconsistent melting throughout welding. Such mixed morphology often leads to pores and voids, particularly in the columnar grain regions, due to uneven solidification and entrapment of shielding gas. The image additionally shows inclusions of oxides and precipitates, disrupting the continuity of grain boundaries and negatively impacting mechanical integrity. The HAZ of sample 8, shown in Figure 57c, features elongated and over-etched grains with clear directional alignment, providing evidence of grain distortion amid thermal exposure. The presence of elongated precipitates, such as Mg₂Si in AA6061, along with oxide particles, suggest partial dissolution and reprecipitation, both consistent with thermal cycling. The dark regions within the micrograph—likely oxide inclusions or porosity—point to weld defects arising from inadequate shielding or turbulent gas flow. These inclusions act as stress concentrators, potentially initiating cracks under thermal or mechanical load.

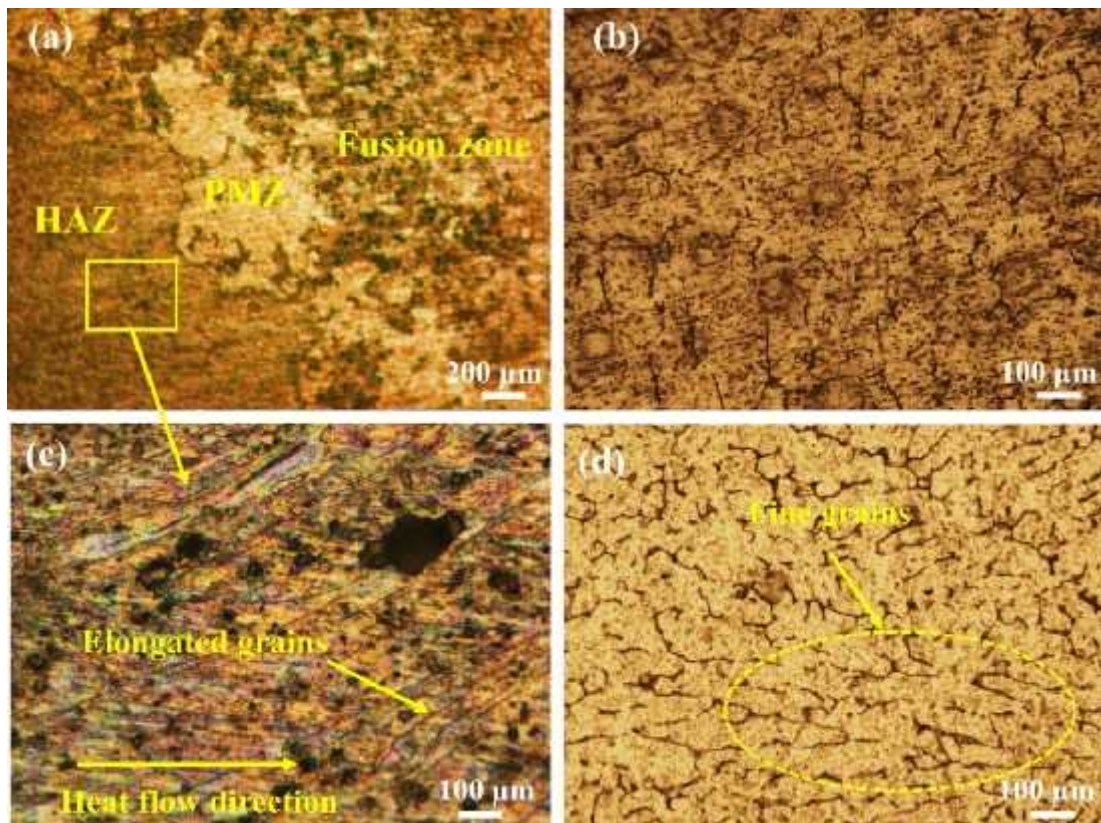


Figure 57: (a) Macrostructure of the welded joint, (b) OM image of weldments at the fusion for sample 8, (c) HAZ image, (d) WFZ for sample 11

By contrast, Figure 57d illustrates the WFZ of sample 11, which was welded under optimal parameters (80 A current, 10 mm/s WS, 14 l/min GFR). The resulting fine-grained uniform microstructure signifies a highly controlled welding environment. The well-defined grain boundaries, free from oxidation or notable porosity, reflect steady thermal gradients and efficient solidification. This improved microstructure enhances weld strength and ductility while minimizing defects. The more uniform

grains also foster better load distribution and resistance to crack initiation—key contributors to the superior mechanical properties achieved in sample 11.

Heat input clearly influences grain refinement and defect minimization: optimal thermal cycles produce smaller solidification grains, refined oxide distribution, and controlled precipitation of secondary phases, all of which contribute to mechanical integrity. A smaller, uniform grain structure limits porosity and increases hardness and tensile strength by reducing the distance for dislocation movement. The presence of residual microstructural heterogeneity across welding zones remains a critical factor. Grain size variations—coarse in HAZ; columnar in PMZ; and intermittent in WFZ of less optimized samples—are direct outcomes of local thermal gradients and alloy-specific solidification behavior. Figure 57a visually captures this structural heterogeneity, demonstrating that the PMZ and HAZ regions possess morphologies distinctly different from the WFZ. The rapid solidification in optimized sample 11 yields a more homogenized microstructure, showing that proper control of current, speed, and GFR can align microstructural evolution across the joint.

Phase transformations, such as the formation of Mg–Si plates and partial dissolution and reprecipitation, particularly in AA6061's HAZ, further complicate microstructure. These changes influence mechanical behavior by altering grain boundary chemistry and phase distribution, lies in its reduced susceptibility to localized crack initiation and increased mechanical consistency throughout the joint. Figure 58a–d offer detailed SEM (Scanning Electron Microscopy) and EDS (Energy Dispersive Spectroscopy) visualizations of the WFZ and adjacent regions in CMT-welded AA6061–AA8011 joints, focusing on samples 7 and 11. These micrographs help characterize grain morphology, precipitate distribution, and elemental segregation that develop under different welding conditions. Figure 58a highlights the WFZ microstructure at a lower welding current (60 A). In this zone, the primary α -Al grains appear coarse and irregularly shaped, surrounded by a network of intergranular precipitates, which are indicated by yellow arrows. This microstructure suggests a slower cooling rate and higher heat input during welding, allowing grains to grow significantly before being frozen in place. The SEM image shows α -Al grains interspersed with pronounced precipitates, consistent with the formation of Mg–Si. The high-temperature exposure also results in micropores of varying sizes—likely due to insufficient back-side shielding—where trapped gases (like O₂ or H₂) nucleate voids before solidification completes. Such micropores can act as stress concentrators and compromise mechanical strength [130].

Moving to Figure 58b, taken at higher welding current (80 A) and optimized WS, the WFZ exhibits a noticeably refined grain structure. Here, α -Al grains are smaller and more equiaxed, with uniformly distributed precipitates along the grain boundaries. This transformation is typical of more stable, optimized welding conditions, as higher current and WS improve heat control, promote nucleation over grain growth, and reduce the time available for grains to coarsen. Consequently, the microstructure becomes more favorable for mechanical properties. The precipitates observed here likely consist of IMCs—primarily Mg–Si but possibly including Al-Fe, Al-Si-Fe, Al-Cu, and Al-Zn phases. In this optimized scenario, the refined precipitate distribution strengthens the joint without creating stress-raising large inclusions. The HAZ, although not directly imaged in Figure 58, can be inferred to present a transitional microstructure between the base material and the weld. Exposed to

significant thermal input but not melting, the HAZ undergoes partial recrystallization, producing finer grains near the fusion edge and potentially coarser grains farther away. Reduced precipitate density here, compared to the WFZ, reflects incomplete phase transformations and precipitation kinetics. Figure 58c–d shift focusses to precipitate morphology and IMC distribution as revealed by EDS mapping. In Figure 58c, the darker precipitated regions align with boundary edges, confirming elemental segregation—particularly of Mg, Si, and Fe—due to localized solidification. Such eutectic precipitates form along intergranular lines and can either strengthen the joint via dispersion hardening or weaken it by serving as crack initiation sites, especially when coarse and angular. Porosity noted in these images confirms suboptimal shielding and thermal conditions during welding.

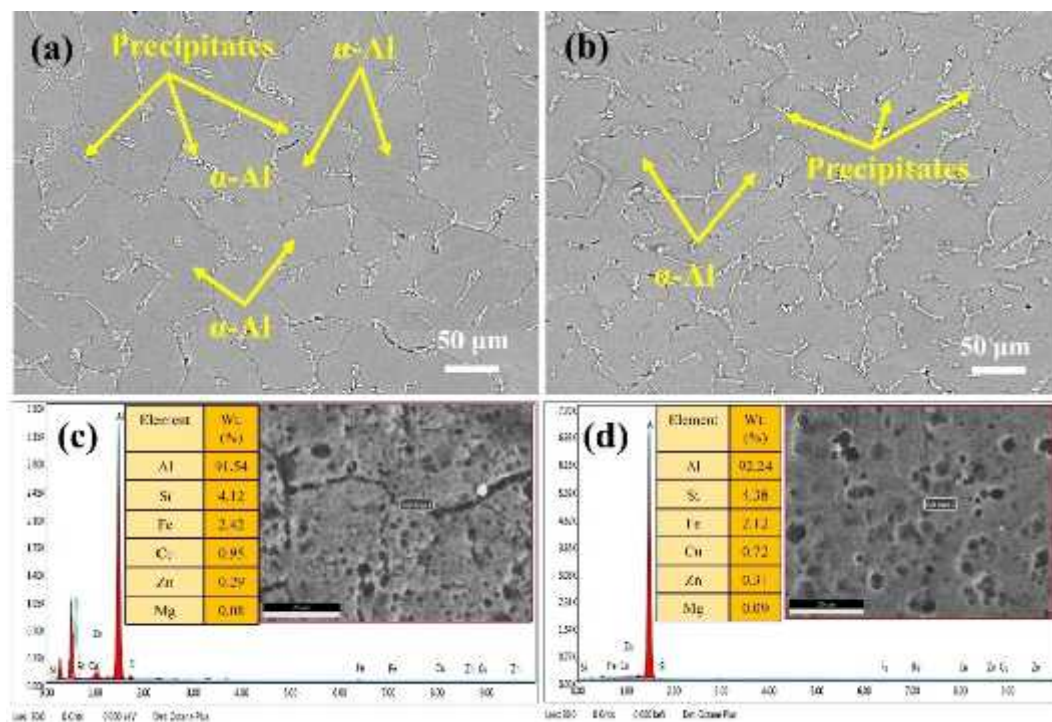


Figure 58: SEM images CMT weldments of AA8011 and AA6061, (a) Sample No 7, (b) Sample No 11, EDS images of the weldments, (c) Sample No. 7, (d) Sample No.

11

Figure 58d, depicting the optimized-weld scenario (sample 11), displays a dense array of tiny, evenly distributed precipitates enveloping fine α -Al grains. The uniform, small-grained IMCs create a strengthening matrix without the detrimental effects of large inclusions. This morphology indicates a well-controlled thermal profile, conducive to mechanical robustness. Importantly, the transformation from coarse irregular grains (Figure 58a) to fine equiaxed grains (Figure 58b), tailored by adjusting welding parameters, directly influences the mechanical properties such as tensile strength, hardness, and ductility. Coarse grains and pores observed in lower-current welds promote crack initiation and premature failure. In contrast, equiaxed grains and refined precipitates lead to improved performance through mechanisms like Hall–Petch strengthening and reduced defect density.

However, it's noteworthy that excessively high current or WS—if not balanced—can cause rapid arc movement, prevent full fusion or promote thermal gradients that produce porosity, hot cracking, or oxidation at the weld interface. Such defects would manifest in oversized HAZ, compromised mechanical performance, or increased distortion. The presence of IMCs in grain boundaries, even under optimal conditions, must be monitored: while beneficial in moderation, their brittleness or volume fraction affects fatigue life and structural reliability. Figure 58c–d illustrates the EDS (Energy Dispersive Spectroscopy) analysis corresponding to the weld regions, offering detailed insight into the elemental distribution across different welded zones of the AA6061–AA8011 CMT joints. The EDS spectrum presented in Figure 58c identifies the chemical composition as 91.54 wt.% Al, 4.12 wt.% Si, 2.42 wt.% Fe, 0.95 wt.% Cu, 0.29 wt.% Zn, and 0.08 wt.% Mg. These values reflect a composition that largely aligns with the AA6061 base alloy, with minor dilution from AA8011. The elevated concentrations of Fe and Cu are notable and suggest the formation of coarse IMCs, as seen in the SEM image of Figure 58a. These coarse precipitates typically segregate at grain boundaries and can influence mechanical properties by serving as stress concentrators or crack initiation sites. Figure 58d demonstrates a slightly altered elemental distribution with 92.24 wt.% Al, 4.38 wt.% Si, 2.12 wt.% Fe, 0.72 wt.% Cu, 0.31 wt.% Zn, and 0.09 wt.% Mg. The subtle increase in aluminum content and the concurrent decrease in Fe and Cu concentrations suggest enhanced alloy mixing and more effective homogenization within the WFZ. This improved distribution is consistent with the refined microstructure observed in Figure 58b, produced at higher current levels. The increased Si content in both weld zones points toward the likely formation of Si-rich phases, known for contributing to greater hardness and wear resistance within the weld region. At an elevated current of 80 A, the WFZ exhibited a well-developed equiaxed and refined grain structure, while the Partially Melted Zone (PMZ) showed a noticeable reduction in its extent. This refinement is attributed to the influence of modulated current frequencies and intense pulse energy, which enable better control over the thermal cycles within the weld region. These controlled thermal profiles promote the breakdown of coarse dendrites and facilitate the formation of a more uniform microstructure, leading to enhanced mechanical behavior. The size variation of the PMZ on either side of the joint is governed by the thermal conductivity of the respective base metals. The PMZ on the AA6061 side is narrower compared to the AA8011 side, which results from the relatively lower thermal conductivity of AA6061. This causes faster heat dissipation and accelerated solidification, limiting grain coarsening and contributing to a smaller PMZ area. The detailed microstructural evaluation of sample 11 confirms the presence of a refined dendritic structure in the WFZ, accompanied by a uniform and evenly distributed arrangement of intermetallic phases. The homogeneous distribution of IMCs reinforces the joint's mechanical integrity, as these phases contribute to improved strength, durability, and wear performance. These findings are supported by the XRD analysis shown in Figure 59, which confirms the even dispersion of the filler material (ER4043) within the WFZ. The XRD data corroborates the presence of strengthening phases and validates the enhanced microstructural features observed through SEM and EDS. Collectively, this structural and compositional information provides a comprehensive

framework for optimizing input heat, managing thermal gradients, and enhancing joint efficiency in CMT welding of dissimilar Al-alloys [130].

4.8 XRD analysis

The XRD analysis was carried out using a BRUKER D8 ADVANCE diffractometer, employing CuK radiation with a wavelength of 1.518 Å to evaluate the phase composition of CMT-weldments fabricated using AA8011 and AA6061 alloys with ER4043 filler metal. The purpose of this analysis was to identify the various crystalline phases present in the weld region as influenced by different process parameters. The weldments were produced under four distinct parameter sets by specifically varying the WS and current, providing a comparative basis for examining how thermal cycles and solidification behavior affect phase formation. As illustrated in Figure 59, the XRD spectra revealed the dominant presence of aluminum phases, which is expected given the high aluminum content in both the base metals and the ER4043 filler.

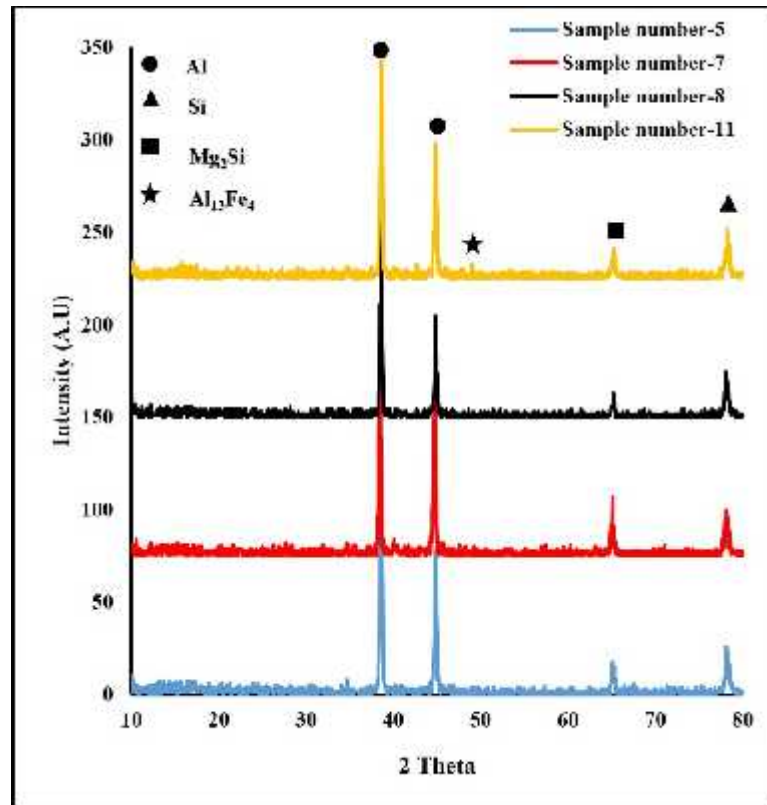


Figure 59: XRD peaks of the weldments

The diffraction pattern prominently displays sharp peaks corresponding to the face-centered cubic (FCC) lattice structure of aluminum. These are observed at 2θ values near 38.5° , 44.7° , 65.1° , and 78.2° , corresponding to the (111), (200), (220), and (311) crystallographic planes, respectively. These peaks were consistently intense across all welding conditions, confirming the stability and prevalence of crystalline aluminum in the weldments. In addition to the aluminum peaks, the spectra also

revealed minor but significant peaks in the 2θ range of approximately 28° – 29° , which are associated with the formation of Al–Fe IMCs. This phase typically results from the interaction between aluminum and iron impurities, which are either inherent in the base material or introduced during the welding process. Though not a dominant phase, the presence of Al–Fe suggests that localized thermal conditions during welding promoted its formation. The appearance of these IMCs is consistent with other microstructural observations indicating the presence of intergranular precipitates, particularly under high heat input conditions. The variation in phase intensities and peak positions across the different welding conditions indicates the sensitivity of phase formation to thermal input and cooling rates. The XRD findings align well with SEM and EDS results and confirm the heterogeneous but controlled phase distribution within the WFZ. These insights are crucial for understanding and optimizing the mechanical and metallurgical performance of dissimilar Al-alloy joints produced via CMT welding [131].

The XRD spectrum presented in Figure 59 highlights the dominant phases formed in the weldments produced from AA8011 and AA6061 alloys using ER4043 filler. Besides the strong aluminum (Al) peaks, only a limited number of secondary phases—specifically Si, Mg–Si, and Al–Fe—were observed. The absence of additional diffraction peaks suggests that these compounds were the most thermodynamically stable phases formed under the prevailing CMT welding conditions [132]. The graph reveals minor peaks corresponding to Mg–Si near $2\theta = 69^{\circ}$ and elemental Si around $2\theta = 75^{\circ}$, albeit with lower intensity. The formation of Mg–Si is expected in Al-based welds due to its role as a precipitation-strengthening phase, which is crucial in enhancing the mechanical performance of the joint. Its presence confirms the precipitation hardening mechanism that occurs during the post-solidification process. The detection of free Si is consistent with the use of ER4043 filler, which contains approximately 5% Si, contributing to the formation of Si-rich interdendritic regions during the solidification of the weld pool. These conditions lead to rapid cooling rates and thermal gradients, which are conducive to finer grain formation and improved structural uniformity. The pronounced aluminum peaks under these conditions suggest improved phase alignment and better metallurgical bonding within the weld region.

Overall, the XRD results affirm that controlled heat input and optimized process parameters favor the formation of stable phases and fine microstructures, improving the mechanical integrity of CMT weldments [132]. To identify the crystalline phases formed in the weld zone under varying process conditions, XRD analysis was conducted using a BRUKER D8 ADVANCE diffractometer. The instrument employed CuK α radiation with a wavelength of 1.518 Å, which is standard for aluminum-based alloys and provides high resolution for distinguishing overlapping peaks. XRD data was collected across a wide 2θ range to ensure comprehensive phase detection. By converting the diffraction angles to interplanar spacing (d-spacing) values, each material's unique crystal structure could be identified, allowing for accurate phase characterization.

The XRD patterns obtained from the CMT welded joints fabricated with ER4043 filler wire clearly confirmed the presence of Mg–Si phases, indicating successful metallurgical bonding and filler integration during the welding process. Additionally, other identifiable phases included elemental aluminum (Al), Si, and the IMC

Al-Fe. The consistent appearance of these four phases across all samples affirms their thermodynamic stability within the solidified weld metal. The absence of diffraction peaks corresponding to any other compounds further validates that no unexpected or unstable phases were formed during the welding process under the selected parameter range.

The intensities of Mg-Si and Al-Fe peaks decreased progressively with increasing welding current. This trend suggests that higher thermal energy promotes the breakdown of coarse eutectic structures, transforming them into finer, more uniformly dispersed phases. This phase refinement contributes to improved microstructural uniformity and may positively influence the mechanical properties of the welded joint. The penetration depth (δ) of the X-ray beam into the welded material was calculated using the relation $\delta = (\sin \theta \cdot \cos \alpha) / \mu$ [43], where θ represents the Bragg diffraction angle, α is the specimen tilt angle, and μ is the linear absorption coefficient. This penetration depth assessment aids in evaluating the depth-specific phase distribution within the weld and supports more accurate structural interpretation of the XRD results. The XRD analysis confirms that no adverse metallurgical reactions occurred between AA8011 and AA6061 during the CMT welding process. The absence of any undesirable phases signifies good metallurgical compatibility between the dissimilar base metals. Additionally, a noticeable decline in phase peak intensities, particularly of Mg-Si and Al-Fe, was observed with increasing welding current, suggesting a favorable transformation within the microstructure. This reduction reflects improved homogenization and refinement of intermetallic phases, which typically enhance weld quality and performance.

The welded region experienced significant thermal gradients, which contributed to an increase in tensile strength due to accelerated solid-state diffusion and localized phase transformations. The grain size had a limited influence on factors such as precipitate formation, dislocation density, and solid solution strengthening. Instead, precipitation behavior played a dominant role in defining the microstructure. Specifically, the formation, dissolution, coarsening, and nucleation of Mg-Si precipitates had a pronounced effect on the welded joint's structural characteristics. Furthermore, the hardness of the welded joint was largely governed by a combination of precipitate density, strain hardening, and grain boundary energy, all of which collectively contributed to the joint's mechanical integrity and resistance to deformation under applied loads.

The calculation of the nucleation rate can be expressed as: [44].

$$J = J_0 \exp \left(-\frac{Q_d}{RT} \right) \times \exp \left[-\left(\frac{E_0}{RT} \right)^3 \left(\frac{1}{\ln \bar{S}/S_e} \right)^2 \right] \quad (4.5)$$

Precipitate dissolution can be expressed as:

$$v = \frac{C_i D - \bar{S}}{C_i r - C_p} \quad (4.6)$$

C_i may be analyzed as [45].

$$C_i = S_e \exp\left(\frac{2V_m \gamma}{TRr}\right) \quad (3)$$

The hardening precipitates contribution to the yield strength (YS) may be written as:

$$\sigma_P = \frac{M}{b^2} \left(\frac{\sum_i F_i N_i}{\sum_i N_i} \right)^{3/2} (2b^2 G \beta)^{-1/2} \left(\frac{3f}{2\pi} \right)^{1/2} \quad (4.7)$$

$$F_i = 2b^2 G \beta \left(\frac{r_i}{r_c} \right) \quad (4.8)$$

When $r_c = r_i$ then $F_i = 2b^2 G \beta$

So, the YS can be written as

$$\sigma_{ss} = k_{Mg} C_{Mg}^{2/3} + k_{Si} C_{Si}^{2/3} + k_{Fe} C_{Fe}^{2/3} \quad (4.9)$$

J_0	$96.6 \times 10^{33} \text{ s/m}^3$
Q_d	129 kJ/mol
R	8.31 J/K/mol
S_e	Solute content in the AMC
C_p	Element's concentration
C_i	Solute's concentration
\bar{S}	Mean solute content in the AMC
f	Volume fraction
b	28.4×10^{-11}
M	3.1 (Taylor constant)
γ	0.2 (Interface energy of particle)
r_i	Radius of particle
β	0.37 (Dissolution constant)
G	$27.0 \times 10^{-11} \text{ N/m}^3$
D	Coefficient of diffusion
E_0	16.22 kJ/mol (Nucleation's energy barrier)
\bar{r}	Mean particle radius
V_m	$39.5 \times 10^{-6} \text{ m}^3/\text{mol}$
r	Radius of particles
r_c	Critical radius
N_i	Particle's density number
C_{Fe}	Scaling factor of Fe
C_{Si}	Scaling factor of Si
C_{Mg}	Scaling factor of Mg
k_{Si}	Concentration of Si
k_{Fe}	Concentration of Fe
k_{Mg}	Concentration of Mg
F_i	Particle radius' function

4.9 Tensile strength

Further some more CMT parameters were analyzed to check the adequacy of the welding results. The stress-strain behavior of the CMT weldments between AA8011 and AA6061 was evaluated in accordance with the ASTM E8 tensile testing standard, as shown in Figure 60. The experiments were conducted using a TINIUS OLSEN UTM H50KS machine, equipped with a load capacity of 50 kN, and operated at a crosshead speed of 1 mm/min. Test specimens were extracted in both transverse and longitudinal orientations to thoroughly assess the mechanical performance and integrity of the weldments. Among all the samples, CMT-P3 demonstrated the highest tensile strength, recording a value of 97.39 MPa.

Table 13: CMT welding parameters

Sample No.	Current (A)	Voltage (V)	Wire feed rate (m/min)	WS (mm/s)	GFR (L/min)	Heat input (kJ)
CMT-P1	50	14.5	4.6	5	15	46.64
CMT-P2	60	15	5.5	10		53.96
CMT-P3	70	15.5	5.8	15		60.57
CMT-P4	80	16.2	6.2	20		61.58

This performance is directly attributed to its optimized welding parameters, specifically a welding current of 70 A and a WS of 15 mm/s, resulting in a calculated heat input of 60.57 kJ. These settings facilitated ideal thermal cycles that contributed to a balanced and refined microstructure in the weld zone. The outstanding performance of CMT-P3 underscores the importance of careful process optimization, as the selection of welding parameters significantly influences the joint's strength and durability. Despite these positive outcomes, it is recognized that weldments typically exhibit lower tensile strength compared to the parent materials. This reduction in strength is often attributed to the formation of welding defects, such as porosity, slag inclusions, and incomplete fusion, which may originate from suboptimal shielding or filler interactions. The tensile strength variation observed across the samples correlates closely with the microstructural differences formed under different welding conditions. At the optimum parameters (70 A and 15 mm/s), the microstructure likely exhibits a homogeneous, fine-grained morphology in the WFZ. Such grain refinement enhances load-bearing capability, contributing to improved mechanical properties and increased reliability of the dissimilar aluminum weldment under tensile loading. At suboptimal welding conditions, specifically at a welding current of 50 A and a WS of 5 mm/s, the weld joint exhibited a compromised microstructure. Under these parameters, the WFZ is subjected to excessive heat input over a prolonged duration, resulting in the formation of coarser grains, dendritic structures, and non-uniform solidification patterns. Such microstructural irregularities negatively impact the weld's mechanical behavior, reducing both strength and joint integrity. The WS plays a crucial role in determining the thermal cycle experienced during the fusion process. When WS is too low, the heat input becomes excessive, promoting slower cooling rates, which facilitates grain growth and adversely affects phase distribution. These coarse and uneven grains can act as

stress concentrators, leading to premature failure under mechanical loading. Conversely, an optimal WS provides a balanced thermal input, allowing for adequate melting, solidification, and grain refinement, thereby enhancing the overall performance of the weld. The influence of welding parameters is quantitatively reflected in the joint efficiency values obtained from tensile testing. As presented in Table 14, the maximum joint efficiency of 80.12% was achieved at the optimized parameters of 70 A current and 15 mm/s WS, correlating with the refined grain structure observed in CMT-P3. In contrast, the lowest joint efficiency of 65.68% was recorded at the 50 A and 5 mm/s combination, directly linked to the coarse and thermally affected microstructure in that weldment.

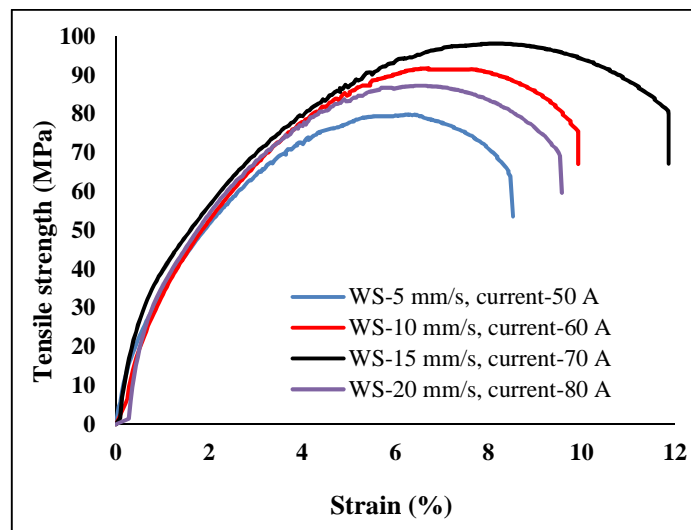


Figure 60: Stress-strain diagram of CMT welded joint

Table 14: Mechanical Properties of the CMT welded joint of AA8011 and AA6061

Materials/Joints	UTS (MPa)	Strain (%)	Average Grain size (μm)	Hardness (HV)	Joint efficiency (%)
AA8011	112.36	8.96	125.48	38 \pm 3	-
AA6061	324.56	16.23	86.67	98 \pm 2	-
CMT-P1	79.84	8.52	36.54	78 \pm 2	65.68
CMT-P2	92.87	9.92	27.29	75 \pm 3	76.39
CMT-P3	97.39	11.86	9.36	69 \pm 2	80.12
CMT-P4	88.29	9.56	12.35	67 \pm 4	72.63

These findings clearly emphasize the importance of precise control over WS and current. Deviations from optimal conditions result in microstructural degradation and reduced mechanical properties, reaffirming the necessity for well-defined and carefully monitored process parameters in the welding of dissimilar Al-alloys.

4.10 Hardness evaluation

The hardness distribution profile across the CMT welded joint between AA8011 and AA6061 was evaluated for different sets of welding parameters, as illustrated in Figure 61. This distribution provides a clear depiction of the non-uniform grain structure and mechanical response throughout the welded regions, especially across the FZ, HAZ, and partially melted zone (PMZ). The variation in hardness is a direct consequence of several interdependent factors such as grain size, particle density, strain rate, and thermal gradients induced during the welding process. One of the most consistent observations across all samples is that the lowest hardness values are recorded in the HAZ. This reduction in hardness is attributed to the metallurgical mixing of the base metals with the ER4043 filler wire, which alters the composition and precipitate stability in the HAZ. Additionally, in this zone, partial dissolution of strengthening phases like Mg₂Si and Al₃Fe occurs, resulting in weakened solid solution strengthening and reduced resistance to indentation. These changes are particularly evident in samples processed under low current conditions, where insufficient thermal input causes incomplete phase formation and localized softening. Although the overall hardness profiles follow a similar distribution pattern—decreasing in the HAZ and rising toward the FZ and PMZ—distinct variations in absolute hardness values are observed depending on the applied current and WS. In the PMZ, variations arise due to inconsistent material flow and localized overheating, which are triggered by changes in welding current, contributing to grain coarsening and non-uniform hardness distribution. Such changes in microstructure create zones with uneven mechanical strength, making them more susceptible to failure under applied stress. In contrast, the CMT-P3 sample, welded with optimized parameters of 70 A current and 15 mm/s WS, demonstrated a finer grain structure and more uniform hardness profile. The enhanced hardness is largely a result of a controlled thermal cycle that promotes rapid solidification and refines the grain structure. This is in agreement with the Hall–Petch relationship, which states that finer grains exhibit higher hardness due to increased grain boundary area acting as barriers to dislocation motion. The reduced temperature in these conditions enhances strain hardening, resulting in improved microstructural stability and higher hardness levels in the FZ.

In the case of CMT-P1, which was welded using lower current and speed, the average hardness in the WFZ exceeded 78 HV, which, at first glance, may appear superior. However, this increased hardness can be misleading. It arises from the formation of coarse and brittle IMCs such as Al₃Fe and Mg₂Si, which, despite their inherent hardness, do not contribute positively to overall joint toughness or ductility. In fact, these phases act as stress risers, increasing the likelihood of crack initiation and propagation under tensile loading. The fluctuation in hardness in these weldments is significant due to the heterogeneous distribution of these IMCs and the weak α -Al matrix that surrounds them. Since α -Al is softer but occupies a large volume fraction, the hardness recorded by the hardness indenter varies substantially depending on whether the tip contacts a hard intermetallic phase or the softer aluminum matrix. Interestingly, although the average hardness in the FZ of CMT-P3 remained below 70 HV, the tensile properties of this joint outperformed others. This outcome emphasizes that mechanical performance is not solely dependent on peak

hardness values but also on the uniformity of phase distribution, grain refinement, and residual stress reduction. In the PMZ, increased hardness is a result of grain coarsening and partial dissolution of hardening precipitates, which leads to a harder but more brittle microstructure. The HAZ, characterized by a sharp grain size gradient and high residual stress, is particularly vulnerable to crack formation and premature failure.

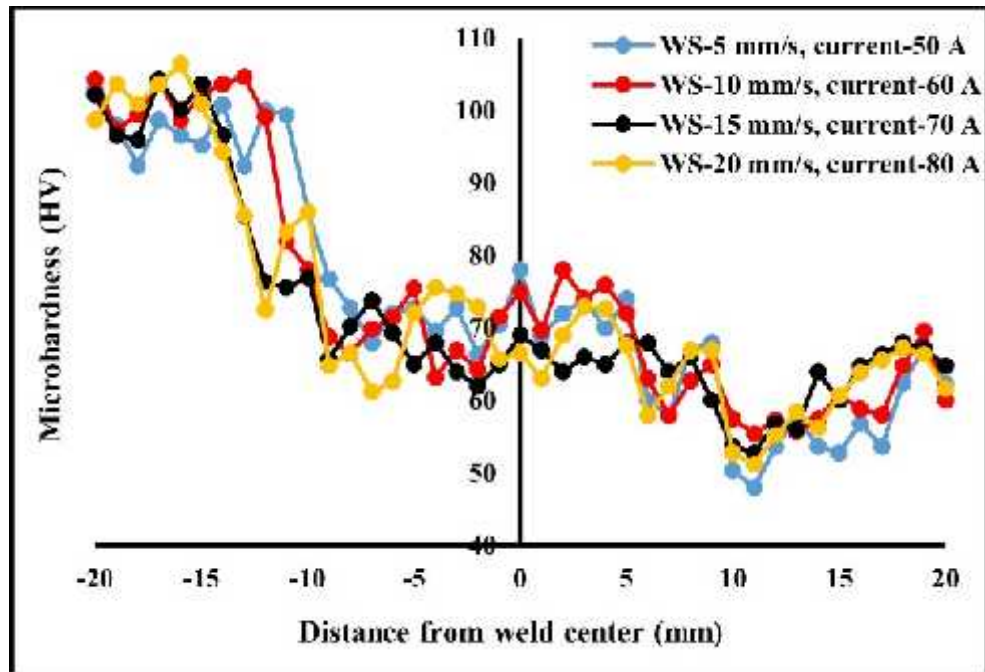


Figure 61: Variation of microstructure of the welded joint from the weld centre

The precipitate dissolution occurring in this region weakens the joint further, especially under cyclic loading conditions. These microstructural inconsistencies create zones of high-stress concentration, which often become the initiation sites for fracture during mechanical testing. As a result, most fracture failures in welded samples are observed to initiate within or near the HAZ. The combination of thermal degradation, microstructural heterogeneity, and distortion significantly reduces the structural integrity in this region. The comparative analysis of the various samples indicates that optimal heat input, as used in CMT-P3, results in a better balance between hardness, strength, and ductility. This balance is essential for industrial applications, where both high mechanical performance and weld reliability are critical. By controlling the welding current and speed, and thus the heat input, it is possible to achieve a uniform grain structure, stable phase dispersion, and consistent hardness, ultimately enhancing the overall performance of the welded joint. When dissimilar Al-alloys AA8011 and AA6061 are joined using the CMT fusion welding technique with an external filler wire of ER4043, the resulting weldment exhibits a complex and heterogeneous microstructure. This heterogeneity is primarily driven by the varied thermal conductivities, melting ranges, and solidification behaviors of the two base metals and the filler material. As the molten pool cools and solidifies, it generates distinct metallurgical zones, each exhibiting unique grain structures and phase compositions. Figure 62 offers a comprehensive visual representation of the

key microstructural zones in the CMT welded joint, specifically highlighting the Parent Metal Zone (PMZ), FZ, and HAZ, thereby facilitating a deeper understanding of the transformations occurring during the welding process. The PMZ is located adjacent to the weld WFZ, extending toward the base metals. This transition region reflects the influence of weld heat without undergoing complete melting. On the AA6061 side, the PMZ is distinctly marked by columnar grain growth, which is directionally aligned with the heat flow during solidification. The thermal gradient in this region promotes directional solidification, resulting in long, aligned columnar grains. In certain sections of the AA6061-PMZ, incipient grain boundary melting is also observed. This behavior is attributed to AA6061's relatively broader freezing range and high sensitivity to heat during welding. Due to its precipitation-hardened nature and rich content of alloying elements such as Mg and Si, the thermal exposure initiates localized partial melting, especially at the grain boundaries [32, 33].

Conversely, on the AA8011 side of the PMZ, the microstructural evolution follows a different trajectory. AA8011, being a non-heat-treatable alloy with a distinct chemical composition, experiences surface grain heating rather than boundary melting. Here, the semi-solid regions of the grains facilitate the nucleation of non-spontaneous grains. These nuclei adhere to the heated grain boundaries and grow in a columnar manner toward the weld centerline. This results in an alternating crystallization pattern, which is indicative of the differing thermal gradients and undercooling phenomena that exist across the weld pool during solidification. The grain growth directionality and alignment toward the weld center in this zone highlight the material's adaptive response to the imposed thermal cycle [34]. Moving outward from the PMZ, the HAZ lies between the PMZ and the unaffected base metal. This region is not subjected to full melting but does undergo significant thermal exposure during welding. The temperatures experienced in the HAZ remain below the melting point of both AA8011 and AA6061. However, they are sufficient to cause grain coarsening, phase dissolution, and recrystallization, depending on the alloy and the local heat input. As shown in Figure 62, the HAZ exhibits a coarse-grained microstructure, mirroring the base alloy morphology but modified by the heat cycle. This coarsening is especially prominent in AA6061, where exposure to elevated temperatures can cause the dissolution of strengthening precipitates and the growth of primary grains. The grain structure in this zone largely resembles that of the corresponding base metals, emphasizing the dominant role of thermal conduction and alloy chemistry in microstructural evolution [35]. The central Weld WFZ or Weld Fusion Center (WFZ) represents the area of complete melting and subsequent solidification. This region integrates molten material from both base metals and the filler metal ER4043. The resulting solidified matrix is a mixture of the contributing elements, leading to the formation of IMCs and various eutectic phases. An Energy Dispersive X-ray Spectroscopy (EDS) analysis conducted in Figure 62b confirms the presence of primary alloying elements such as Al, Si, Fe, Mg, and Cu. These elements are involved in the formation of complex intermetallic phases, most notably Mg_2Si and Al_3Fe , which are commonly found in aluminum fusion welds incorporating ER4043 filler. The presence and uniform dispersion of these IMCs in the FZ is a strong indication of the effective distribution and compatibility of ER4043 within the weld metal. Due to its high Si content, ER4043 improves the fluidity of the weld pool and lowers the melting point, facilitating better mixing with

the molten base metals. Moreover, its chemical compatibility with both AA8011 and AA6061 contributes to the homogeneous microstructure and minimizes the likelihood of defect formation such as hot cracks or incomplete fusion. This compatibility plays a pivotal role in enhancing the weld joint's mechanical integrity and corrosion resistance, which is crucial for applications demanding structural durability.

The CMT process's ability to control heat input with precision further supports the uniform morphology and consistent grain refinement across the weldment. The low spatter, minimal distortion, and controlled arc behavior inherent to CMT ensure that even when dissimilar Al-alloys are joined, the metallurgical transitions are gradual rather than abrupt, reducing the risk of residual stresses and premature failure.

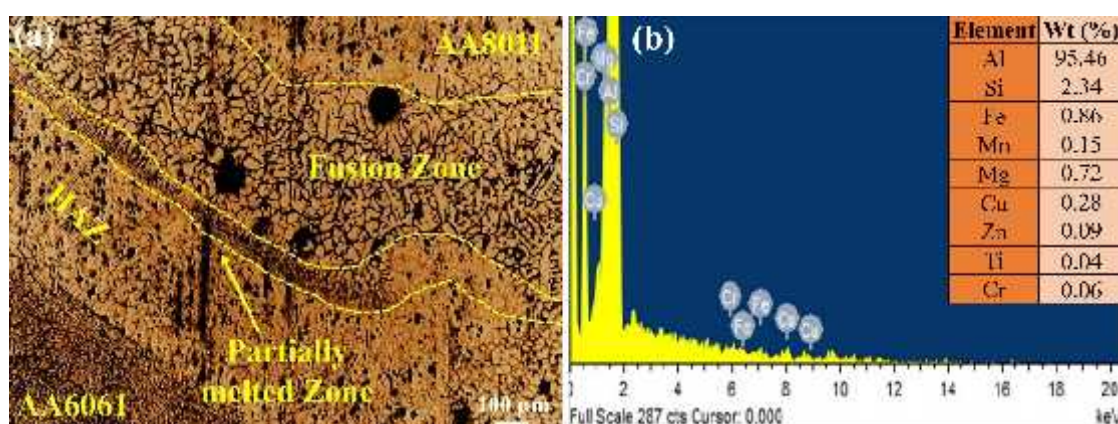


Figure 62: Different zone of CMT weldments of AA8011 and AA6061 with filler ER4043

The detailed microstructural examination of the WFZ at different WS (WS) is presented in Figure 63, which clearly illustrates the formation of grain boundaries, densely packed grains, and precipitates across the FZ. This microstructural evolution is primarily influenced by the low heat inputs utilized during the welding process. Reduced heat input limits the overall thermal energy delivered to the weldment, thereby decreasing the size of the molten weld pool and significantly constraining the extent of the HAZ. As a direct consequence, the molten pool undergoes rapid solidification, which promotes fine grain structures within the FZ and restricts excessive grain coarsening.

However, this rapid cooling also shortens the available time for the escape of gases such as oxygen and hydrogen, which tend to dissolve into the molten metal during welding. Due to the accelerated solidification rate, these gases become entrapped within the weld pool, leading to the formation of micro-voids or porosity within the solidified WFZ. Such voids compromise the metallurgical continuity and mechanical strength of the weld, reducing its overall structural integrity. One of the key contributors to the presence of hydrogen and oxygen is moisture, which can originate from multiple sources, including the filler wire, surrounding atmosphere, electrodes, and the surface of the base alloys themselves [36]. These moisture sources release gases during the high-temperature welding process, further increasing the risk of gas entrapment and pore formation.

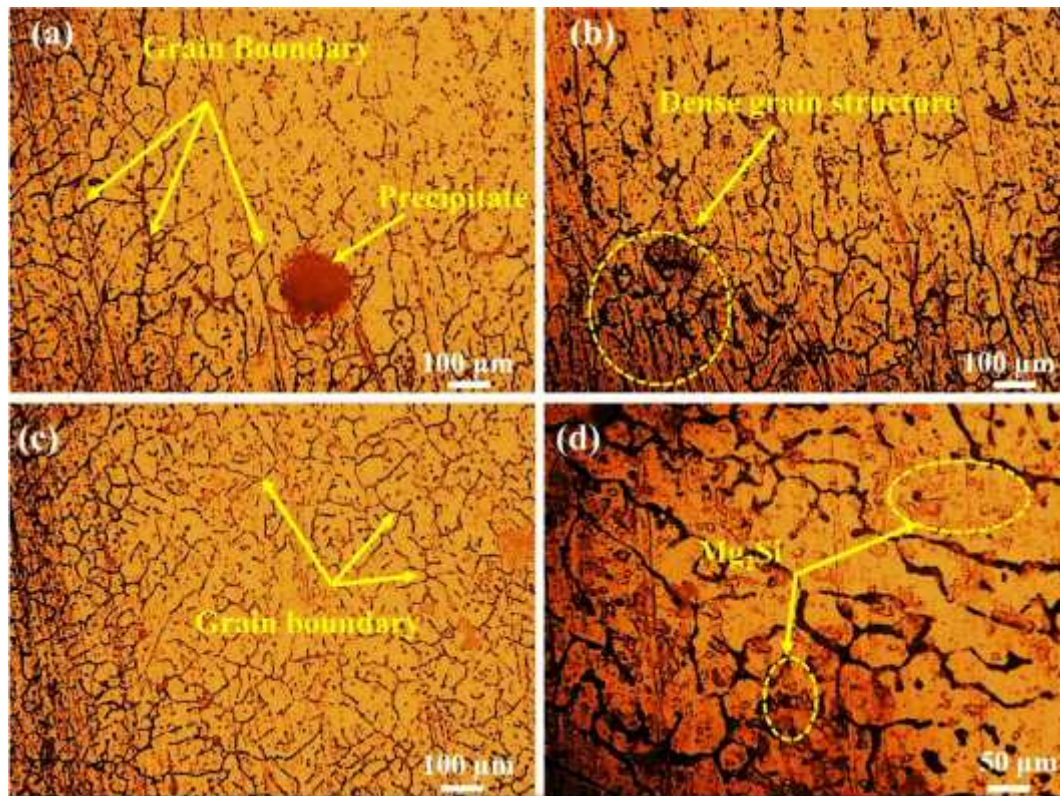


Figure 63: Optical microstructure of the CMT welded joint of AA8011 and AA6061 at the WFZ, (a) WS-5mm/s, current 50 A, (b) WS-10mm/s, current 60 A, (c) WS-15 mm/s, current 70 A, (d) WS- 20 mm/s, current 80 A

The interaction between thermal dynamics, moisture-induced gas generation, and rapid cooling rates adds complexity to the welding operation, especially in dissimilar Al-alloy joints. The heterogeneous microstructure observed across different regions of the welded joint highlights the importance of understanding thermal gradients, cooling behavior, and material compatibility in fusion welding. These observations emphasize the challenges involved in achieving high-integrity welds, particularly when dealing with dissimilar alloys and varying process parameters, reinforcing the necessity for controlled thermal input and optimized welding conditions to minimize defects and enhance weld performance. The detailed optical and scanning electron micrographs presented in Figure 63 provide insight into the microstructural characteristics of the WFZ for various CMT welding parameters, specifically CMT-P1, CMT-P2, CMT-P3, and CMT-P4. Among these, the sample designated as CMT-P3, which was processed at a WS of 15 mm/s and a welding current of 70 A, displayed a significantly fine and equiaxed grain structure. This refined microstructure is primarily attributed to the synergistic effect of high current and elevated WS, which collectively contribute to rapid solidification. The result is an improved grain morphology that plays a critical role in enhancing mechanical properties, such as tensile strength and hardness, while simultaneously reducing the likelihood of defects like porosity and cracking.

The optimized parameters in CMT-P3 foster favorable thermal gradients and undercooling conditions, encouraging uniform grain nucleation and growth. This refinement not only improves the mechanical performance but also enhances the

visual appearance and weld bead quality, reducing surface irregularities and discontinuities. The precise control over heat input and solidification rate inherent to the CMT process provides a major advantage in welding dissimilar Al-alloys like AA8011 and AA6061, where managing thermal stress and metallurgical compatibility is crucial. Further analysis using high-magnification Scanning Electron Microscopy (SEM), as depicted in Figure 64, reveals detailed features of the microstructure at the WFZ under varying process parameters. The SEM images indicate the presence of precipitated Mg Si phases and globular α -Al particles, particularly located along the grain boundaries. These microstructural features are typical of aluminum-Si weldments, especially when ER4043 (a Si-rich filler) is used. The high thermal input during certain welding conditions promotes grain growth, yielding an average grain size of 19.52 μm in the WFZ and 24.85 μm in the HAZ—both of which are notably finer than the coarse grains present in the parent metals, AA8011 and AA6061. Within the WFZ, the microstructure comprises dispersed Mg Si eutectic precipitates embedded in a primary α -Al matrix. The fine α -Al particles, situated along the grain boundaries, contribute to the weld's mechanical strength and resistance to cracking. In contrast, the HAZ exhibits a coarser microstructure with sparser α -Al particle precipitation, primarily due to the exposure to prolonged thermal cycles during welding. This transformation indicates that the HAZ undergoes microstructural coarsening, resulting in altered mechanical behavior compared to the base metals. A notable observation across the WFZ is the presence of microspores of varying sizes, which are attributed to insufficient shielding gas coverage, especially on the rear (bottom) surface of the weld. In the CMT process, while the top surface of the weld pool is adequately protected by shielding gas (argon), the bottom surface remains partially exposed to atmospheric conditions. This exposure leads to the ingress of air through gaps between the plates, introducing oxygen and moisture into the weld pool. The moderate cooling rate of the CMT process is insufficient for the complete expulsion of hydrogen, which subsequently gets trapped during solidification. The entrapped hydrogen leads to the formation of porosity and even microfractures surrounding these voids, ultimately compromising the weld joint's structural integrity [37].

As the welding current and speed are varied, a clear evolution in microstructure is observed. An increase in current, particularly at 72 A, results in reduction of dendritic structures in the base metal. This indicates that higher heat input during CMT welding leads to enhanced dispersion and improved mixing of materials across the weld pool. One of the most important outcomes of this condition is the reduction in the area fraction of eutectic Mg Si precipitates, which are known to embrittle the weld. The combination of higher WS and appropriate heat input facilitates better particle dispersion, leading to a larger fraction of refined, equiaxed grains revealed in Figure 63 and Figure 64. However, excessively high welding parameters may reverse these beneficial effects. At a very high current of 80 A combined with a WS of 20 mm/s, the rapid traversal of the welding torch limits the time available for the molten pool to solidify adequately. This insufficient cooling time causes incomplete solidification, leading to weld defects such as increased porosity, micro-cracks, and even hot tearing. Additionally, the larger heat input under these extreme conditions expands the HAZ, altering the microstructure and mechanical properties of the region adjacent to the weld. The resulting thermal stresses and residual deformation

may deteriorate the structural performance of the joint, especially under cyclic loading conditions or in corrosive environments.

These findings collectively underline the significance of optimizing welding parameters to achieve a balance between heat input and solidification time. The results suggest that moderate current (around 70–72 A) coupled with optimized WS (around 15 mm/s) ensures favorable microstructural evolution, enhanced mechanical properties, and minimal weld defects. On the contrary, extreme parameters increase the likelihood of instability and defects, highlighting the importance of precision in process parameter selection for achieving high-integrity dissimilar Al-alloy welds using the CMT process.

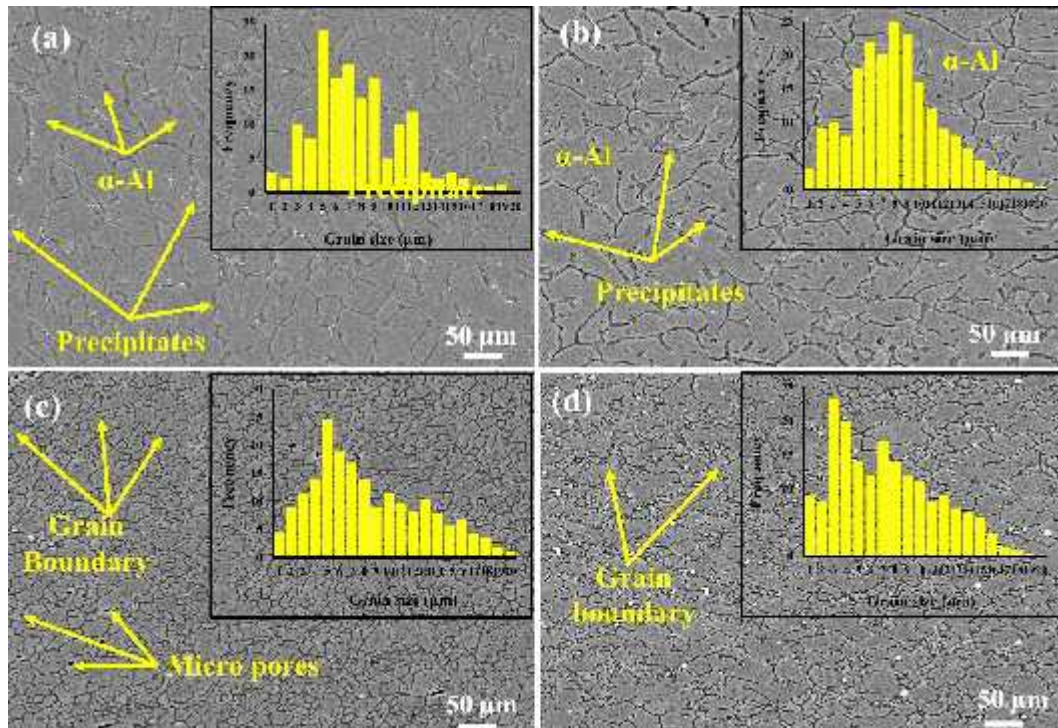


Figure 64: High magnification SEM images of CMT welded joint at the WFZ, (a) CMT-P1, (b) CMT-P2, (c) CMT-P3, (d) CMT-P4

A refined grain structure was distinctly observed in the WFZ of the CMT-P3 sample, particularly when subjected to higher welding currents. The enhanced current not only facilitated greater heat input but also promoted the breakdown of coarse dendritic structures into finer and more equiaxed grains. This grain refinement is directly influenced by the controlled thermal cycles induced through intense pulse currents and precise frequency modulation, which disrupt the dendritic growth pattern typically seen in lower heat input conditions. The process effectively enables a more homogeneous solidification front and encourages the development of a compact and uniform microstructure within the WFZ [39].

A notable reduction in the partially melted zone (PMZ) was also observed under these high current conditions. The PMZ area in the CMT-P3 sample was significantly smaller compared to that in samples welded with lower current inputs. Interestingly, the extent of the PMZ on the AA8011 side was less than that on the

AA6061 side. This difference in PMZ size is primarily attributed to the higher thermal conductivity of AA8011, which accelerates the dissipation of heat, promoting faster cooling and solidification. As a result, the grain growth is curtailed, leading to a smaller affected area near the AA8011 interface [40]. The overall microstructural assessment of the CMT-P3 welded joint reveals several beneficial characteristics: a finer dendritic pattern in the WFZ, a reduced PMZ width, and a uniform distribution of IMCs. These improvements contribute directly to the structural soundness and mechanical strength of the joint. The presence and even dispersion of filler elements were confirmed through spot XRD, which detected the presence of secondary phases within the WFZ. The proper integration of filler material throughout the joint plays a critical role in minimizing localized weaknesses and enhancing load-bearing capacity. Thus, the combination of optimized welding parameters and refined microstructure provides valuable guidance for the fabrication of high-integrity dissimilar Al-alloy joints [41].

4.11 TEM analysis of welded joint

Figure 65 presents a comprehensive Transmission Electron Microscopy (TEM) microstructural analysis, offering critical insights into the morphology, distribution, and behavior of precipitates and dislocations in the HAZ and WFZ of the CMT welded joint between AA8011 and AA6061. The high-resolution imaging distinctly reveals microstructural variations between the two zones, each shaped by different thermal and mechanical histories during welding. In the HAZ, precipitates are observed to be coarse and continuously aligned along grain boundaries. These are predominantly identified as Mg Si particles, which are a common strengthening phase in heat-treatable Al-alloys. The continuous nature of these precipitates is indicative of slower cooling rates and extended thermal exposure in this region, facilitating their coarsening and alignment along grain boundaries. The formation and stability of these coarse particles significantly influence mechanical properties, especially fracture toughness, as they can act as stress concentrators under loading conditions.

The Partially Melted Zone (PMZ), situated between the FZ and the base metal, displays a distinct microstructural character. Here, grain boundary precipitates are smaller in size, sparsely distributed, and often associated with dislocation networks. This combination of fine precipitates and dislocation interaction indicates that the PMZ underwent localized melting followed by rapid solidification, promoting fine-scale precipitation and recrystallization-induced strain accommodation.

In contrast, the WFZ exhibits a more uniform dispersion of precipitates within the matrix, with a significantly greater density of these particles compared to the HAZ. This finer and more consistent distribution results from the rapid solidification that occurs in the FZ, which promotes homogeneous nucleation and inhibits excessive coarsening. The uniform dispersion of precipitates enhances the weld's strength and stability by impeding dislocation motion and promoting load transfer. A notable microstructural feature is the spacing between precipitates. In the HAZ, the inter-precipitate spacing is considerably larger than in the FZ. This difference in spacing serves as a microstructural indicator of the distinct thermal cycles experienced by each zone. The wider spacing in the HAZ is associated with slower cooling and

longer exposure to elevated temperatures, allowing precipitates to grow and coarsen. Conversely, the narrow spacing in the FZ suggests rapid cooling, which limits precipitate growth and favors fine, densely packed structures. This contrast underscores the impact of recrystallization in the HAZ, which is responsible for the formation of new, strain-free grains and the redistribution of precipitates. An important metallurgical aspect identified through TEM is the thermal sensitivity of Mg Si precipitates. Their dissolution behavior is particularly critical in understanding the material's response to welding heat input. It was observed that all Mg Si precipitates completely dissolve when the material is exposed to temperatures around 410 °C. Furthermore, heating beyond 445 °C—which remains below the solid solution temperature of Mg Si (505 °C)—also leads to significant dissolution [42]. This dissolution at sub-solid-solution temperatures indicates a highly temperature-sensitive response of Mg Si, reinforcing the importance of precise thermal control during welding. The dynamic behavior of these precipitates across different temperature thresholds reveals how easily their stability can be disrupted, further affecting the overall strength and integrity of the weld.

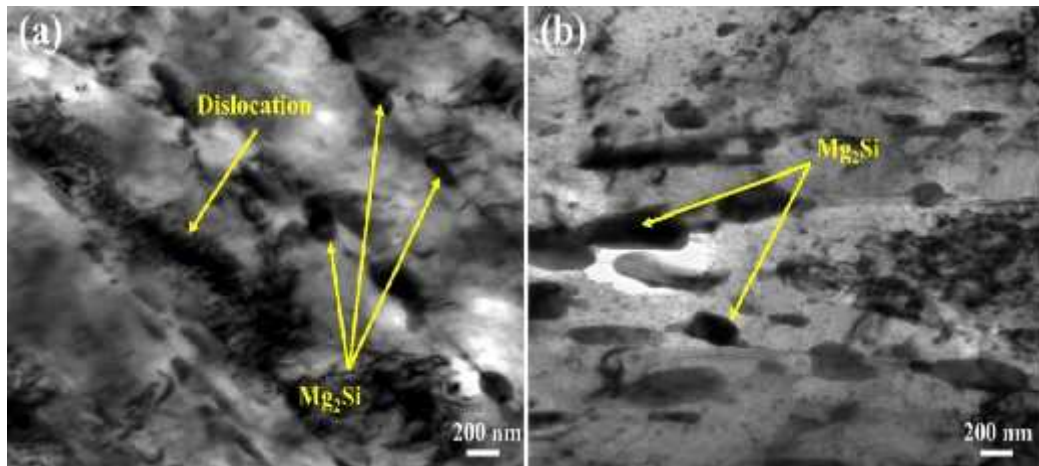


Figure 65: High magnification TEM images of CMT welded joint of AA8011 and AA6061, (a) FZ, (b) HAZ

4.12 Fractography analysis

Figure 66a presents the SEM fractograph of the fractured surface of specimen 5 from the CMT welded joint between AA8011 and AA6061, offering critical insights into the failure behavior under tensile loading. This specimen, fabricated using a lower welding current of 60 A, a WS of 6 mm/s, and a shielding GFR of 16 l/min, exhibited a relatively low UTS of 72.69 MPa and a joint efficiency of 58.28%. The SEM image clearly displays a surface populated with numerous dimples interspersed with large voids, indicating a predominantly ductile fracture mode. However, the presence of these large and irregular voids reveals evidence of incomplete fusion, gas porosity, and weak interfacial bonding, most likely caused by insufficient heat input during the welding process. These microstructural imperfections serve as stress concentration sites, accelerating void nucleation and coalescence during mechanical loading, thereby contributing to premature failure of the joint. Although the observed dimples suggest a certain degree of plastic deformation and toughness, the significant

voids highlight the non-uniform energy distribution and inadequate metallurgical bonding in the weldment. These imperfections align with the moderate hardness value of 75.46 HV and a residual stress of -21 MPa, both of which indicate a lack of effective strengthening mechanisms and limited internal stress accommodation.

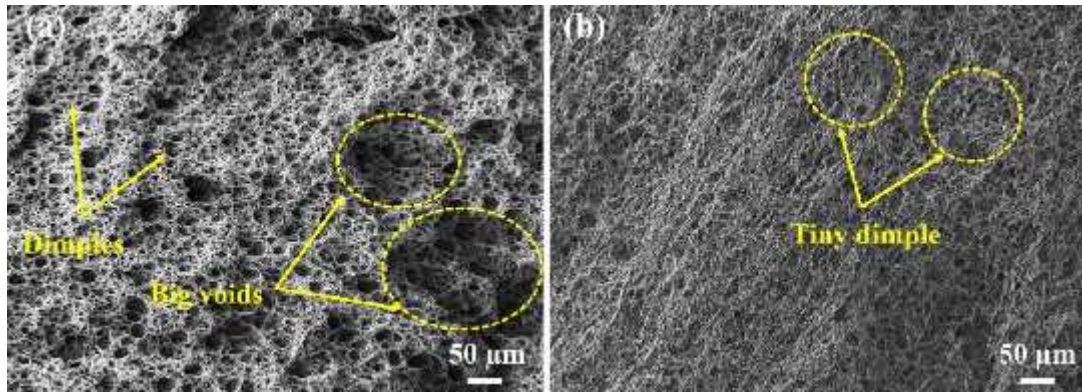


Figure 66: SEM images of fractured surface, (a) specimen number 5, (b) Specimen number 11

Figure 66b presents the SEM image of the fractured surface of specimen 11 from the CMT welded joint of AA8011 and AA6061, showcasing its superior mechanical integrity under tensile stress. This specimen was fabricated using optimized welding parameters, specifically a high current of 80 A, a WS of 10 mm/s, and a moderate GFR of 14 l/min. These optimized conditions yielded exceptional mechanical properties, including a UTS of 108.74 MPa, a joint efficiency of 87.19%, and a strain value of 11.23%, marking it as one of the highest-performing specimens in the study. The SEM fractograph exhibits a dense distribution of fine dimples across the fracture surface. These tiny, uniformly spaced dimples are indicative of a refined ductile fracture, suggesting that plastic deformation occurred consistently throughout the joint before failure. The refined dimple morphology implies a homogeneous microstructure and effective metallurgical bonding between the dissimilar Al-alloys, likely attributed to the optimized heat input and controlled solidification. This interpretation aligns with the high strain value, which reflects enhanced ductility, and the measured hardness of 74.69 HV, confirming a balanced thermal cycle that prevented excessive grain coarsening or phase transformation. Moreover, the compressive residual stress of -65 MPa recorded for this sample suggests a favorable stress distribution that likely helped delay crack initiation and propagation during mechanical loading, thereby improving the overall fracture resistance. In conclusion, specimen 11, as shown in Figure 66b, demonstrates that carefully controlled welding parameters result in a uniform fracture surface, improved mechanical strength, and greater structural reliability of the CMT welded joint.

4.13 Damping behavior of CMT welded joints of AA 8011 and AA6061

Figure 67 presents the time-domain acceleration response curves for four different CMT welded joints—(a) CMT-P1, (b) CMT-P2, (c) CMT-P3, and (d) CMT-P4—corresponding to transient dynamic excitation. These graphs illustrate how the acceleration amplitude decays over time, indicating the damping behavior and

dynamic stability of each welded joint formed between dissimilar aluminum alloys AA8011 and AA6061. The transient acceleration response is directly influenced by the mechanical integrity, microstructural homogeneity, and stiffness of the welded joint, which in turn are functions of the thermal cycle and grain structure developed during the welding process. Figure 67a, representing the CMT-P1 joint, exhibits a relatively prolonged and irregular decay in acceleration amplitude, suggesting lower damping capacity and higher vibrational response. This behavior is consistent with its mechanical data from Table 14, where CMT-P1 has the lowest ultimate tensile strength (UTS) of 79.84 MPa, a moderate strain of 8.52%, and the largest grain size among the welded samples (36.54 μm). The higher grain size and lower hardness (78 HV) point to reduced strength and increased susceptibility to vibrational excitation, reflected in its lower joint efficiency of 65.68%.

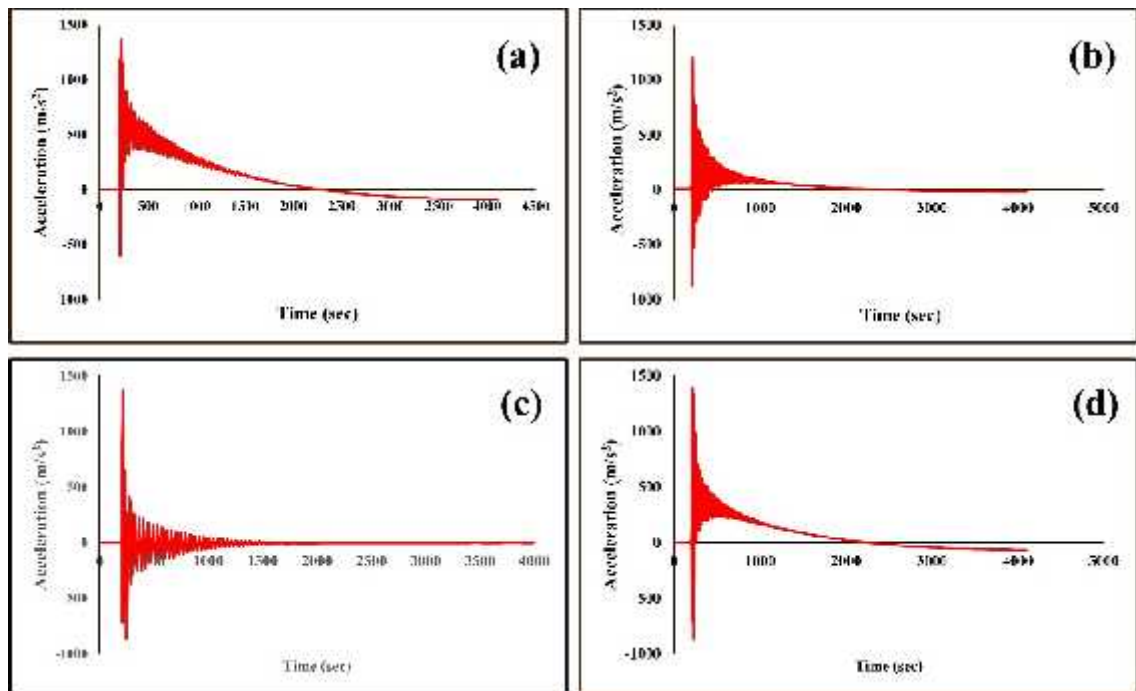


Figure 67: Time-Domain Acceleration Response of CMT Welded Joints (a) CMT-P1, (b) CMT-P2, (c) CMT-P3, and (d) CMT-P4 for AA6061–AA8011 Dissimilar Welds

Figure 67b, corresponding to CMT-P2, shows a comparatively faster decay in acceleration, with a higher initial amplitude followed by a smoother reduction. This indicates improved damping behavior and mechanical resilience. Table 14 confirms this through an improved UTS of 92.87 MPa and a finer average grain size of 27.29 μm . The joint efficiency of 76.39% indicates enhanced weld quality relative to CMT-P1, and the hardness value remains relatively stable at 75 HV. The improved microstructure supports better vibrational resistance and stiffness, consistent with the smoother decay in its acceleration response. Figure 67c, representing CMT-P3, shows the most rapid attenuation of vibrational amplitude, indicating superior damping capability and the most stable dynamic behavior among all four joints. According to Table 14, CMT-P3 achieves the highest UTS of 97.39 MPa and the maximum strain of 11.86%, indicating excellent ductility and tensile strength. Most

notably, it possesses the finest grain structure ($9.36\ \mu\text{m}$) and a relatively high hardness of 69 HV. These properties contribute to increased internal friction and energy dissipation, making CMT-P3 the most mechanically optimized and dynamically stable weld joint with the highest joint efficiency of 80.12%. Figure 67d, associated with CMT-P4, shows intermediate vibrational damping behavior, falling between the responses of CMT-P2 and CMT-P3. The acceleration curve is broader than that of CMT-P3, but more stable than P1. As per Table 14, CMT-P4 has a UTS of 88.29 MPa, strain of 9.56%, and a moderately fine grain size of $12.35\ \mu\text{m}$. The hardness value of 67 HV and joint efficiency of 72.63% support the observed acceleration profile, indicating a moderately strong joint with decent vibrational resistance.

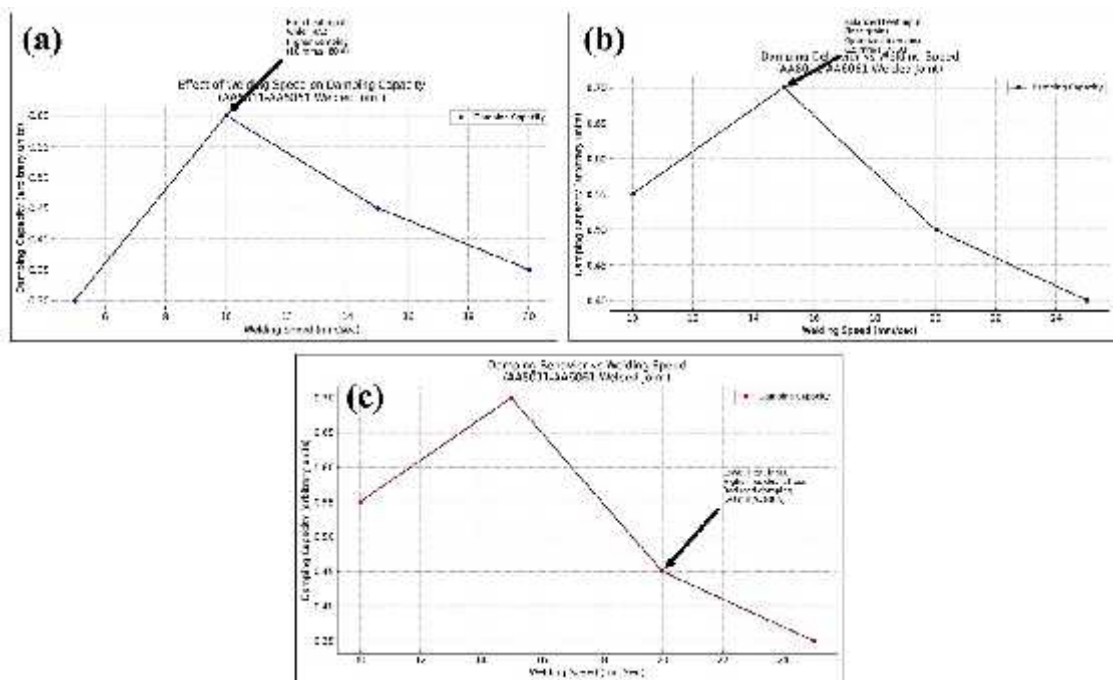


Figure 68: Damping behaviour of the CMT welded joints, (a) 10 mm/sec and 60 A, (b) 15 mm/sec and 70 A, (c) 20 mm/sec and 80 A,

Figure 68 illustrates the variation in damping behavior of CMT welded joints at different welding speeds and current levels. The subfigures—(a), (b), and (c)—depict the influence of process parameters on damping capacity. In Figure 68(a), corresponding to a welding speed of 10 mm/sec and a current of 60 A, the damping capacity shows a significant increase, peaking around 0.62 arbitrary units. This higher damping is attributed to increased heat input, which leads to wider heat-affected zones, reduced residual stresses, and the formation of coarser grains—factors that generally enhance the energy dissipation capacity of the material under cyclic loading.

Figure 68(b) presents the behavior at a welding speed of 15 mm/sec and 70 A current. The damping capacity reaches a maximum value of approximately 0.70, indicating optimal welding conditions. Here, the heat input is balanced, resulting in refined microstructure and reduced porosity, which collectively improve damping characteristics while maintaining mechanical integrity. Figure 68(c), with a 20

mm/sec speed and 80 A current, exhibits a decline in damping capacity to below 0.45. This reduction is associated with a lower heat input due to faster welding, leading to higher residual stresses, insufficient grain refinement, and narrower heat-affected zones. These conditions hinder the microstructural capacity to dissipate vibrational energy, thereby degrading the damping performance.

CHAPTER-5

Conclusions

The fabrication of AA6061 and AA8011 successfully fabricated through cold metal transfer welding process. This study focuses on optimizing the input parameters and evaluating the output responses of AA8011 and AA6061 alloy joints fabricated using the CMT welding process, and found the following conclusions.

- The input parameters, were found to have significant effects on the output responses, as evidenced by their P-values being below 0.05. The F-values for UTS, % strain, hardness value at WFZ, and residual stress were 21.96, 15.32, 18.13, and 16.81 respectively, indicating the significance of all three models.
- The microstructure in the WFZ consists of precipitates Mg_2Si and globular primary $-Al$, with $-Al$ -particles aligned along the grain boundaries. The HAZ, which undergoes a more intense thermal cycle, exhibits fewer $-Al$ particles and less precipitation, distinguishing it from the base metal's structure.
- The maximum UTS of 108.74 MPa was recorded for sample number 11, while the minimum UTS of 72.69 MPa observed for sample number 5. Enhanced hardness and UTS in the welded zone were attributed to the occurrence of a refined grain structure and fine secondary phases in the WFZ.
- The maximum compressive residual stress (-65 MPa) was observed at the welding current of 80-amp, WS of 10 mm/s, and GFR of 14 l/min, while the minimum residual stress (-9 MPa) was observed at the welding current of 60-amp, WS of 10 mm/s, with GFR of 18 l/min.
- The optimized input parameters, current, WS, and GFR were observed as 77.86 A, 9.26 mm/s, and GFR of 15.26 l/min respectively. While optimized output value for tensile strength, % strain, hardness, and residual stress were observed 89.19 MPa, 11.36, 78.88 HV, and -36.47 MPa respectively.
- The weld zone microstructure varies significantly across different welding regions (WFZ, PMZ, HAZ), demonstrating how local thermal gradients and alloy-specific properties govern grain morphology — with coarse grains in the HAZ and PMZ highlighting the need for precise heat input control to prevent strength loss.
- Specimens welded under suboptimal conditions show dual-grain structures with coarse columnar grains and equiaxed grains, as well as inclusions like oxides and intermetallic compounds (IMCs). These features lead to porosity and microstructural discontinuities that reduce mechanical integrity and create potential crack initiation sites.
- Optimized welding parameters, such as higher current and balanced travel speed, result in a fine, equiaxed grain structure within the weld fusion zone. This uniform microstructure, with refined and evenly distributed precipitates, enhances mechanical strength, ductility, and resistance to crack propagation.

- XRD analysis confirms the formation of stable strengthening phases like Mg₂Si and Al₃Fe within the weld metal. Proper thermal control during CMT welding refines these phases, reduces coarse IMCs, and promotes phase homogeneity, which directly contributes to higher hardness and tensile strength.
- Overall, the study demonstrates that precise management of welding parameters (current, travel speed, shielding gas flow) effectively refines grain size, minimizes porosity, and controls phase formation — resulting in better joint efficiency and improved structural reliability when joining dissimilar aluminum alloys by CMT welding.
- A welded joint produced with lower heat input and suboptimal parameters shows clear signs of incomplete fusion and gas porosity, as revealed by large, irregular voids on the fractured surface. These imperfections act as stress concentrators, leading to premature failure under tensile loading, which is reflected in its low tensile strength and reduced joint efficiency.
- Despite exhibiting some ductile features such as visible dimples, the same low-heat-input specimen demonstrates a non-uniform microstructure and inadequate metallurgical bonding. This imbalance limits the material's ability to accommodate internal stress and fully utilize its plastic deformation capacity, resulting in moderate hardness and weak overall mechanical performance.
- A welded joint fabricated under optimized welding conditions displays a uniformly dimpled fracture surface, indicating refined ductile failure and consistent plastic deformation throughout the joint. This high-quality microstructure, coupled with compressive residual stress and a balanced thermal cycle, translates into significantly higher tensile strength, joint efficiency, and improved structural reliability under mechanical loading.
- The CMT-P3 welded joint exhibits the most effective damping behavior and superior dynamic stability among all the samples, as shown by its rapid reduction in acceleration amplitude during transient vibration. This performance aligns with its highest tensile strength, maximum ductility, finest grain structure, and highest joint efficiency, indicating optimal mechanical integrity and energy dissipation capability.
- The CMT-P1 joint shows the weakest damping performance, with prolonged and irregular decay of acceleration amplitude under dynamic excitation. This inferior response is consistent with its lowest tensile strength, coarsest grain structure, and lowest joint efficiency, highlighting the negative impact of larger grain size and reduced hardness on vibrational stability.
- Moderate heat input conditions produce a balanced microstructure with refined grains and lower residual stresses, resulting in higher energy dissipation and improved damping, whereas excessive or insufficient heat input leads to coarser grains or increased residual stresses, thereby reducing the overall damping performance.

5.1 Future works and scope

The welding of dissimilar aluminum alloys, particularly AA6061 and AA8011, using the CMT technique has shown promising results in producing high-quality joints with reduced heat input and minimal distortion. However, despite its advantages, several challenges remain that limit its full industrial implementation. The complexity of metallurgical transformations, the formation of brittle intermetallic phases, and the variation in thermal and mechanical properties between the base metals require further investigation. Therefore, future research must focus on refining process parameters, understanding microstructural evolution, enhancing mechanical performance, and developing robust simulation and predictive models. The following future works may be drawn from the existing work.

- The CMT process involves multiple controllable parameters such as wire feed speed, arc voltage, travel speed, and shielding gas composition. These variables have a direct influence on heat input, weld bead geometry, dilution, and defect formation. Future research should aim to develop predictive models and employ optimization techniques (e.g., Taguchi method, Response Surface Methodology, Genetic Algorithms, or Machine Learning) to achieve superior joint quality with minimal porosity, controlled intermetallic layer thickness, and improved mechanical properties. Parameter optimization will also contribute to repeatability and process standardization for industrial-scale applications.
- AA6061 and AA8011 differ significantly in composition and thermal properties, which often leads to the formation of brittle intermetallic compounds (IMCs) or uneven grain structures during welding. Future work can explore advanced characterization techniques (EBSD, TEM, XRD) to understand grain boundary behavior, precipitate evolution, and phase distribution in the fusion zone and HAZ. This microstructural insight will guide alloy design, filler wire selection, and process modifications to engineer more homogeneous microstructures with refined grains and enhanced mechanical performance.
- Many applications of AA6061 and AA8011, such as in automotive chassis and heat exchangers, require the welded joints to endure fluctuating and prolonged loading conditions. The CMT process, being a low-heat-input method, is believed to positively influence fatigue performance by reducing residual stress and soft zones. Future scope includes high-cycle and low-cycle fatigue testing, S-N curve development, and creep life prediction under service-like environments. Understanding failure mechanisms under these conditions is vital for design validation and service life estimation.
- Post-weld treatments can significantly alter the residual stress distribution and mechanical properties of dissimilar CMT welds. Techniques like post-weld heat treatment (PWHT), solution treatment followed by artificial aging (T6 tempering), shot peening, or cryogenic treatment can help restore hardness in softened regions and reduce tensile residual stresses. Research should investigate the optimal post-processing route for AA6061-AA8011 combinations to tailor hardness profiles, improve fatigue life, and enhance corrosion resistance.
- The precise control of heat input in the CMT process makes it suitable for use in Wire Arc Additive Manufacturing (WAAM), particularly for aluminum-based structures. Future studies could explore integrating CMT with layer-by-layer

deposition techniques to manufacture functionally graded components or repair damaged aerospace/automotive parts involving dissimilar aluminum alloys. Hybrid welding-printing methods can be developed for lightweight, complex geometries with controlled material transitions.

- The fusion of dissimilar aluminum alloys often results in galvanic couples or the formation of corrosion-prone intermetallic phases. AA8011, being a softer and more corrosion-prone alloy compared to AA6061, can deteriorate the joint's corrosion resistance. Detailed studies involving salt spray testing, electrochemical impedance spectroscopy (EIS), and tribo corrosion testing should be conducted to evaluate the long-term corrosion and wear behavior of these welds. Surface modification techniques such as anodizing or laser remelting could also be evaluated to improve surface integrity.
- Numerical simulations using FEA and CFD can offer valuable insights into temperature gradients, residual stress distribution, solidification behavior, and phase transformation in the CMT process. Future work could include the development of comprehensive multi-physics models that incorporate thermal, mechanical, and metallurgical aspects of dissimilar aluminum welding. These models can be validated with experimental data and used to predict defects, optimize joint design, and reduce the trial-and-error effort in process development.

References

- [1] Wang, P., Zhang, H., Hu, S., Yin, F., & Ma, S. (2020). Microstructure and mechanical behaviour of CMT-welded Mg/Al dissimilar joint using Inconel 625 as filler metal. *Science and Technology of Welding and Joining*, 25(1), 10–19.
- [2] Selvamani, S. T. (2021). Microstructure and stress corrosion behaviour of CMT welded AA6061 T-6 aluminum alloy joints. *Journal of Materials Research and Technology*, 15, 315–326.
- [3] Sharma, A., Verma, A., Vashisth, D., & Khanna, P. (2022). Prediction of bead geometry parameters in MIG welded aluminum alloy 8011 plates. *Materials Today: Proceedings*, 62, 2787–2793.
- [4] Feng, J., Zhang, H., & He, P. (2009). The CMT short-circuiting metal transfer process and its use in thin aluminum sheets welding. *Materials and Design*, 30, 1850–1852.
- [5] Kumar, J., Kumar, G., & Mehdi, H. (2023). Optimization of FSW parameters on mechanical properties of different aluminum alloys of AA6082 and AA7050 by response surface methodology. *International Journal of Interactive Design and Manufacturing*. <https://doi.org/10.1007/s12008-023-01425-2>
- [6] Jain, S., Mishra, R. S., Mehdi, H., Gupta, R., & Dubey, A. K. (2023). Optimization of processing variables of friction stir welded dissimilar composite joints of AA6061 and AA7075 using response surface methodology. *Journal of Adhesion Science and Technology*. <https://doi.org/10.1080/01694243.2023.2243682>
- [7] Mehdi, H., & Mishra, R. S. (2021). Effect of friction stir processing on mechanical properties and heat transfer of TIG welded joint of AA6061 and AA7075. *Defence Technology*, 17(3), 715–727.
- [8] Reyaz, M. S. B., Sinha, A. N., & Mehdi, H. (2023). Effect of Pulsed TIG Welding Parameters on the Microstructural Evolution and Mechanical Properties of Dissimilar AA6061-T6 and AA7075-T6 Weldments. *Arabian Journal for Science and Engineering*. <https://doi.org/10.1007/s13369-023-08563-5>
- [9] Mehdi, H., Batra, L., Singh, A. P., & Others. (2023). Multi-response optimization of FSW process parameters of dissimilar aluminum alloys of AA2014 and AA6061 by response surface methodology (RSM). *International Journal of Interactive Design and Manufacturing*. <https://doi.org/10.1007/s12008-023-01409-2>
- [10] Pickin, C. G., Williams, S. W., & Lunt, M. (2011). Characterisation of the cold metal transfer (CMT) process and its application for low dilution cladding. *Journal of Materials Processing Technology*, 211(3), 496–502.
- [11] Hermans, M. J. M., & Den Ouden, G. (1999). Process behavior and stability in short circuit gas metal arc welding. *Welding Journal*, 78, 137–141.
- [12] Li-Li, G., Ling-Shen, F., & Ming-Yang, Z. (2012). Research on the line of laser tailor welded blanks. In *Information Engineering and Applications* (pp. 315–322).
- [13] Gery, D., Long, H., & Maropoulos, P. (2005). Effects of welding speed, energy input and heat source distribution on temperature variations in butt joint welding. *Journal of Materials Processing Technology*, 167, 393–401.
- [14] Aslanlar, S., Ogur, A., Ozsarac, U., Ilhan, E., & Demir, Z. (2007). Effect of welding current on mechanical properties of galvanized chromided steel sheets in electrical resistance spot welding. *Materials and Design*, 28, 2–7.
- [15] Msomi, V., Mabuwa, S., Ngonda, T., Mehdi, H., & Saxena, K. K. (2023). Microstructure and mechanical properties of tungsten inert gas welded dissimilar aluminum alloys joint subjected to normal multi-pass friction stir process. *Proceedings of the Institution of Mechanical Engineers, Part E: Journal of Process Mechanical Engineering*. <https://doi.org/10.1177/095440892312074>

- [16] Mehdi, H., & Mishra, R. S. (2020). Influence of friction stir processing on weld temperature distribution and mechanical properties of TIG-welded joint of AA6061 and AA7075. *Transactions of the Indian Institute of Metals*, 73, 1773–1788.
- [17] Liu, J., Wang, A., Zheng, Y., Liu, X., Gandra, J., Beamish, K., Petre, A., & Wang, L. L. (2017). Hot stamping of AA6082 tailor welded blanks for automotive applications. *Procedia Engineering*, 207, 729–734.
- [18] Rajeshkumar, R., Niranjani, V. L., Devakumaran, K., & Banerjee, K. (2021). Structure-property correlation of weld metal zone and interface regions of cold metal transfer welded dissimilar Al-Mg-Mn alloys joint. *Materials Today: Proceedings*, 46, 2498–2509.
- [19] Liu, X., Frankel, G. S., Zoofan, B., & Rokhlin, S. I. (2007). In-situ observation of intergranular stress corrosion cracking in AA2024-T3 under constant load conditions. *Corrosion Science*, 49, 139–148.
- [20] Li, J. R., Yu, J. M., Wang, L., Vogel, F., Wang, X. N., Shen, X. J., Song, B. N., & Nagaumi, H. (2023). Effect of filling materials on microstructure and properties of CMT-laser beam oscillation hybrid welding behavior of dissimilar Al–Mg–Si alloys. *Journal of Materials Research and Technology*, 26, 8272–8288.
- [21] Petroyiannis, P. V., Kamoutsis, E., Kermanidis, A. T., Pantelakis, S. G., Bontozoglou, V., & Haidemenopoulos, G. N. (2005). Fatigue. *Fatigue & Fracture of Engineering Materials & Structures*, 28, 565.
- [22] Liang, Y., Shen, J., Hu, S., Wang, H., & Pang, J. (2018). Effect of TIG current on microstructural and mechanical properties of 6061-T6 aluminum alloy joints by TIG–CMT hybrid welding. *Journal of Materials Processing Technology*, 255, 161–174. <https://doi.org/10.1016/j.jmatprotec.2017.12.006>
- [23] Mehdi, H., & Mishra, R. S. (2020). Effect of friction stir processing on microstructure and mechanical properties of TIG welded joint of AA6061 and AA7075. *Metallography, Microstructure, and Analysis*, 9, 403–418.
- [24] Elrefaey, A., & Ross, N. G. (2015). Microstructure and mechanical properties of cold metal transfer welding similar and dissimilar aluminum alloys. *Acta Metallurgica Sinica (English Letters)*, 28, 715–724.
- [25] Ahmad, R., & Bakar, M. A. (2011). Effect of a post-weld heat treatment on the mechanical and microstructure properties of AA6061 joints welded by the gas metal arc welding cold metal transfer method. *Materials and Design*, 32, 5120–5126.
- [26] Vimal, K. E. K., Srinivas, M. N., & Rajak, S. (2021). Wire arc additive manufacturing of aluminum alloys: A review. *Materials Today: Proceedings*, 41, 1139–1145.
- [27] Izan, N., et al. (2023). Process and heat resources for wire arc additive manufacturing of aluminum alloy ER4043: A review. *Journal of Mechanical Engineering*, 20(1), 2550–164. <https://doi.org/10.24191/jmeche.v20i1.21077>
- [28] Charoenrat, S., & Prasomthong, S. (2022). The optimization of welding hardfacing on wear resistance of FC-25 grey cast iron steel substrate by response surface methodology (RSM). *SNRU Journal of Science and Technology*, 14(2), 245154.
- [29] Boulos, M. I., Fauchais, P. L., & Pfender, E. (2023). Plasma torches for cutting, welding, and PTA coating. In *Handbook of Thermal Plasmas*. Springer, Cham. https://doi.org/10.1007/978-3-030-84936-8_47
- [30] Sharma, A., & Dwivedi, V. K. (2020). Comparison of microstructural and mechanical properties of aluminium alloy AA6062 on FSW and TIGW processes. *Materials Today: Proceedings*, 25(4), 903–907.

- [31] Lv, X., Wang, Z., Su, H., Xu, L., & Jing, H. (2022). Analysis of droplet growth of positive and negative electrode on cold metal transfer welding of aluminum wire. *Journal of Manufacturing Processes*, 78, 330–340.
- [32] Feng, Y., Jiang, Q., & Fan, D. (2024). Effect of auxiliary wire feeding on cold metal transfer directed energy deposition of stainless steel: A study on droplet transfer, formation characteristics, and microstructure. *Journal of Materials Research and Technology*, 33, 9313–9324.
- [33] Sun, Z., Lv, Y., & Xu, B. (2015). Investigation of droplet transition behaviors in cold metal transfer (CMT) process on welding Ti-6Al-4V alloy. *International Journal of Advanced Manufacturing Technology*, 80, 2007–2014. <https://doi.org/10.1007/s00170-015-7197-9>
- [34] Praveen, P., Yarlalagadda, P. K. D. V., & Kang, M. J. (2005). Advancements in pulse gas metal arc welding. *Journal of Materials Processing Technology*, 164–165, 1113–1119. <https://doi.org/10.1016/j.jmatprotec.2005.02.100>
- [35] Little, R. L. (1973). *Welding and welding technology*. McGraw Hill Education.
- [36] Ghosh, S. K. (1984). Processes and materials of manufacture. *Journal of Mechanical Working Technology*, 9, 327–328. [https://doi.org/10.1016/0378-3804\(84\)90115-3](https://doi.org/10.1016/0378-3804(84)90115-3)
- [37] Lindbergh, R. A. (2015). *Processes and materials of manufacture*. In *Processes and Materials of Manufacture* (pp. 623–692).
- [38] Sathiya, P., Mishra, M. K., Soundararajan, R., & Shanmugarajan, B. (2013). Shielding gas effect on weld characteristics in arc-augmented laser welding process of super austenitic stainless steel. *Optics & Laser Technology*, 45, 46–55.
- [39] Wang, J., Feng, J. C., & Wang, Y. X. (2008). Microstructure of Al–Mg dissimilar weld made by cold metal transfer MIG welding. *Materials Science and Technology*, 24, 827–831. <https://doi.org/10.1179/174328408X278411>
- [40] Shang, J., Wang, K., Zhou, Q., Zhang, D., Huang, J., & Li, G. (2013). Microstructure characteristics and properties of Mg/Al dissimilar metals made by cold metal transfer welding with ER4043 filler metal. *Rare Metal Materials and Engineering*, 42, 1337–1341. [https://doi.org/10.1016/S1875-5372\(13\)60081-8](https://doi.org/10.1016/S1875-5372(13)60081-8)
- [41] Madhavan, S., Kamaraj, M., Vijayaraghavan, L., & Srinivasa Rao, K. (2017). Cold metal transfer welding of dissimilar A6061 aluminum alloy–AZ31B: Effect of heat input on microstructure, residual stress and corrosion behavior. *Transactions of the Indian Institute of Metals*, 70, 1047–1054. <https://doi.org/10.1007/s12666-016-0893-9>
- [42] Wang, P., Hu, S., Shen, J., Liang, Y., & Pang, J. (2016). Effects of electrode positive/negative ratio on microstructure and mechanical properties of Mg/Al dissimilar variable polarity cold metal transfer welded joints. *Materials Science and Engineering: A*, 652, 127–135. <https://doi.org/10.1016/j.msea.2015.11.080>
- [43] Tian, Y., Shen, J., Hu, S., Wang, Z., & Gou, J. (2019). Microstructure and mechanical properties of wire and arc additive manufactured Ti–6Al–4V and AlSi5 dissimilar alloys using cold metal transfer welding. *Journal of Manufacturing Processes*, 46, 337–344. <https://doi.org/10.1016/j.jmapro.2019.09.006>
- [44] Sun, Q., Li, J., Liu, Y., Jiang, Y., Kang, K., & Feng, J. (2018). Arc characteristics and droplet transfer process in CMT welding with a magnetic field. *Journal of Manufacturing Processes*, 36, 48–56.
- [45] Cao, R., Sun, J. H., & Chen, J. H. (2013). Mechanisms of joining aluminum A6061-T6 and titanium Ti–6Al–4V alloys by cold metal transfer technology. *Science and Technology of Welding and Joining*, 18, 425–433. <https://doi.org/10.1179/1362171813Y.0000000118>

- [46] Li, J., Sun, Q., Liu, Y., Cai, C., & Feng, J. (2017). Cold metal transfer welding–brazing of pure titanium TA2 to aluminum alloy 6061-T6. *Advanced Engineering Materials*, 19(2), 1–8. <https://doi.org/10.1002/adem.201600494>
- [47] Babu, S., Panigrahi, S. K., Janaki Ram, G. D., Venkitakrishnan, P. V., & Suresh Kumar, R. (2019). Cold metal transfer welding of aluminum alloy AA 2219 to austenitic stainless steel AISI 321. *Journal of Materials Processing Technology*, 266, 155–164. <https://doi.org/10.1016/j.jmatprotec.2018.10.034>
- [48] Liu, Y., Sun, Q., Liu, J., Wang, S., & Feng, J. (2015). Effect of axial external magnetic field on cold metal transfer welds of aluminum alloy and stainless steel. *Materials Letters*, 152, 29–31. <https://doi.org/10.1016/j.matlet.2015.03.077>
- [49] Mezrag, B., Deschaux-Beaume, F., Sabatier, L., Wattrisse, B., & Benachour, M. (2020). Microstructure and properties of steel–aluminum Cold Metal Transfer joints. *Journal of Materials Processing Technology*, 277, 116414. <https://doi.org/10.1016/j.jmatprotec.2019.116414>
- [50] Sravanthi, S. S., Acharyya, S. G., Phani, P. P., & Padmanabham, G. (2019). Integrity of 5052 Al–mild steel dissimilar welds fabricated using MIG-brazing and cold metal transfer in nitric acid medium. *Journal of Materials Processing Technology*, 268, 97–106. <https://doi.org/10.1016/j.jmatprotec.2019.01.010>
- [51] Singh, J., Arora, K. S., & Shukla, D. K. (2020). Lap weld-brazing of aluminum to steel using novel cold metal transfer process. *Journal of Materials Processing Technology*, 283, 116728. <https://doi.org/10.1016/j.jmatprotec.2020.116728>
- [52] Yang, S., Zhang, J., Lian, J., & Lei, Y. (2013). Welding of aluminum alloy to zinc coated steel by cold metal transfer. *Materials & Design*, 49, 602–612. <https://doi.org/10.1016/j.matdes.2013.01.045>
- [53] Silvayeh, Z., Vallant, R., Sommitsch, C., Götzinger, B., Karner, W., & Hartmann, M. (2017). Influence of filler alloy composition and process parameters on the intermetallic layer thickness in single-sided cold metal transfer welding of aluminum-steel blanks. *Metallurgical and Materials Transactions A*, 48, 5376–5386. <https://doi.org/10.1007/s11661-017-4277-5>
- [54] Niu, S., Chen, S., Dong, H., Zhao, D., Zhang, X., Guo, X., & Wang, G. (2016). Microstructure and properties of lap joint between aluminum alloy and galvanized steel by CMT. *Journal of Materials Engineering and Performance*, 25, 1839–1847. <https://doi.org/10.1007/s11665-016-2035-2>
- [55] Cao, R., Yu, G., Chen, J. H., & Wang, P. C. (2013). Cold metal transfer joining aluminum alloys-to-galvanized mild steel. *Journal of Materials Processing Technology*, 213, 1753–1763. <https://doi.org/10.1016/j.jmatprotec.2013.04.004>
- [56] Singh, I. J., Murtaza, Q., & Kumar, P. (2025). A comprehensive review on effect of cold metal transfer welding parameters on dissimilar and similar metal welding. *Journal of Engineering Research*, 13(2), 1184–1201.
- [57] Mou, G., Hua, X., Shen, C., & Wang, M. (2020). Effects of thermal distribution strategy on a Ti-6Al-4V/304L dissimilar joint fabricated using the variable polarity cold metal transfer arc-brazing method. *Materials & Design*, 191, 108619. <https://doi.org/10.1016/j.matdes.2020.108619>
- [58] Mou, G., Hua, X., Wu, D., Huang, Y., Lin, W., & Xu, P. (2019). Microstructure and mechanical properties of cold metal transfer welding-brazing of titanium alloy (TC4) to stainless steel (304L) using V-shaped groove joints. *Journal of Materials Processing Technology*, 266, 696–706. <https://doi.org/10.1016/j.jmatprotec.2018.09.019>
- [59] Pardal, G., Ganguly, S., Williams, S., & Vaja, J. (2016). Dissimilar metal joining of stainless steel and titanium using copper as transition metal. *International Journal of*

- Advanced Manufacturing Technology*, 86, 1139–1150. <https://doi.org/10.1007/s00170-015-8110-2>
- [60] Chang, J., Cao, R., & Yan, Y. (2019). The joining behavior of titanium and Q235 steel joined by cold metal transfer joining technology. *Materials*, 12(15), 2413. <https://doi.org/10.3390/ma12152413>
 - [61] Tang, X., Zhang, S., Cui, X., Zhang, C., Liu, Y., & Zhang, J. (2020). Tribological and cavitation erosion behaviors of nickel-based and iron-based coatings deposited on AISI 304 stainless steel by cold metal transfer. *Journal of Materials Research and Technology*, 9, 6665–6681. <https://doi.org/10.1016/j.jmrt.2020.04.064>
 - [62] Mehdi, H., Jain, S., Salah, A. N., Singh, A. P., & Chawla, S. (2023). Effect of friction stir welding parameters on microstructure and mechanical properties of the dissimilar alloys of AZ91D and AA7075. *Proceedings of the Institution of Mechanical Engineers, Part E: Journal of Process Mechanical Engineering*. <https://doi.org/10.1177/09544089231195444>
 - [63] Mehdi, H., Jain, S., Msomi, V., et al. (2023). Effect of intermetallic compounds on mechanical and microstructural properties of dissimilar alloys Al-7Si/AZ91D. *Journal of Materials Engineering and Performance*. <https://doi.org/10.1007/s11665-023-08302-9>
 - [64] Hu, S., Zhang, H., Wang, Z., Liang, Y., & Liu, Y. (2016). The arc characteristics of cold metal transfer welding with AZ31 wire. *Journal of Manufacturing Processes*, 24, 298–306. <https://doi.org/10.1016/j.jmapro.2016.10.001>
 - [65] Zhang, H., Hu, S. S., Wang, Z. J., & Liang, Y. (2015). The effect of welding speed on microstructures of cold metal transfer deposited AZ31 clad. *Materials & Design*, 86, 894–901.
 - [66] Ola, O. T., & Doern, F. E. (2014). A study of cold metal transfer clads in nickel-base INCONEL 718 superalloy. *Materials & Design*, 57, 51–59.
 - [67] Zhang, H., Hu, S., Wang, Z., & Liang, Y. (2015). The effect of welding speed on microstructures of cold metal transfer deposited AZ31 clad. *Materials & Design*, 86, 894–901. <https://doi.org/10.1016/j.matdes.2015.07.143>
 - [68] Shang, J., Wang, K., Zhou, Q., Zhang, D., Huang, J., & Li, G. (2012). Wire-arc additive manufacturing of AZ31 fabricated by cold metal transfer heat source: Processing, microstructure, and mechanical behavior. *Materials & Design*, 34, 559–565.
 - [69] Zhang, H., Hu, S., Wang, Z., & Liang, Y. (2015). The effect of welding speed on microstructures of cold metal transfer deposited AZ31 clad. *Materials & Design*, 86, 894–901.
 - [70] Gao, M., Zeng, X., Tan, B., & Feng, J. (2009). Study of laser MIG hybrid welded AZ31. *Science and Technology of Welding and Joining*, 14, 274–281.
 - [71] Gou, J., Wang, Z., Hu, S., Shen, J., Tian, Y., Zhao, G., & Chen, Y. (2020). Effects of ultrasonic peening treatment in three directions on grain refinement and anisotropy of cold metal transfer additive manufactured Ti-6Al-4V thin wall structure. *Journal of Manufacturing Processes*, 54, 148–157. <https://doi.org/10.1016/j.jmapro.2020.03.010>
 - [72] Farabi, E., Klein, T., Schnall, M., & Primig, S. (2023). Effects of high deposition rate during cold metal transfer additive manufacturing on microstructure and properties of Ti-6Al-4V. *Additive Manufacturing*, 71, 103592. <https://doi.org/10.1016/j.addma.2023.103592>
 - [73] Liu, K., Chen, X., Shen, Q., Pan, Z., Singh, R. A., Jayalakshmi, S., & Konovalov, S. (2020). Microstructural evolution and mechanical properties of deep cryogenic treated Cu–Al–Si alloy fabricated by Cold Metal Transfer (CMT) process. *Materials Characterization*, 159, 110011. <https://doi.org/10.1016/j.matchar.2019.110011>

- [74] Azar, A. S. (2015). A heat source model for cold metal transfer (CMT) welding. *Journal of Thermal Analysis and Calorimetry*, 122, 741–746. <https://doi.org/10.1007/s10973-015-4809-4>
- [75] Cadiou, S., Courtois, M., Carin, M., Berckmans, W., & Le Masson, P. (2020). 3D heat transfer, fluid flow and electromagnetic model for cold metal transfer wire arc additive manufacturing (CMT-WAAM). *Additive Manufacturing*, 36, 101541. <https://doi.org/10.1016/j.addma.2020.101541>
- [76] Ogino, Y., Asai, S., & Hirata, Y. (2018). Numerical simulation of WAAM process by a GMAW weld pool model. *Welding in the World*, 62, 393–401. <https://doi.org/10.1007/s40194-018-0556-z>
- [77] Koli, Y., Yuvaraj, N., Aravindan, S., & Vipin. (2021). CMT joining of AA6061-T6 and AA6082-T6 and examining mechanical properties and microstructural characterization. *Transactions of the Indian Institute of Metals*, 74, 313–329. <https://doi.org/10.1007/s12666-020-02134-0>
- [78] Raut, L. P., & Taiwade, R. V. (2021). Wire arc additive manufacturing: A comprehensive review and research directions. *Journal of Materials Engineering and Performance*, 30, 4768–4791. <https://doi.org/10.1007/s11665-021-05871-5>
- [79] Pal, K., & Pal, S. K. (2011). Effect of pulse parameters on weld quality in pulsed gas metal arc welding: A review. *Journal of Materials Engineering and Performance*, 20, 918–931. <https://doi.org/10.1007/s11665-010-9717-y>
- [80] Selvamani, S. T., Velmurugan, S., Balasubramanian, V., & Palanikumar, K. (2020). Effects of heat distribution during cold metal transfer arc welding on galvanized steel using volumetric heat source model. *Journal of Materials Research and Technology*, 9, 10097–10109. <https://doi.org/10.1016/j.jmrt.2020.07.004>
- [81] David, S. A., & Vitek, J. M. (1989). Correlation between solidification parameters and weld microstructures. *International Materials Reviews*, 34(1), 213–245. <https://doi.org/10.1179/imr.1989.34.1.213>
- [82] rizalp, A. O., Durmu , H., Yüksel, N., & Türkmen, . (2016). Cold metal transfer welding of AA1050 aluminum thin sheets. *Revista Materia*, 21(3), 615–622. <https://doi.org/10.1590/S1517-707620160003.0059>
- [83] Eassa, H. E. D. E. H. (1985). The effect of high-frequency pulsing of a welding arc. *IEEE Transactions on Industry Applications*, IA-21(5), 1294–1299. <https://doi.org/10.1109/TIA.1985.349557>
- [84] Radaj, D. (1992). *Heat effects of welding*. Springer. <https://doi.org/10.1007/978-3-642-48640-1>
- [85] Nishimura, R., Ma, N., Liu, Y., Li, W., & Yasuki, T. (2021). Measurement and analysis of welding deformation and residual stress in CMT welded lap joints of 1180 MPa steel sheets. *Journal of Manufacturing Processes*, 72, 515–528.
- [86] Cadiou, S., Courtois, M., Carin, M., Berckmans, W., & Le Masson, P. (2020). 3D heat transfer, fluid flow and electromagnetic model for cold metal transfer wire arc additive manufacturing (CMT-WAAM). *Additive Manufacturing*, 36, 101541. <https://doi.org/10.1016/j.addma.2020.101541>
- [87] Wang, P., Zhang, H., Hu, S., Yin, F., & Ma, S. (2020). Microstructure and mechanical behaviour of CMT-welded Mg/Al dissimilar joint using Inconel 625 as filler metal. *Science and Technology of Welding and Joining*, 25, 10–19.
- [88] Selvamani, S. T. (2021). Microstructure and stress corrosion behaviour of CMT welded AA6061 T-6 aluminum alloy joints. *Journal of Materials Research and Technology*, 15, 315–326.

- [89] Sharma, A., Verma, A., Vashisth, D., & Khanna, P. (2022). Prediction of bead geometry parameters in MIG welded aluminum alloy 8011 plates. *Materials Today: Proceedings*, 62, 2787–2793.
- [90] Feng, J., Zhang, H., & He, P. (2009). The CMT short-circuiting metal transfer process and its use in thin aluminum sheets welding. *Materials & Design*, 30(5), 1850–1852.
- [91] Kumar, J., Kumar, G., Mehdi, H., et al. (2023). Optimization of FSW parameters on mechanical properties of different aluminum alloys of AA6082 and AA7050 by response surface methodology. *International Journal on Interactive Design and Manufacturing (IJIDeM)*. <https://doi.org/10.1007/s12008-023-01425-2>
- [92] Jain, S., Mishra, R. S., Mehdi, H., Gupta, R., & Dubey, A. K. (2023). Optimization of processing variables of friction stir welded dissimilar composite joints of AA6061 and AA7075 using response surface methodology. *Journal of Adhesion Science and Technology*. <https://doi.org/10.1080/01694243.2023.2243682>
- [93] Mehdi, H., & Mishra, R. S. (2021). Effect of friction stir processing on mechanical properties and heat transfer of TIG welded joint of AA6061 and AA7075. *Defence Technology*, 17(3), 715–727.
- [94] Reyaz, M. S. B., Sinha, A. N., & Mehdi, H. (2023). Effect of Pulsed TIG Welding Parameters on the Microstructural Evolution and Mechanical Properties of Dissimilar AA6061-T6 and AA7075-T6 Weldments. *Arabian Journal for Science and Engineering*. <https://doi.org/10.1007/s13369-023-08563-5>
- [95] Mehdi, H., Batra, L., Singh, A. P., et al. (2023). Multi-response optimization of FSW process parameters of dissimilar aluminum alloys of AA2014 and AA6061 by response surface methodology (RSM). *International Journal on Interactive Design and Manufacturing (IJIDeM)*. <https://doi.org/10.1007/s12008-023-01409-2>
- [96] Pickin, C. G., Williams, S. W., & Lunt, M. (2011). Characterisation of the cold metal transfer (CMT) process and its application for low dilution cladding. *Journal of Materials Processing Technology*, 211(3), 496–502.
- [97] Hermans, M. J. M., & Den Ouden, G. (1999). Process behavior and stability in short circuit gas metal arc welding. *Welding Journal*, 78, 137–141.
- [98] Li-Li, G., Ling-Shen, F., & Ming-Yang, Z. (2012). Research on the line of laser tailor welded blanks. In *Information Engineering and Applications* (pp. 315–322).
- [99] Gery, D., Long, H., & Maropoulos, P. (2005). Effects of welding speed, energy input and heat source distribution on temperature variations in butt joint welding. *Journal of Materials Processing Technology*, 167, 393–401.
- [100] Aslanlar, S., Ogur, A., Ozsarac, U., Ilhan, E., & Demir, Z. (2007). Effect of welding current on mechanical properties of galvanized chromided steel sheets in electrical resistance spot welding. *Materials and Design*, 28(2), 2–7.
- [101] Msomi, V., Mabuwa, S., Ngonda, T., Mehdi, H., & Saxena, K. K. (2023). Microstructure and mechanical properties of tungsten inert gas welded dissimilar aluminum alloys joint subjected to normal multi-pass friction stir process. *Proceedings of the Institution of Mechanical Engineers, Part E: Journal of Process Mechanical Engineering*. <https://doi.org/10.1177/095440892312074>
- [102] Mehdi, H., & Mishra, R. S. (2020). Influence of friction stir processing on weld temperature distribution and mechanical properties of TIG-welded joint of AA6061 and AA7075. *Transactions of the Indian Institute of Metals*, 73, 1773–1788.
- [103] Liu, J., Wang, A., Zheng, Y., Liu, X., Gandra, J., Beamish, K., Petre, A., & Wang, L. L. (2017). Hot stamping of AA6082 tailor welded blanks for automotive applications. *Procedia Engineering*, 207, 729–734.
- [104] Rajeshkumar, R., Niranjani, V. L., Devakumaran, K., & Banerjee, K. (2021). Structure-property correlation of weld metal zone and interface regions of cold metal

- transfer welded dissimilar Al-Mg-Mn alloys joint. *Materials Today: Proceedings*, 46, 2498–2509.
- [105] Liu, X., Frankel, G. S., Zoofan, B., & Rokhlin, S. I. (2007). In-situ observation of intergranular stress corrosion cracking in AA2024-T3 under constant load conditions. *Corrosion Science*, 49, 139–148.
 - [106] Li, J. R., Yu, J. M., Wang, L., Vogel, F., Wang, X. N., Shen, X. J., Song, B. N., & Nagaumi, H. (2023). Effect of filling materials on microstructure and properties of CMT-laser beam oscillation hybrid welding behavior of dissimilar Al-Mg-Si alloys. *Journal of Materials Research and Technology*, 26, 8272–8288.
 - [107] Petroyiannis, P. V., Kamoutsi, E., Kermanidis, A. T., Pantelakis, S. G., Bontozoglou, V., & Haidemenopoulos, G. N. (2005). Fatigue behaviour of laser welded aluminium alloys. *Fatigue & Fracture of Engineering Materials & Structures*, 28, 565.
 - [108] Liang, Y., Shen, J., Hu, S., Wang, H., & Pang, J. (2018). Effect of TIG current on microstructural and mechanical properties of 6061-T6 aluminum alloy joints by TIG–CMT hybrid welding. *Journal of Materials Processing Technology*, 255, 161–174. <https://doi.org/10.1016/j.jmatprotec.2017.12.006>
 - [109] Mehdi, H., & Mishra, R. S. (2020). Effect of friction stir processing on microstructure and mechanical properties of TIG welded joint of AA6061 and AA7075. *Metallography, Microstructure, and Analysis*, 9, 403–418.
 - [110] Elrefaey, A., & Ross, N. G. (2015). Microstructure and mechanical properties of cold metal transfer welding similar and dissimilar aluminum alloys. *Acta Metallurgica Sinica (English Letters)*, 28, 715–724.
 - [111] Ahmad, R., & Bakar, M. A. (2011). Effect of a post-weld heat treatment on the mechanical and microstructure properties of AA6061 joints welded by the gas metal arc welding cold metal transfer method. *Materials & Design*, 32, 5120–5126.
 - [112] Vimal, K. E. K., Srinivas, M. N., & Rajak, S. (2021). Wire arc additive manufacturing of aluminum alloys: A review. *Materials Today: Proceedings*, 41, 1139–1145.
 - [113] Izan, N., Noor, A. F. M., Yahya, M. Y., Khairuddin, M. H., & Ishak, M. (2023). Process and heat resources for wire arc additive manufacturing of aluminum alloy ER4043: A review. *Journal of Mechanical Engineering*, 20(1), 2550–264. <https://doi.org/10.24191/jmeche.v20i1.21077>
 - [114] Cao, X., Yi, Z., Xu, C., Luo, Z., & Duan, J. (2021). Study on laser/DP-MIG hybrid welding-brazing of aluminum to Al-Si coated boron steel. *Journal of Manufacturing Processes*, 64, 333–340.
 - [115] Cao, X., Duan, J., Li, Z., Chang, B., Xu, C., & Xie, Z. (2022). An investigation on laser/DP-MIG hybrid weldability of aluminum to Al-Si coated boron steel. *Optics & Laser Technology*, 150, 107939.
 - [116] Singh, I. J., Kumar, P., & Murtaza, Q. (2024). An overview of cold metal transfer welding of similar materials. *International Journal on Interactive Design and Manufacturing (IJIDeM)*. <https://doi.org/10.1007/s12008-023-01719-5>
 - [117] Singh, I. J., Murtaza, Q., & Kumar, P. (2023). A comprehensive review on effect of cold metal transfer welding parameters on dissimilar and similar metal welding. *Journal of Engineering Research*. <https://doi.org/10.1016/j.jer.2023.12.009>
 - [118] Kumar, J., Kumar, G., Mehdi, H., et al. (2023). Optimization of FSW parameters on mechanical properties of different aluminum alloys of AA6082 and AA7050 by response surface methodology. *International Journal on Interactive Design and Manufacturing (IJIDeM)*. <https://doi.org/10.1007/s12008-023-01425-2>
 - [119] Jain, S., Mishra, R. S., Mehdi, H., Gupta, R., & Dubey, A. K. (2023). Optimization of processing variables of friction stir welded dissimilar composite joints of AA6061

- and AA7075 using response surface methodology. *Journal of Adhesion Science and Technology*. <https://doi.org/10.1080/01694243.2023.2243682>
- [120] Elrefaey, A., & Ross, N. G. (2015). Microstructure and mechanical properties of cold metal transfer welding similar and dissimilar aluminum alloys. *Acta Metallurgica Sinica (English Letters)*, 28, 715–724.
 - [121] Nait Salah, A., Mehdi, H., Mehmood, A., Hashmid, A. W., Malla, C., & Kumar, R. (2021). Optimization of process parameters of friction stir welded joints of dissimilar aluminum alloys AA3003 and AA6061 by RSM. *Materials Today: Proceedings*, 56(4), 1675–1684. <https://doi.org/10.1016/j.matpr.2021.10.288>
 - [122] Ahmad, R., & Bakar, M. A. (2011). Effect of a post-weld heat treatment on the mechanical and microstructure properties of AA6061 joints welded by the gas metal arc welding cold metal transfer method. *Materials & Design*, 32, 5120–5126.
 - [123] Adin, H., Sa lam, Z., & Adin, M. . (2021). Numerical investigation of fatigue behavior of non-patched and patched aluminum/composite plates. *European Mechanical Science*, 5(4), 168–176. <https://doi.org/10.26701/ems.923798>
 - [124] Liang, Y., Shen, J., Hu, S., Wang, H., & Pang, J. (2018). Effect of TIG current on microstructural and mechanical properties of 6061-T6 aluminum alloy joints by TIG–CMT hybrid welding. *Journal of Materials Processing Technology*, 255, 161–174.
 - [125] Adin, M. . (2022). Investigation of mechanical properties of aluminum alloys welded by laser welding and optimization of welding parameters using Taguchi and ANOVA methods. *Journal of Science, Technology and Engineering Research*, 3(2), 50–59.
 - [126] Yang, B., Fu, Z., Li, T., Shan, M., Guo, K., Chen, B., Gou, G., & Gao, W. (2019). Microstructure and fracture toughness properties of CMT repairing welded 7075-T651 MIG welding joint. *Materials Research Express*, 6(12), 1265d6.
 - [127] Singh, I. J., Murtaza, Q., & Kumar, P. (2025). Effect of CMT welding process parameters on the microstructural and mechanical properties of dissimilar aluminum alloys of AA8011 and AA6061. *Transactions of the Indian Institute of Metals*, 78(3). <https://doi.org/10.1007/s12666-024-03471-0>
 - [128] rizalp, A. O., Durmu , H., Yüksel, N., & Türkmen, . (2016). Cold metal transfer welding of AA1050 aluminum thin sheets. *Materia*, 21(3), 615–622.
 - [129] Kumar, N. P., Vendan, S. A., & Shanmugam, N. S. (2016). Investigations on the parametric effects of cold metal transfer process on the microstructural aspects in AA6061. *Journal of Alloys and Compounds*, 658, 255–264.
 - [130] Gungor, B., Kaluc, E., Taban, E., & Aydin, S. I. K. (2014). Mechanical and microstructural properties of robotic Cold Metal Transfer (CMT) welded 5083-H111 and 6082-T651 aluminum alloys. *Materials & Design*, 54, 207–211.
 - [131] Maurya, A. K., Khan, W. N., Patnaik, A., Kumar, R., Sharma, V., & Kumari, K. (2024). Tribological performance of gas tungsten arc welded dissimilar joint of sDSS 2507/IN-625 for marine application. *Archives of Civil and Mechanical Engineering*, 24, 23. <https://doi.org/10.1007/s43452-023-00832-2>
 - [132] Kolia, Y., Yuvaraja, N., Aravindan, S., & Vipin. (2021). Multi-response mathematical model for optimization of process parameters in CMT welding of dissimilar thickness AA6061-T6 and AA6082-T6 alloys using RSM-GRA coupled with PCA. *Advances in Industrial and Manufacturing Engineering*, 2, 100050. <https://doi.org/10.1016/j.aime.2021.100050>

List of Publications

Journal Publication

1. Indra Jeet Singh, Qasim Murtaza, Paras kumar, A comprehensive review on effect of cold metal transfer welding parameters on dissimilar and similar metal welding, Journal of Engineering Research, 2023, <https://doi.org/10.1016/j.jer.2023.12.009>. (Elsevier)
2. Indra Jeet Singh, Qasim Murtaza, Paras kumar, Effect of welding speed on metallurgical characterization of CMT welding of dissimilar aluminium alloys of AA6061 and AA8011, Silicon, 2024, <https://doi.org/10.1007/s12633-024-02961-6>. (Springer)
3. Indra Jeet Singh, Qasim Murtaza, Paras kumar, Effect of CMT Welding Process Parameters on the Microstructural and Mechanical Properties of Dissimilar Aluminum Alloys of AA8011 and AA6061, Transactions of the Indian Institute of Metals, 2024, <https://doi.org/10.1007/s12666-024-03471-0>. (Springer)
4. Indra Jeet Singh, Qasim Murtaza, Paras kumar, Optimization of input and output process parameters and microstructural analysis of CMT dissimilar aluminum welded joint of AA8011 and AA6061. Journal of Materials Engineering and Performance, 2025, <https://doi.org/10.1007/s11665-025-11632-5>. (Springer)
5. Indra Jeet Singh, Qasim Murtaza, Paras kumar, Optimization of process parameters and microstructural analysis of CMT welded joints of dissimilar aluminum alloys. JOM, 2025, <https://doi.org/10.1007/s11837-025-07871-5>. (Springer).

Conference Publications

1. Indra Jeet Singh, Qasim Murtaza, Paras kumar, An overview of cold metal transfer welding of similar materials, International Journal on Interactive Design and Manufacturing (IJIDeM), 2024, <https://doi.org/10.1007/s12008-023-01719-5>. (Springer)
2. Indra Jeet Singh, Qasim Murtaza, Paras kumar, An Overview of Dissimilar Metals Welding by Cold Metal Transfer Technique, Journal of Polymer & Composites, 2024, DOI (Journal): 10.37591/JoPC (STM Journals)



A comprehensive review on effect of cold metal transfer welding parameters on dissimilar and similar metal welding

Indra Jeet Singh^{*}, Qasim Murtaza, Paras kumar

Department of Mechanical Engineering, Delhi Technological University, Delhi 110042, India

ARTICLE INFO

Keywords:

Cold metal transfer welding
Microstructure analysis
Dissimilar metals weld
Similar metals weld
Heat models
Shielding gases

ABSTRACT

Cold Metal Transfer (CMT), an advanced technology developed from the conventional metal inert gas (MIG) process, has revolutionized the joining of similar and dissimilar metals due to low heat input. The authors analyzed the physics of welding involved in the process, the metallurgical effect on the alloys, and different mechanical and corrosion properties due to variations in the parameters involved during welding. The shielding gas/es effect is studied to understand the bead modification in different environments and its impact on mechanical properties. Moreover, comparing the modified technique to the conventional method showed considerable improvement in weld defects, the heat-affected zone (HAZ) width, and the weld finish on the surface. An analysis of the heat input model and heat input calculation is also carried out to ease the study of the simulation of the CMT process. These analyses had drawn some critical research gaps in the research conducted in the past, which the upcoming researchers in this field can address.

Introduction

Dissimilar metal joining is widely employed across various industries for specific applications where combining distinct metal properties is essential. In aerospace, this technique enables the creation of light-weight structures with optimized strength, addressing the unique requirements of different components in aircraft and spacecraft [1,2]. In the automotive sector, dissimilar metal joints contribute to weight reduction, improved fuel efficiency, and the integration of materials with diverse characteristics for enhanced vehicle performance. In nuclear engineering, these joints are critical in constructing components capable of withstanding extreme conditions, managing heat dissipation, and optimizing neutron absorption. The versatility of dissimilar metal joining ensures tailored solutions in each industry, addressing specific challenges and contributing to advancements in technology and material science [3]. New welding phenomena must also meet industrial standards. Austrian company Fronius invented CMT welding in 2004. [4,5]. CMT welding is a tweaked Metal Inert Gas/Metal Arc Gas (MIG/MAG) process [6]. Compared to the traditional MIG, only 10% of the heat input is used in the CMT process, so the name is 'Cold' [7]. The approach focuses on the step-by-step pave layer theory, improving the welding joints' solidification process resulting in grain refinement [8]. Post-welding, a heterogeneous microstructure, necessitates precise heat

treatment. Controlling temperature and time is crucial to attain the desired microstructure and mechanical properties for dual-phase weld joints (DWJ). Stabilizing the microstructure is essential for effective performance in ferritic/martensitic-austenitic joints under elevated temperature and pressure, achievable through appropriate post-welding heat treatment [9]. This three-phase low-temperature welding equipment uses gout transfer to reduce molten material (spatters) drops at joints [10]. Recent experiments have revealed that CMT has a low dilution level (3–4%) for welding hard materials like Stellite 21 on substrates like H13 steel, making it acceptable for hard-facing turbines and other applications [11]. At an equal filler wire rate, the CMT process of aluminum alloy resulted in lower weld dilution than typical GMAW [12]. CMT has 100% content efficiency [10]. CMT welding is used in aircraft, bridges, locomotives, microelectronics devices, and steel constructions due to its high tensile strength, better joint microstructure, and ability to weld dissimilar composites [13,14]. Apart from the traditional process, the procedure includes a range of arc modes, viz., the pulse CMT (CMT-P), the advanced CMT (CMT-ADV), and the advanced pulse CMT (CMT-PAD) [15]. As the CMT technique, an advanced welding process has found application in many industries, the research on this technique is continuously attempted for improvement. This research is focused on understanding the effect of various parameters (like current, welding speed, and shielding gases) on different

^{*} Corresponding author.

E-mail address: iindrajeett@gmail.com (I.J. Singh).

<https://doi.org/10.1016/j.jer.2023.12.009>

Received 11 October 2023; Received in revised form 21 December 2023; Accepted 23 December 2023

Available online 30 December 2023

2307-1877/© 2023 The Author(s). Published by Elsevier B.V. on behalf of Kuwait University. This is an open access article under the CC BY-NC-ND license (<http://creativecommons.org/licenses/by-nc-nd/4.0/>).



Effect of Welding Speed on Metallurgical Characterization of CMT Welding of Dissimilar Aluminium Alloys of AA6061 and AA8011

Indra Jeet Singh¹ · Qasim Murtaza¹ · Paras Kumar¹

Received: 21 February 2024 / Accepted: 21 March 2024 / Published online: 5 April 2024
© The Author(s), under exclusive licence to Springer Nature B.V. 2024

Abstract

Dissimilar AA6061 and AA8011 aluminum alloys were subjected to Cold Metal Transfer (CMT) welding using ER4043 (Si-rich) filler wire. The study focused on establishing correlations between the mechanical properties and microstructure of the welded joints. Microstructural analysis unveiled an equiaxed dendritic structure at the weld center and elongated grains at the periphery of the partially molten zone (PMZ). The XRD results indicated the presence of α -Al, Mg_2Si , and $Al_{13}Fe_4$ intermetallic phases in the PMZs and the weld center. The equiaxed dendrite structure in the WFZ contributed to higher hardness and strength, which can be attributed to the dilution effect and the absence of defects. The interface region on the AA8011 side exhibited enhanced tensile strength and microhardness due to the higher volume of fine secondary phases in the PMZ and finer grains at the WFZ. This comprehensive analysis sheds light on the intricate relationship between mechanical properties and microstructure of the CMT-welded joints, providing valuable insights into the factors influencing the integrity of the welds and interface regions. The maximum tensile strength (97.39 MPa) was observed at a current of 70 A with a welding speed (WS) of 20 mm/s, while the minimum tensile strength (79.84 MPa) was perceived at a WS of 5 mm/s with a current of 50 A.

Keywords CMT welding · Microhardness · Tensile strength · Microstructure

1 Introduction

The CMT technique is an advanced development of the Metal Inert Gas (MIG) welding method. Contrary to its name, "cold" primarily refers to its fusion welding approach, characterized by minimal thermal heat input (THI). This results in negligible distortion, even during short-circuiting due to a non-zero current [1]. A groundbreaking aspect of CMT lies in its wire movement control. It uses digital process control to regulate the power supply during short circuits, ensuring precise wire retraction and detachment of the liquid metal droplet from the wire tip. This method distinguishes itself from MIG welding by minimizing the impact of electromagnetic force, leading to reduced heat input and weld spatter [2]. In the present scenario, aluminum is being used as a substitute for steel in several industries, such as aerospace, shipbuilding, automotive vehicle body parts,

boiler manufacturing, external and internal body panels, and structural and weldable components. The main factor that intensifies the adoption of aluminum over steel is its lightweight, significantly reducing the transportation cost and energy consumed by the vehicle, paralleling sustainable environmental needs. Aluminum and its alloys are known for their excellent corrosion resistance and high strength. AA 8011 comprises the main alloying elements of Si, Fe, and Mn [3]. Al 8011 offers excellent corrosion resistance against oxidation because of its high Mg (0.05%) and Mn (0.20%) content. The mechanical properties like hardness or strength of Al 8011 can be enhanced by heat treatment, reducing the chances of crack formation. Globally, thin aluminum sheets are gaining momentum across industries, especially in the automotive sector. Their popularity stems from attributes like lightweight, durability, and recyclability, prompting car manufacturers to embrace the trend. The resultant products are receiving commendable market response [4, 5]. Adopting these sheets translates to lighter vehicles, enhancing fuel efficiency and engine performance. Various aluminum grades stand out for their pivotal role in vehicle components, contributing to weight reduction. In essence, aluminum

✉ Indra Jeet Singh
iindrajeett@gmail.com

¹ Mechanical Engineering Department, Delhi Technological University, Delhi, India



Effect of CMT Welding Process Parameters on the Microstructural and Mechanical Properties of Dissimilar Aluminum Alloys of AA8011 and AA6061

Indra Jeet Singh¹ · Qasim Murtaza¹ · Paras Kumar¹

Received: 21 February 2024 / Accepted: 24 November 2024 / Published online: 13 December 2024
© The Indian Institute of Metals - IIM 2024

Abstract The cold metal transfer welding process is a highly effective joining process of similar and dissimilar aluminum alloy plates due to its minimal spatter, stable arc, and low heat input. This work focuses on the joining of dissimilar alloys AA8011 and AA6061 with filler wire of ER4043 with different process parameters and investigates the correlation between the microstructure and mechanical properties of the weldments. Microstructural analysis revealed the presence of coarse grains along the partially melted zone (PMZ) boundaries and the equiaxed dendritic structures at the welded region. The equiaxed dendritic morphology in the weld fusion zone (WFZ) revealed enhancement of weld strength and hardness value, mainly due to effective dilution and the nonappearance of welding defects. This study highlights the complex interactions between microstructural features and mechanical performance in the weldments. The welded zone exhibited increased microhardness and tensile strength, resulting from the presence of delicate secondary phases in the weldments and a refined grain structure in the WFZ. X-ray diffraction confirmed the formation of critical intermetallic phases, including $Al_{13}Fe_4$, Mg_2Si , and $\alpha-Al$, distributed across the PMZ and welded region. The minimum ultimate tensile strength (UTS) of 79.84 MPa was perceived for sample-1, while the maximum UTS of 97.39 MPa was observed for sample-3. Overall, the study concludes that controlling the process parameters minimizes defects like phase imbalance and porosity while maintaining homogeneous properties.

Keywords Microstructure · Tensile strength · Microhardness · CMT welding

1 Introduction

The CMT welding process represents an advancement in the MIG welding process. Despite its name suggesting a “cold” process, CMT is characterized by its low thermal heat input (THI), which is crucial for minimizing distortion and controlling the welding process more precisely during short circuits when current is present [1].

Aluminum has increasingly replaced steel in various industries, such as aerospace, shipbuilding, and automotive manufacturing, due to its favorable properties. Aluminum alloys, including AA 8011, are particularly valued for their high strength-to-weight ratio and excellent corrosion resistance. AA 8011 contains silicon (Si), iron (Fe), and manganese (Mn) as its primary alloying elements [2]. Its resistance to corrosion is further enhanced by its magnesium (0.05%) and manganese (0.20%) content, which improves its oxidation resistance. Moreover, heat treatment can enhance the mechanical properties of AA 8011, such as hardness and UTS, and reduce the risk of crack formation during fabrication and welding. The critical feature of CMT is its digital control system, which regulates the power supply efficiently during short circuits, ensuring smooth wire retraction and accurate detachment of molten metal droplets from the wire tip. This control minimizes the impact of electromagnetic forces, which in turn reduces heat input and weld spatter, distinguishing it from traditional MIG welding methods [3]. Welding thin aluminum sheets presents unique challenges due to aluminum's distinct thermal properties compared to steel. The high thermal conductivity and low melting point of aluminum can lead to issues such as over-penetration,

✉ Indra Jeet Singh
iindrajeett@gmail.com

¹ Mechanical Engineering Department, Delhi Technological University, Delhi, India



ORIGINAL RESEARCH ARTICLE

Multi-Response Optimization of Process Parameters for Cold Metal Transfer Welded Joints of Dissimilar Alloys AA8011 and AA6061

Indra Jeet Singh , Qasim Murtaza, and Paras Kumar

Submitted: 23 March 2025 / Revised: 20 May 2025 / Accepted: 5 June 2025

AA8011 and AA6061 alloys are particularly suited for applications in the aerospace, automotive, and packaging industries, where weight reduction, durability, and reliable mechanical performance are critically important. This study focuses on optimizing the input parameters and evaluating the output responses of AA8011 and AA6061 alloy joints fabricated using the cold metal transfer (CMT) welding process. These alloys were joined using filler ER4043, with a comprehensive microstructural and mechanical analysis conducted on the weldments. Microstructural observations revealed elongated grains in the partially melted zone (PMZ) and equiaxed dendritic at the weld fusion zone (WFZ), enhancing hardness and strength due to the absence of welding defects and effective dilution. The maximum ultimate tensile strength (UTS) of 109 MPa was recorded for sample number 11, while the minimum UTS of 73 MPa was observed for sample number 5. Enhanced hardness and UTS in the welded zone were attributed to the occurrence of a refined grain structure and delicate secondary phases in the WFZ. This work provides critical insights into the intricate correlation between input and output responses of the CMT welded joints of AA6061 and AA8011 dissimilar aluminum alloys. The findings underscore the importance of optimizing welding parameters to achieve superior mechanical properties and structural integrity in dissimilar aluminum alloy joints. The optimized input parameters, current, WS, and GFR were observed as 77.86 A, 9.26 mm/s, and GFR of 15.26 l/min, respectively. While optimized output value for tensile strength, % strain, hardness, and residual stress were observed 89.19 MPa, 11.36, 78.88 HV, and – 36.47 MPa, respectively.

Keywords cold metal transfer, microstructure, response surface methodology (RSM), tensile strength

1. Introduction

CMT welding is a controlled short-circuiting arc welding process that uses pulsed currents to improve heat control, enhancing weld quality, minimizing spatter, and enabling precision in thin material welding, it operates with minimal thermal heat input (THI), which reduces distortion (Ref 1). The defining feature of CMT is its precise control over wire movement through digitally control process. This control allows for accurate wire separation and retraction of the molten droplets, minimizing the influence of electromagnetic forces and reducing both heat input and weld spatter (Ref 2).

This invited article is part of a special topical issue of the Journal of Materials Engineering and Performance on Advances in Dissimilar Welding. The issue was organized by Dr. Chandan Pandey, Indian Institute of Technology, Jodhpur; Dr. Sachin Sirohi, SRM Institute of Science and Technology Delhi, NCR Campus; Prof. Dariusz Fydrych, Gdańsk University of Technology; and Dr. Shailesh Mani Pandey, National Institute of Technology, Patna.

Indra Jeet Singh, Qasim Murtaza, and Paras Kumar, Mechanical Engineering Department, Delhi Technological University, Delhi, India. Contact e-mail: iindrajeett@gmail.com.

Abbreviations

CMT	Cold metal transfer
PMZ	Partially melted zone
XRD	X-ray diffraction
IMC	Intermetallic compound
UTS	Ultimate tensile strength
WFZ	Weld fusion zone
HAZ	Heat-affected zone
HVAC	Heating, ventilation, and air-conditioning
WFS	Wire feed speed
WMH	Weld metal hardness
PMMs	Predictive mathematical models
ALC	Arc length correction
MIG	Metal inert gas
SEM	Scanning electron microscopy
RSM	Response surface methodology
TS	Traverse speed
GFR	Gas flow rate
MH	Microhardness
EDM	Electrical discharge machining
WS	Welding peed

Aluminum is increasingly replacing steel in various automobile, shipbuilding, and aerospace industries due to its lightweight and excellent mechanical properties. The reduced weight lowers transportation costs and improves energy



TECHNICAL ARTICLE

Optimization of Process Parameters and Microstructural Analysis of CMT Welded Joints of Dissimilar Aluminum Alloys

INDRA JEET SINGH ^{1,2} QASIM MURTAZA,¹ and PARAS KUMAR¹

1.—Mechanical Engineering Department, Delhi Technological University, Delhi, India.
2.—e-mail: iindrajeett@gmail.com

This study optimizes process parameters and evaluates the mechanical properties and microstructural analysis of CMT-welded joints of dissimilar alloys of AA6061 and AA8011. Welding was performed using ER4043 filler wire, followed by a comprehensive characterization of the weldments to establish the correlation between mechanical properties and microstructure. Detailed metallographic analysis revealed elongated grains within the partially melted zone (PMZ) and fine, equiaxed dendritic structures in the weld fusion zone (WFZ). These microstructural features improved hardness and tensile strength, primarily due to the defect-free weld formation and effective material mixing under optimized CMT conditions. X-ray diffraction (XRD) analysis confirmed the formation of intermetallic compounds (IMCs), particularly Mg_2Si and $\text{Al}_{13}\text{Fe}_4$. Mechanical testing demonstrated that at a welding current of 100 A, welding speed of 12 mm/s, and gas flow rate of 14 l/min, the highest ultimate tensile strength (UTS) was 117.84 MPa, whereas at a welding current of 90 A, welding speed of 12 mm/s, and gas flow rate of 16 l/min, the lowest value was 68.92 MPa. The enhanced mechanical performance is attributed to refined grain structures and uniformly dispersed strengthening phases in the WFZ.

INTRODUCTION

CMT welding is an advanced short-circuiting arc welding technique that allows precise control over heat input. By using pulsed currents and a digitally controlled wire feed, CMT enables the controlled transfer of molten droplets, which minimizes the effect of electromagnetic forces on the weld pool. This precise control reduces spatter and allows for low heat input, which is particularly advantageous when joining thin materials, as it mitigates distortion and maintains weld quality. The CMT process balances heat management and deposition rate, ensuring consistent weld formation and reliability, even in complex Al assemblies.^{1,2} Al alloys are increasingly used in the automobile, aerospace, and marine sectors. These characteristics contribute to reduced vehicle weight, improved fuel efficiency, and lower environmental impact. AA8011 is a

widely utilized Al alloy in industrial applications because its combination of iron, silicon, and manganese provides excellent strength and corrosion resistance.^{3–5} AA6061, part of the 6xxx series, is valued for its high mechanical strength due to its magnesium and silicon content, making it suitable for vehicle structural components.^{6–9} However, welding Al alloys presents unique challenges. Al's high thermal conductivity and low melting point can result in excessive distortion, poor weld penetration, and defects such as porosity if heat input is not carefully controlled. CMT welding addresses these challenges by providing precise heat management and minimizing spatter, making it suitable for joining thin Al sheets. Argon (Ar) is commonly used as the shielding gas, offering better ionization characteristics and thermal conductivity than helium, which enhances arc stability, weld penetration, and overall quality.¹⁰ The process also enables the fabrication of tailor-welded blanks, which combine Al alloys into a single component, and it reduces vehicle weight, optimizes component strength, and improves fuel efficiency in high-

(Received May 22, 2025; accepted September 23, 2025)



An overview of cold metal transfer welding of similar materials

Indra Jeet Singh¹ · Paras Kumar¹ · Qasim Murtaza¹

Received: 24 September 2023 / Accepted: 11 December 2023

© The Author(s), under exclusive licence to Springer-Verlag France SAS, part of Springer Nature 2024

Abstract

This review paper offers a comprehensive analysis of the cold metal transfer (CMT) welding process in the context of similar metals and alloys. With a focus on recent advancements and key research contributions, the paper synthesizes a wealth of information to provide an understanding of the technique's applicability and potential in welding similar metals and alloys. By delving into the intricate interplay of process parameters, such as welding current, wire feed speed and shielding gas composition, the paper elucidates their influence on critical aspects of weld quality, including bead morphology, microstructure, and mechanical properties. In summation, this review consolidates the collective knowledge surrounding CMT welding of similar metals and alloys, providing researchers, practitioners, and industries with a comprehensive resource to navigate the intricacies of this technique. As the industrial landscape seeks to elevate welding standards, minimize post-weld processing, and optimize resource utilization, the insights presented in this review pave the way for the continued evolution and widespread adoption of CMT welding in the field of similar metals and alloys.

Keywords Cold metal transfer welding · Similar metals · Microstructure · Bead morphology · Mechanical properties

1 Introduction

Cold metal transfer (CMT) welding is a novel technique for joining similar and dissimilar metals. It offers advantages such as reduced heat input, clear weld morphology, and high reproducibility. CMT welding has been successfully used for joining aluminum alloy to galvanized low carbon steel, resulting in visually acceptable welds with clear fish-scale ripples [1]. Friction stir welding (FSW) is another non-fusion process that has been employed for steel-aluminum joining, offering a viable alternative for dissimilar welding [2]. CMT welding technique, an improvised version of gas metal arc welding (GMAW), has been found to be ideal for joining thin sheets and plates, with reduced spatter and distortion [3]. The growth of intermetallic compounds (IMCs) in Al/steel dissimilar joints, particularly the Fe₂Al₅ layer, significantly affects joint strength and reliability [4]. Twin-wire

CMT with Al–Si filler has been used for dissimilar joining of stainless steel and aluminum, resulting in satisfactory joint performance with the presence of IMCs [5]. The use of cold metal transfer (CMT) welding technique for dissimilar metal welding has gained significant attention due to its ability to produce improved weld bead aesthetics, controlled metal deposition, and low heat input [6]. This method has been particularly effective in joining dissimilar metals, such as aluminum and steel, with better results than other welding techniques [7]. The process parameters and material properties play a crucial role in achieving a good welding joint [8]. Recent advancements in CMT welding have focused on enhancing the mechanical properties of aluminum alloys and improving the efficiency of the welding system [9]. However, further research is needed to address the challenges and improve the methods for joining dissimilar metals using CMT welding.

CMT stands for cold metal transfer and is known for its ability to minimize distortion and reduce the risk of effects in welded joints. It achieves this by using a controlled short-circuiting transfer mode, resulting in precise and controlled heat input. Additionally, CMT offers improved control over the welding process, making it suitable for applications requiring high-quality welds with minimal spatter. Contrary to conventional welding, CMT welding utilizes an

✉ Indra Jeet Singh
iindrajeett@gmail.com

Paras Kumar
paraskumar@dtu.ac.in

Qasim Murtaza
qasimmurtaza@dce.ac.in

¹ Delhi Technological University, New Delhi, India

An Overview of Dissimilar Metals Welding by Cold Metal Transfer Technique

Indra Jeet Singh^{1*}, Paras Kumar², Qasim Murtaza³

Abstract

Cold Metal Transfer (CMT) welding has emerged as a promising technique for joining dissimilar materials, offering enhanced weld quality and mechanical properties. This review article explores the application of CMT welding in joining different metal alloys, focusing on two significant cases: magnesium-aluminium and aluminium-stainless steel combinations. CMT welding minimizes intermetallic compound formation and produces high-strength joints in magnesium-aluminium combinations. CMT welding with a friction-surfaced aluminum coating offers strong metallurgical bonding in aluminum-stainless steel joints. Precise penetration control and superior tensile strength compared to MIG welding are notable advantages. Optimizing welding parameters and understanding microstructure characteristics are crucial for successful CMT welding of dissimilar materials, presenting promising applications across industries. The review also discusses the impact of welding parameters on the properties of CMT-welded joints, emphasizing the importance of optimizing these parameters to achieve desired results.

Keywords: Cold Metal Transfer (CMT), Microstructure, Mechanical properties, Dissimilar metals.

INTRODUCTION

Cold metal transfer (CMT) welding is a technique used for joining different fragile metals metals using low-power and green technology processes [1]. It has gained interest due to its potential to reduce heat input, improve gap-bridging ability, and increase deposition rate [2]. CMT welding has been applied in various industries, including aerospace, for fabricating aluminum structures [3]. The technique involves using a welding wire that is fed into the weld pool in a controlled manner, resulting in a stable arc and reduced spatter [4]. The quality of CMT welds depends on parameters such as welding speed, accuracy, and the depth of the weld root into the base material [5]. CMT welds' weld geometry and failure modes have been studied to determine the ultimate shear strength and accurately predict failure modes. Overall, CMT welding offers advantages such as low power consumption, improved weld quality, and the ability to join dissimilar metals.

CMT welding stands out as an advanced and increasingly important technique, particularly in the realm of welding dissimilar materials. This innovative method provides practical and effective strategies for the seamless joining of aluminum alloys, encompassing series such as 2xxx, 5xxx, 6xxx, and 7xxx because of low heat input, precision droplet detachment, minimal spatter, distortion reduction and versatility in aluminium alloys [6]. With its adaptability to various aluminum alloys, including series 2xxx, 5xxx, 6xxx, and 7xxx, CMT welding emerges as a preferred choice. Its versatility addresses the diverse needs of industries working with different aluminum alloys. It has been found that CMT

*Author for Correspondence

Indra Jeet Singh

¹PhD Scholar, Mechanical Engineering Department, Delhi Technological University, Delhi, India

^{2,3}Professor, Mechanical Engineering Department, Delhi Technological University, Delhi, India

Received Date: October 30, 2023

Accepted Date: December 23, 2024

Published Date: April 01, 2024

Citation: Indra Jeet Singh, Paras Kumar, Qasim Murtaza. An Overview of Dissimilar Metals Welding by Cold Metal Transfer Technique. Journal of Polymer & Composites. 2023; 11(Special Issue 13): S167–S174.

Qasim Murtaza

Dissertation for Plagiarism.pdf

 Delhi Technological University

Document Details

Submission ID

trn:oid:::27535:122280533

Submission Date

Nov 21, 2025, 7:25 PM GMT+5:30

Download Date

Nov 21, 2025, 7:31 PM GMT+5:30

File Name

Dissertation for Plagiarism.pdf

File Size

9.1 MB

144 Pages**54,024 Words****308,199 Characters**





9% Overall Similarity

The combined total of all matches, including overlapping sources, for each database.




Filtered from the Report

- Bibliography
- Quoted Text
- Cited Text
- Small Matches (less than 10 words)

Match Groups



-  **257 Not Cited or Quoted 9%**
Matches with neither in-text citation nor quotation marks
-  **0 Missing Quotations 0%**
Matches that are still very similar to source material
-  **0 Missing Citation 0%**
Matches that have quotation marks, but no in-text citation
-  **0 Cited and Quoted 0%**
Matches with in-text citation present, but no quotation marks

Top Sources

- 1%  Internet sources
- 8%  Publications
- 2%  Submitted works (Student Papers)

Integrity Flags

2 Integrity Flags for Review

-  **Replaced Characters**
26 suspect characters on 15 pages
Letters are swapped with similar characters from another alphabet.
-  **Hidden Text**
5 suspect characters on 5 pages
Text is altered to blend into the white background of the document.

Our system's algorithms look deeply at a document for any inconsistencies that would set it apart from a normal submission. If we notice something strange, we flag it for you to review.

A Flag is not necessarily an indicator of a problem. However, we'd recommend you focus your attention there for further review.

Indra Jeet Singh

Phd Mechanical Engineering
Department of Mechanical Engineering
Delhi Technological University, Delhi,
India, 110042



Profile Summary

A dedicated and result-oriented Mechanical Engineering professional with a PhD from Delhi Technological University (DTU). Gold Medalist in M.Tech from Galgotias University and First-Class B.Tech graduate from UPTU. Strong research background with multiple SCI/ESCI publications and a patent. Skilled in CAD design tools, including SolidWorks, AutoCAD, and Simufact.

Educational Qualifications

PhD in Mechanical Engineering
Delhi Technological University (DTU)
Published 6 SCI papers, 3 ESCI papers, and filed 1 patent.

M.Tech in Automobile Engineering
Galgotias University
Gold Medalist for academic excellence.

B.Tech in Mechanical Engineering
Uttar Pradesh Technical University (UPTU)
Graduated with First Class.

Technical Skills

Design Software: SolidWorks, AutoCAD, Simufact

Research Skills: Experimental design, material testing, data analysis, welding process optimization.

Tools & Techniques: CMT welding, mechanical testing (UTM), microscopy, DOE approaches.

Research Output

SCI Publications: 6

ESCI Publications: 3

Patent: 1 filed

Areas of Expertise

Welding of dissimilar materials, Cold Metal Transfer (CMT) welding, Mechanical characterization, CAD modelling, Design and analysis